Development and Validation of an *In Vitro* Model to Explore Mechanisms of Skeletal Muscle Toxicity

Thesis submitted for the degree of
Doctor of Philosophy
at the University of Leicester

By William Dott

Department of Cardiovascular Sciences
University of Leicester
2014

Abstract

Development and Validation of an *In Vitro* Model to Explore Mechanisms of Skeletal Muscle Toxicity

William Dott, Cardiovascular Department, University of Leicester

The validation of *in vitro* skeletal muscle models may play a pivotal role in capturing safety endpoints early within the research and development process. Therefore, the primary aim of this project was to investigate the extent of translation from an *in vivo* rat model to an *in vitro* skeletal muscle model, using a toxicogenomics approach. To this end, the mechanisms of toxicity of three novel sulfonyl isoxazoline (SI) herbicides (two triazoles and one phenyl) developed by Syngenta were investigated *in vivo* and *in vitro*. *In vivo* histopathology studies identified striated muscle as the target organ of SI triazole toxicity, and the stomach and liver as the target organs of SI phenyl toxicity. Mechanistic toxicogenomics was carried out on liver, heart and skeletal muscle tissues from rats treated with sub-toxic doses of the SI triazoles (177 and 197) and phenyl (907) compounds for 28 days. The biological processes perturbed by SI triazoles included mitochondrial dysfunction, oxidative stress, energy metabolism, cell death, protein regulation and cell cycle. In contrast, perturbation of cholesterol biosynthesis was identified as the SI phenyl mechanism of toxicity. Using an *in vitro* rat skeletal muscle cell line (L6), it was demonstrated that the SI triazoles induced mitochondrial dysfunction, mitochondrial superoxide production, cell cycle arrest, hypertrophy and apoptosis. These *in vitro* results were consistent with the *in vivo* toxicogenomics data, providing validation that these models may predict skeletal muscle toxicity. To increase detection of xenobiotic-induced mitochondrial effects in skeletal muscle, L6 cells were forced to rely on mitochondrial oxidative phosphorylation by substituting galactose for high glucose in the growth media. In galactose-grown cells, oxygen consumption was increased, glycolysis was repressed and susceptibility to mitochondrial toxicants correspondingly increased. Future work should aim to further develop the L6 model to better mimic the *in vivo* model using 3D and microfluidic technologies.

Acknowledgements

I would like to start by thanking the BBSRC and Syngenta for providing the funding that made this project a reality. Syngenta have been a fantastic company to work with and they have given me a real insight into the industrial side of scientific research. A special thanks to my industry supervisors, Pratibha Mistry and Jayne Wright at Syngenta, who have always provided me with encouragement, support and good advice. Without Pratibha's enthusiasm, hard work and dedication this project would not have been possible, so I am incredibly grateful to her. It has been a real pleasure to get to know and work with both Pratibha and Jayne and I shall miss our catch up meetings in the local curry house.

A massive thank you to my academic supervisor, Dr. Karl Herbert, whose guidance, knowledge and sense of humour has got me through these past four years. Karl has been a great supervisor and a good friend and his patience and understanding have always been appreciated. It has been a lot of fun being part of the Herbert group and so thank you to all those past and present members who have made my experience so enjoyable and memorable. Thank you also to all my colleagues at the CVS department. We have shared a lot of great times, beers and cakes over the years and it's been a great department to be apart of.

There are a number of people I would like to thank who have provided invaluable assistance with experimental techniques and equipment. A big thanks to Helen Collins (for helping me to grind my way through all the RNA extractions), Reshma Vaghela and Nicolas Sylvius (who were instrumental in the completion of the microarray work), Tim Gants group at the MRC Toxicology Unit and Tim Barnes (for providing vital assistance with the microarray analysis) and Kelvin Caine and his group at the MRC Toxicology Unit (who provided the technical equipment and expertise for the XF analyzer work). Thank you also to all those people who have provided me with any help and encouragement throughout this project.

Last, but by no means least, a massive thank you to all my family and friends. Their support and encouragement has provided me with the fuel to carry out this project and I am eternally grateful to them all.

Contents

List of Figures

List of Tables

List of Abbreviations

%	Percent
~	Approximately
<	Less than
>	More than
±	Plus or minus
≤	Less than or equal to
≥	More than or equal to
°C	Degrees centrigrade
2D	Two-dimensional
2-DG	2-deoxyglucose
3D	Three-dimensional
3R's	Reduction, replacement and refinement
5-HT6	5-hydroxytryptamine 6
AA	Ascorbic acid
ACC2	Acetyl CoA carboxylase 2
ADME	Absorption, distribution, metabolism, and excretion
ADP	Adenosine diphosphate
AhR	Aryl hydrocarbon receptor
AIF	Apoptosis inducing factors
AKT	Protein kinase B
ALT	Alanine aminotransferase
AMA	Antimycin A
Ames	Ames bacterial mutagenesis
AMP	Adenosine monophosphate
AMPK	Amp-activated protein kinase
ANOVA	Analysis of variance
ANT	Adenine nucleotide translocase
APAP	Acetaminophen
ARE	Antioxidant response elements
AST	Aspartate aminotransferase
ATCC	American type culture collection
ATP	Adenine triphosphate
AUC	Area under curve
Ca^{2+}	Calcium
$CaCl_2$	Calcium chloride
CACT	Carnitine–acylcarnitine translocator
CCK-8	Cell counting kit-8
cDNA	Complementary dna
CK	Creatine kinase
C_{max}	Maximum concentratino in test system
CO_2	Carbon dioxide
CoA	Coenzyme A
CoQ	Coenzyme Q10
CPA	Cyclophosphamide

CPD	Cumulative population doublings
CPT	Carnitine palmitoyltransferase
cRNA	Complementary rna
cTnI	Cardiac troponin I
cTnT	Cardiac troponin T
CYP	Cytochrome p450
CytC	Cytochrome c
D	Day
DAVID	Database for annotation visualisation and integrated discovery
DEG	Differentially expressed gene
DEPC	Diethylpyrocarbonate
dH_2O	Distilled water
DHA	Dehydroascorbate
DHE	Dihydroethidium
DIC	Dicarboxylate carrier
DMEM	Dulbecco's modified eagle's medium
DMSO	Dimethyl sulfoxide
DNA	Deoxyribonucleic acid
DNase	Deoxyribonuclease
dNTPs	Deaoxynucleotide triphosphates
DOX	Doxorubicin
DPBS	Dulbecco's phosphate-buffered saline
DT	Doubling time
DTT	Dithiothreitol
ECAR	Extracellular acidification rate
EDTA	Ethylenediaminetetraacetic acid
eiF2	Eukaryotic initiation factor 2
eiF4	Eukaryotic initiation factor-4
EPA	Environmental protection agency
ER	Endoplasmic reticulum
ERK	Extracellular signal-regulated kinases
ERRα	Estrogen-related receptor alpha
ETC	Electron transport chain
EtOH	Ethanol
FA	Fatty acids
FACS	Fluorescence-activated cell sorting
FAD	Flavoprotein
FAD+	Flavin adenine dinucleotide
$FADH_2$	Flavin adenine dinucleotide
FAO	Fatty acid oxidation
FBS	Foetal bovine serum
FC	Fold change
FCCP	Carbonyl cyanide p-[trifluoromethoxy]-phenyl-hydrazone
FDR	False discovery rate
FITC	Fluorescein isothiocyanate
FSC	Foward scatter
FWER	Family-wise error rates

FXR	Farnesoid x receptor
g	G-force
GADD45a	Growth arrest and DNA-damage-inducible protein45 alpha
GCL	Glutamate cysteine ligase
GCN2	Eif2a kinase
Genomics	Gene expression profiling
GGPP	Geranylgeranylpyrophosphate
GGT	Gamma-glutamyltransferase
GLDH	Glutamate dehydrogenase
GO	Gene ontology
GPCRs	G protein coupled receptors
GSH	Glutathione
GST	Glutathione-*s*-transferase
H_2O	Water
H_2O_2	Hydrogen peroxide
HBSS	Hank's balanced salt solution
HCA	Hierarchical clustering analysis
HCl	Hydrochloric acid
HCS	High-content screening
HEPES	4-(2-hydroxyethyl)piperazine-1-ethanesulfonic acid sodium salt
hERG	Human *ether-à-go-go*-related gene
hESC-CMs	Human embryonic stem cell–derived cardiomyocytes
HI	Heat-inactivated
HIF	Hypoxia-inducible factor
HMG-CoA	3-hydroxy-3-methyl-glutaryl-coenzyme a
HRI	Heme-regulated eif2a kinase
HTS	High-throughput screening
Hyb	Hybridization
IC50	Half maximal inhibitory concentration
I_{kr}	Delayed rectifier potassium current
IMM	Inner mitochondrial membrane
IMS	Industrial methylated spirits
IMM	In vitro master mix
Inc.	Incorporated
IPA	Ingenuity pathway analysis
IPKB	Ingenuity pathway knowledge base
ISO	Isoproterenol
ITS	Integrated testing strategy
IU	International unit
KCNH2	Potassium voltage-gated channel, subfamily h (eag-related), member 2
kDa	Kilodalton
KEGG	Kyoto encyclopaedia of genes and genomes
kg	Kilogram
LLL	Left lobe liver
LLNA	Local lymph node assay
log	Logarithm
LVH	Left ventricular heart

MAPK	Mitogen-activated protein kinases
MDMA	3,4-methylenedioxymethamphetamine
MEIC	Multicenter evaluation of *in vitro* cytotoxicity
mg	Milligram
Mg^{2+}	Magnesium
min	Minute
miRNA	MicroRNA
ml	Millilitre
MLA	Mouse lymphoma assay
mM	Millimolar
mm	Millimeter
mm^3	Millimeter cubed
MnSOD	Manganese superoxide dismutase
MPTP	Mitochondrial permeability transition pore
mRNA	Messengerrna
mtDNA	Mitochondrial DNA
mTOR	Mammalian target of rapamycin
MTT	3-(4,5-dimethylthiazol-2-yl)-2,5-diphenyltetrazolium bromide
Myopathy	Skeletal muscle injury
Myotoxicity	Skeletal muscle toxicity
NAC	N-acetylcysteine
NaCl	Sodium chloride
NAD+	Nicotinamide adenine dinucleotide
NADH	Reduced nicotinamide adenine dinucleotide
NADPH	Nicotinamide adenine dinucleotide phosphate
NaOH	Sodium hydroxide
NAT	*N*-acetyltransferase
NCBI	National center for biotechnology information
NFkB	Nuclear transcription factor kb
NGS	Next generation sequencing
nm	Nanometer
nM	Nanomolar
NMR	Nuclear magnetic resonance
NO	Nitric oxide
NOEL	No observed effect level
NRC	National research council
Nrf1	Nuclear respiratory factor 1
Nrf2	Nuclear factor (erythroid-derived 2)-like 2
NRs	Nuclear receptors
NRTIs	Nucleotide reverse transcriptase inhibitors
NSAIDs	Non-steroidal anti-inflammatories
nt	Nucleotide
O_2	Molecular oxygen
$O_2^{\bullet-}$	Superoxide
OCR	Oxygen consumption rate
OD	Optical density
OH•	Hydroxyl radical

Oligo(dT)	deoxy-thymine nucleotides
OMM	Outer mitochondrial membrane
OS	Oxidative stress
OXPHOS	Oxidative phosphorylation
p53	P53 tumour suppressor
p70S6K	P70 ribosomal protein s6 kinase 1
PBPK	Physiologically based pharmacokinetic
PC	Principal component
PCA	Principal component analysis
PD	Population doubling
PDH	Pyruvate-dehydrogenase
PDHC	Pyruvate dehydrogenase complex
PE	Phycoerythrin
PERK	PKR-like endoplasmic reticulum kinase
PE-T-R	PE-texas-red
PGC-1α	Peroxisome proliferator-activated receptor gamma co-activator
PI	Propidium iodide
PI3K	Phosphatidylinositide 3-kinases
PiC	Phosphate carrier
PK	Pharmacokinetics
PKR	Protein kinase R
pmf	Protonmotive force
PPAR	Peroxisome proliferator activated receptor
PPAR-α	Peroxisome proliferator activated receptor alpha
ppm	Parts per million
PPP	Pentose phosphate pathway
PS	Phosphatidylserine
PTEN	Phosphatase and tensin homolog
PyC	Pyruvate carrier
qRT-PCR	Quantitative real time PCR
QSAR	Quantitative structure activity relationships
R&D	Research and development
RAR	Retinoic acid receptor
RCR	Respiratory control ratio
REACH	Registration, evaluation, authorisation and restriction of chemicals
RefSeq	Reference sequence
RET	Reverse electron transport
RhoA	Ras homolog gene family, member a
RIN	RNA integrity number
RLU	Relative light Units
RNA	Ribonucleic acid
RNase	Ribonuclease
RNS	Reactive nitrogen species
ROS	Reactive oxygen species
rpm	Revolutions per minute
rRNA	Ribosomal RNA
RT	Room Temperature

RXRα	Retinoid x receptor alpha
RyR	Ryanodine receptors
S	Supplementary
SD	Standard deviation
Sec	Second
SEM	Standard error of the mean
SI	Sulfonyl isoxazoline
SNPs	Single nucleotide polymorphisms
SOD	Superoxide dismutase
SRS	Standard reaction solution
SSC	Side scatter
SSMM	Second strand master mix
SULT	Sulfotransferase
TCA	Tricarboxylic acid cycle
TdP	*Torsades de pointes*
TMM	Transcription master mix
TMRE	Tetramethylrhodamine, ethyl ester, perchlorate
Tn	Troponin
Top2α	Topoisomerase-iiα
Top2β	Topoisomerase-iiβ
Tox	Toxicity
Toxicogenomics	Application of genomics to toxicology
TPP	Triphenylphosphonium
TRAIL	Tnf-related apoptosis-inducing ligand
tRNA	Transfer RNA
TSM	Thigh skeletal muscle
UCP	Uncoupling proteins
UGT	Udp-glucuronosyltransferase
UPP	Ubiquitin-proteasome pathway
UQ	Ubiquinone
UV	Ultra violet
V	Volts
$^{v}/_{v}$	Volume per volume
VEGF	Vascular endothelial growth factor
VLCFA	Very-long-chain-fatty acid
WST-8	2-(2-methoxy-4-nitrophenyl)-3-(4-nitrophenyl)-5-(2,4-disulfophenyl)-2h-tetrazolium
XF	Extracellular flux
XMEs	Xenobiotic metabolizing enzymes
α	Alpha
β	Beta
Δp	Protonmotive force/electrochemical gradient
ΔpH	Ph gradient across the inner mitochondrial membrane
Δψm	Mitochondrial membrane potential
µg	Microgram
µl	Microlitre
µM	Micromolar

CHAPTER ONE

Introduction

1.1 Xenobiotic-induced toxicity

The cost of research and development (R&D) of novel xenobiotics (i.e. a drug or agrochemical that is foreign to living organisms) has been increasing for many years, with the average cost of developing a successful compound estimated at more than £1 billion (Guengerich, 2011). In spite of the increased spending, the decrease in productivity is perhaps the greatest challenge facing the agrochemical and pharmaceutical industries (Kramer *et al*, 2007). One of the major reasons for attrition of compounds 25 years ago was due to poor pharmacokinetics (PK). However, improvement in the throughput and sensitivity of techniques like mass spectrometry and an increased understanding of metabolism and transport of compounds has reduced PK attrition (Guengerich, 2011). As a result, the number one reason for attrition in the development phase of a compound is organ toxicity, accounting for approximately one-third of all cases (Kramer, 2007; Dykens and Will, 2007) (Figure 1.1).

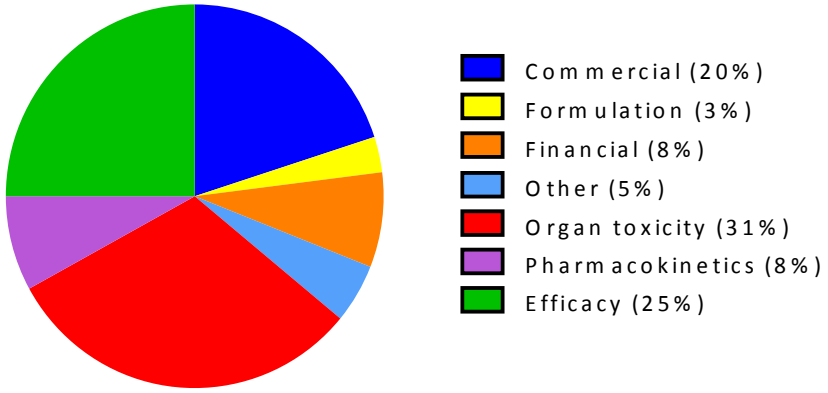

Figure 1.1 Estimated breakdown of attrition of compounds in developmental phase (Guengerich, 2011).

The most common organ toxicities leading to attrition in all stages of R&D are cardiovascular (27.3%) and hepatic (14.8%), and to a lesser extent skeletal muscle (3.4%) (Guengerich, 2011). Of the compounds that were approved by the FDA between 1994 and 2006, 38 have been withdrawn from the market because of safety concerns, the majority being hepatotoxic (14) and cardiotoxic (17) (Dykens and Will, 2007). In addition, skeletal muscle toxicity has become an area of concern, highlighted by the withdrawal of cerivastatin from the market in 2001 due to potentially fatal

muscle injury (rhabdomyolysis) (Charatan, 2001). Furthermore, the incidence of skeletal muscle injury is becoming increasingly more prevalent in the R&D of novel compounds (Vassallo *et al*., 2009). As a consequence, much research is now focused on identifying adverse toxicities early in the R&D process to improve the design and/or selection of xenobiotic candidates that are safe and effective.

Xenobiotic-induced toxicity can be broadly categorised into 5 classes on the basis of the mechanism underlying toxicity (Table 1.1). Although these categories are historically established, well-recognized concepts and involve clear mechanistic distinctions, there is some mechanistic overlap (Guengerich, 2011). Ultimately, the pathological effect of these toxicities culminates in either cell death/tissue injury, altered phenotype/function, cancer or a combination of each (Liebler and Guengerich, 2005).

Type	Definition	Example	Reference
On-Target	Toxicity that occurs because of modulation to primary target (i.e. enzyme, receptor), whether in the same cell tissue or not	Statins	Itagaki *et al*., 2009
Hypersensitivity and Immunological	Xenobiotics, or their metabolites, react with proteins to induce antibody and immune responses	Pencillin	Padovan *et al*., 1997
Off-target	Adverse effects resulting from interaction of a xenobiotic with targets other than intended target.	Terfenadine	Taglialatela *et al*., 2000
Biological activation	Biological transformation of a xenobiotic to toxic metabolites which often results in organ and tissue-specific toxicity.	Acetaminophen	James *et al*., 2003
Idiosyncratic	Rare toxicities that represent unique susceptibility of affected individuals.	Halothane	Uetrecht *et al*., 2007

Table 1.1 Mechanistic causes of toxicity. (Liebler and Guengerich, 2005; Guengerich, 2011).

1.1.1 Striated muscle toxicity

Cardiac and skeletal muscles are grouped together under the term striated muscle. This refers to the ordered and regular arrangement of the sub cellular contractile elements, the sarcomeres, which have a striped appearance under the microscope. Although cardiac and skeletal muscle appears similar at the cellular and molecular levels, activation and regulation of each has evolved to achieve different, highly-controlled functions (Gordon *et al*.,2001).

1.1.2 Skeletal muscle toxicity

Skeletal muscle accounts for around 45% of total body weight and is characterised by a high rate of blood flow. Consequently, it is highly exposed to circulating xenobiotics (Owczarek *et al*., 2005). In addition, skeletal muscle is one of the most metabolically active tissues, along with the heart and liver, and so requires a large amount of mitochondria for ATP production, making it particularly prone to xenobiotic-induced mitochondrial toxicity (Dykens and Will, 2007; Neustadt and Pieczenik, 2008). Skeletal muscle injury (myopathy) induced by a toxin is referred to as myotoxicity and is defined as the subacute, and rarely acute manifestation of myopathic symptoms such as muscle weakness, fatigue, myalgia, creatine kinase (CK) elevation or myoglobinuria (Dalakas, 2009). Although myopathy is usually a non-fatal injury, it can be potentially life threatening, resulting in rhabdomyolysis, in which skeletal muscle disintegration releases large quantities of toxic muscle cell components into the plasma. Excessive leakage of toxic muscle components, such as myoglobin, can cause direct deterioration of renal function and ultimately renal failure and death (Hohenegger, 2012). Notably, xenobiotics have become frequent causative agents in 81% of cases of rhabdomyolysis (Coco and Klasner, 2004). A wide variety of xenobiotics are known to induce myotoxicity and so xenobiotic-induced myopathies are often categorised according to the type of injury induced in the muscle fibre or specific organelle (Table 1.2).

Some xenobiotics, such as Emetine and colchicines are on-target toxicities and so their side effects are directly linked to their intended mechanism of action. For example,

colchicine, a treatment for gout, inhibits polymerization of microtubules by interacting with tubulin.

Type of myopathy	Common xenobiotics causing myopathy	Reference
Necrotising myopathy	Statins	Kaufmann *et al*., 2006; Itagaki *et al*., 2009
Inflammatory myopathy	Inteferon-α	Venezia *et al*., 2005
Mitochondrial myopathy	Zidovudine	Scruggs and Naylor, 2008
Type II muscle fibre atrophy	Steroids	Schakman *et al*., 2008
Lysosomal storage myopathy	Chloroquine	Kimura, *et al*., 2007
Antimicrotubular myopathies	Colchicine	Choi *et al*., 1999
Myofibrillar myopathy	Emetine	Sieb and Gillessen, 2002
Recreational drugs	Alchohol	Owczarek *et al*., 2005

Table 1.2 . Types of myopathies induced by xenobiotics (Sieb and Gilleson, 2002; Dalakas, 2009).

Since membranous organelles, including lysosomes and autophagic vacuoles, are conveyed along the microtubule-dependent cytoskeletal network, disruption by colchicines results in accumulation of autophagic vacuoles and subsequent injury of the lysosomal membrane (Sieb and Gillessen, 2002). It has been hypothesised that proteolytic enzymes released from injured lysosomes may cause myofibril degeneration in a mechanism similar to chloroquine-induced lysosomal myopathy (Choi *et al*., 1999). This example serves to illustrate that the myopathy-type categories are not mutually exclusive and some compounds fit into more than one category.

Similarly, proposed mechanisms of statin-induced myopathy relate to both necrotising and mitochondrial-type myopathies (Kaufmann *et al*., 2006; Dalakas, 2009). Statins (3-hydroxy-3-methyl-glutaryl-coenzyme A (HMG-CoA) reductase inhibitors) impair cholesterol production by inhibiting mevalonate, a critical intermediary in the cholesterol pathway (Kaufmann *et al*., 2006). Although generally well-tolerated, they can produce myotoxicity ranging from muscle pain to rhabdomyolysis. Notably, cerivastatin was voluntarily withdrawn from the market in August 2001 because of 100 rhabdomyolysis-related deaths (Charaten, 2001). The exact mechanism of statin-induced toxicity is not fully understood, although a number of mechanisms have been proposed. One hypothesis is an ‘on-target’ mechanism, in which a decrease in the

synthesis of isoprenoid intermediates by statins (produced by mevalonate) adversely affects myocyte function. For example, Itagaki *et al* (2009) have shown that a reduction in the mevalonate derivative, geranylgeranylpyrophosphate (GGPP), in L6 muscle cells results in RhoA dysfunction and statin-induced apoptosis. A number of studies have demonstrated that statin-induced mitochondrial impairment could be largely implicated in the deleterious effects of statins (Kaufmann *et al*., 2006; Sirvent *et al*., 2008; Bouitbir *et al*., 2011). It has been proposed that a decrease in the isoprenoid, ubiquinone (coenzyme Q10), which is an essential electron transporter of the mitochondrial electron transport chain (ETC), has a deleterious function on mitochondrial function in skeletal muscle (Marcoff and Thompson, 2007). Investigations have also shown that statins have a direct effect on mitochondrial function by inhibiting complex I of the ETC and interfering with calcium homeostasis (Sirvent *et al*., 2008). Recently, Bouitbir *et al* (2011) have shown that statin-induced mitochondrial reactive oxygen species (ROS) production plays an important role in the pathogenesis of skeletal muscle myopathy. They demonstrated that statins induced a small increase of ROS in cardiac muscle, which activated mitochondrial biogenesis and improved antioxidant capacity. Conversely, in skeletal muscle statins induced a large augmentation of ROS production resulting in oxidative stress and mitochondrial impairments. The authors suggested that the level of ROS induced by statins explained the beneficial role of statins in the cardiac muscle and the toxicity to skeletal muscle (Bouitbir *et al*., 2011).

1.1.3 Cardiac muscle toxicity

Cardiac muscle toxicity (cardiotoxicity) is one of the most common and serious adverse effects associated with xenobiotic insult. Cardiotoxicity is a cause of severe morbidity and mortality due to the relative inability of the myocardium to recover from a significant insult without lasting detrimental effects (Schimmel, 2004; Hirakawa *et al*., 2008). Xenobiotic-induced cardiotoxicity affects all components and functions of the cardiovascular system and can manifest as functional (alteration of the mechanical function of the myocardium) or structural (morphological damage to cardiomyocytes or loss of viability) in nature (Pointon *et al*., 2013). There are examples in almost every class of xenobiotics that have produced unanticipated cardiotoxicity. Well known

among these are the anthracyclines (Simunek *et al*., 2009), trastazumab (Sengupta *et* al*.,* 2008) and other chemotherapeutic drugs (Gradishar and Vokes, 1990). In addition, antiretrovirals, antifungals, antiarrhythmics, antipsychotics, antibiotics and antihistamines have also been associated with cardiotoxicity (Wallace *et al*., 2004).

The most common xenobiotic-induced functional cardiotoxicity is QT interval prolongation, which results in a distinctive polymorphic ventricular arrhythmia, termed *torsades de pointes* (TdP) (Kannankeril *et al*., 2010). The mechanism by which xenobiotics induce QT interval prolongation is almost always by block of the delayed rectifier potassium current, I_{kr} (encoded by KCNH2, formerly termed hERG) (Heist and Ruskin, 2010). The KCNH2 channel is a 'promiscuous' channel and so is blocked by many different classes of xenobiotics with diverse structures (Kannankeril *et al*., 2010).

The mechanisms of structural cardiotoxicity vary and can result in a range of clinical manifestations including hypertension, ischaemia/myocardial infarction, cardiac hypertrophy, cardiomyopathy, and cardiac failure. Perhaps the most studied cardiotoxic compound is the chemotherapeutic agent, doxorubicin. Several hypotheses have been reported for the mechanism of cardiotoxicity, including redox cycling and ROS production, mitochondrial dysfunction through cardiolipin binding and altered iron homeostasis (Pointon *et al*., 2010). A recent study, by Zhang *et al* (2012) showed that doxorubicin cardiotoxicity is not solely due to redox cycling and implicates topoisomerase-IIβ (Top2β) as an essential driver in mitochondrial dysfunction. Doxorubicin binds to Top2α in tumour cells to inhibit growth, and also binds Top2β expressed in cardiomyocytes, which markedly alters the transcriptome, resulting in defective mitochondrial biogenesis and metabolic failure (Zhang *et al*., 2012). Thus, if the reported data are reproducible, doxorubicin cardiotoxicity can be considered an 'on-target' toxicity.

1.2 Bringing Toxicology into the 21st Century

1.2.1 Traditional approach to toxicity testing

Toxicity testing and the assessment of safety of drugs, veterinary products and chemicals are essential in today's society. Toxicology has traditionally focused primarily on the observation of adverse effects in laboratory animals through intensive studies done one chemical at a time (Houck and Kavlock, 2008). Today, *in vivo* toxicity testing accounts for about 10% of animal use, equating to over €2 billion worldwide every year (Hartung and Daston, 2009). Toxicology studies rely heavily on the use of vertebrate animals to evaluate a broad range of toxicological responses in order to classify compounds by their potential for causing adverse health effects. These animal studies include acute, subacute and subchronic and/or chronic tests to identify end points such as target organ lesions (using histopathological examination of tissues and biomarkers) and oral, dermal and ocular toxicity (Xia *et al*., 2008). In addition, these studies aim to identify similarities and differences in sensitivity between species and sexes, and to determine the shape of the dose-response curve (Chhabra *et al.*, 2003). Depending upon the information needed for a particular chemical, these studies may also include the evaluation of a number of other toxicity endpoints that serve as a screen for immunotoxicity, genotoxicity, neurotoxicity or behavioural and reproductive toxicity (Chhabra *et al.*, 2003).

The advantage of testing *in vivo* is that the basic technology is simple and accounts for the complexity of tissue and physiological reactions. In addition, there are animal models for a vast range of toxicant-induced diseases, indicating that the animal models contain the same molecular targets or pathways as humans (Hartung and Daston, 2009). While the animal models are clearly useful, there are a number of disadvantages and shortcomings of the *in vivo* approach. Animal tests are low throughput, relatively expensive and intrinsic differences in species sensitivities hinder the extrapolation of animal data for predicting human responses (Shukla *et al.*, 2010). The use of relatively large numbers of animals raises increasing ethical issues and is inconsistent with emphasis on the reduction, replacement and refinement (3R's) of animal use (Krewski *et al*., 2010). The main problem is the inability to discern

mechanisms of toxicity using the “black box” whole animal assays, making cross-species extrapolation and low-dose, real-life exposure effects difficult to appropriately assess (Houck and Kavlock, 2008). For example, carcinogenicity studies are conducted using a 40-year old model requiring ~400 animals and two years of exposure at a cost of millions of dollars (Houck and Kavlock, 2008). Results of these assays suggest maximal 70% correlation between rodent species implying about 80-90% false-positive findings (Hartung and Daston, 2009).

Notably, there have been huge advancements with *in vitro* testing platforms and technologies that have contributed largely to the biotech revolution of recent years. Regulatory toxicology has embraced them in part, including assays for metabolic activity (cytochrome P450 activity) and genotoxicity (Ames *Salmonella typhiumurium* assay) (Liebler and Guengerich, 2005), although acceptance and adaptation have been slow. One reason for the slow adaptation to the advances in science and technology are the internationally harmonized guidelines in place (Hartung, 2009). However, the increasing public concern over the minimal toxicity information available for thousands of chemicals has resulted in new guidelines implemented by REACH (registration evaluation authorization and restriction of chemicals), which requires a registration of ~30,000 chemical substances over a period of 11 years. This new legislation would require millions of animals and billions of pounds to conduct the appropriate safety assessment with the traditional methods (Houck and Kavlock, 2008). While the current *in vivo* methods would provide useful information on these chemicals, they are low-throughput and a lack of mechanistic understanding makes them inadequate. Therefore, it is important that development, translation and validation of alternative methods for assessing the safety of new (and old) compounds are found that will ensure consumer safety and decrease the reliance on animals. Furthermore, the high rate of compound attrition due to organ toxicity in the R&D of new compounds, as described previously, means there is a need for robust predictive *in vitro* models to identify toxic effects earlier in the R&D process (Van Hummelen and Sasaki, 2010).

1.2.2 The future paradigm for toxicity testing

Toxicity testing is currently undergoing a transformation brought about by the emergence of a large range of advances in molecular biology, cell culture biology, computer science and bioinformatics (Kramer *et al.*, 2009). The future strategy for a new paradigm encompasses the need to; develop a more robust scientific and mechanistic basis for assessing health effects, reduce the cost and time required for toxicity testing, and minimize the use of animals in testing (Andersen and Krewski, 2009). To achieve this strategy, the traditional toxicology assays need to be refined and a new system of toxicity testing, based on rapid, mechanism-based, predictive *in vitro* screens needs to be developed (Hartung, 2009; Shukla *et al*., 2010).

In 2007, the National Research Council (NRC) provided a report on the vision for the future of toxicity testing based around 4 key components; chemical characterisation (e.g. physical and chemical properties, environmental fate and transport, metabolism and interaction with cellular components), toxicity pathways (defined as a 'cellular response pathways, that when sufficiently perturbed, are expected to result in adverse health effects'), targeted *in vivo* testing (to further explore and quantify information obtained by exploring toxicity pathways) and dose-response and extrapolation modelling (which includes dose-response models *in vitro* and/or *in vivo*, physiologically based pharmacokinetic (PBPK) models to extrapolate to human exposure and dose-response models for toxicity pathways) (NRC, 2007). Combined, these elements provide the basis for a more informed assessment of health risks based on deeper understanding of the mode of action by which toxic effects are induced, including the key molecular and biological targets in the pathways (Houck and Kavlock, 2008).

Central to the NRC strategy is the use of high-throughput *in vitro* tests of toxicity pathway responses to characterize the potential for toxicity and understand mechanisms of action (Andersen and Krewski, 2009). An example of a toxicity pathway is the Nrf2 antioxidant-response pathway that is activated in response to oxidative stress (Krewski *et al*., 2010).

An improvement in the mechanistic understanding of toxic events will result in safer drugs and chemicals and a more efficient R&D process (Blomme *et al*., 2009). For example, if more than one compound in a project's lead series exhibits the same toxicity, a mechanistic understanding of the nature of the toxicity provides guidance to discovery chemistry for designing out the toxicity and improves safety margins in back-up programmes (Kramer *et al*., 2007). Moreover, more mechanistic understanding will help elucidate common pathways of toxicity and susceptibility (Sipes *et al*., 2013).

The eventual goal of a future vision is to integrate a range of *in vitro, in silico* and *in vivo* approaches into a high-throughput pathway-based risk assessment, where relevant concentration of compound perturbing a pathway of toxicity can be modelled to predict human risk (Van Vliet, 2011). Targeted *in vivo* testing will always be required to further understand the metabolism and pharmacokinetics of compounds as well as further characterise the mechanisms of toxicity of compounds (Andersen and Krewski, 2009). For example, mechanistic information from *in vivo* toxicity tests could be achieved through examining changes in gene transcript levels (toxicogenomics) in key tissues at end of life studies (Foster *et al.*, 2007).

1.3 Technologies and approaches for toxicity testing

The modern technologies and tools available to improve the current system of toxicity and develop a new testing system are detailed in table 1.3 and include cell-based assays, omics technologies, bioinformatics, image technology, high-throughput testing and *in silico* (computer-based) modelling.

1.3.1 Toxicogenomics

The recent advances in omics technologies, such as microarray, mass spectroscopy, nuclear magnetic resonance (NMR) allow the transcriptome, proteome and metabolome to be investigated (Hewitt and Herget, 2009). Of these bimolecular components, transcriptomics has become the "universal language" with which to

describe cellular processes (Lamb *et al.*, 2006). This is attributed to the high-throughput and highly descriptive data produced by microarrays.

Toxicity testing tools	Summary
Cell-based assays	Cell lines, primary cells and stem cells can be used to assess a range of parameters including, cytotoxicity, metabolism, genotoxicity (Van Vliet, 2011).
High-throughput screening (HTS)	High-throughput screening technology enables screening of compounds with a large range of assays using multi-well plates and relies heavily on automation and robotics. Allows analysis of toxicity pathway perturbations across a range of doses and molecular and cellular targets (Houck and Kavlock, 2008).
Imaging technologies	High content screening of cell-based models enables a range of parameters to be assessed in a high-throughput and quantitative analysis using automated, epifluorescence imaging platforms and robust image analysis platforms. (O'Brien *et al*., 2006; Pointon *et al*., 2013).
Omics technologies	Microarray, mass spectroscopy and nuclear magnetic resonance (NMR) allow the transcriptome, proteome and metabolome to be analysed, respectively (Gatzidou *et al*., 2007).
Bioinformatics	Software is available to interpret complex multivariable data from HTS and 'omic studies in relation to mechanistic investigations and biomarkers discovery. (Huang *et al*., 2009).
Systems biology	The combination of biochemical knowledge of cellular pathways with genomics, proteomics and metabolomics enables a systems biology approach to toxicity testing.
***In silico* modelling**	PBPK (physiology-based pharamaco-/toxico-, kinetic modelling) and QSAR (quantitative structure activity relationships). (Mumtaz *et al*., 2012).
Biomarkers	Biomarkers of biological change representing specific perturbations of toxicity pathways. These biomarkers could be genomic, proteomic or metabolomic in nature. (Hewitt and Herget, 2009).

Table 1.3 Summary of the available tools that can be used for toxicity testing.

Microarrays allow the simultaneous analysis of thousands of genes (through measurement of mRNA levels) under various physiological conditions. Significantly, it provides a detailed overview of the cell-wide changes in gene expression following exposure to a toxin (Gatzidou *et al*., 2007). The application of microarray gene expression profiling (genomics) to toxicology has resulted in the sub-discipline of toxicogenomics (Tennant, 2002). Toxicogenomics, using microarray technologies,

generates a characteristic transcriptional profile that serves as a 'gene expression signature', which is able to detect subtle changes of biochemical and signalling pathways induced by a toxic compound (Afshari *et al*., 2011). Consequently, toxicogenomics can be applied to; mechanistic toxicology, concerned with elucidating mechanisms of toxicity and predictive toxicology, which involves identifying the potential of compounds to induce a specific toxicity response using genomic biomarkers (figure 1.2) (Ellinger-Ziegelbauer *et al*., 2008; Pointon *et al*., 2010, Zhang *et al*., 2012; Nishimura *et al*., 2013). As highlighted in figure 1.2, both of these toxicological applications require the implementation of state-of-the-art bioinformatics tools and methodologies to interpret data (Blomme *et al.,* 2009; Kienhuis *et al.,* 2011).

1.3.1.1 Toxicogenomics for mechanistic toxicology

Since gene expression is of central importance in the response of living systems to xenobiotics, toxicogenomic technologies are highly applicable in mechanistic studies to formulate hypotheses related to the mechanisms of toxicity of well-characterised ('model') and novel compounds (Gatzidou *et al*., 2007; Blomme *et al*., 2009; Afshari *et al*., 2011; Kienhuis *et al*., 2011). Currently, there are two main approaches for identification of mechanisms of toxicity using a gene expression signature. The first involves comparing a gene expression signature of an unknown agent (e.g. a compound or drug) to a group of defined gene signatures (corresponding to well-characterised reference compounds with known mechanisms of toxicity) in a reference database (Lamb *et al*., 2006). A match to a group of gene signatures can provide hypotheses about the underlying mechanism for the unknown agent. The second approach is a functional analysis to enable investigation of the underlying toxicity pathways affected by a compound (Kienhuis *et al*., 2011). Integral to both approaches is the use of bioinformatics tools to analyse and interpret complex datasets.

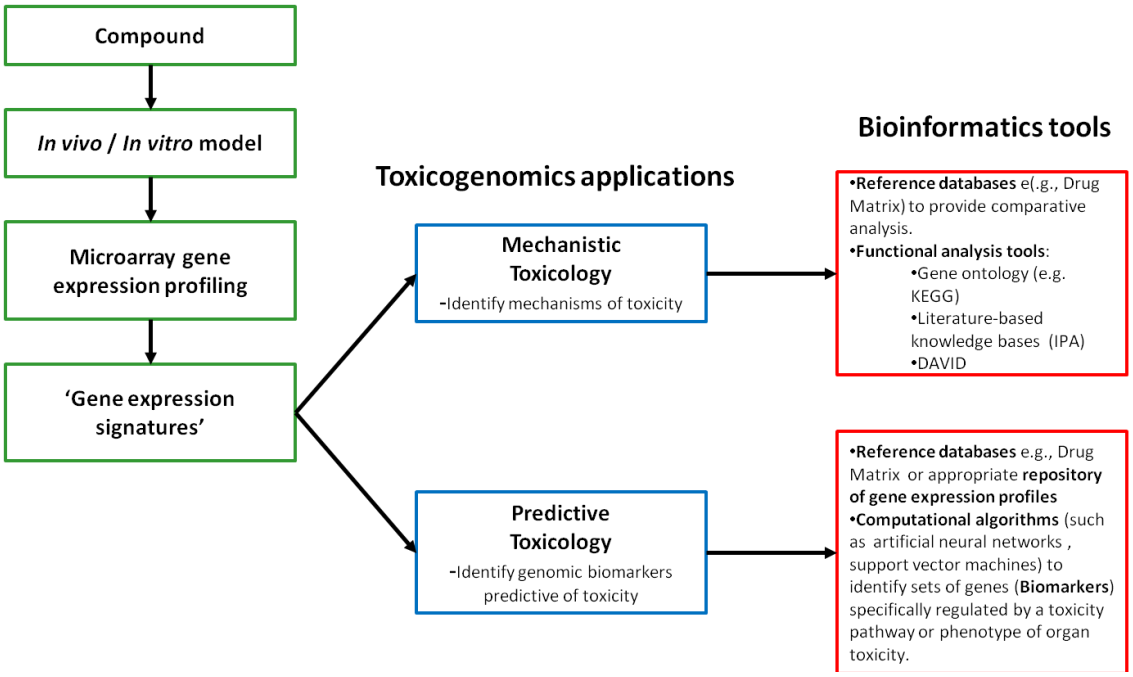

Figure 1.2. An *in vivo / in vitro* model is treated with a compound (i.e. a therapeutic or environmental chemical) and microarray gene expression profiling is carried out. A 'gene expression signature' is, put simply, the list of genes differentially expressed in any biological distinction, e.g. derived by a t-test between control and treated samples with the appropriate p-value (e.g. $P<0.05$) and fold change (e.g. >2) cut-offs (Lamb, 2007). Using the 'gene expression signature', mechanistic or predictive toxicology can be carried out with the appropriate bioinformatics tools.

Within the last 10 years, there has been the development of toxicogenomics databases, which contain a repository of gene expression profiles representing a number of compounds that affect biological systems through a variety of mechanisms (Afshari *et al*., 2011). One of these is DrugMatrix, a large molecular toxicology reference database containing a unique reference set of gene expression profiles based on 600 different compounds (therapeutic, industrial and environmental) that have been administered to rats and rat cell lines and are anchored to classical pharmacology, toxicology and clinical pathology measurements (Ganter *et al*., 2005). Waring *et al* (2008) used the DrugMatrix database to investigate the mechanism of action of two novel Acetyl CoA carboxylase 2 (ACC2) inhibitors; one active and one inactive enantiomer. It was found that both the active and inactive enantiomer were equally effective at reducing glucose and triglycerides, suggesting a mechanism of action distinct from inhibition of the AC22. The authors compared the liver gene expression signatures of the two ACC2 inhibitors to the DrugMatrix database and found that both compounds had a high degree of similarity to a variety of known

peroxisome proliferator activated receptor alpha (PPAR-α) agonists including bezafibrate, clofibrate and fenofibrate. Follow up experiments confirmed that the compounds interacted either directly or indirectly with PPAR-α, suggesting that this is a plausible mechanism for the similar pharmacological findings with active and inactive enantiomers of an ACC2 inhibitor.

There are a plethora of high-throughput bioinformatics tools available to evaluate the biological processes effected after compound-induced toxic stress in a functional way, i.e. by analysis of toxicity pathways (Huang *et al*., 2009; Kienhuis *et al.,*2011). The importance of identifying toxicity pathways was highlighted in the NRC (2007) report and there is an ongoing effort in cell biology to identify, characterise and map these pathways involved in various cell processes, including metabolism, energy homeostasis, cell fate (apoptosis, cell cycle). In this vein, mechanistic toxicogenomics, using bioinformatics tools, will be key to elucidating biological processes involved in the manifestation of toxicity.

A number of high-throughput enrichment analysis tools have been developed in the last 10 years (Huang *et al*., 2009). The range of publicly available bioinformatics tools includes Kyoto Encyclopedia of Genes and Genomes (KEGG), Database for Annotation Visualisation and Integrated Discovery (DAVID) (Huang *et al*., 2007), Biocarta, PathVisio, and Reactome. These tools draw on biological knowledge from databases (e.g. gene ontology (GO)) to carry out enrichment analysis, which statistically highlights the most overrepresented biological processes (such as GO categories) and pathways of a gene signature (Huang *et al*., 2007). Commercial analysis tools include Pathway Assist, MetaCore, ePathArt and Ingenuity Pathway Analysis (IPA). Notably, IPA draws on a literature knowledge base to enrich gene expression signatures to toxicological processes, canonical pathways and networks, providing a focused toxicological evaluation of compound effects. The use of multiple bioinformatics tools is important since no single resource provides information about all available biological pathways (Huang *et al*., 2009). A number of studies have implemented a range of these tools to elucidate mechanisms of toxicity from gene expression signatures (Pointon *et al*., 2010; Lee *et al*., 2011; Zhang *et al*., 2012). For example,

Pointon *et al* (2010) used IPA and KEGG pathway analysis to investigate the cardiotoxic effects of doxorubicin (DOX) in mice and identified mitochondrial oxidative phosphorylation (OXPHOS) as the most enriched pathway. More recently, a study used IPA to identify the essential role that Top2 β plays in the alteration of the transcriptome that selectively affects oxidative phosphorylation and mitochondrial biogenesis in doxorubicin-induced cardiotoxicity (Zhang *et al*., 2012).

Ideally, the gene expression changes associated directly with the primary effect of a compound would be elucidated prior to the appearance of the phenotypic changes (Afshari *et* al., 2011). In this respect, mechanistic studies should only be carried out with a dose of compound (sub-toxic dose), or time point where histopathology is minimal (Foster *et al*., 2007). In addition, it is important that *in vivo* mechanistic toxicogenomics studies are complemented with traditional endpoints (such as histopathology and clinical chemistry) to 'phenotypically anchor' the interpretations of the study (Foster *et al*., 2007; Kienhuis *et al*., 2011).

1.3.1.2 Toxicogenomics for predictive toxicology

Beyond its use for identifying mechanisms of toxicity, toxicogenomics represents an ideal approach to develop novel biomarkers that can be used as sensitive indicators of compound-induced toxicity (Ellinger-Ziegelbauer *et al*., 2008; Blomme *et al*., 2009; Nishimura *et al*., 2013). In toxicology studies, cardiac and skeletal muscle toxicity is traditionally identified through histopathological findings and clinical pathology biomarkers, such as troponins (Tn), creatine kinase (CK) and lactate dehydrogenase (Wallace *et al*., 2004). Although this approach may robustly detect muscle toxicities, these changes only occur after prolonged periods and provide no mechanistic insight into the toxicity. Toxicogenomics is able to detect toxicity of a low dose toxicant *in vivo* before the adverse histopathological phenotype is observed by histopathology (Heinloth, *et al*., 2004). Therefore, genomic biomarkers are more sensitive than traditional approaches and so are able to more reliably and specifically predict toxicity before phenotypic manifestation. This genomic biomarker approach is therefore referred to as toxicogenomics for predictive toxicology (Blomme *et al*., 2009). The underlying assumption of predictive toxicogenomics is that compounds that induce

toxicity through similar mechanisms will elicit characteristic gene expression patterns. By grouping the gene expression of well characterised model compounds, a gene expression signature (genomic biomarker) related to a specific mechanism or mode of toxicity can be generated (Blomme *et al*., 2009). The process of selecting predictive genomic biomarkers requires a repository of gene expression profiles (i.e. from a database such as DrugMatrix) of compounds sharing a similar mechanism of toxicity and an appropriate computational algorithm (i.e. artificial neural networks). For example, Ellinger-Ziegelbauer (2008) applied toxicogenomics to rat livers treated with 5 genotoxic hepatocarcinogens, 5 non-genotoxic hepatocarcinogens and 3 non-carcinogens to identify a biomarker set that distinguishes genotoxic from non-genotoxic carcinogens, a process that normally requires a 2 year bioassay.

With respect to cardiotoxicity, Nishimura *et al* (2013), used three cardiotoxic compounds (isoproterenol, doxorubicin or carbofuran) to identify a gene signature of 8 genes that exhibited a much higher diagnostic accuracy than that observed for plasma cardiac troponin I (cTnI). Furthermore, this multi-gene biomarker was able to predict cardiotoxicity in rats before cardiac histopathological lesions were present or cTnI was elevated in the plasma (Nishimura *et al*., 2013). Genomic biomarkers are also able to provide detail on the mechanism of toxicity of a compound and thereby classify them according to their specific mechanism of toxicity. For example, McMillan *et al* (2004) were able to identify distinct gene expression signatures that could differentiate between three classes of hepatotoxicants (macrophage inhibitors, peroxisome proliferators and oxidative stressors/reactive metabolites) based on the mechanism by which they induced oxidative stress. Using these genomic biomarkers, the authors were able to categorize over 100 compounds successfully based on their oxidative stress potential in rat liver.

1.3.2 High-throughput toxicity testing

High-throughput screening (HTS) technologies have advanced in recent years and the latest systems now rely on multi-plate formats (96-well to 3456-well plates) and/or automation (using robotics), enabling throughput ranges from hundreds to thousands of samples tested daily (Van Vliet, 2011). Initially, HTS techniques were used by

pharmaceutical companies as a screening step in drug lead discovery (Mayr and Bojanic, 2009). However, they are now being applied to toxicity testing to screen drugs and chemicals against a large number of assays, which is the converse of drug discovery where many compounds are tested against one biological target (Houck and Kavlock, 2008). HTS technology is applied to assess a range of endpoints including biochemical targets (e.g. ion channel inhibition/activation, receptor binding, enzyme activity), cytotoxicity (e.g. oxidative stress, cell proliferation, mitochondrial function, apoptosis, cell cycle, cell proliferation) genotoxicity and metabolism (phase I and II metabolism) using biochemical assays, *in vitro* cellular model systems and/or model organisms (Houck and Kavlock, 2008; Schoonen *et al*., 2009; Van Vliet, 2011). Thus, HTS technologies are applicable to all areas of toxicity testing and the ability to generate large amounts of high quality data is important for application of these approaches to mechanism-based toxicity testing.

1.3.3 Cell-based *in vitro* toxicity testing

1.3.3.1 Cell models for toxicity testing

The use of cellular models provides a much higher level of complexity than simple biochemical assays. *In vitro* cell-based toxicity testing is typically carried out with either immortalised cell lines (e.g., SV40 transformation and cancer-derived cell lines) or primary cells (Anson *et* al., 2011; Roggen, 2011). Immortalised cell lines are advantageous since they are readily available, easily maintained, relatively well characterised and provide a homogeneous phenotype (Scanu *et al*., 2011). However, cell lines are genetically altered and consequently may show an altered phenotype and response to a toxic compound compared with cells *in vivo* (Scanu *et al*., 2011; Roggen, 2011). Primary cells are considered a better model, although they rapidly lose their *in vivo* phenotype in culture, exhibit high batch-batch variability and are limited in quantity (Anson *et al*., 2011). Moreover, with respect to animals, the approach is not conducive to reducing animal use in research (3Rs) and with respect to humans, it is not possible to attain a regular supply of primary cells for research. A promising alternative is the use of embryonic, adult or induced pluripotent stem cells for generating an unlimited supply of identical *in vivo*-like cells (Van Vliet, 2011). However, there are a number of challenges and limitations before the full promise of

stem cells can be realised. As well as the ethical concern regarding embryonic stem cells, the functional and genetic stability of stem cells is unknown and differentiation of stem cells results in a heterogeneous population of cells with different phenotypes (Anson *et al*., 2011; Van Vliet, 2011). Therefore, the purity and functionality of differentiated stem cell cultures still needs to be improved to achieve *in vivo*-like characteristics.

Numerous methods have been developed to improve the microenvironment of cell cultures to more faithfully mimic *in vivo* cell function and behaviour and include techniques for three-dimensional (3D) and microfluidic (flow) modelling. Studies have shown that 3D cultures have improved cell-cell interactions, signal transduction and gene expression compared to monolayer cultures and consequently more closely reflect the structure and function of native tissues (Mazzoleni *et al*., 2008; Elliot and Yuan, 2010; Curtis *et al*., 2010). Importantly, it has been shown that hepatocyte 3D cultures preserve drug-metabolising capabilities for longer periods than monolayer cultures and provide more realistic physiological responses to xenobiotic compounds (Bokhari *e* al., 2007; Mazzoleni *et al*., 2008). Another technology being applied to cell culture is microfluidic models, which simulate the effects of flow *in vivo,* and are used to generate gradients of xenobiotic concentrations, create specific physical microenvironments (e.g. shear stress) and to construct a circulatory system to better mimic the physiological state (Wu *et al*., 2010). With respect to toxicity testing, studies have shown that flow-based hepatocyte cultures have improved xenobiotic clearing and metabolite production compared to static cultures (Novik *et al*., 2009). A study by Toh *et al* (2009) combined 3D culture and microfluics, creating the 3D HepaTox chip, to study xenobiotic toxicity. They found that the IC50 values of 5 model drugs correlated well with *in vivo* IC50 values, demonstrating the value of an integrated platform for toxicity testing (Toh *et al*., 2009).

1.3.4 Endpoints studied using *in vitro* models

1.3.4.1 Cytotoxicity assays

Of the endpoints applied to *in vitro* toxicity testing, cytotoxicity assays are often among the earliest assays to be conducted (Kramer *et al*, 2007). Cellular cytotoxicity

may result from a range of mechanisms, including a disturbance or imbalance of energy metabolism, signal transduction pathways, mitochondrial function, cytoskeletal organization, membrane integrity or cell-specific functions, such as uptake and secretion of metabolic waste products or glycogen storage (Schoonen *et al.*, 2009). Knowledge of the biological processes affected provides detail on the mechanism of toxicity of a compound.

General cytotoxicity can be determined in almost any cell type given that all cells have the basic machinery for cell survival, replication (if immortalized) and cell injury pathways that can be activated after xenobiotic insult (Lin and Will, 2012). However, tissue-specific functions may be needed to elucidate the toxic effect of certain compounds, in which case tissue-specific and relevant cell lines, primary cells or stem cells may be needed (Schoonen *et al.*, 2009). Variations in the antioxidant capacity, mitochondrial capacity or expression of enzymes/proteins of different tissue cell-types may all determine differential tissue sensitivity to certain compound toxicities. For example, the order of antioxidant capacity has been determined as liver > heart > muscle (Venditti *et al*., 1998; Masuda *et al*., 2003; Katalinic *et al*., 2005), while susceptibility to oxidative stress is heart >muscle >liver (Venditti *et al*., 1998). Thus, these differences in antioxidant capacity may explain why the heart and skeletal muscle are more susceptible to certain ROS-inducing toxicants, while the liver is relatively resistant to damage. Venditti *et al* (1998) showed that the increased sensitivity of the heart to doxorubicin-induced damage compared to the liver was related to the antioxidant defences of the tissues. Furthermore, the liver has a greater ability to metabolize compounds than cardiac and skeletal muscle, which may either confer protection via detoxification or provoke a toxicity response, via bioactivation (Dekant, 2009). The liver is therefore particularly susceptible to toxicity of bioactivated compounds that result in reactive metabolites, such as acetaminophen (APAP) (Chan *et al*., 2001).

A number of studies have investigated the utility of using organ-specific cell lines to predict cardio-, hepato- and nephro-toxicities (Inoue *et al*., 2007; Li *et al*., 2004; Zhang *et al*., 2007; Xia *et al*., 2008, Lin and Will, 2012). These studies demonstrated that in

some cases compounds did elicit tissue-specific toxicities. For example, Xia *et al* (2008) tested 1408 compounds in 13 human and rodent cell lines from six common targets of xenobiotic toxicity (liver, blood, kidney, nerve, lung and skin) and found that some compounds were cytotoxic to all cells at similar concentrations, whereas others exhibited species or cell type specific cytotoxicity.

Cytotoxicity measurement of compound effects *in vitro* are carried out using either single or multiple endpoints using plate based or high content screening assays (Lin and Will, 2012). Cytotoxicity assays implementing a single endpoint tend to utilise 'easy-to-interpret' endpoints such as ATP content, membrane leakage, or cell number (Houck and Kavlock, 2008). The Multicenter Evaluation of *in vitro* cytotoxicity (MEIC) programme demonstrated that this type of cytotoxicity data is useful for identifying acutely toxic compounds and showed good predictive ability for 50 toxicants *in vivo* (Walum *et al*. 2005).

Although single endpoint cytotoxicity assays are useful, they are hindered in their ability to provide mechanistic information on the toxicity of compounds. Given that there are a number of pathways that can induce toxicity, a combination of multiple endpoints should be used for the evaluation of the mechanism of toxicity (Schoonen *et al*., 2009). Among the many endpoints that can be quantified, the most common endpoints investigated relate to mitochondrial dysfunction (ATP content, mitochondrial membrane potential), energy metabolism status, protein expression, levels, cell death pathways (caspase activity), nuclear morphology (e.g. Hoechst 33342 dye), intracellular calcium levels (e.g. fluo-4 dye), oxidative stress (ROS production and glutathione levels) and cell proliferation (e.g. CCK-8, cell cycle profile) (Houck and Kavlock, 2008; Schoonen *et al*., 2009). *In vitro* assays relating to mitochondrial dysfunction will be discussed further in section 1.4.

1.3.4.2 High content Imaging

Recent advancements in the automation of quantitative epifluorescence microscopy and robust imaging analysis, together with the application of microfluorescent, multiprobe technology has resulted in high-content screening (HCS) (Zanella *et al*.,

2010). HCS enables high-throughput, quantitative analysis *in vitro* of individual cells in real time for multiple parameters that are involved in the mechanism of toxicity (Giuliano *et al*., 1997). Therefore, this technology can be applied early in the *in vitro* toxicity testing paradigm to identify mechanisms of compound-induced toxicity. Studies in liver and cardiomyocyte models have demonstrated the utility of HCS in the *in vitro* detection of xenobiotic-induced hepato- and cardiotoxicity (O'Brien *et al*., 2006; Pointon *et al*., 2013). Pointon *et al* (2013) used human embryonic stem cell–derived cardiomyocytes (hESC-CMs) and the rat myoblastic H9c2 cell line to phenotypically profile a panel of structural cardiotoxins by live cell fluorescent imaging of mitochondrial membrane potential (TMRE), endoplasmic reticulum integrity (ER-Tracker blue, Ca^{2+} mobilization (Fluo-4AM), and membrane permeability (TOTO-3) combined with an assessment of cell viability (ATP depletion). The authors concluded that this HCS provided mechanistic insight into structural cardiotoxicity and that hESC-CMs were the more sensitive and specific model to assess structural cardiotoxicity at therapeutically relevant *in vivo* concentrations.

1.3.4.3 Metabolism

Metabolism of xenobiotics is carried out by two enzyme categories, Phase I (oxidation, reduction and hydrolysis reactions) and Phase II (conjugation reactions) metabolizing enzymes, as well as Phase III transporters (Omiecinski *et al*., 2011). The most important Phase I enzymes are the cytochrome P450 (CYP) enzymes, while there is a diverse range of Phase II enzymes, including subtypes for glutathione-*S*-transferase (GST), UDP-glucuronosyltransferase (UGT), sulfotransferase (SULT) and *N*-acetyltransferase (NAT) (Schoonen *et al*., 2009). Metabolism of xenobiotics or interference with the activities of these enzymes can result in toxicities manifested in a number of ways. Firstly, metabolism of certain xenobiotics can result in the production of metabolites with a higher potential for toxicity than the parent compound, in a process known as bioactivation (Dekant, 2009). Secondly, inhibition or induction of CYPs by xenobiotics can result in a range of unwanted and potentially toxic side-effects. For example, induction of CYPs may reduce the therapeutic efficacy of co-medications (drug-drug interactions), create an undesirable imbalance between detoxification and bioactivation as a result of increased production of reactive

metabolites, and/or increase the production of ROS (Paolini *et al*., 2001; Lin, 2006). Therefore, it is important for industrial and pharmaceutical companies to screen for the effects of metabolism on xenobiotics and conversely, to assess the effects of xenobiotics on the activity of metabolism enzymes. With respect to bioactivation, a system consisting of a metabolism component (i.e. primary hepatocytes, S9 fraction, microsomes) coupled with one or more target cells provides a means to incorporate bioactivation into cytotoxicity screening (Ozolins *et al*., 1994; Vignati *et al*., 2005). Covalent binding assays can also be carried out to assess the interaction of reactive metabolites with metabolizing substrates, such as glutathione (GSH), which result in a depletion in metabolic and antioxidant capability (Liebler and Guengerich, 2005). To assess the effects of xenobiotics on metabolizing enzymes, such as the CYPs, the enzyme activity in primary hepatocytes cultures following compound exposure, can be measured using sensitive techniques like liquid chromatography tandem mass spectrometry (Lahoz *et al*., 2008). Reporter gene assays for nuclear receptors (such as pregnane X receptor (PXR) and aryl hydrocarbon receptor (AhR) controlling drug metabolism enzyme induction (such as CYP1A) are also carried out as an alternative, high-throughput method to assess CYP activity (Moore and Kliewer, 2000; Yueh *et al*., 2005).

1.3.4.4 Genotoxicity

To assess the potential genotoxic activity of compounds, a battery of *in vitro* assays including the mouse lymphoma *tk* gene mutation assay, Ames bacterial reverse mutation test and the micronucleus clastogenicity assay are traditionally used (Houck and Kavlock, 2008). However, these standard genotoxicity assays are not high-throughput, are relatively costly and suffer from low specificity leading to large numbers of false positives (Kirkland *et al*., 2005). As described in section 1.3.1.2, predictive toxicogenomics has the potential to rapidly and sensitively distinguish genotoxic carcinogens from non-genotoxic carcinogens (Ellinger-Ziegelbauer *et al*., 2008). In addition, alternative, high-throughput methods have been developed to detect mutagenicity and clastogenicity (Kramer, 2007). For example, Hastwell *et al* (2006) developed a high-throughput assay for detecting DNA damage that used a green fluorescent protein reporter gene under the regulation of the human GADD45a

gene. GADD45a is induced in a p53-dependent manner in response to a wide variety of DNA damaging agents. A validation study with 75 compounds revealed good sensitivity and specificity for distinguishing genotoxic and non-genotoxic carcinogens (Hastwell *et al*., 2006).

1.3.5 Validation of *in vitro* cell-based models

Whether *in vitro* tests are based on primary cells, immortalised cell lines or stem cells, it is important that the system adequately mimics the key events of the *in vivo* mechanisms of action triggered in animals in response to a toxic compound. In this respect, the *in vitro* model may not express mechanisms that *in vivo* are required for a compound to be toxic, or conversely, they may express mechanisms not active *in vivo* (Roggen, 2011). Therefore, it is important to determine if the *in vitro* cell-based system reveals adequate *in vivo* functionality, i.e. expresses the relevant toxicity pathways of interest. To address the issue of *in vitro* validation, toxicogenomics has been used to determine the ability of *in vitro* models to accurately mimic certain *in vivo* responses (Kienhuis *et al*., 2006; Blomme *et al*., 2009).

A number of studies have used mechanistic toxicogenomics to compare *in vitro* and *in vivo* responses to toxicants to assess the correlation between the two systems (Kienhuis *et al*., 2006 and 2009; Dere *et al*., 2006; Boess *et al*., 2007; Jo *et al*., 2012). From these studies, it was concluded that the comparison at the level of pathway analysis was more effective than comparison at the individual gene level. In addition, all these studies demonstrated good concordance between the *in vitro* and *in vivo* systems, and showed that the toxic potential of compounds could be assessed *in vitro*. For example, Boess *et al* (2007) compared the effects of two 5-HT6 receptor antagonists between rats *in vivo* and rat hepatocytes *in vitro* using gene expression and biochemical endpoints. They found that the *in vitro* gene expression analysis results and biochemical analyses supported the findings observed *in vivo* and also allowed the differentiation of both compounds with regards to hepatotoxic potential. Notably, the induction of CYP 2B and CYP 3A1 correlated between *in vitro* and *in vivo*. This example serves to illustrate the point of using a cell-type specific model to assess

toxicity. Without the expression of relevant hepatocyte-specific CYP activity, the hepatotoxic potential of the compounds may not have been evident *in vitro*.

Studies have also shown that toxic compounds can be classified using gene expression profiles and genomic biomarkers generated from *in vitro* systems. For instance, Sawada *et al* (2005) developed an *in vitro* screening assay for phospholipodosis in HepG2 cells using 12 phospholipodosis-inducing compounds. They identified 17 marker genes that showed significant concordance with the *in vivo* phenotype of phospholipodosis. Studies have since been carried out to confirm the utility of this genomic biomarker set to detect phospholipodosis. Atienzar *et al* (2007) used the same cell line and showed that of 26 compounds tested all positive compounds known to induce phospholipodosis were identified as such and all the negative controls (six compounds) were also confirmed.

1.3.6 Potential strategy for toxicity testing

The aim of a new toxicity testing strategy is to integrate the myriad of technologies and *in vitro, in vivo,* and *in silico* assays into an integrated testing strategy (ITS) (Van Vliet, 2011; Berg *et al*., 2011). Figure 1.3 displays a scheme of how toxicity testing could be efficiently utilised to screen compounds based on two models presented by Dix *et al* (2007) and Houck and Kavlock (2008). The scheme presented is based on a tiered testing approach with interim decision points between successive tiers. At each decision point, the results are evaluated to decide whether there is sufficient information about a chemical or if additional testing is required. Initially, the strategy implements a range of high-throughput cell-based assays (e.g. HCS), model organism assays and omics analysis (e.g. predictive and mechanistic toxicogenomics) to define effects on toxicity pathways. Compounds with activity in one or more of these pathways would then be screened for their effects on a range of biochemical targets, such as GPCRs and kinases, using *in vitro* assays. These datasets can then be linked within a database of reference compounds to classify toxicants of unknown toxicity based on the similarity of their bioactivity signatures to those of chemicals of known mechanism in the database. Integration of all this data through computational analysis, together with information on exposure and PBPK data, provides hypotheses

on the mechanism of toxicity and a hazard prediction that would drive decisions about the necessity of additional selective biochemical, cellular and/or animal testing. Targeted animal testing may be required to provide additional information on pharmacokinetic parameters, as well as additional mechanistic information. An important consideration at an early phase of toxicity testing is the potential for bioactivation, so a metabolic component would have to be included.

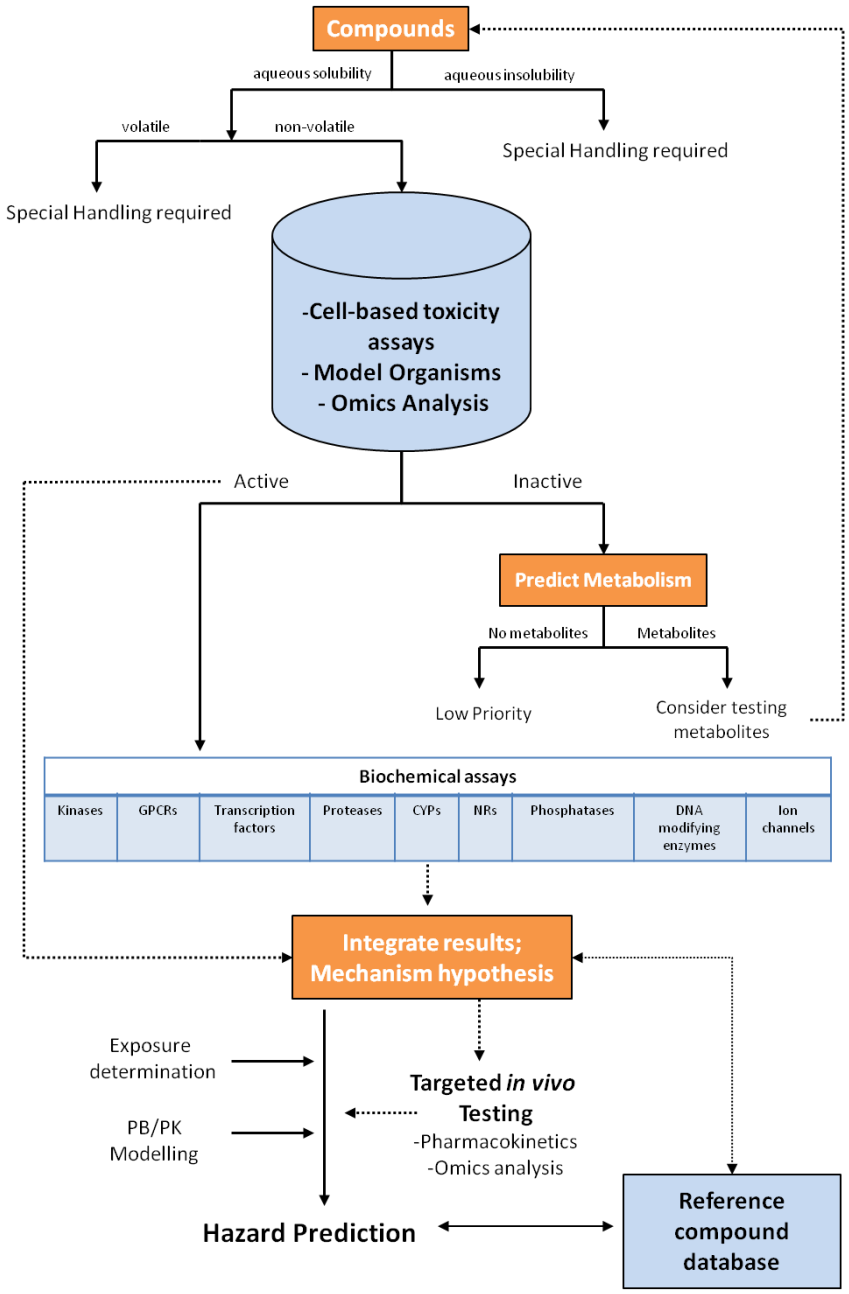

Figure 1.3. Possible toxicity testing flow scheme. (GPCRs – G protein coupled receptors; NRs – Nuclear Receptors; CYPs – Cytochrome P450 monooxygenase.) Adapted from Dix *et al* (2007) and Houck and Kavlock, 2008.

A database of reference compounds would also allow deeper exploration of the relationships linking biological activities to toxicology and thereby help demonstrate which pathways can be confidently called toxicity pathways (Sipes *et al*., 2013). To generate a toxicological database requires the collation of information on several hundred reference compounds of differing structural and toxicological outcomes. In 2007, the EPA set up the ToxCast program to address this challenge (Dix *et al*., 2007). The aim of the ToxCast project was to acquire information on a range of compounds so that 'bioactivity profiles' or '*in vitro* signatures' could be identified that predict patterns of toxicity or phenotypes observed in traditional animal testing (Dix *et al*., 2007). These predictive bioactivity signatures were developed based upon physiochemical properties, biochemical activities and cell-based phenotypic assays, gene expression analyses, and physiological responses in model organisms (non mammalian) (Kavlock *et al*., 2012). To date, the ToxCast database contains over 1000 characterised compounds, most of them being pesticides, commercial chemicals and failed pharmaceuticals (Kavlock *et al*., 2012).

1.4 Mitochondrial toxicity

Only in the last decade has the notion that mitochondrial impairment could be an inadvertent 'off-target' effect of xenobiotic exposure that contributes to organ toxicities become more widely acknowledged (Dykens and Will, 2007). Indeed, many xenobiotic failures or withdrawals have been associated with mitochondrial toxicity, including tolcapone, troglitazone and cerivastatin (Chan *et al.,* 2005). By hampering mitochondrial energy production and/or releasing mitochondrial pro-apoptotic proteins into the cytoplasm, xenobiotics can trigger apoptosis or necrosis of the cell, e.g. myocyte (Labbe *et al*., 2008). Organs such as cardiac and skeletal muscle, liver and the brain are the metabolically most active, implying a higher dependence on mitochondrial ATP, with a consequent increase in tissue damage resulting from xenobiotic-induced mitochondrial failure (Pereira *et al*., 2011).

1.4.1 Mitochondria structure and function

Mitochondria are ubiquitous intracellular organelles that are bound by two lipid bilayer membranes. The outer mitochondrial membrane (OMM) is permeable to ions and solutes up to 14kDa and the inner mitochondrial membrane (IMM) encloses an aqueous compartment, the matrix, where mitochondrial DNA (mtDNA) and various soluble enzymes, such as those of the tricarboxylic acid (TCA) cycle and the β-oxidation pathway, are located (figure 1.4) (Wallace and Starkov, 2000). The IMM is not freely permeable to ions and metabolites and so contains special membrane bound transporters that allow for selective entry of endogenous metabolites (e.g. ADP, pyruvate, fatty acids, glutathione) and possibly xenobiotics (Begriche *et al*., 2010). The lipid composition of the IMM is unique in that it contains large amounts of cardiolipin and virtually no cholesterol (Wallace and Starkov, 2000). The IMM forms a cristae structure and, importantly, contains the proteins that participate in various metabolic activities, including ATP synthesis through oxidative phosphorylation (OXPHOS) (Cohen, 2010).

Mitochondria are the powerhouses of the cells and make approximately 90% of the cell's ATP, utilizing OXPHOS, which couples the oxidation of NADH and $FADH_2$ to the phosphorylation of ADP to form ATP, by utilization of the ETC (a series of five enzyme complexes) in the IMM (Cohen, 2010). Mitochondria oxidise many metabolites including fatty acids, pyruvate (generated from glycolysis) and several amino acids (such as glutamine, valine, leucine) to generate the reducing equivalents, NADH and $FADH_2$, via the TCA cycle and β-oxidation, for ATP production (Labbe *et al*., 2008) (figure 1.4).

As well as ATP production, additional functions of the mitochondria include the generation and detoxification of ROS, involvement in some forms of apoptosis, regulation of cytoplasmic and mitochondrial matrix calcium (Ca^{2+}), synthesis and catabolism of metabolites (e.g. urea, haem and cholesterol) and the transport of the organelles themselves to correct locations within the cell (Chan *et al*., 2005; Dykens and Will, 2007; Brand and Nicholls, 2011).

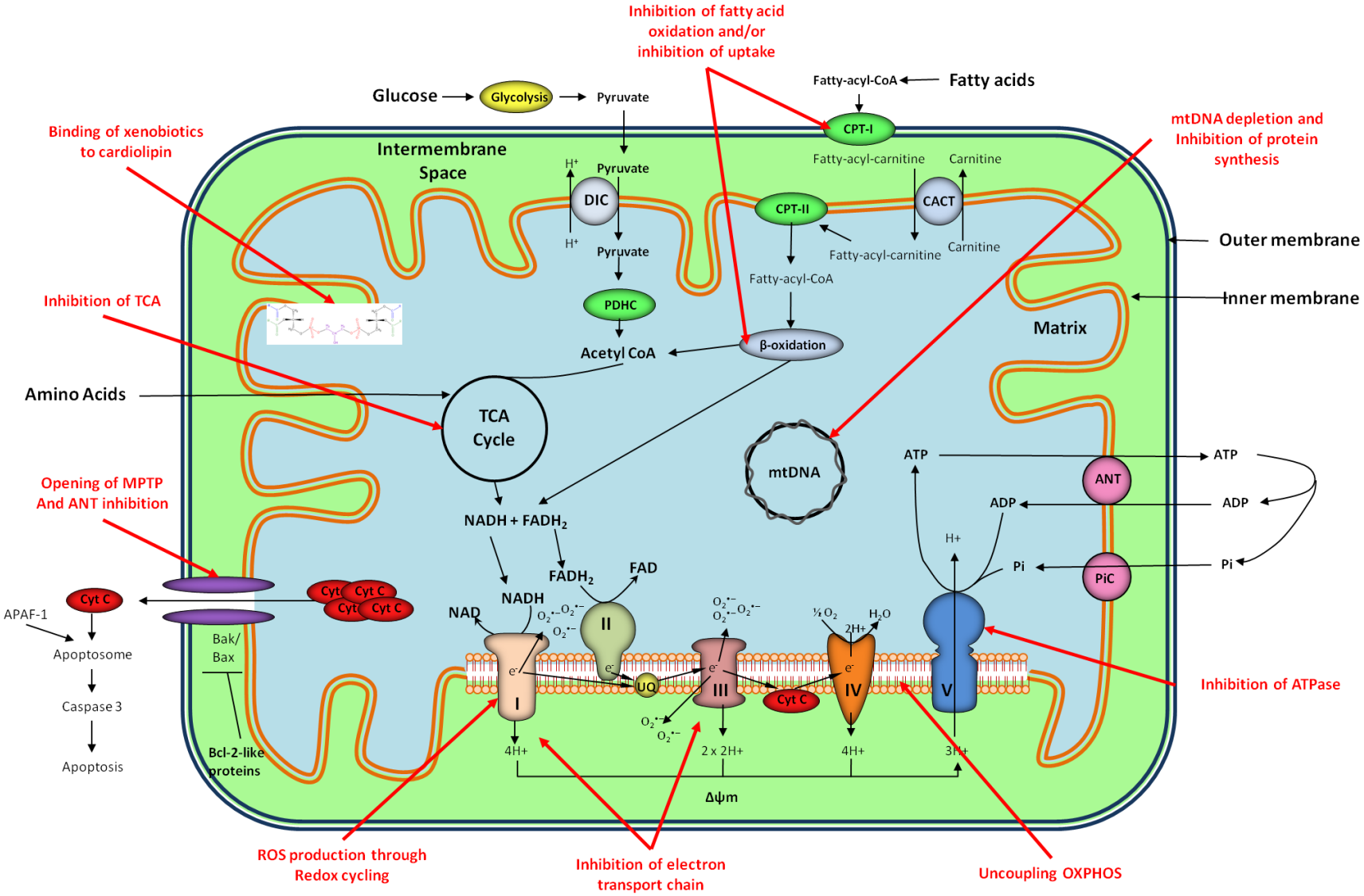
Inhibition of fatty acid oxidation and/or inhibition of uptake
Glucose
Glycolysis
Pyruvate
Fatty-acyl-CoA
Fatty acids
CPT-I
Binding of xenobiotics to cardiolipin
Intermembrane Space
mtDNA depletion and Inhibition of protein synthesis
H+
Pyruvate
DIC
Fatty-acyl-carnitine
Carnitine
CACT
CPT-II
Outer membrane
Inner membrane
Fatty-acyl-CoA
Inhibition of TCA
PDHC
Matrix
Acetyl CoA
β-oxidation
Amino Acids
TCA Cycle
mtDNA
ATP
ANT
ADP
Opening of MPTP And ANT inhibition
NADH + FADH2
FADH2
FAD
NADH
NAD
H+
Pi
PiC
Cyt C
APAF-1
Apoptosome
Caspase 3
Apoptosis
Bak/ Bax
Bcl-2-like proteins
UQ
I
II
III
IV
V
½ O2
H2O
2H+
4H+
2 x 2H+
3H+
Δψm
Inhibition of ATPase
ROS production through Redox cycling
Inhibition of electron transport chain
Uncoupling OXPHOS

Figure 1.4. Mitochondrial ATP production and xenobiotic targets. The metabolites, fatty acids, pyruvate (generated from glycolysis) and amino acids (such as glutamine) are transported into the mitochondria and oxidized to generate reducing equivalents nicotinamide adenine dinucleotide (NADH) and flavin adenine dinucleotide (FADH2), which donate electrons to the electron transport chain (ETC). Electrons enter the ETC through complex I (via NADH) or complex II (via $FADH_2$). Ubiquinone (UQ) (Coenzyme Q_{10}) shuttles electrons from complex I and II to complex III. Cytochrome c (CytC) then shuttles electrons from complex III to complex IV, which utilises the electrons and hydrogen ions to reduce molecular oxygen to water. The energy released by the electron transport pumps dehydrogenase-derived protons through complexes I, III and IV. This process creates an electrochemical proton gradient ($\Delta\psi m$) across the IMM that is used to drive complex V (F_0F_1-ATP synthase), a rotary motor that converts ADP to ATP. Concomitantly, the transient decrease in $\Delta\psi m$ promotes electron transfer in the ETC and the coupled ejection of protons towards the intermembrane space, which restores the $\Delta\psi m$. ROS is simultaneously generated in this process, as $O_2^{\bullet-}$ is generated via complexes I and III. Xenobiotics can impair mitochondrial function through different mechanisms, which are highlighted in red and include: (i) by inducing MPTP opening, leading to release of pro-apoptotic factors such as cytochrome c, (ii) by causing mtDNA depletion (impair DNA replication or protein synthesis), which can reduce the synthesis of mtDNA-encoded ETC polypeptides, impair ETC activity and increase the generation of the superoxide anion and other reactive oxygen species (ROS), (iii) by directly impairing OXPHOS, through inhibition of the ETC or uncoupling of it from ATP synthesis, (IV) by production of ROS through redox cycling, (V) by directly altering fatty acid oxidation (FAO) via the inhibition of β-oxidation enzyme(s), and/or by indirectly impairing FAO through the sequestration of the FAO cofactors, L-carnitine and coenzyme A, (VI) Inhibition of the TCA cycle and (VII) by direct effects of xenobiotics on cardiolipin. Abbreviations: ANT, adenine nucleotide translocator; CACT, carnitine–acylcarnitine translocator; CoA, coenzyme A; CPT, carnitine palmitoyltransferase; complex I, NADH dehydrogenase; complex II, Succinate dehydrogenase; complex III, ubiquinone–cytochrome- *c* oxidoreductase; complex IV, cytochrome-*c* oxidase; complex V, F_0/F_1-ATPase; DIC, dicarboxylate carrier; MPTP, mitochondrial permeability transition pore; $O_2^{\bullet-}$, superoxide; PiC, phosphate carrier; PDHC, pyruvate dehydrogenase complex; PyC, pyruvate carrier; TCA, tricarboxylic acid. (Adapted from Lowell *et al*., 2000; Dykens and Will, 2007; Labbe *et al*., 2008, Murphy, 2009).

1.4.2 Mitochondrial ROS generation

Mitochondria are an important source of ROS, which underlies oxidative damage in many pathologies and contributes to retrograde signalling from the organelle to the cytosol and nucleus (Murphy, 2009). During aerobic metabolism, a small but constant leak of electrons from the mitochondrial ETC induces a one-electron reduction of O_2, forming the superoxide anion ($O_2^{\bullet-}$) (Pereira *et al*., 2009). During normal

mitochondrial activity, about 1% of total oxygen consumed is estimated to be converted to $O_2^{\bullet-}$ (Pereira *et al*., 2011).

Superoxide is the precursor of most ROS and a mediator in oxidative chain reactions. Dismutation of $O_2^{\bullet-}$ (either spontaneously or through a reaction catalysed by superoxide dismutases) produces hydrogen peroxide (H_2O_2), which in turn may be fully reduced to water or partially reduced to hydroxyl radical (OH•), one of the strongest oxidants in nature (Turrens, 2003). In addition, $O_2^{\bullet-}$ may react with other radicals, including nitric oxide (NO) resulting in reactive nitrogen species (RNS), such as peroxynitrite (Turrens, 2003). The production of $O_2^{\bullet-}$ occurs primarily in the NADH dehydrogenase (complex I) and in the CoQ cycle in complex III (figure 1.4) (Murphy, 2009). The deleterious effects of ROS formation in the mitochondria are largely prevented by antioxidant defences, such as manganese superoxide dismutase (MnSOD), glutathione peroxidise, glutathione reductase and cytochrome c (Pereira *et al.,* 2009). Oxidative stress is the term used to describe the deleterious process when the levels of ROS exceed the capacity of antioxidant defence systems, resulting in damage to DNA, protein and lipid (Scandalios, 2002).

Xenobiotics are able to interact with the mitochondrial ETC and increase the rate of $O_2^{\bullet-}$ production through two different mechanisms. Xenobiotics may either (1) directly inhibit the ETC increasing the reduction level of carriers located upstream of the inhibition site or (2) accept an electron from a respiratory carrier and transfer it to molecular oxygen (redox cycling), thereby stimulating $O_2^{\bullet-}$ production without inhibiting the ETC.

Non-mitochondrial sources of $O_2^{\bullet-}$ include enzymatic production via NAD(P)H oxidases, cytochrome P450-dependent oxygenases, xanthine oxidase and non-enzymatic production via redox cycling (Turrens, 2003). For example, the vasoactive agent, angiotensin II, stimulates NAD(P)H oxidase activity in vascular smooth muscle cells, resulting in the generation of $O_2^{\bullet-}$ (Herbert *et al*., 2008).

1.4.3 Xenobiotic-induced mitochondrial toxicity

Considering the complexity of mitochondria, it is not surprising that they are often the target of xenobiotic-induced toxicity. The range of mechanisms through which xenobiotics induce mitochondrial toxicity is detailed in figure 1.4. There is a large diversity of compound structure that can cause mitochondrial dysfunction, including anti-cancer drugs (tamoxifen), statins (cerivastatin) antiretrovirals (zidovudine), antibiotics (isoniazid, antimycin A), non-steroidal anti-inflammatories (NSAIDs), anaesthetics (bupivicaine), antidiabetics (troglitazone), herbicides (chlorophenols) and insecticides (rotenone) (Chan *et al*., 2005; Dykens and Will, 2007). As previously highlighted, cardiac and skeletal muscle, as well as the liver, are particularly prone to xenobiotic-induced mitochondrial toxicity due to their high metabolic capacity and high level of exposure to xenobiotics. (Pereira *et al*., 2011).

1.4.4 Mitochondrial toxicity testing in R&D

The fact that mitochondrial toxicity was responsible for the withdrawal of at least three compounds (troglitazone, cerivastatin, and tolcapone) of the 38 withdrawn from the market between 1994 and 2006 and has been described for many different classes of compounds, underscores the utility of mitochondrial screening in R&D (Chan *et al*., 2005; Dykens and Will, 2007). By implementing a suite of assays capable of detecting mitochondrial function and/or replication early in R&D will reduce compound attrition and yield safer compounds (Pereira *et al*., 2009). Since mitochondrial toxicity is induced through a variety of mechanisms (figure 1.4) there are several *in vitro*, *in vivo* and *in silico* tools and new technologies that are being used to reveal mitochondrial liabilities.

Various high-throughput *in vitro* analytical tools employed to investigate mitochondrial function include; measurement of ATP levels using the luciferin-luciferase luminescent assay; measurement of mitochondrial dehydrogenase activities using Alamar Blue or MTT; assessment of ROS production using fluoroprobes; measurement of mitochondrial membrane potential ($\Delta\psi m$) using fluorescent dyes (e.g. TMRM), assessment of mitochondrial calcium retention capacity using fluorescent dyes (such as Calcium Green-5N); and measurement of oxygen

consumption (Pereira *et al*., 2009; Schoonen *et al*., 2009). Mitochondrial ROS levels can be measured using specific probes that react with $O_2^{\bullet-}$ to produce a fluorescent derivative. Recently, a novel fluoroprobe, MitoSox, has been developed for selective detection of $O_2^{\bullet-}$ in the mitochondria of live cells (Mukhopadhyay *et al*., 2007). Since electron transport components can be directly inhibited by xenobiotics, high-throughput measurements of respiratory complex activities have been developed using immunocapture technology (Nadanaciva *et al*., 2007). In addition, inhibitors (antibiotics and NRTIs) of mtDNA and protein synthesis, can be investigated using radiolabeled deaoxynucleotide triphosphates (dNTPs) and [^{35}S]-methionine incorporation, respectively.

The most useful general test of mitochondrial function is measurement of oxygen consumption (cell respiration) (Brand and Nicholls, 2011). Until recently, oxygen consumption was determined using the low-throughput polarographic Clark-type electrode. More recently, several techniques have been described for monitoring oxygen consumption using a phosphorescent probe in a multi-well format (Dykens and Will, 2007). The Seahorse XF24 and XF96 extracellular flux analysers have refined this technology, using a piston to reversibly enclose a small volume above the cells, monitoring oxygen consumption in that volume, then raising the piston, allowing the media to re-equilibrate (Ferrick *et al*., 2008). The ability to sequentially inject four compounds during the experiment enables the assessment of many mitochondrial parameters. In addition, the Seahorse measures the rate of glycolysis (proton release) in parallel and so allows for a full understanding of effects on cellular bioenergetics.

Traditionally, cell culture is carried out using high glucose media and so most cells are able to compensate for mitochondrial impairment by utilizing glycolysis for ATP generation, and therefore, are more resistant to mitochondrial toxicities. To generate a cell model that more sensitively detected mitochondrial impairment, Marroquin *et al* (2007) replaced high glucose in the growth media with galactose. Unlike with glucose, the oxidation of galactose to pyruvate is too slow to meet the cells energy requirements, forcing cells to have an increased reliance on mitochondrial OXPHOS to generate sufficient ATP for cell survival (Robinson *et al*., 1992). Therefore, galactose

grown cells are more susceptible to mitochondrial toxicants (Marroquin *et al*., 2007; Dykens *et al*., 2008; Rana *et al.*, 2011).

The advancements in technologies, such as toxicogenomics, allows for hypotheses on potential mechanisms of mitochondrial perturbations to be made. In addition, characterisation of sufficient numbers of mitochondrial toxicants would enable development of theoretical models to assess quantitative structure-activity relationships (QSARs) that predict potential mitochondrial toxicants (Pereira *et al*., 2009). This approach would also permit the design of novel compounds with decreased mitochondrial toxicity.

As well as *in vitro* approaches, animal models that more sensitively reveal mitochondrial toxicity have been developed. For example, a heterozygous knockout mouse has been developed where expression of the mitochondrial isoform of the antioxidant MnSOD (SOD2) has been halved (Lebovitz *et al*., 1996). Using this $SOD2^{+/-}$ mouse model, Ong *et al* (2007), were able to reveal hepatotoxicity induced by troglitazone that was not detected in wild-type mice.

1.5 Syngenta compound summary

A background to the compounds used in this thesis

Syngenta developed a novel group of herbicidal compounds that were able to effectively eradicate weeds through the inhibition of very-long-chain-fatty acid (VLCFA) synthesis. These compounds belong to a novel sulfonyl isoxazoline (SI) chemistry developed by Syngenta and consist of both triazole and phenyl based chemistries. Three of these SI compounds were used in this thesis; two triazole compounds, 177 and 197 and one phenyl compound, 907. Although the exact chemical structures of the Syngenta SI triazole and phenyl compounds were unavailable, generic SI, triazole and phenyl chemical structures are displayed in figure 1.5.

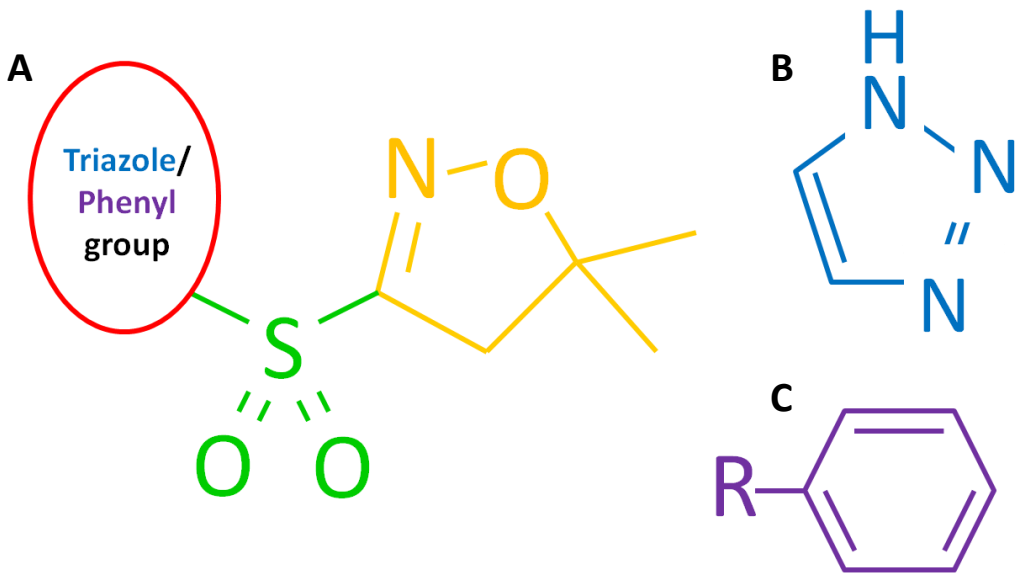

Figure 1.5. Generic sulfonyl isoxazoline (SI), triazole and phenyl structures. (A) Generic SI structure (provided by Syngenta chemists); the sulfonyl group is illustrated in green and the isoxazoline group in yellow. A triazole or phenyl group was attached to the sulfonyl group as indicated by the red circle. **(B) A triazole structure (blue),** which in this example is a 1,2,3-triazole, with the numbers referring to the position of nitrogen in the five memebered ring. **(C) A phenyl structure (purple),** which is a hexagonal ring of six carbons, five of which are bonded to individual hydrogens and one which is bonded to an R-group.

Syngenta carried out a number of studies with the SI compounds to define the safety profile on mammals. *In vitro* and *in vivo* studies were performed early in research to assess a range of toxicity parameters including; genotoxicity, sensitisation, and the effect of short-term repeat dose studies in rats, mice and dogs. The study designs, methods and results are detailed in additional file 1 (addenda). It has to be noted that details of all the studies were not available for all the compounds. A summary of the available toxicological profiles of the compounds are presented.

1.5.1 Genotoxicity, sensitisation and acute toxicity

A battery of tests was carried out to determine the genotoxicity and skin sensitisation toxicity of 177 and 197, which have been summarised in table S7 (additional file 1, addenda). Genotoxicity studies, using the Ames bacterial mutagenesis (Ames) test and Mouse Lymphoma Assay (MLA), were used to predict if the compounds were mutagenic. The results for both tests were negative, providing evidence that 177 and

197 were not mutagenic compounds. Skin sensitisation was assessed using the local lymph node assay (LLNA), which identified 177 and 197 as moderate skin sensitizers.

1.5.2 Repeat Dose animal studies with SI compounds

Experimental approach of repeat dose animal studies

Repeat dose studies with the triazole (177 & 197) and phenyl (907) compounds were carried out for Syngenta at Charles River Laboratories Inc. as part of the chemical safety R&D process. In these optimisation studies, CD-1 mice, Han Wistar rats and dogs (Beagle) were treated with a range of concentrations of SI compounds. Compounds were administered in diet or by gavage over a time course with sampling at days (D) 4, 7, 14 or 28. At each time point; body weight, organ weight, clinical chemistry, urinalysis, toxicokinetics and troponin analysis were assessed and organs harvested for histopathology. The results of all the repeat dose studies are summarised in tables S2-S6 in additional file 1 (addenda).

Summary and conclusions of the repeat dose animal studies

It is important to note that for the following summaries; striated muscle encompasses the cardiac and skeletal muscle and skeletal muscle is further subdivided into the femoris (thigh), soleus (calf) and diaphragm muscles. The femoris was simply referred to as skeletal muscle in all of the studies.

1.5.2.1 Triazole 197

There were four studies carried out with 197; a 14 D oral study in Beagle dogs, a 7 day oral (gavage) study in both mice and rats and a 28 day oral (dietary) study in rats (table S2, additional file 1, addenda).

The compound was severely toxic to dogs, with 30/mg/kg/day and 100mg/kg/day lethal after 2 and 1 day respectively. The low dose, 10mg/kg/day, resulted in the increase of both liver and muscle biomarkers in blood including; glutamate dehydrogenase (GLDH), creatine kinase (CK) and aspartate aminotransferase (AST). GLDH has been identified as an effective, sensitive and tissue specific biomarker of hepatocellular injury (O'Brien, 2002). AST and CK are non-specific markers since AST is

distributed in both the liver and muscle tissue, and CK is abundant in both the heart and skeletal muscles (Tonomura *et al.*, 2012). The histopathology analysis showed a myositis and myodegeneration in the diaphragm, skeletal and soleus muscle at 10mg/kg/day, as well as inflammation and necrosis of the liver at 30 and 100mg/kg/day. There was also a marked increase in cardiac troponin I (cTnI), a biomarker specific for cardiac damage, at 10mg/kg/day, although there were no histopathological or electrocardiographic changes in the heart to correlate with this. Studies have shown that peak troponin levels precede maximal lesion severity (York *et al*., 2006). It was concluded from this study that skeletal muscle was the primary target organ for adverse toxicity.

The 7 day studies in rat were confirmation that striated muscle was the primary target for adverse toxicity of 197. The compound was more toxic to rats than mice, but less toxic than it was to dogs. In mice, the 'No observed effect level (NOEL) was 1500mg/kg/day and at this dose there was no adverse striated muscle toxicity evident. The only observations were an increase in liver weights and an elevation in excretion of glucose and creatinine in the urinalysis. Creatinine is the breakdown product of creatine phosphate and so is indicative of non-specific muscle injury. In rats there was myositis and myodegeneration of the skeletal muscle at 150, 500 and 1500mg/kg/day in most animals. Minimal myositis and myodegeneration of the myocardium was identified at 1500mg/kg/day, which correlated with a subsequent increase in heart weight. No clinical chemistry or toxicokinetic changes were detected, but there were marked changes in the urinalysis. Citric acid cycle intermediates α-ketoglutarate and citrate were decreased, which represent stress markers of reduced feeding. Increases in sugars including glucose and myo-inositol were also detected and in toxicity studies these serve as markers of general stress.

The 28 day rat study revealed a greater range of toxicity and further validated the striated muscle as a principle toxicity finding. By 28 days, liver toxicity was also present, indicating a cumulative effect of 197 in the development of liver toxicity. The achieved doses for 0, 150, 1500 and 5000ppm, were 0, 16, 157, and 500mg/kg/day for males and 0, 16, 156 and 549mg/kg/day for females. At doses of 1500 and 5000ppm

there was minimal to moderate myodegeneration in the myocardium, skeletal, soleus, and diaphragm muscle. At 1500 and 5000ppm, there was minimal to moderate diffuse hepatocyte hypertrophy, mild hepatocyte degeneration and some necrotic and apoptotic hepatocytes. This was coupled with a dose dependent increase in liver weight, becoming significant at 1500 and 5000ppm. The clinical chemistry showed an increase in a number of biomarkers of muscle and liver injury, including alanine aminotransferase (ALT) (liver marker), AST (a non-specific marker of muscle injury) and CK (a non-specific marker of muscle injury). The study also revealed differences in gender sensitivities, with females proving more sensitive to 197 treatment. For example, at 1500ppm, there were 2/5 females with degeneration of the myocardium and diaphragm, but only 1/5 males. The overall conclusions from the 197 studies are summarised in the table 1.4.

Toxicological parameter	Conclusion
7 day rat tissue Sensitivities	Skeletal muscle>Cardiac muscle>Liver
28 day rat tissues sensitivities	Skeletal muscle=Cardiac muscle=Liver
Biomarkers	Correlated with liver and muscle pathology or indicated an underlying toxicity
Gender sensitivities	Female > Male
Species sensitivities	Dog >Rat >Mice
Time and Dose	The toxicity of 197 was time and dose dependent

Table 1.4. Overall conclusions on the toxicity of 197.

1.5.2.2 Triazole 177

There were 3 studies performed with 177 in rats; a 4 day dietary study, a 7 day oral (gavage) study and a 28 day dietary study (table S4, additional file 1, addenda). The 4 day study revealed no toxicokinetic, troponin or histopathological findings that were attributable to administration of 177. The achieved dose from the 4 day study with 150ppm was estimated at 16mg/kg/day for males and females.

In the 7 day study, cardiac and skeletal muscle histopathology predominated, as with 197. There was minimal myositis and myodegeneration of the myocardium and minimal to moderate myositis and myodegeneration of the skeletal muscle found at concentrations of 50 and 150mg/kg/day. The myocardial histopathology correlated

with a dose dependent effect on serum cTnI levels and an increase in relative heart weights in animals treated at 50 and 150mg/kg/day. Clinical chemistry revealed an increase in the general muscle injury biomarkers, AST and CK at 50 and 150mg/kg/day. The urinalysis was similar to 197 findings with a decrease in energy metabolites, α-ketoglutarate and citrate, and increases in sugars, glucose and myo-inositol.
By comparing the 7 day studies for both 197 and 177, it was evident that 177 was more potent. There were histopathological findings at 50 mg/kg/day with 177, but not with 197 and cTnI showed a dose and time dependent effect in 177, while there were no cTnI findings with 197.

The highest dose used in the 28 day 177 study, 150ppm, was the lowest dose used in the 197 28 day study. The achieved doses for 0, 5, 30 and 150ppm were 0, 0.6, 3.2 and 16.2 mg/kg/day in males 0, 0.6, 3.4 and 16.9 mg/kg/day. There were no haematological, clinical chemistry or toxicokinetic findings that were related to 28 day treatment with 177. There were histopathological effects at 30 and 150ppm in the diaphragm, soleus and skeletal muscle, but the incidence and severity of the effects were not related to dose. There was minimal myositis and myodegeneration of the diaphragm in 1/5 males and 2/5 females at 150ppm and minimal myositis of the soleus muscle was found in 3/5 females and 1/5 males at 30ppm and 1/5 females at150ppm. Minimal myositis was found in the skeletal muscle in 1/5 females at 30ppm and in 1/5, 1/5 and 2/5 males at 0, 5 and 30ppm respectively. At 150ppm, there was inflammatory cell infiltration in liver, periportal in 3/5 females and diffuse glycogen vacuolation in 1/5 males. There were no histopathological findings related to the heart in the study, but cTnT was elevated at 150ppm. Gender differences in the development of toxicity seem to be apparent, with females showing a greater amount of histopathology in the diaphragm, soleus and the liver. This is consistent with the 197 findings that females were slightly more sensitive to the treatment with the triazole compounds than males.

The main conclusion from the 28D study was that while myositis and myodegeneration of the soleus, diaphragm and skeletal muscle were detected, the incidence and severity could not be related to dose. As with 197, there was a

cumulative effect of 177 treatment, with development of liver toxicity dependent on duration of treatment. The overall conclusions on the toxicity of 177 based on all the studies are presented in table 1.5.

Toxicological parameter	Conclusion
Tissue Sensitivities	Skeletal muscle > Cardiac muscle> Liver
Biomarkers	Correlated with pathology or indicated an underlying toxicity.
Gender Sensitivities	Female > Male
7 day compound toxicity	177 > 197
28 day compound toxicity	Unable to determine the difference in toxicity after a 28 day treatment as no comparable doses.
Time and Dose	The toxicity of 177 was time and dose dependent

Table 1.5. Overall conclusions on the toxicity of 177.

1.5.2.3 Phenyl 907

A 28 D oral (dietary) study was carried out in rats (Han Wistar) with 907 for 28 days (table S6, additional file 1, addenda). The achieved doses for 0, 150, 500, 1500 and 3500ppm were 0, 16, 56, 166 and 375 mg/kg/day for females and 0, 16, 53, 152 and 368 mg/kg/day for males. At the highest concentration, 3500ppm, there were histopathological findings in the liver, testis and non-glandular stomach. Organ weight increase and associated blood chemistry correlated with liver histopathology findings. At 150ppm, there were no findings and so this was determined as the NOEL. At 3500ppm, there was; hepatocyte hypertrophy in all animals and degeneration of the seminiferous epithelium and sperm retention in testis of all males, which was associated with oligospermia in the epididymis. Findings in the liver, testis and epididymis were no longer present $\leq$1500ppm. The histopathology data in liver was supported by significant increases in liver weight (males at $\geq$150ppm and females at $\geq$500ppm) as well as an increase in a number of biomarkers of liver injury. There was a significant increase in gamma-glutamyltransferase (GGT), as well as a non significant increase in aspartate aminotransferase (AST) and glutamate dehydrogenase (GLDH), in males and females at 3500ppm. In addition, there was a statistically significant increase in cholesterol in all animals treated with 3500ppm, which provided further indication of liver injury. There were also findings in the stomach, with hyperkeratosis and squamous hyperplasia of the non-glandular stomach at $\geq$500ppm in all animals and minimal atrophy of the glandular stomach at 3500ppm. There were no adverse

cardiac and skeletal muscle findings as seen with the triazoles, 177 and 197, suggesting a distinct difference in toxicity targets for the triazole and phenyl compounds. The overall conclusions on the toxicity of 907 based on all the studies are presented in table 1.6.

Toxicological parameter	Conclusion
Tissue Sensitivities	Stomach> Liver > Testes
Biomarkers	Correlated with pathology or indicated an underlying toxicity.
Compound toxicity	197 > 907
Time and Dose	907 toxicity was dose dependent.

Table 1.6. Overall conclusions on the toxicity of 907.

1.5.2.4 Overall conclusions on the toxicity profiles of 177, 197 and 907

Based on assessment of all the animal studies carried out for the triazole and phenyl SI compounds, the overall conclusions on the toxicity of the compounds are presented in table 1.7.

Toxicological parameter	Conclusion
Overall Compound Toxicity	Triazoles > Phenyl
Striated muscle toxicity	Triazoles > Phenyl
Triazole striated muscle toxicity	Skeletal muscle > Cardiac muscle
Liver toxicity	Primary toxic target for phenyl 907 and present as a secondary target with triazoles. 197 and 177 > 907
Biomarkers	Correlated with predicted underlying toxicities
Dose Response	Toxic effects were dose dependent with all compounds
Time Response	A time dependent toxicity response was detected with triazole compounds
Gender sensitivity with Triazoles	Females > Males
197 species sensitivities	Dog > Rats > Mice

Table 1.7 Overall conclusions on the toxicity profiles of the triazole and phenyl SI compounds.

1.5.2.5 Detailed Summary and conclusions of the 28 day 197, 177 and 907 studies in female rats treated with 150ppm

A more detailed summary of the 28 day studies with female rats treated with 150ppm 197, 177 and 907 will be presented, as this concentration and time point was used for

microarray analysis in this thesis. The three groups of tissue selected were; left lobe liver (LLL), thigh skeletal muscle (TSM) and left ventricular heart (LVH) and so the focus here was on effects seen in these tissues.

Triazole 197

The achieved dosage for 150ppm was 16mg/kg/day in males and females. There were no haematological, clinical chemistry, urinalysis or body and organ weight change findings that correlated with 150ppm treatment. While there were some histopathological effects seen at 150ppm in both males and females, these were minimal and not significant (table S3, additional file 1, addenda). There were only 1/5 male and female animals with minimal hepatocyte degeneration and myofibre degeneration of skeletal muscle, and 1/5 females with myocardial degeneration. Minimal myofibre degeneration of the soleus muscle was found in 2/5 females, but this was not present in males. Overall, the histopathological effects were isolated and were not correlated with any other physiological effects. The three tissues of interest to this study, LLL, LVH and TSM, were considered not to exhibit any significant toxicity and therefore 150ppm represented a sub-toxic dose.

Triazole 177

The achieved doses for 150ppm 177 were analogous to 197, at 16.2 and 16.9 mg/kg/day in males and females respectively. There were no haematological or clinical chemistry findings and no histological findings in the skeletal muscle or cardiovascular system (table S5, additional file 1, addenda). Despite the lack of cardiac muscle pathology, there was an increase in cTnT, a cardiac specific biomarker, in males and females. There were some minor histopathological findings in the liver, with 1/5 males having diffuse vacuolation and 3/5 females having inflammatory cell infiltration. Therefore, as with 197, for the tissues of interest 150ppm of 177 was considered a sub-toxic dose.

Phenyl 907

The NOEL level for the 28 day 907 study was 150ppm, so along with 177 and 197, this was considered a sub-toxic dose.

1.6 Thesis aims and objectives

The validation of *in vitro* skeletal muscle models may play a pivotal role in capturing safety endpoints early within the research and development process. The primary aim of this project was to investigate the extent of translation from an *in vivo* rat model to an *in vitro* skeletal muscle model, using a toxicogenomics approach. It was hypothesised that the *in vitro* model would accurately reflect the findings *in vivo*, thereby validating it as a useful model for investigating skeletal muscle toxicity. Moreover, an *in vitro* skeletal muscle model that more sensitively detects mitochondrial toxicity was developed and validated.

These aims will be addressed by the following objectives:

- To generate gene expression profiles of LLL, LVH and TSM from female Han Wistar rats treated with subtoxic doses of SI triazoles (177 and 197) and phenyl (907) for a subchronic time point.

- To identify potential toxic mechanisms of action (toxicity pathways) of 177, 197 and 907 from LLL, LVH and TSM tissues using toxicogenomics. From this investigation, hypotheses on the adverse effects of the compounds will be generated, which will be further investigated and validated using *in vitro* models.

- To investigate the translation of the *in vivo* triazole toxicity pathways, identified by *in vivo* toxicogenomics, into the L6 *in vitro* model. In doing this, both the L6 *in vitro* model to predict *in vivo* outcomes and the *in vivo* toxicogenomics data will be validated.

- To develop and validate an *in vitro* skeletal model system that more sensitively reports mitochondrial toxicity. It was hypothesised that replacing glucose with galactose in the culture media of L6 skeletal muscle cells would increase their reliance on mitochondrial OXPHOS, thereby making them more sensitive to mitochondrial toxicants.

CHAPTER TWO:

Materials and Methods

2.1 Materials and Equipment

All pipettes were from Gilson Scientific, UK and used with TipOne Filter Tips (sterile and certified RNase, DNase, DNA and Pyrogen free) from StarLab (UK) Ltd, Milton Keynes, UK, unless otherwise stated.

2.1.1 Total RNA extraction from tissues

Modified RNeasy Fibrous Kit Protocol

The RNeasy fibrous kit and RNase-free DNase set were purchased from Qiagen Ltd, Manchester, UK. Surgical scalpel blades (No.22) were acquired from Swann Morton, Sheffield, UK. The analytical balance was from Mettler Toledo AB54-S/FACT. The β-mercaptoethanol, ethanol (EtOH) and industrial methylated spirits (IMS) were purchased from Sigma-Aldrich Company Ltd., Dorset, UK. The mortar/pestle set and the IKA Ultra Turrax T 25 homogeniser with 8mm tip were from Fisher Scientific UK Ltd, Loughborough, UK. The diethylpyrocarbonate (DEPC) and RNase Zap® were purchased from Ambion and Invitrogen respectively (Life Technologies Ltd, Paisley). The RNase-free microtubes were from Sarstedt Ltd, Leicester, UK and the microcentrifuge collection tubes without caps were fram StarLab (UK) Ltd, Milton Keynes, UK. The MSE Micro Centaur microcentrifuge was from MSE (UK) Ltd, London, UK.

2.1.2 Quantitation and quality control of RNA

The NanoDrop ND-1000 UV spectrophotometer was from NanoDrop Products, Thermo Scientific. The Agilent Bioanalyzer, RNA 6000 Nano LabChip® kit and Chip station were from Agilent Technologies Ltd, Berkshire, UK. The IKA Vortexer and Eppendorf (5424) microcentrifuge were from Fisher Scientific UK Ltd, Loughborough, UK. The GD100 water bath was from Grant Instruments Ltd, Cambridge, UK.

2.1.3 Transcription profiling using microarrays

2.1.3.1 Whole Genome Gene Expression Bead Chips

RatRef-12 Whole genome Gene Expression BeadChips (table 2.1) were from Illumina, Inc, US. The RatRef-12 BeadChip allowed for the analysis of 22,519 probes per sample,

targeting 21,910 genes selected primarily from the NCBI RefSeq database and processed 12 samples per chip.

BeadChip	RatRef-12
NCBI RefSeq Database (Release 16NM)	6,274
NCBI RefSeq Database (Release 16 XM)	15,983
NCBI RefSeq Database (Release 16 XR)	12
UniGene	250
Total	22,519

Table 2.1 Whole Genome Gene Expression BeadChips. Table containing detail on the probes present on the RatRef-12 BeadChip and the databases used to develop it.

2.1.3.2 Direct Hybridization assay

cRNA amplification and Sample Labelling

The Ambion Illumina® TotalPrep RNA amplification Kit was purchased from Ambion, Inc, AMIL1791, Applied Biosystems, UK. All reagents used were ACS reagent grade from Sigma-Aldrich. Equipment used included; a vortex mixer from Vortex Genie-2, Scientific Industries, New York, US, a VWR Galaxy mini microcentrifuge from OyaGen Inc, NY, US, a Jouan B4I Multifunction Centrifuge from Fisher Scientific UK Ltd, Loughborough, UK, a Hybridization oven from Illumina Inc, US, a thermal cycler (Thermo Hybaid MBS 0.2 G) from Thermo Scientific, UK and a QB A2 heat block from Grant Instruments (Cambridge) Ltd, UK.

Assessing cRNA Yield and Quality

cRNA yield and quality were determined using the same materials and equipment as for total RNA analysis (section 2.1.2).

Vacuum centrifugation

A Savant DNA120 SpeedVac Concentrator from Thermo Scientific, UK was used to vacuum centrifuge cRNA samples to an adequate cRNA concentration.

2.1.3.3 Hybridisation and scan

All equipment, materials and reagents used are detailed in the 'Whole Genome Gene Expression Direct Hybridization Assay guide' and supplied by Illumina unless otherwise stated. The same thermal cycler, vortexer and hybridization oven were used as detailed in section 2.1.3.2.

Post Hybridization Wash and Staining

Streptavidin-Cy3 (1mg/ml RNase free water) was purchased from Sigma-Aldrich Company Ltd., Dorset, UK. The Hybex water bath and water bath insert (SciGene Hybex Microsample Incubator, heating base, 230V) were purchased from SciGene, CA, US and the Stuart mini orbital shaker SSM1 was from Bibby Scientific Limited, Staffordshire, UK. The Jouan B4I Multifunction Centrifuge was from Fisher Scientific UK Ltd, Loughborough, UK.

Scanning of microarrays

Microarray slides (BeadChips) were scanned on an Illumina BeadArray Reader with Bead scan Software.

2.1.4 Cell Culture and Treatments

2.1.4.1 Cell lines

The L6 myogenic cell line was originally isolated from primary cultures of rat thigh muscle maintained for the first two passages in the presence of methyl cholanthrene (Yaffe, D. 1968). The L6.G8.C5 cells are a subclone of the L6 cell line and were a kind gift from Dr Alan Bevington (University of Leicester, UK).The cell line will be referred to as simply 'L6' for the duration of the thesis.

The H9c2 cell line was derived through selective serial passaging of cells from the ventricular part of an embryonic E13 BDIX rat heart. H9c2 cells were purchased as an established cell line in a 1ml frozen ampule ($6.5x10^5$) from the American Type culture Collection (ATCC).

HepG2 cells were originally isolated from a human liver biopsy taken from a male patient (15 years old) with hepatocellular carcinoma. HepG2 cells were purchased as an established cells line in a 1ml frozen ampule (5.8×10^6) from ATCC.

2.1.4.2 Cell culture Equipment and consumables

Tissue culture treated 75 cm^2, canted neck flasks (T.75), CELLSTAR® 96 well clear polystyrene wells flat bottom plates (with lid), CELLSTAR® 6 well culture plates (with lid) were purchased from Greiner Bio-One Ltd., UK. Deep 96 Well Plate (sterile Clear V-Bottom 0.5mL Polypropylene) and TC-Treated 96 well flat clear bottom white polystyrene microplates were purchased from Corning B.V. Life Sciences, Netherlands. Falcon tubes (15 and 50ml) were purchased from BD Biosciences, Oxford, UK and the centrifuge Jouan CR 312 refrigerated centrifuge from Fisher Scientific UK Ltd. The CoolCell was from BioCision, LLC, CA, US and the microscope was from AMG Evos XL, AMG, Life Technologies, UK.

Basal media

The basal medium Dulbecco's Modified Eagle's Medium (DMEM) with high glucose (containing 4500mg/mL glucose, 4mM Glutamine and phenol red) and DMEM without glucose (containing 4mM L-Glutamine and phenol red) were purchased from Gibco, Life Technologies Ltd, Paisley, UK.

Cell media additives and supplements

Foetal bovine serum (FBS), certified, heat inactivated (HI), US origin, HEPES (N-2-hydroxyethylpiperazine-N-2-ethane sulfonic Acid), 1M solution, sodium pyruvate, 100mM solution, L-glutamine, 200mM solution and Dulbecco's phosphate-buffered saline (DPBS) without Ca^{2+} and Mg^{2+} were purchased from Gibco, Life Technologies Ltd, Paisley, UK. Penicillin (10,000 IU) and streptomycin (10,000 µg/ml) solution in a 100-fold working concentration was purchased from PAA Laboratories Ltd, Yeovil Somerset, UK. Hyclone Trypsin, 0.25% 1X, with 2.5g porcine trypsin (1:250/L gamma irradiated) in HBSS with 1g/L EDTA, without calcium, magnesium (liquid) was purchased from Hyclone Laboratories Inc., Thermo Scientific. D-(+)-galactose powder and dimethyl sulfoxide (DMSO) were purchased from Sigma-Aldrich.

2.1.4.3 Cell Treatment Reagents

The table below details all the compounds and reagents used to treat cells and where they were purchased or acquired from (table 2.2).

Compound	Company
177	Syngenta
197	Syngenta
907	Syngenta
H_2O_2	Sigma-Aldrich
Antimycin A	Sigma-Aldrich
Nocodazole	Sigma-Aldrich
FCCP	Sigma-Aldrich
Oligomycin	Sigma-Aldrich
NAC	Sigma-Aldrich
Staurosporine	Sigma-Aldrich
Troglitazone	Sigma-Aldrich
DMSO	Sigma-Aldrich

Table 2.2. Cell treatment reagents.

2.1.5 Cell Viability

Cell counting kit-8 (CCK-8) assay

The cell counting kit-8 (CCK-8) assay was purchased from Sigma-Aldrich and the BioTek Elx800 plate reader was from BioTek UK, Bedfordshire, UK.

ATP measurement

The ATP determination kit was purchased from Molecular Probes Inc., Life Technologies UK Ltd. The kit contained; D-luciferin (5x 3 mg of lyophilized powder), firefly recombinant luciferase (40 µL of a 5 mg/mL solution in 25 mM tris-acetate, pH 7.8, 0.2 M ammonium sulfate, 15% (v/v) glycerol and 30% (v/v) ethylene glycol), dithiothreitol (DTT) (25 mg) and a 20X reaction buffer (10 mL of 500 mM Tricine buffer, pH 7.8, 100 mM MgSO4, 2 mM EDTA and 2 mM sodium azide). DPBS without Ca^{2+} and Mg^{2+} was purchased from Gibco, Life Technologies Ltd, Paisley, UK. The plate

shaker (Wesbart IS89) was from Wesbart Ltd., West Sussex, UK and the NOVOstar luminometer was from BMG Lab Technologies, Aylesbury, UK.

Caspase 3/7

The Caspase-Glo® 3/7 assay (containing Caspase-Glo® buffer and Caspase-Glo® substrate (lyophilised)) were purchased from Promega, Chilworth Science Park, Southampton, UK. The plate shaker (Wesbart IS89) was from Wesbart Ltd., West Sussex, UK and the NOVOstar luminometer was from BMG Lab Technologies, Aylesbury, UK.

2.1.6 General Flow Cytometry equipment and consumables

Fluorescence-activated cell sorting (FACS) tubes (5 ml Polystyrene Round Bottom) were purchased from BD Biosciences and FACS caps were purchased from Elkay Laboratory Products (UK) Ltd, Hampshire, UK. Distilled water (dH_2O) was prepared in-lab and filtered through a Millex GP 0.2 µm filter (PES membrane) purchased from Merck Millipore, UK. The CyAn ADP Analyzer flow cytometer and the Summit v4.3.02 software used to analyse the flow cytometry data were from Beckman Coulter (UK) Ltd., High Wycombe, UK.

2.1.7 Flow cytometry assays

Annexin V/PI

The Annexin V-FITC Apoptosis Detection Kit was purchased from Abcam, Cambridge, UK. DPBS with Ca^{2+} and Mg^{2+} was purchased from Gibco, Life Technologies Ltd, Paisley, UK. The kit contained; Annexin V-FITC, Propidium iodide and Annexin Binding Buffer (50 mM HEPES, 700 mM NaCl, 12.5 mM $CaCl_2$, pH 7.4).

Cell cycle analysis and measurement of cell size

Propidium Iodide solution (1.0 mg/ml in water), RNase A (1.0mg/ml) and EtOH were purchased from Sigma-Aldrich. DPBS without Ca^{2+} and Mg^{2+} was purchased from Gibco Life Technologies Ltd, Paisley, UK.

ROS and mitochondrial membrane potential measurements

The fluoroprobes dihydroethidium (DHE) and MitoSox^{TM} Red mitochondrial superoxide indicator were purchased from Molecular Probes, Inc., Life Technologies UK Ltd. DMSO was from Sigma-Aldrich and HBSS (with Ca^{2+} and Mg^{2+}) was from Gibco, Life Technologies UK Ltd. MitoTracker® Red CMXRos was purchased from Molecular Probes, Inc., Life Technologies UK Ltd.

2.1.8 Metabolic profiling using Extracellular flux (XF) analysis

XF24 Sensor Cartridge plates, XF cell culture plates Seahorse Bioscience and XF24 calibrant, pH7.4, were purchased from Seahorse Biosciences, US. The Seahorse XF24 instrument and software belonged to the MRC Toxicology Unit, University of Leicester and were purchased from Seahorse Biosciences, US. The Memmert Precision Model INE 550 incubator (set at 37°C without CO_2) was from Memmert.

Unbuffered media

Dulbecco's Modified Eagle's Medium Base 8.3g/l, 200mM glutaMax, 100mM sodium pyruvate, sodium chloride (NaCl) and phenol red powder, D-(+)-glucose and D-(+)-galactose, sodium hydroxide (NaOH) and hydrochloric acid (HCL) were purchased from Sigma-Aldrich. Millex GP 0.2 µm filters (PES membrane) were purchased from Merck Millipore, UK.

Mito Stress kit

Oligomycin, FCCP, antimycin A and DMSO were purchased from Sigma-Aldrich. The Eppendorf single-channel electronic pipette was from ThermoScientific, UK.

2.1.9 Total cell Protein extraction

CelLytic M Cell Lysis Reagent and Bradford Reagent (for 1-1,400 µg/ml protein) were purchased from Sigma-Aldrich. The plate shaker (Wesbart IS89) was from Wesbart Ltd., and the BioTek Elx800 plate reader was from BioTek UK, Bedfordshire, UK. CELLSTAR® 96 well clear polystyrene wells flat bottom plates (with lid) were purchased from Corning B.V. Life Sciences. Multi-channel pipettes and 50ml Reagent reservoir were from Gilson Scientific Ltd., UK.

2.2 Methods

2.2.1 Total RNA extraction from tissues

2.2.1.1 Modified RNeasy Fibrous Kit Extraction protocol

The RNA extraction protocol was modified and optimised until a sufficient yield and quality of RNA extraction was achieved with all three tissues; left lobe liver (LLL), left ventricle heart (LVH) and thigh skeletal muscle (TSM). The final kit used for extractions from all 3 types of tissue was the Qiagen RNeasy Fibrous kit with the following major modifications:

1) the use of less starting material
2) the use of mortar and pestle for pulverisation of frozen tissue
3) the extension of centrifugation times
4) the inclusion of more collection tube changes
5) the thorough rinsing of columns with wash buffer
6) the final elution in a smaller volume to concentrate the RNA.

Before Starting

The entire workstation and all the equipment were first decontaminated with IMS followed by RNase zap solution. Buffer RLT and Qiagen DNase were prepared as detailed in the manufacturer's instructions and DEPC and IMS were aliquoted fresh each day.

Weighing and Pulverisation of tissues

The collection tubes (2ml microtubes), scalpel blade, forceps, weighing tray, tissue samples and mortar and pestle were placed on dry ice in a polystyrene box. To avoid tissue thawing and subsequent RNA degradation, all the procedures, apart from the weighing, were carried out on dry ice as quickly as possible. Each sample was placed into the mortar and a section between 18 and 23mg (~27mm^3) was weighed out rapidly on a weighing tray. This was the optimised weight to achieve high RNA yield and integrity. Each sample was then pulverised to a fine powder using the pestle and distributed into 2ml microtubes on dry ice. In between each sample, the equipment

was thoroughly cleaned using IMS and Rnase Zap and the scalpel blade was changed to prevent sample cross-contamination. Pulverising the sample into a fine powder proved to increase the effectiveness of the digestion and thus increase the yield and quality of the RNA. At this stage, the samples were stored on dry ice or in the -80°C freezer until required for tissue homogenisation.

Disruption, Homogenisation and Digestion

The rotor-stator homogeniser (8mm tip) was first decontaminated with IMS, followed by RNase Zap and DEPC. The Buffer RLT and DNase 1 were prepared freshly each day as detailed in the kit. A volume of 300µl Buffer RLT was added to each sample, homogenised for 40 seconds then placed on wet ice until required. This length of homogenisation was pre-determined as an adequate time to ensure considerable tissue disruption and was the standardised time used for all three tissue types. The homogeniser was cleaned thoroughly in between each sample using Rnase zap followed by DEPC, which served to reduce contamination of samples and prevent any carry-over of tissue from one sample to the next.

A volume of 590µl RNase-free water was added to each lysate, followed by 10µl of proteinase K solution and mixed thoroughly by pipetting. The samples were immediately incubated at 55°C for 10 min in a heating block, after which they were placed back on ice. The samples were then centrifuged for 5 minutes at 13,000 rpm and avoiding disruption of the pellet, the supernatant was removed (approximately 900µl) and transferred to a fresh 2ml microcentrifuge tube.

Washing and Binding

Ethanol (70%) was added at 0.5 volume (450µl) to each cleared lysate and mixed well by pipetting. A 700µl aliquot of each sample was then added to an RNeasy spin column, centrifuged at 10,000 rpm for 2 minutes and the flow-through discarded. The remaining sample (500µl) was passed through the RNeasy spin column, by centrifuging again at 10,000 rpm for 2 minutes, the collection tube discarded and the column placed into a fresh collection tube.

Another ethanol based buffer, RW1 buffer (350µl) was then added to the column and centrifuged at 10,000 rpm for 2 minutes and the flow-through discarded. DNase (80µl) was added to each spin-column and left to incubate for 30 minutes at room temperature after which another wash with RW1 buffer (350µl) was performed under the same conditions as previously mentioned. The collection tube was again changed and Buffer RPE (500µl) was then added to each spin-column and left to incubate at room temperature for 5 minutes prior to centrifugation at 10,000rpm for 2 minutes. This stage was repeated once more with the centrifugation period extended to 4 minutes to dry the membrane in the spin-column and prevent solvent contamination of RNA. To further dry the spin-column membrane, an additional "dry spin" was performed at 10,000 rpm for 5 minutes with a clean collection tube.
The collection tube was then replaced with an RNase-free Eppendorf and the column aired out at RT for 1 minute to ensure all the buffers and ethanol evaporated off.

Elution

The RNA was eluted by addition of 25µl RNase-free water to each spin column and centrifugation at 10,000rpm for 2 minutes. The eluted sample (eluate) was then passed through the column again and centrifuged at 10,000rpm for 2 minutes. The eluted RNA samples were then placed on ice and aliquoted out into three tubes of 10µl, 10µl and 5µl respectively. The two 10µl samples were placed on dry ice and stored in the -80°C until required for downstream analysis (Bioanalyzer, microarray). The 5 µl aliquot was placed on ice, to prevent RNA degradation, until spectrophotometric analysis of the RNA yield and purity could be performed.

2.2.2 Quantitation and quality control Of RNA

To ensure the RNA extracted was of a high enough yield and quality for downstream analysis quantitation and quality control was carried out using a UV spectrophotometer and Agilent Bioanalyzer.

2.2.2.1 NanoDrop ND-1000 UV spectrophotometer Protocol

A NanoDrop ND-1000 UV (Thermo Scientific, NanoDrop technologies) spectrophotometer was used to determine RNA concentration and purity. The software calculated the concentration as a 10mm absorbance path for convenience, displaying the concentration in ng/µl. The purity of the RNA was determined by calculating the ratios for OD260/280 (260nm - peak nucleic acid absorbance, 280nm - peak protein absorbance) and OD260/230 (260nm - peak nucleic acid absorbance, 230nm - peak carbohydrates, peptides, phenols, aromatic compounds absorbance). A ratio of between 1.8 and 2.07 was classified as the acceptable range for 260/280, indicating RNA relatively free from protein contamination. For 260/230, a ratio of 1.8-2.2 was the acceptable range and demonstrated a low level of contamination from molecules that absorb in the 230nm range. Any RNA samples outside of these ranges were discarded and an RNA re-extraction was performed from a separate sample of tissue.

2.2.2.2 Agilent 2100 Bioanalyzer

The quality of the RNA isolated from the tissue samples was assessed on the Agilent 2100 Bioanalyzer using the Eukaryotic RNA Assay with the RNA 6000 Nano LabChip® Kit. While the NanoDrop provided information regarding the RNA quantity and purity, it gave no indication on the RNA integrity (i.e. how degraded the RNA was). The Agilent Bioanalyser for analysis of nucleic acids is an electrophoretic assay based on traditional gel electrophoresis principles that have been transferred to a chip format.

Nano gel, ladder and Sample preparation

Upon kit arrival, the RNA 6000 Nano gel (simplified here to nano gel) and ladder were first prepared according to manufacturer's instructions. The nano gel was spin filtered at 1500g for 10 minutes at room temperature and 65µl aliquots were distributed in 0.5 ml RNnase-free microfuge tubes and stored at 4°C (all kit reagents were stored at 4°). The ladder was heat denatured for 2 minutes in a 70°C water bath, immediately cooled on ice, aliquoted into RNase-free vials and stored at -80°C. Before use each time, the kit reagents were removed from 4°C and equilibrated to room temperature for 30 minutes. Meanwhile, a single aliquot of ladder and a 10µl aliquot of each RNA

sample were removed from the -80°C and thawed out on ice. The RNA samples were heat denatured in a 70°C water bath for 2 minutes and immediately placed back on ice until required.

Bioanalyzer and Chip priming Station preparation

The Chip priming station was then set up by adjusting the base plate to position C and the syringe clip to the top position. The electrodes of the Bioanalyzer were decontaminated with RNAseZap and RNase free water. Two electrode cleaners were filled; one with 350µl RNaseZap, another with 350µl RNase free water and the RNaseZap was placed into the machine for 1 minute, followed by the RNase free water for 10 seconds. The machine was then left to air dry for 10 seconds.

Gel Dye preparation and loading

Once the reagents had equilibrated, the RNA 6000 Nano dye concentrate (nano dye) was vortexed for 10 seconds, centrifuged briefly and 1µl added to a 65µl aliquot of filtered nano gel. The solution was vortexed well and centrifuged at 13000g for 10 minutes at room temperature. All the dye and dye mixtures were kept out of the light to avoid dye decomposition, which would have reduced the signal intensity and compromised detection. Following preparation of the gel-dye mix, a new RNA Nano chip was placed on the chip priming station and 9µl of gel-dye mix were loaded into the well, marked G (fourth column, third row). Importantly, when pipetting into the chip the pipette tip was inserted to the bottom of the well to avoid introducing bubbles and ensure good results. The chip priming station was closed and the plunger pressed down until held in place by the clip. After 30 seconds, the clip was released and after a further 5 seconds, the plunger was slowly returned to the 1 ml mark on the syringe. The chip priming station was opened and 9 µl of the gel-dye mix were pipetted in the two additional wells marked G (fourth column, first and second rows).

Marker, Sample and Ladder loading

A volume of 5µl RNA 6000 Nano marker was pipetted into each of the 12 RNA wells and the well, marked ‘ladder’. A volume of 1 µl of prepared ladder was then pipetted into the latter well and 1µl of RNA sample into each of the 12 sample wells. To

thoroughly mix the sample and regents, the chip was placed in the adapted vortexer and vortexed for 1 minute at 2400rpm.

Running the Chip on the Bioanalyzer

The chip was run on the Agilent 2100 bioanalyzer within 5 minutes of being prepared to ensure the reagents did not evaporate and affect the quality of the results.
The Agilent Expert 2100 software was opened and the chip was carefully placed into the receptacle of the Agilent Bioanalyzer. The EukaryoteTotal RNA Nano assay was selected and the analysis was initiated by selecting the 'start' button. Once the Chip run had finished, the chip was removed from the Bioanalyzer, disposed of appropriately and the electrodes were cleaned with RNaseZap and RNase free water as previously described.

Agilent Bioanalyzer Analysis

The Agilent software provided the results in a slab-gel like image and an electropherogram, which provide a detailed visual assessment of the quality of the RNA sample. Although messenger RNA (mRNA) is the important RNA in terms of microarray analysis it only comprises 1-3% of total RNA and so is not readily detectable even with the most sensitive methods. Since rRNA makes up >80% of total RNA samples, with the majority of that comprised by the 28S and 18S rRNA, these RNA species are used as the platform for determining RNA integrity. Mammalian 28S and 18S rRNAs are approximately 5kb and 2kb in size respectively and the theoretical 28S:18S ratio is approximately 2.7:1; but a 2:1 ratio has long been considered the benchmark for intact RNA. However, a ratio of 2:1 rarely occurs because 28S is very unstable, degrading more rapidly than 18S rRNA and reducing the ratio. Therefore, any rRNA ratio above 1 was considered acceptable. The Bioanalyzer software automatically calculated the ratio of the 18S to 28S ribosomal subunits for RNA integrity assessment. However, recent research has shown that the rRNA ratios are often an inaccurate assessment of RNA integrity (Mueller *et al*., 2004). Therefore, researchers at Agilent technologies developed a standardized method of RNA integrity interpretation. This new tool for RNA quality assessment is known as the RNA integrity number (RIN).

RNA Integrity Number (RIN)

The RIN was developed to remove individual interpretation of RNA quality and takes into account the entire electrophoretic trace, not just the 18S and 28S fragments. The RIN software algorithm classifies eukaryotic total RNA based on a numbering system from 1 to 10, with 1 being the most degraded and 10 being the most intact. This algorithm was developed from 1300 total RNA samples in three mammalian species (human, rat and mouse), from various tissues, all with varying levels of integrity. While a low RIN number, like 5.0 may be suitable for analysis with qRT-PCR, a RIN of 7.0 is the minimum acceptable value of RNA integrity when performing microarray analysis. Therefore, any RNA samples with a RIN of lower than 7.0 were discarded and RNA re-extracted from tissue samples.

2.2.3 Transcriptional Profiling Using Microarray

There are a number of different microarray platforms that all utilise the same basic principles. Essentially, a nucleic acid is immobilised on a solid surface (Chip) for hybridization with a fluorescently labelled RNA sample. The most widely used platforms include the Stanford microarray system, Affymetrix gene chips and Illumina microarrays. Stanford type microarrays are two colour microarrays, in which hybridization of differentially labelled control and test RNA is carried out simultaneously. Affymetrix gene chips are manufactured by synthesizing 25-mer oligonucleotide probes onto a silicon chip using a photolithography method. Unlike the Stanford method, the Illumina and Affymetrix microarrays are hybridized with a single sample at one time.

2.2.4 Illumina Bead Microarray

Conventional microarrays, like Affymetrix, are manufactured by spotting or synthesizing probes onto two-dimensional substrates at known locations. In contrast, Illumina employ BeadArray technology based on the random self-assembly of quantitated pooled bead libraries into etched microwell substrates (Michael et al., 1998). Each bead is 3µm in diameter and has approximately 700,000 covalently attached oligonucleotide probes of a unique sequence. The probes are made up of a 50-mer gene specific probe plus a 29-mer address sequence for decoding the location

of the bead. The size and dimension of the bead and patterned substrate mean the density of a randomly assembled 3-µm-diameter bead array is ~40,000 times higher than a spotted array (Michael et al., 1998). Data quality and reproducibility are also supported by the high level of bead type redundancy (an average of 30 beads per probe) on every array. The main advantages for using the Illumina Expression Beadchips are; the ability to run multiple samples in parallel on the same chip, thereby reducing the batch effects and cost per sample, the bead-type redundancy, which meant for each bead type there are about 30 randomly positioned replicates and the decoding strategy, which ensured 100% quality control of Illumina microarrays (Michael et al., 1998).

Control and treated samples of cRNA were made and hybridised onto individual arrays using a direct labelling technique. Direct labelling involved incorporation of biotin during reverse transcription, followed by hybridization to the microarray. A post-hybridization secondary detection step was used to introduce the fluorophore, Streptavidin-Cy3 conjugate, for signal generation. The microarray chips were then scanned for the signal generated.

2.2.4.1 Direct Hybridization assay

Sample labelling (cRNA synthesis and Labelling)

Input RNA Preparation

The recommended amount of input total RNA for the cRNA amplification procedure was between 50 and 500ng in a maximum volume of 11µl RNase-free water. Each RNA sample was thawed out on wet ice, diluted to 250ng in a volume of 11µl RNase free water and transferred to an RNase-free 0.2ml microcentrifuge tube. The samples were then stored at -80°C until required for cRNA preparation. The Ambion Illumina® TotalPrep RNA amplification Kit was used for the cRNA amplification and labelling procedure as detailed in the manufacturer's instructions.

Reverse Transcription to Synthesize First strand cDNA

The prepared total RNA samples (250ng in 11µl RNase free water) were removed from -80°C storage and thawed out on wet ice. Meanwhile, the wash buffer was prepared

by addition of 24ml 100 % ethanol and the hybridization oven was pre-heated to 42°C. At room temperature, the Reverse Transcription Master Mix (RTMM) was prepared (table 2.3) in a 1.5 ml nuclease-free tube, mixed well by vortexing and centrifuged briefly (~5 seconds) to collect the mix at the bottom of the tube and placed on ice. RTMM (9µl) was added to each sample, mixed thoroughly by pipetting and flicking and centrifuged briefly to collect the reaction solution at the bottom of the tube. The samples were placed into the 42°C hybridization oven, incubated for 2 hours and then placed on ice.

Reverse Transcription Master Mix (for a single 20µl reaction)	
Amount	Component
1µl	T7 Oligo(dT) Primer
2µl	10X First Strand Buffer
4µl	dNTP Mix
1µl	RNase Inhibitor
1µl	Arrayscript

Table 2.3: Reverse transcription master mix. The components in the table were added in the order listed to a 1.5 ml nuclease-free tube at room temperature, mixed well by vortexing and centrifuged briefly to collect the mix at the bottom on the tube.

Second Strand cDNA synthesis

The thermal cycler was programmed for one run of 16°C (heat-lid disabled) for 2 hours, and placed on hold until required. It was important the heat-lid was disabled as excess heat from the lid could have inhibited the reaction. On ice, the Second Strand Master Mix (SSMM) was prepared (table 2.4) mixed well by vortexing and centrifuged briefly (~5 seconds) and placed back on ice. SSMM (80µl) was pipetted into each sample, mixed thoroughly by pipetting and flicking and centrifuged briefly (~5 seconds). The tubes were then placed in the 16°C thermal cycler and the 2 hour run started. During this 2 hour incubation a minimum of 20µl per sample of Nuclease-free water were heated to 55°C in a water bath in preparation for the cDNA purification. After the 2 hour incubation at 16°C, the samples were placed on ice and cDNA purification was carried out immediately.

Second Strand Master Mix (for a single 100µl reaction)	
Amount	Component
63µl	Nuclease-free water
10µl	10X reaction buffer
4µl	dNTP reaction mix
2µl	DNA polymerase
1µl	RNase H

Table 2.4: Second Strand master mix. The components in the table were added in the order listed to a 1.5 ml nuclease-free tube on ice, mixed well by vortexing and centrifuged briefly to collect the mix at the bottom on the tube.

cDNA purification

At room temperature, 250µl of cDNA binding buffer were aliquoted into 2 ml hydrologix tubes and each sample (100µl) was added, mixed by pipetting and flicking and centrifuged briefly (~5 seconds). Proceeding quickly, the cDNA sample/cDNA binding buffer mix (350µl) was pipetted onto the centre of a cDNA filter cartridge (column) and centrifuged at 10,000g for 1 minute. The flow through was discarded and the column washed by addition of 500µl wash buffer and centrifugation at 10,000g for 1 minute. The flow through was again discarded and the column centrifuged for a further minute to remove trace amounts of wash buffer. The column was then transferred to a fresh 2ml hydrologix tube and 20µl of 55°C nuclease-free water were added to the centre of the column and incubated for 2 minutes at room temperature. The sample was eluted by centrifugation at 10,000g for 1 minute and the samples placed on ice. The hybridization oven was pre-heated to 37°C before proceeding to the next step.

***In vitro* transcription to synthesize cRNA**

At room temperature, the IVT Master Mix (IMM) (table 2.5) was prepared in a nuclease-free microcentrifuge tube, mixed well by vortexing, centrifuged briefly (5-seconds) and placed on ice. IMM (7.5 µl) was added to each sample, mixed and incubated in the pre-heated 37°C hybridization oven for 14 hours. The reaction was stopped by adding 75µl nuclease-free water to each cRNA sample, which brought the final volume to 100µl and mixed well by vortexing.

IVT Master Mix (IMM) (for a single 25µl reaction)	
Amount	Component
2.5µl	T7 10x reaction buffer
2.5µl	T7 enzyme Mix
2.5µl	Biotin-NTP mix

Table 2.5: *In Vitro* master mix (IMM). The components in the table were added in the order listed to a 1.5 ml nuclease-free at room temperature, mixed well by vortexing and centrifuged briefly to collect the mix at the bottom on the tube.

cRNA purification

Before starting the cRNA purification, a minimum of 200µl of nuclease-free water were heated to 55°C in a water bath. cRNA binding buffer (350µl) was then added to each of the samples, followed by addition of 250µl of ACS reagent grade 100% ethanol and mixed well by pipetting up and down 3 times. Proceeding immediately, each sample (700µl) was pipetted to the centre of a cRNA filter cartridge (column) and centrifuged for 1 minute at 10,000g. The flow through was discarded and the sample was washed by addition of 650µl wash buffer and centrifugation at 10,000g for 1 minute. The flow through was again discarded and the column was spun for an additional 1 minute at 10,000g to remove excess wash buffer. The column was transferred to a fresh cRNA collection tube and 200µl nuclease-free water (at 55°C) was added to the centre of each column. The samples were incubated in a 55°C heat block for 10 minutes and then eluted by centrifugation at 10,000g for 1.5 minutes. Aliquots (5 µl) were placed into a 96-well plate for analysis on the NanoDrop and Bioanalyzer and the remainder stored at -20°C.

2.2.4.2 Assessing cRNA Yield and Quality

The cRNA samples were quantified using the NanoDrop ND-8000 UV spectrophotometer, which follows the same principles as described in section 2.2.2.1, but is able to run 8 samples in parallel. The concentration was the important factor with cRNA and the purity levels were not taken into consideration, unless there was serious contamination evident. If a cRNA sample had a concentration lower than 150ng/µl it was concentrated down by vacuum centrifugation as described below. This is because the hybridization assay required 750ng in 5µl, giving a minimum concentration of 150ng/µl.

The cRNA quality was assessed on the Agilent 2100 Bioanalyzer using the EukaryoteTotal RNA Nano assay following the same protocol as detailed in section 2.2.2.2. The bioanalyzer provided an accurate size distribution profile of the cRNA samples. Amplified cRNA appeared as a distribution of sizes from 250 to 5000 nt with most of the cRNA at 1000 to 1500 nt. This can be explained by the fact that the average size of biotin-labelled cRNA is approximately 1200nt. The RIN was not a factor with cRNA and if the sample showed the correct size distribution on the electropherogram, it was used for microarray analysis.

2.2.4.3 Vacuum centrifugation

Vacuum centrifugation uses centrifugal force in combination with a heated vacuum environment to vaporize the water in a sample and concentrate the cRNA . cRNA samples were concentrated if they had a concentration less than 150ng/µl. The volume of nuclease free water required to achieve the appropriate cRNA concentration was determined for each sample before vacuum centrifugation. Therefore, the volume of water that needed evaporating off was known. Before use, the SpeedVac instrument was pre-heated at 65°C for 10 minutes. The samples to be concentrated were then thawed out on wet ice and placed into the device. Importantly, the heater time was set at half the time of the run, i.e. for a 30 minute run; the heater was set for 15 minutes. The machine was started and progress of the samples was checked every 30 minutes.

2.2.5 Hybridization and scan

Hybridization

The cRNA samples were diluted with RNase Free water to 750ng in 5 µl, transferred to 0.5ml PCR tubes and stored on ice. The BeadChip Hybridization (Hyb) Chamber was assembled and the Hybridization Buffer (HYB) and Humidity Control Buffer (HCB) were incubated in an oven at 58°C for 10 minutes to dissolve salts in the solution. HCB (200µl) was dispensed into the humidifying buffer reservoirs of the Hyb chamber, the lid sealed and kept at room temperature. HYB (10µl) was then added to each cRNA sample and the assay sample was incubated at 65°C for 5 minutes using a thermal cycler. The samples were then vortexed briefly and the sample equilibrated to room

temperature before use. Meanwhile, the BeadChips were carefully removed from their packaging using tweezers and inserted into the Hyb chamber insert. Each sample (15µl) was pipetted onto the centre of each inlet port and the sample was drawn onto the chip microarray by capillary flow. The lid to the humidified Hyb chamber was sealed and incubated for 18 hours at 58°C (hybridization oven) with a rocker speed of 5. The 1 X High-Temp wash buffer (500ml) was prepared as instructed in the assay guide and transferred to the Hybex waterbath, which was set to 55°C and incubated overnight in preparation for the chip washes the following day.

Post Hybridization Wash and Staining

The Wash E1BC solution, Block E1 buffer with and without Streptavidin-Cy3 were prepared as detailed in the manufacturer's instruction manual. The BeadChips were then removed from the Hyb chamber, the coverseal of each chip removed and slides transferred to a slide rack. The racked slides were submerged in a dish containing 250ml solution and then transferred to the 55°C High-Temp Wash buffer for 10 minutes. After 10 minutes, the slide rack was transferred back to the Wash E1BC dish and incubated on an orbital shaker for 5 minutes. The orbital shaker speed was set to the highest possible speed without allowing solution to spill. The chips were then washed in 250 ml 100% ethanol and incubated on the orbital shaker for 10 minutes, followed by another wash in 250ml Wash E1BC on the orbital shaker for 2 minutes. Block E1 buffer (4 ml) was pipetted into a wash tray and the BeadChips were inserted, face up and incubated on a rocker (at medium speed) for 10 minutes. To stain the microarrays, the BeadChips were transferred (face up) to a fresh wash tray containing 2 ml Block E1 buffer (+ Streptavidin-Cy3), a cover placed on the tray and rocked for 10 minutes. The chips were placed back in the rack and a final wash was performed in 250 ml Wash E1BC on the orbital shaker for 5 minutes. Finally, the Chips were dried by centrifugation at room temperature for 4 minutes and stored in an opaque box to protect from light prior to scanning.

Scanning of microarrays

The decode data files for each chip (containing the information on the position of each bead type on each chip) were downloaded into the Bead scan software prior to

scanning. Microarray slides (BeadChips) were scanned on an Illumina BeadArray Reader with Bead scan Software. Before scanning, the barcode on each BeadChip was scanned to ensure effective data management. The raw Illumina BeadArray data produced consisted of .tif images produced by the scanner, accompanied by .locs and .txt files containing details of bead locations and their intensities within the image.

2.2.6 Microarray Data Analysis

Following microarray scanning, GenomeStudio software developed by Illumina was used to produce bead summary data from the raw data. The bead summary data consisted of; a probe ID (Illumina Probe (correlates to a gene)), an average signal of each probe on the unlogged scale, the average number of beads per probe, an average bead standard error and a detection P value. This data was exported from GenomeStudio as a custom report using the 'ArrayExpress Data submission Report plug-in V2.0.0' and the average probe signal, probe ID and detection P value was imported into ArrayTrack™ for; normalisation, cluster analysis differential gene expression analysis, filtration of genes, and functional analysis. ArrayTrack software developed at the National Center for Toxicological Research provides an integrated solution for managing, analyzing, and interpreting microarray gene expression data. It is MIAME (Minimum Information about a Microarray Experiment) supportive for storing and analysing microarray data. ArrayTrack allows users to; select a normalization method and a statistical method applied to a stored microarray dataset, to cluster genes into different groups according to expression profiles, to determine a list of differentially expressed genes (significant genes), and to link the gene list directly to pathways and gene ontology for functional analysis (Tong *et al*., 2003). (http://www.fda.gov/nctr/science/centers/toxicoinformatics/ArrayTrack/)

2.2.6.1 Normalisation

Normalization of microarray data is an essential analysis step, where the objective is to adjust the individual hybridization intensities to balance them appropriately so that meaningful biological comparisons can be made (Quackenbush, 2002). This ensured that unwanted technical variation was removed and the expression values from the different arrays were comparable. Quantile normalisation was used to make the

distribution, median and mean of probe intensities the same for every sample and is based on the assumption that all samples have similar distributions of transcript abundance (Dunning *et al*., 2008). The raw data for each array was log (base 2) transformed and quantile normalisation without background subtraction was carried out in ArrayTrack™.

2.2.6.2 Correlation Analysis

To assess the quality and reproducibility of microarrays and identify outlier samples, Pearson's correlation coefficient of pair-wise log2 intensity correlation was calculated. This was carried out using the Correlation matrix tool in ArrayTrack. The entire normalised data and log (2) transformed data set was used (a total of 22, 519 probes), without a specific cut off. Samples were considered highly reproducible >0.9 and any samples <0.8 were discarded from further analysis.

2.2.6.3 Clustering Analysis

Cluster analysis organises gene expression data into groups that share related gene expression profiles, making it possible to visually assess similarities and differences between samples and determine whether samples that are grouped. Two forms of clustering analysis were used is this thesis, hierarchical clustering analysis (HCA) and principle component analysis (PCA). Both HCA and PCA were carried out in ArrayTrack™. The entire quantile normalised and log (2) transformed data set was used (a total of 22, 519 probes) for clustering analysis, without a specific cut off.

2.2.6.4 Principal Component Analysis

PCA is a useful linear approach to obtain a simplified visualization of entire datasets, without losing experimental information (variance). PCA uses analysis of principal sources of variance (principal components) in data and displays this graphically in either 2 or 3-dimensions (Ringner, 2008). The first principle component explains the largest amount of total variance in the data and each subsequent component is constructed so as to explain the largest amount of variance uncorrelated with (orthogonal to) previously constructed components (Cangelosi and Goriely, 2007).

To carry out PCA, the data was pre-processed using centre scaling, in which data are standardized such that each gene is centered to zero average expression level (Ringner, 2008). PCA was then carried out and represented in either a 2D or 3D format. The components selected to represent the data were dependent on the phenotype of interest or the components that included most of the variation in the data.

2.2.6.5 Hierarchical Clustering Analysis

HCA groups genes based on their expression and organises data points in a dendogram tree in which the branch lengths represent the degree of similarity between the values. In this study, HCA with dual clustering was carried out using Ward's minimum variance linkage clustering algorithm.

2.2.6.6 Detection of differential gene expression

Differential gene expression analysis was carried between control and treated samples to determine the significantly up and down-regulated genes and apply statistical significance. The normalised expression lists were log (2) transformed and a student t-test was carried out between control and treated samples, since it was assumed that samples had equal variances. To account for the problem of multiple testing, P-values were adjusted for the number of genes tested using Benjamani and Hochberg's false-discovery rate (FDR) (Benjamani and Hochberg, 1995). Differences in relative expression were considered significant at an FDR-adjusted $P<0.05$. If the FDR was too strict, then an unadjusted P-value of <0.05 was deemed acceptable for the purpose of this investigation. An unadjusted P-value was considered acceptable in the current study, since most biologists are willing to accept some errors will occur in microarray, as long as findings and hypotheses can be made (Allison *et al*., 2006). To identify common genes between significant gene lists, Manufacture ID's were used with the Venn diagram tool in ArrayTrack™.

2.2.6.7 Functional Analysis

To infer biological meaning to the transcriptomic data and aid in the understanding of biological pathways and possible mechanisms of toxicity, functional analysis was

carried out. To this end, pathway analysis and gene ontology were used. The use of multiple tools is highly recommended for functional analysis of microarray data, since they draw on different knowledge bases and enrich genes with different statistical methods. (Huang *et al*., 2009).

Ingenuity Pathway Analysis

Ingenuity Pathway Analysis (IPA, Ingenuity Systems Inc., Redwood City, CA, USA) (www.ingenuity.com) is a commercial, web-based interface that uses a variety of computational algorithms to identify and establish cellular networks, pathways and biological processes that statistically fit the input gene list and expression values from experiments. The analysis uses a database of gene interactions culled from the literature by PhD level scientists and updated every quarter of the year. This database is referred to as the Ingenuity Pathway Knowledge Base (IPKB) and contains information drawn from journal articles, review articles, text books and KEGG Ligand. Lists of differentially expressed genes identified by ArrayTrack, containing GeneBank accession IDs, fold changes and p values were uploaded into IPA. The IPA 'Core Analysis' function was used to interpret the data in the context of canonical pathways, toxicity (Tox) lists and networks. Right-tailed Fisher's exact test is applied to determine the level of significance for each network, pathway and list and the p-value is displayed as a score, which is the negative log of that p-value. For canonical pathways and ToxLists, a score of ≥ 1.3, which equats to a $P \leq 0.05$, was consisdered significant. Only networks with a score of ≥ 3, $P \leq 0.001$, were considered significant. An option is available in IPA to perform a multiple testing correction, which is calculated using the Benjamani-Hochberg method, and is displayed for functions, pathways and list analyses.

DAVID (the database for annotation, visualization and integrated discovery)

DAVID is one of many tools that systematically maps a large number of interesting genes in a list to the associated biological annotation (e.g. gene ontology terms), and statistically highlights the most enriched (overrepresented) biological annotations out of thousands of linker terms and contents (Huang *et al*., 2009). DAVID has an advanced data collection bank, (the DAVID Knowledgebase) that creates a solid

annotation data foundation for the various DAVID analytic tools, which include; gene functional classification, functional annotation chart, function annotation clustering and function annotation table. The DAVID knowledgebase is a highly integrated gene-annotation database with comprehensive data coverage built from 40 annotation databases (e.g. GO terms, pathways, protein-protein interactions and literature) (Huang *et al*., 2007). The significance of gene-term enrichment is calculated using a modified Fisher's exact test (EASE score) and a P-value $\leq$0.05 is considered significant. To globally correct enrichment *P values* to family-wide false discovery under certain rate (e.g. P<0.05) multiple testing correction could be applied in DAVID (Bonferroni, Benjamani and FDR). An enrichment score is used to rank overall importance (enrichment) of gene/functional annotation groups and is calculated as the geometric mean of all the enrichment *P-values* (EASE score) for each annotation term associated with the gene members in the group. Since the geometric mean is a relative score instead of an absolute P-value, minus log transformation is applied on the average P-values. Enrichment score 1.3 is equivalent to non-log scale 0.05.

The same gene lists as for IPA were uploaded into DAVID using GenBank Accession ID, and the entire annotated Illumina RatRef array was used as background. Analysis was run using the default functional tools of DAVID. Results with an EASE score of $\leq$0.1 were considered, unless terms were enriched with a Benjamani-Hochberg multiple correction test, in which case an adjusted P-value $\leq$0.05 was used as the cut-off. Functional Annotation Clustering and gene functional classification tools were used with the $\geq$medium classification stringency in order to group redundant terms and determine their overall enrichment score. For clustering, an enrichment score of $\geq$1.3 (equivalent to P<0.05) was considered in the analysis.

2.2.7 Cell Culture and treatments

2.2.7.1 Cell Culture

Culturing and passaging of cells

When L6 cells reach confluence they will differentiate to form multinucleated myotubes and striated fibers. Once cultures have fused they cannot be recloned. Therefore, to prevent L6 myoblasts differentiating, L6 cells were subcultured at 70%

confluence and if the cells reached 90-100% confluence, the cells were thrown away and a fresh batch cultured. Cells were used between passages 6 – 23.

Like L6 cells, H9c2 cells will differentiate upon reaching confluence, which can be accelerated in low serum conditions. Therefore, cells were subcultured at 70% confluence, discarded if they reached 90-100% and used between passages 10-30.

HepG2 cells are adherent, epithelial-like cells that grow as monolayers and in small aggregates. The cells were sub-cultured during the log phase of growth (approximately 80%) and used between passages 1-30.

L6, H9c2 and HepG2 cells were cultured with high glucose (25mM) DMEM media containing 10% ($^{v}/_{v}$) FBS and the additional supplements; 5mM HEPES and penicillin (100IU)/streptomycin (100µg/ml). The cells were cultured in 15ml of media, incubated at 37°C in an incubator with 5% ($^{v}/_{v}$) carbon dioxide (CO_2) and were sub-cultured by trypsinization.

All cells used in this project were stored in liquid nitrogen. To culture, the cells were removed from liquid nitrogen storage and thawed out for 2 minutes in a 37°C water bath. Once thawed, they were immediately pipetted into a 15ml Falcon tube containing 5ml of pre-warmed (37°C) complete media and centrifuged at 1000rpm for 5 minutes. The supernatant was removed and the cells were resuspended in 1ml of fresh media. The cells were sub-divided into T.75 flasks to the relevant density and fed with 15ml of fresh complete media. The cells were incubated in a 37°C humidified incubator with 5% ($^{v}/_{v}$) CO_2 and fed with fresh complete media every 48 hours.

Once the cells had reached the specified confluence in T.75 flasks, the media was removed; 10ml was discarded and 5ml was aliquoted into a 15ml Falcon tube. The cells were washed with 5ml PBS and then 3 ml of pre-warmed (37°C) Trypsin-EDTA was added to the cell surface of the flask. The flask was placed into the 37°C incubator until all the cells had displaced from the flask surface, as observed by microscopy. L6 and H9c2 cells took about 2 minutes to trypsinize, while HepG2 required at least 5

minutes, and all required gentle tapping to dislodge remaining cells. The trypsin was neutralised by addition of 5ml of old media and the whole cell suspension (8ml) was added back to the 15ml Falcon tube and centrifuged for 1000rpm for 5 minutes. The supernatant was discarded and the cell was resuspended in 2ml of fresh media. The cells were either sub-cultured to the relevant ratio, or a cell count was performed using a haemocytometer. Specified cell numbers could then be seeded into T.75 flasks, or 96- and 6-well plates, as described in section 2.2.7.2.

Cells were frozen at low passage to maintain competent stocks for each cell line. All cells were frozen using cryopreservation medium, which consisted of complete culture medium supplemented with 5% (v/v) DMSO. Briefly, once cells had reached desired confluence, they were trypsinised and resuspended in 1ml of cryopreservation media. The cells were immediately transferred to a CoolCell® and incubated at -80°C, for controlled -1ºC/minute cell freezing. After 24 hours, the cells were transferred for permanent storage in liquid nitrogen.

Cumulative Population Doublings (CPD) and Doubling Time (DT)

At each passage, cells were counted using a haemocytometer and the population doubling (PD) and doubling time (DT) were calculated using the following formula:

$$\boldsymbol{PD} = (\log_{10}\boldsymbol{Y} - \log_{10}\boldsymbol{Z}) / \log_{10}(2)$$

$$\boldsymbol{DT} = \boldsymbol{T}\ (h)\ \log_{10}(2) / (\log_{10}\boldsymbol{Y} / \log_{10}\boldsymbol{Z})$$

(***Y*** indicates the number of cells harvested; ***Z*** indicates the number of cells seeded; **T** (h) indicates time in hours). CPD was calculated as the sum of the PD with every successive passage.

Galactose media adaption

Cells were grown in complete glucose or galactose-containing media, and kept in 37°C humidified incubator with 5% ($^{v}/_{v}$) CO_2. The cells were adapted to galactose media for a minimum of 7 days before experiments were carried out. To confirm that the cells had adapted to galactose media, a dose response with the mitochondrial toxicant antimycin A was carried out with the ATP assay as detailed in section 2.2.8.2.

2.2.7.2 Cell plate Seeding and treating

Treatments

Cell treatments were prepared in their relevant solvent to a stock concentration and stored as indicated in table2.6.

Compound	Solvent	Stock Concentration	Storage
177	DMSO	100mM	-20°C
197	DMSO	100mM	-20°C
907	DMSO	100mM	-20°C
H_2O_2	H_2O	9.8M	4°C
Antimycin A	DMSO	30mM	-20°C
Nocodazole	DMSO	1mg/ml	-20°C
FCCP	DMSO	10mM	-20°C
Oligomycin	EtOH	10mM	-20°C
NAC	dH_2O	500mM	-20°C
Staurosporine	DMSO	100µM	-20°C
Troglitazone	DMSO	30mM	-20°C
DMSO	-	-	RT

Table 2.6. Cell treatment compound preparation and storage.

96-well plate protocol

On day 1, L6, H9c2 and HepG2 cells were seeded in a 96-well microplate at their respective cells densities (table 2.7) in a final volume of 200µl media. The plates were incubated in a 37°C humidified incubator with 5% ($^{v}/_{v}$) CO_2 for 24 hours to reach 70-80% confluence. The optimum seeding densities were determined for each cell line for both CCK-8 and ATP assays (data not shown).

Cell Line	Cell No. seeded	
	CCK-8 Assay	**ATP Assay**
L6.G8.C5	5,000	10,000
H9c2	7,500	7,500
HepG2	20,000	20,000

Table 2.7 The seeding densities of L6.G8.C5, H9c2 and HepG2 cell lines used for the CCK-8 and ATP assays.

On day 2, the compounds to be used were dissolved with DMSO to their stock concentration. In a clear 96-well plate, a compound plate was prepared by double

diluting the highest concentration of each compound in DMSO to give a 100 X stock of the final concentration. A DMSO only negative control and H_2O_2 (diluted in media) positive control were included on each compound plate.

Media was warmed in a 37°C water bath and 495µl was added into 96-well deep well plates for each treatment concentration. A volume of 5µl was pipetted from the compound plate into the deep-well plate for each treatment to give the final concentration (1:100 dilutions). The media was then removed from the cell plate and 100µl of compound/medium mixture was dispensed into each well in triplicate for each treatment concentration. The plates were then incubated for a defined time in a 37°C humidified incubator with 5% ($^{v}/_{v}$) CO_2.

6-well plate protocol

L6 and H9c2 cells were seeded in clear 6-well plates with $2x10^5$ and $3x10^5$ cells/well respectively in 2ml media. The plates were incubated in a 37°C humidified incubator with 5% ($^{v}/_{v}$) CO_2 for 24 hours to reach 70-80% confluence. Treatments were carried out in 2ml/well for the desired length of time. Following treatment, the media was removed from the wells and placed into 15ml falcon tubes. The cells were washed with 1ml of PBS and trypsinised with 1ml 0.25% Trypsin-EDTA for 5 minutes or less. The trypsin was neutralised with 2ml of fresh media and the cell suspension transferred to the 15ml falcon tubes containing treatment media. The cells were then centrifuged at 1000rpm for 5 minutes and cells used accordingly.

2.2.8 Cell viability and ATP content measurements

2.2.8.1 Cell Counting Kit-8 (CCK-8)

Cell proliferation and viability were determined using the sensitive colorimetric CCK-8 assay. The assay is based on the reduction of the highly water-soluble tetrazolium salt, WST-8, by dehydrogenase activities in the cells to give a yellow-colour formazan dye, which is soluble in the tissue culture media. The amount of the formazan generated is directly proportional to the number of living cells. The advantage of using CCK-8 is; increase sensitivity compared to other tetrazolium salts, such as MTT, and its low toxicity to the cells.

Cells were seeded into a clear 96-well microplate (as previously detailed section 2.2.7.2 for individual cell densities etc). Treatments were carried out with the relevant media type and a blank containing only media was included. After treatment the manufacturer's protocol suggests adding 10µl of CCK-8 solution to each well (giving a final dilution of 1:10). However, with this concentration of CCK-8, microscopic analysis indicated a loss of cell viability shortly after addition. Therefore, following treatment, a reduced volume of 5µl (1:20 dilution) was added to each well using a multichannel pipette. The CCK-8 was mixed by gentle agitation of the plate and incubated in a 37°C humidified incubator with 5% ($^{v}/_{v}$) CO_2 for 1 hour. Absorbance was measured at 450nm using the Bio Tek microplate reader. To correct for background levels produced by media and CCK-8, the absorbance of the well containing vehicle media, CCK-8, without cells was subtracted from all the other wells.

2.2.8.2 ATP Determination Kit

A bioluminescent assay utilising recombinant firefly luciferase and its substrate D-luciferin was used for quantitative determination of ATP. The assay reaction is based on the principle that luciferase generates light from the reaction with ATP and luciferin:

$$\text{luciferin} + \text{ATP} + O_2 \xrightarrow[\textit{luciferase}]{Mg^{2+}} \text{oxyluciferin} + \text{AMP} + \text{pyrophosphate} + CO_2 + \text{light}$$

The light intensity generated is directly proportional to the ATP concentration. Cells were seeded into white 96-well plates as previously detailed (section 2.2.7.2 for individual cell densities etc.) and grown to confluence. Treatments were carried out with the relevant media type and made up to a final volume of 100µl. After treatment, the required amount of standard reaction solution (SRS) was made up in the dark, as instructed in the manufacturer's protocol. The SRS was gently mixed by inverting the tube and protected from light. All the media was removed from the treatment plates and the cells were washed twice with 200µl of PBS. The SRS was aliquoted into a lab trough and 100µl was added to each well using a multichannel pipette. A background well containing 100µl SRS without cells was included to account for luminescence

produced by the SRS alone, and this value was subtracted from all other wells for subsequent analysis. The plate was agitated at medium speed on a platform shaker for 30 seconds at RT and then incubated for 5 minutes in the NOVOstar luminometer at 28°C, the optimum temperature for the reaction. Luminescence (Relative light units per second (RLU/sec)) was measured on a luminometer at 5, 10 and 15 minute time points to capture the peak luminescence signal.

2.2.9 Cell death measurements

2.2.9.1 Annexin V/PI

Soon after initiating apoptosis, cells translocate membrane phosphatidylserine (PS) (located on the inner face of the plasma membrane) to the cell surface, which can be detected by staining with a fluorescent conjugate of Annexin V. Propidium iodide (PI) staining can be used to detect necrosis and is based on the fact that necrotic cell's DNA becomes exposed to PI dye. Cells were seeded in 6-well plates with 2ml of media and incubated for 24 hours in a 37°C humidified incubator with 5% ($^{v}/_{v}$) CO_2. When the cells were treated, the following controls were included for instrument set-up and compensation on the flow cytometer, as detailed below in table 2.8.

Cell treatment	Stain
Cells + media vehicle	Non
Cells + media vehicle	5µl Annexin V-FITC
Cells + media vehicle	5µl PI
Cells + media vehicle	5µl Annexin V-FITC + 5µl PI
Apoptosis induced positive control (250nM Staurosporine)	5µl Annexin V-FITC + 5µl PI
Necrosis induced positive control (1mM H_2O_2)	5µl Annexin V-FITC + 5µl PI

Table 2.8 Control sample set up for Annexin V/PI staining. Controls are required for; compensation (annxin V-FITC and PI individual stains), negative control (Annexin V-FITC+PI) and positive control (Apoptosis, Staurosporine and necrosis, Hydrogen peroxide).

Following treatment, the cells were trypsinised as detailed in section 2.2.7.1 and washed twice with 1ml PBS containing calcium and magnesium with centrifugation at 1000rpm for 5 minutes. After the washes, the cells were resuspended in 100µl of 1X Binding Buffer and transferred to sterile Fluorescence Activated Cell Sorter (FACS)

tubes. The relevant control samples were set up as specified in table 2.8 and 5µl Annexin V-FITC and 5µl PI added to all the remaining samples. After incubation for 5 minutes, at room temperature in the dark, 400µl of 1 X binding buffer was added to each tube and the cells gently mixed. The samples were stored on ice and analysed on the flow cytometer within 30 minutes of staining. The samples were analysed using a CyAn ADP flow cytometer with 488nm excitation and Annexin V-FITC and PI were measured using FL-1 (515-545nm) and FL-2 (564-606) respectively. Data was also collected in FSC (forward scatter) and SSC (side scatter) and 10,000 events were collected for each sample. Cell debris, as characterised by distinctly low FSC and SSC were gated out. The three control samples; no stain, Annexin V-FITC only and PI only, were run first and the relevant analytical procedure carried out for each of these (table 2.9).

Tube No.	Stain	Action
1	Unstained Cells + media vehicle	Set threshold, gain and use to select and gate on cell population of interest.
2	Annexin V-FITC only Cells + media vehicle	Adjust FL-1 (FITC) detector so cell population in FL-1 histogram is between 10^0-10^1.
3	PI only Cells + media vehicle	Adjust FL-2 (phycoerythrin) detector so cell population in FL-2 histogram is between 10^0-10^1.

Table 2.9 Samples used to set up the flow cytometer for compensation.

Since the FL-1 and FL-2 emission spectra overlap, it was necessary to correct for this using the process of fluorescence compensation. For these experiments, compensation was determined automatically with the summit V4.3.02 software using the control Annexin V-FITC and PI only stained cells, as detailed in figure 2.1.

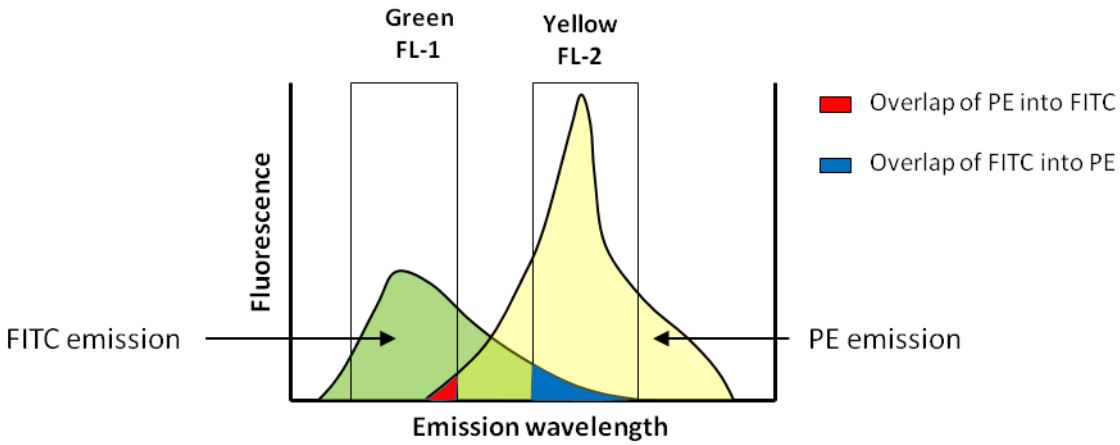

Figure 2.1 Spectral overlap between the fluorophore's FITC and PE with the FL-1 and FL-2 detectors. The emission spectra of FITC (green) and PE (yellow) fluorophore's overlap, and so compensation is needed to account for this. Compensation method: The amount of compensation applied to the dataset is calculated by first running Annexin-V FITC (FL-1) through the flow cytometer on its own and recording the % of its total emission that is detectable in the FL-2 (overlap). The procedure was then repeated with PE (FL-2) except this time FL-1 overlap recorded. Based on these % values, the summit software is able to apply the relevant level of compensation for each FL detector to the experimental dataset.

2.2.9.2 Caspase 3/7 activity

Caspases are an evolutionarily conserved family of cysteine proteases that play a central role in the execution of apoptosis. Caspases are activated in response to a diverse range of intrinsic and extrinsic stimuli that ultimately dismantle the cell through restricted proteolysis of a broad spectrum of cellular proteins. Caspase 3 and 7 are effector caspases that cleave various substrates, such as cytokeratins and the plasma membrane cytoskeletal protein alpha fodrin, ultimately resulting in the morphological and biochemical changes seen in apoptotic cells (Elmore, 2007).
To quantitate the activity of caspase 3 and 7, the luminescent assay Caspase-Glo® 3/7 assay was used. The assay contains a proluminescent caspase-3/7 substrate, DEVD-aminoluciferin and a thermal stable luciferase/ cell lysis reagent in a simple "add-mix-measure". The cell is lysed, the caspase 3/7 cleaves the substrate, releasing the aminoluciferin, which reacts with luciferase to produce a luminescent signal. This signal is proportional to the caspase 3/7 activity.

Cells were seeded at the specified density (section 2.2.7.2) in white 96-well microplates A (200µl media per well) and incubated for 24h to grow cells to confluence. After cell treatment, the microplate was equilibrated to RT for 30 minutes prior to the end of the treatment period.

The Caspase-Glo® 3/7 reagents were thawed and equilibrated to RT for 30 to 45 minutes. The Caspase-Glo® 3/7 buffer was transferred into the bottle of Caspase-Glo® 3/7 substrate and the contents were mixed by inverting and swirling to form the Caspase-Glo® 3/7 reagent. A volume of 100µl reagent was added to each well and the plate was agitated at medium speed on a platform shaker for 30 seconds at RT to aid cell lysis. The plate was incubated at RT for 2 hours and then luminescence (RLU/sec) was measured on the luminometer, maintained at 24°C. A blank reaction consisting of vehicle and culture medium without cells was included to measure background luminescence associated with the cell culture system. This blank value was subtracted from the measurements of treated cells.

2.2.10 Cell cycle analysis

To analyse the cell cycle, DNA content was measured using PI staining (Chen et al, 2000). In this protocol, EtOH was used to fix and permeabilize the cells to make them accessible to PI. RNase A was included to digest double stranded sections of RNA that can also stain PI, thereby increasing specificity of the DNA staining.

Cells were seeded in 6-well plates with 2ml of media and incubated for 24 hours in a 37°C humidified incubator with 5% ($^{v}/_{v}$) CO_2 to grow to near confluence. Cells were treated for 24h in 2ml of media, and to judge whether cell cycle was progressing to G_2/M, the cells were co-treated with nocodazole (132nM) for 20h before measurement (Oyama *et al.*, 2011). Following treatment, the cells were trypsinised as described in section 2.2.7.1 and washed with 1ml PBS with centrifugation at 1000rpm for 5 minutes. The supernatant was removed, the cells were resuspended in 100µl of PBS and 1ml of ice cold 70% EtOH was added slowly to fix the cells. The samples were stored on ice for 30 minutes and then transferred to 4°C to incubate for 24 hours. After fixation, the cells were washed twice with 1ml PBS by centrifugation at 1000rpm

for 5 minutes. Meanwhile, PI stain was freshly prepared by addition of 5µg/ml PI and 5µg/ml RNase A to PBS. Following the washes, the cells were resuspended in 1ml of PI stain and incubated in a 37°C incubator for 30 minutes. After transferring the cells to sterile FACS tubes, the samples were run on a CyAn ADP flow cytometer with 488nm excitation and PI was measured in the FL-3 detector (PE-Texas-Red 610/20-A detector). Data was also collected in FSC (forward scatter) and SSC (side scatter) and a total of 20,000 events were collected for each sample. Cell debris, as characterised by distinctly low FSC and SSC, was gated out. A negative control sample was used to place gates on the three phases of the cell cycle; the G_1, S and G_2/M populations, as well as the sub-G_1 population for apoptosis, in the PE-Texas-Red (PE-T-R) Lin histogram (figure 2.2). For accurate analysis of samples, the voltage of the PE-T-R detector was altered from one sample to the next to place the G_1 peak in the same position for each sample. This meant the gate positioned remained unaltered when analysing the data, making the data more reproducible.

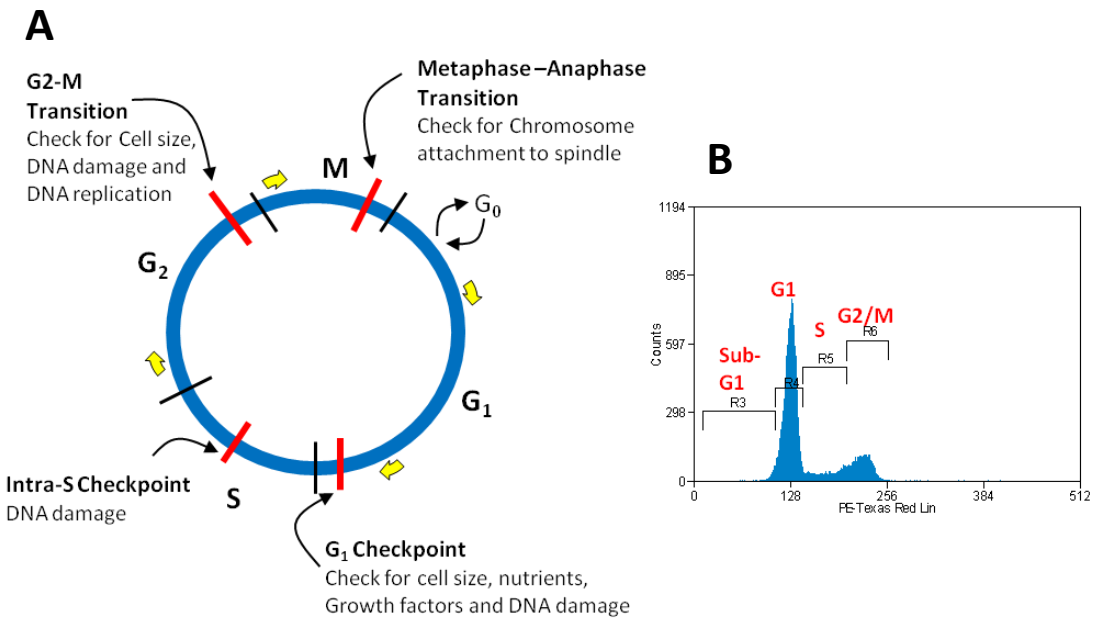

Figure 2.2. Cell cycle and checkpoints. (A) The cell cycle in eukaryotic cells consists of four phases, gap (G)1, synthesis (S), G2, and mitosis (M), and one phase outside the cell cycle, G0. In the G1 phase, RNA (transcription) and proteins (translation) are synthesised and in the subsequent S phase, DNA is replicated. During G2, the cell grows and makes extra proteins and then continues to the M phase, in which mitosis takes place. The four cell cycle checkpoints are indicated by red lines. (Adapted from Tyson *et al*., 2002 and Houtgraff *et al*., 2006) **(B)** Representative histogram illustrating the distribution of each cell cycle phase and sub-G1 (apoptosis). The amount of PE-Texas Red fluorescence is proportional to the amount of DNA.

2.2.11 Measurement of cell size

Forward light scatter (by flow cytometry) is the most accurate method to measure cell size. However, there are difficulties in evaluating cell size with compounds that affect cell proliferation. During the cell cycle, cell size increases physiologically from G1 to M phase and studies have shown that the mean cell size in G_1 is smaller than the G_2 population (Monkawa *et al.*, 2002). Therefore, for these experiments, forward light scatter was measured for individual phases of the cell cycle.

Cells were seeded in 6-well plates and grown to confluence for 24h. After treatment, the cells were harvested by trypsinisation as previously described (section 2.2.7.1) and were washed with 1ml PBS by centrifugation at 1000rpm for 5 minutes. The cells were fixed with 70% EtOH as described in section 2.2.10, and kept at -20°C until analysis. Fixed cells were washed with 1ml PBS, resuspended in 1ml of PI staining solution (section 2.2.10) and incubated at 37°C for 10 minutes. After transferring the cells to sterile FACS tubes, the samples were run on a CyAn ADP flow cytometer with 488nm and PI was measured in the FL-3 detector (PE-T-R). Typically 20,000 events were collected for each sample and cell debris, as characterised by distinctly low FSC and SSC, was gated out for analysis. Cell size was determined by plotting FSC and SSC histograms gated from the G_1 and G_2 cell populations. Control cells were gated such that an arbitrary 10% of the cells were presumed to represent the large-sized cells in a given cell population (Oyama *et al*., 2011).

2.2.12 ROS measurements

Measurement of cytosolic and mitochondrial superoxide

The superoxide indicator dihydroethdium (DHE) is the most popular fluorogenic probe used for detecting intracellular superoxide radical anion. The reaction between DHE and superoxide results in a highly specific red fluorescent product, 2-hydroxyethidium (2-OH-E^+). To detect mitochondrial superoxide, DHE has been modified by conjugating DHE to a triphenylphosphonium (TPP) moiety, resulting in the novel, fluorogenic probe, MitoSox. The TPP moiety increased the accumulation of the compound into mitochondria. Like with DHE, MitoSox is oxidised by superoxide to produce red fluorescence.

Cells were seeded into 6-well plates to the appropriate density and grown to 70-80% confluence. Treatments were prepared in 2ml of fresh media and the cells were incubated for the desired time course. The required number of MitoSox vial's (50µl) were reconstituted with DMSO to give a stock concentration of 5mM. DHE or MitoSox was added to a final concentration of 5µM according to manufacturer's recommendations (a 1:1000 dilution of 5mM stock) 30 minutes prior to the end of the treatment period. After the cells had loaded DHE or MitoSox for 30 minutes, the cells were trypsinised and washed with HBSS (with Ca/Mg) by centrifugation at 1000rpm for 5 minutes. The cells were resuspended in 500µl of HBSS (with Ca/Mg) and transferred to sterile FACS tubes. The samples were stored on ice during subsequent analysis on the flow cytometer. The samples were run on a CyAn ADP flow cytometer with 488nm excitation to measure oxidized DHE and MitoSox in the FL-2 and FL-3 detectors (PE and PE-T-R). Data were also collected in FSC (forward scatter) and SSC (side scatter) and a total of 10,000 events were collected for each sample. Cell debris, as characterised by distinctly low FSC and SSC, was gated out.

2.2.13 Measurement of mitochondrial membrane potential

Mitochondrial membrane potential was measured using MitoTracker Red CMXRos; a red-fluorescent dye that stains mitochondria in live cells in a membrane potential dependent manner. L6 cells (2×10^5) were seeded in a 6-well plate in the appropriate medium and grown to 70-80% over 24 hours. A 50µg vial of lyophilised MitoTracker was reconstituted in 94µl DMSO to give a 1mM stock concentration. This was further diluted in PBS with 1%FBS to give a final concentration of 500nM. After the desired confluence was achieved, or after treatment, the media was removed and 2ml of pre-warmed MitoTracker Red (500nM) were added to each well. The cells were incubated for 30 minutes at 37°C in the dark. After staining was complete, the cells were trypsinised and washed with 1ml HBSS (with Ca^{2+}/Mg^{2+}) at 1000rpm for 5 minutes. The cells were resuspended in 500µl of HBSS (with Ca^{2+}/Mg^{2+}), transferred to sterile FACS tubes and stored on ice until analysis on the flow cytometer. The samples were run on the CyAn ADP flow cytometer with the same settings as detailed in section 2.2.12.

2.2.14 Metabolic profiling using XF analysis

The XF Analyzer simultaneously measures oxygen consumption rate (OCR) and extracellular acidification rate (ECAR) as a quantification of mitochondrial respiration and glycolysis respectively. Cellular oxygen consumption (respiration) and proton excretion (glycolysis) causes rapid, easily measurable changes to the concentrations of dissolved oxygen and free protons in a "transient microchamber" created within each well (Ferrick *et al*., 2008).

2.2.14.1 XF24 Assay

Unbuffered media composition

Unbuffered media consisted of Dulbecco's Modified Eagle's Medium Base 8.3g/l, 2mM Glutamax, 1mM Sodium Pyruvate, 1.85g/l NaCl, and 15mg/l Phenol Red and was supplemented with 25mM glucose or 10mM galactose. The pH was adjusted to 7.4 using 5M NaOH and 5M HCl, filter sterilised through a 0.2µM filter and stored at 4°C until required.

Two-step seeding process

Cells were seeded in a two-step seeding process in XF24 cell culture plates, to ensure a consistent and even monolayer. Cells were resuspended to obtain a final seeding density in 100µl of growth media per well. Background correction wells were left unseeded (A1, B4, C3 and D6) and only 100µl media was placed into these cells. After 2 hours in a 37°C incubator, cells were adhered and a further 150µl media was added to each well (including background correction wells), bringing the total volume in each well to 250µl. The cells were incubated for 16 hours in a 37°C humidified incubator with 5% ($^{v}/_{v}$) CO_2.

Preparing Sensor Cartridge for the XF24 assay

To hydrate the XF24 sensor cartridge, 1 ml of Seahorse Bioscience XF24 Calibrant pH 7.4 media was added to each well of the utility Seahorse Bioscience 24-well plate. The sensor cartridge was placed back on top of the utility plate and stored at 37°C without CO_2 overnight.

XF24 plate treatments

Cell treatments were prepared in growth media and 250µl was used to treat each well for a defined time course. The final concentration of DMSO solvent in the treatments was kept at 0.2% and a DMSO vehicle negative control to match this concentration was included. All treatments were carried out in at least triplicate and cells were incubated in a 37°C humidified incubator with 5% ($^{v}/_{v}$) CO_2.

Mito Stress Kit

The Mito Stress kit is derived from classical experiments to assess the physiological and pathophysiologic function of mitochondria, and to predict the ability of cells to respond to stress. In the assay, cells are treated with three compounds in succession, that each alters the bioenergetic profile of the cell. The first compound, Oligomycin, inhibits the ATP synthase, providing an approximation on the coupling efficiency of the mitochondria. The second compound, uncoupling agent carbonyl cyanide p-[trifluoromethoxy]-phenyl-hydrazone (FCCP), introduces a high artificial proton conductance into the membrane, demonstrating the spare respiratory capacity of the mitochondria. The final compound, antimycin A (AMA), inhibits the electron transport chain and gives estimation of the non-mitochondrial respiration.

Compound preparation

The Mito stress kit compounds Oligomycin (10mM), FCCP (10mM) and Antimycin A (5mM) were diluted to 10 x concentrated stock of the final treatments in 5ml of unbuffered media. The compounds and a 5ml aliquot of unbuffered media were stored at 37°C without CO_2 until loading of the sensor cartridge.

Cell plate preparation with unbuffered media

The cell plate was removed from the incubator and checked for a confluent, even monolayer. Unbuffered media was warmed in a 37°C water bath and 750µl was added to each well of the cell plate, making the final volume 1ml. A volume of 900µl was removed from each well and 900µl of unbuffered media was added back to the 100µl in the wells. This was repeated and 900µl was again removed. To the remaining 100µl,

575µl unbuffered media was added to give a total volume of 675µl. The cells plate was incubated at 37°C without CO_2 for 30 minutes.

Loading the XF Sensor cartridge with compounds

The Mito stress compounds and XF sensor cartridge were removed from the 37°C (without CO_2) incubator. The compounds; Oligomycin (75µl), FCCP (83 µl), Antimycin A (90 µl) and unbuffered media (75 µl) were loaded into the injection ports A, B, C & D respectively using a 1ml single-channel electronic pipette. The XF sensor cartridge was placed back in the 37°C incubator for 10 minutes prior to running the plate, to allow the plate to equilibrate to temperature.

Calibrating the sensors and running an experiment

The XF24 software and machine were switched ON and the instrument stabilized to 37°C at least 2 hours before an experiment was run. An experimental template was designed for each experiment using the assay wizard and the template loaded prior to running the experiment. Once the XF sensor cartridge had reached temperature, the assay was started and the plate loaded into the machine in the correct orientation for calibration. At the end of the pre-programmed calibration procedure (30 minutes), the utility plate was replaced with the cell plate and the assay was started. The mix/wait/measure cycle used for this experiment was 2 min/2 min/3 min. When the run was complete, the protein content from each sample was calculated (section 2.2.15) and these data were used to normalize the XF analysis data.

2.2.15 Cell Lysis

The growth media was removed from the wells and the cells were washed with 1ml pH 7.4 PBS. CellLytic MT lysis reagent was added to each well (200µl/well) and incubated for 15 minutes at room temperature on a shaker at 500rpm. The lysed cells were then transferred to a 1.5ml eppendorf and centrifuged for 15 minutes at 16,000g. The supernatent was then transferred to a fresh eppendorf tube and stored at -80°C until further analysis.

2.2.16 Protein quantitation

Protein concentrations were determined using the Bradford reagent. This colorimetric assay is based on the formation of a complex between the Brilliant Blue G dye and proteins in the solution. An absorbance shift from 465 to 595nm occurs as the dye binds to protein by donating a free proton to the ionisable protein group, thus exposing hydrophobic structures allowing non-covalent binding to non-polar regions of the coomassie dye via Van Der Waals forces. The amount of absorption at 595nm is proportional to the protein content. The protein of a sample was derived by reference to a BSA standard curve. A standard curve was prepared by diluting 1.4mg/ml BSA in cell lysis buffer (used for protein extraction) to a concentration range between 0.1mg/ml-1.4mg/ml. The BSA standards and sample protein (5µl) were added to a clear 96-well microplate in triplicate. The Bradford reagent was brought to room temperature, mixed and 245µl was added to each well. The plate was mixed at a medium speed on a shaker for 30 seconds and then absorbance was measured at 595nm at 15 and 30 minutes. A control containing lysis buffer and Bradford reagent was included to account for background absorbance and was subtracted from the standard curve and sample values. Protein concentrations were calculated against the BSA standard curve in excel. The standard curve was plotted, with protein concentration on the Y-axis and absorbance on the X-axis and a polynomial regression was fitted to the data. Using the equation from this trendline, the unknown protein concentrations were calculated using their absorbance values.

2.2.17 Data analysis and statistical testing

All data are presented as mean and standard error of the mean (SEM) or standard deviation (SD) as appropriate. Statistical analyses were performed using Graphpad Prism® 6 software (GraphPad Software, Inc., La Jolla, CA, USA). Statistical significance of the data was assessed by paired student's t-test, one-way Analysis of Variance (ANOVA) (with Dunnett's multiple comparison test) or two-way ANOVA (with Sidak's or Tukey's multiple comparison test) as appropriate. A P-value of ≤ 0.05 was considered significant. IC50 values were calculated in Graphpad Prism using a nonlinear regression curve fit with 4 parameters. The maximum (DMSO control) and minimum values (total cell kill) were fixed.

CHAPTER THREE
Mechanistic toxicogenomic analysis of SI compound exposure in a rat model

Chapter 3: Mechanistic toxicogenomic analysis of SI compound exposure in a rat model

3.1 Introduction

3.1.1 Sulfonyl Isoxazoline *in* vivo toxicity studies

In chapter 1 (section 1.5), toxicity studies carried out by Syngenta on three novel sulfonyl isoxazoline (SI) herbicides were summarised in detail. Two classes of SI compounds were investigated; two triazole compounds, 177 and 197 and one phenyl compound, 907. These studies identified clear class differences in toxicity phenotypes between the triazoles and phenyl. Overall, the triazoles were potently toxic to striated muscle (cardiac and skeletal muscle), whereas the phenyl was not, but produced a stomach, liver and testicular toxicity phenotype.

The triazole (177 and 197) 7 day rat studies showed that cardiac and skeletal muscle were the principle toxicity target tissues, with skeletal muscle proving slightly more sensitive to treatment. Analysis of similar concentrations of the triazole compounds at 7 days demonstrated that 177 proved slightly more potent than 197. However, the picture with the 28 day study was more complex. The only overlapping concentration of 177 and 197 at 28 days was relatively subtoxic (150ppm), making it difficult to draw conclusions on the difference in potency of the triazoles at this time point. By 28 days, there was an equivalent magnitude of liver toxicity present with both compounds, suggesting a cumulative toxic effect of triazoles in the liver. This implied that liver was better able to deal with triazole toxicity (after 7 days) and thus may give an insight into why muscle was more sensitive. Analysis of the 4 and 28 day 177 studies revealed that the toxicity of striated muscle was time dependent, with no adverse effects recorded at the subacute (4 day) time point, yet after subchronic (28 day) treatment there was evidence of toxicity . As with the liver toxicity, these results insinuate a cumulative effect of the compounds in the development of striated muscle toxicity. Only a 28 day study for the phenyl compound (907) was available and comparison between 197 and 907 liver toxicity demonstrated that 197 was slightly more potent. The inclusion of the 907 phenyl served as a non muscle toxicant comparison, as well as a comparison for liver toxicity. From a mechanistic investigation point of view, this was important as it

enabled the discrimination between general toxicity mechanisms and compound and tissue-specific mechanisms.

Overall, the most significant and important findings from these studies was the development of cardiac and skeletal muscle toxicity with the triazole compounds. Cardiac and skeletal muscle toxicity represents a serious side effect of a large range of compounds in research and development (R&D) pipelines and so identifying the underlying mechanisms of these toxicities is an important challenge for agrochemical companies. It is anticipated that a more in-depth understanding of the relation between toxicity and biological pathways will make it possible to reduce the need for animal testing by using testing strategies that allow for assessment of the mechanisms of action by which compounds induce toxicity (Roggen, 2011). The current standard toxicity assays applied in the R&D of new compounds are able to identify a toxicity phenotype, but are insufficient at effectively characterising mechanisms underlying target organ toxicity (Hirawaka *et al*., 2008). The integration of 'omics technologies (genomics, proteomics and metabolomics) with toxicology provide opportunities to apply additional new endpoints in toxicological evaluation (Fabre *et al*., 2009). Thus, these technologies represent a new approach to predict and determine the toxic mechanism of new compounds, and thereby improve the decision making process in the R&D pipeline.

3.1.2 Toxicogenomics

The incorporation of genomics into toxicology has resulted in the sub-discipline of toxicogenomics (Pennie and Kimber, 2001). Toxicogenomics is highly applicable to mechanistic toxicology studies since changes in gene expression accompany virtually every toxic response (Daston, 2008). Toxicogenomics technologies using microarray, profile the cell-wide changes in gene expression following exposure to a toxic insult. This provides a characteristic transcriptional profile that serves as a 'gene expression signature', which is able to detect subtle changes of biochemical and signalling pathways caused by a toxic compound (Gatzidou et al., 2007). By examining these changes it is possible to generate hypotheses as to the underlying mechanisms driving toxic events. Importantly, transcriptional data should be viewed as a starting point

rather than an end point in toxicology studies (Lord, 2004). Therefore, if the mechanism is unknown, then toxicogenomics can help to identify more definitive endpoints to analyse in other systems, i.e. using relevant *in vitro* models. When a good correlation between gene expression and a toxic mechanism exists then the genomic data provides supportive evidence for that mechanism (Gatzidou *et al*., 2007). To detect accurate and relevant mechanisms reflective of a toxic compound, it is important that 'gene expression signatures' are generated in model systems using subtoxic levels of a toxicant. This ensures that changes in gene expression are related to the toxic mechanism of the compound and are not the result of overt pathological changes induced by toxic doses (Heinloth *et al*., 2004).

The ability of toxicogenomics to identify mechanisms of action makes it a valuable tool in predictive toxicology. The sensitivity of the methodology means 'gene expression signatures' generated after xenobiotic treatments can be used to detect toxicity before phenotypic changes are evident (Heinloth *et al*., 2004). In this respect, toxicogenomics can be used to identify predictive biomarkers that serve as sensitive, informative and reproducible markers of early deleterious effects (Bloome *et al*, 2008).

Toxicogenomics has also been applied to address a range of important toxicological issues including; gender differences (Uehara *et al*., 2008), species differences (Lauer *et al*., 2009), compound classification and *in vitro-in vivo* comparisons (Boess *et al*., 2007). The utility of toxicogenomics to develop and validate *in vitro* models may ultimately have the most impact on improving detection of adverse toxicities early in R&D pipelines (Van Hummelen and Sasaki, 2010).

3.1.3 Application of Toxicogenomics for R&D mechanistic studies

In the R&D of compounds, toxicogenomics studies are either focused mechanistic studies or additional endpoints to safety repeat dose studies. Focused mechanistic studies generally involve multiple compounds, time points, species and tissues, although they do not typically contain the full range of traditional endpoints.

In the case where toxicogenomics is applied as an additional endpoint to retrospectively assess mechanisms of toxicity from repeat dose studies, results are phenotypically anchored to traditional endpoints within the study (Daston, 2008). This is important, since it reduces the over interpretation of transcriptional findings in the absence of traditional endpoint data. In this approach profiling of tissues with more than minimal histopathological findings is avoided, under the presumption that transcriptional evaluation of overt lesions would be less mechanistically informative (Foster *et al*., 2007). In these studies the liver is the standard tissue analysed, with additional tissues profiled if there are other target organ toxicities (Foster *et al*., 2007). Profiling the liver provides mechanistic information on potential hepatic or extra-hepatic toxicity that occurs at later time points or at higher doses. In addition, the liver profile gives information on the metabolism of the compounds, an important consideration in toxicology testing.

3.1.4 Toxicogenomics data analysis: Bioinformatics

The most important consideration with toxicogenomics is the analysis and interpretation of the large amount of data generated through microarray. This represents a big challenge, and many researchers have made great efforts to make available biostatistical and bioinformatics tools to support the interpretation of these results. The application of analyses at the global microarray level early on during analysis avoids potential bias. For example, analytical tools such as principal component analysis (PCA) and hierarchical clustering (HCA) summarize and group large amounts of data, thereby focusing subsequent analyses (Ringner *et al*., 2008). To infer biological meaning from microarray data, functional analysis can be carried out, which enriches gene lists to pathways and gene annotations. There are a number of high-throughput technologies that draw on biological knowledge accumulated in public databases (e.g. gene ontology), making it possible to assemble a summary of the most enriched and pertinent biology (Huang *et al*., 2007). It is recommended that multiple tools are used to interpret data, since each tool uses different methods to analyse gene lists (Rhee *et al*., 2008).

3.2 Overall Aim and hypothesis

The overall aim of this study was to define and investigate gene expression profiles of the left ventricular heart (LVH), thigh skeletal muscle (TSM) and left lobe liver (LLL) from Han Wistar rats that had been administered a subtoxic dose of 177, 197 or 907 for a subchronic time course. It was hypothesised that alterations in gene expression patterns of tissues from rats treated with subtoxic doses of SI compounds would result in the identification of key mechanisms through which the compounds exhibit their target organ toxicity.

Specific aims

- To generate gene expression profiles of LLL, LVH and TSM from female Han Wistar rats treated with a subtoxic dose (150ppm) of SI compounds (177, 197 & 907) for a subchronic (28 day) time point.

- To determine the relationship between the gene expression profiles and the traditional endpoints measured during Syngenta's R&D of the compounds (section 1.5), with specific focus on the compound class and tissue differences.

- To identify potential toxic mechanisms of action of 177, 197 and 907 from LLL, LVH and TSM tissues. From this investigation, hypotheses on the adverse effects of the compounds will be made, which will be further investigated and validated using *in vitro* models (chapter 4 and 5).

3.3 Experimental Approach

3.3.1 Tissue sample selection for microarray profiling

The transcriptional studies carried out in this thesis are an additional endpoint to the repeat dose studies carried out with the SI compounds by Syngenta. Therefore, the time points, doses, genders and species of the samples selected were based on what was available and that would fit the experimental aims of this project. The list of tissue samples selected for microarray profiling are presented in table 3.1. A detailed summary of the time and dose selected for the gene expression profiling is available for each compound in section 1.5.1.4.

Compound	Species	Time point (days) Repeat dose	Dose	No. of animals/ Gender	Tissues
177	Han Wistar	28 (Dietary)	150ppm	n=4 C&T female	LLL, LVH, TSM
197	Han Wistar	28 (Dietary)	150ppm	n=4 C&T female	LLL, LVH, TSM
907	Han Wistar	28 (Dietary)	150ppm	n=4 C&T female	LLL, LVH, TSM

Table 3.1 Tissues selected for microarray profiling. Key: LLL = left lobe liver, LVH = left ventricular heart and TSM = thigh skeletal muscle, C = control and T = treated.

The primary toxicity observed with the triazole compounds was in skeletal and cardiac muscle and to a lesser extent the liver. In contrast, 907 was most toxic to the stomach, with toxicity in the liver and testes occurring at higher doses. In this study, we were most interested in the triazole cardiac and skeletal muscle toxicity and so left ventricular heart (LVH) and thigh skeletal muscle (TSM) tissues were profiled. Left lobe liver (LLL) samples were profiled as a standard tissue (Foster *et al*., 2007), providing additional mechanistic information, and because it was one of the toxic targets of all three compounds. In this respect, the LLL served as a mechanistic comparison between the triazoles and the phenyl. This also allowed us to investigate if the gene expression changes reflected the tissue specific histopathology observed with these compounds. The tissues were taken from the 28 day (subchronic) study since the same subtoxic dose was evident in all three compounds at this time point, thus

allowing for comparison between them. Although the 7 day study would have provided an ideal dose response with the triazole compounds, the availability of tissues limited the study design. Tissues from rats treated with 150ppm were chosen for all three compounds as this was a subtoxic dose, which, in this study, was defined as no more than minimal histopathological findings (section 1.5.1.4). This was advantageous since we could be sure that the differential gene expression changes were indicative of physiological changes and not of overt pathology. What is more, studies have shown that alterations in expression patterns at a low, subtoxic dose may reveal signs of subtle cellular injury that are exacerbated at higher concentrations (Heinloth *et al*., 2004; Powell *et al*., 2006). Females were the preferred gender for these studies as they proved the most sensitive to treatment (section 1.5.1.2). Four biological replicates for control and treated were selected to allow for statistical significant comparisons to be made.

3.3.2 Sampling for genomics studies

Multiple samples of LLL, LVH and TSM were taken and snap frozen in liquid nitrogen from all animals at termination of the repeat dose studies. All samples were taken as quickly as possible and stored at -80°C until analysis with gene expression profiling. The samples were stored in RNase free tubes prior to freezing.

3.3.3 Gene expression profiling using Illumina Microarray

A modified Qiagen RNeasy fibrous kit (section 2.2.1.1) was used to extract sufficient yield and quality total RNA from all LLL, LVH and TSM tissues detailed in table 3.1. To assess the impact on the whole annotated rat genome, gene expression profiling was performed using a direct hybridization assay with Illumina RatRef-12 Gene Expression BeadChips (as detailed in section 2.2.4).

3.3.4 Data analysis - Bioinformatics

Analysis of gene expression data was carried out as depicted in the work flow, figure 3.1. Briefly, raw data was imported into ArrayTrack™ (section 2.2.6), the data was log2-transformed and quantile normalisation without background subtraction was carried out (section 2.2.6.1). The normalised data were used for; quality control with

correlation analysis (section 2.2.6.2), cluster analysis (section 2.2.6.3) and to carry out t-tests to determine differentially expressed genes (DEG) between control and treated samples. Differences in gene expression were considered significant at $P<0.05$. In the cases where it was possible, FDR was used to account for multiple testing correction. In ArrayTrack™ Venn diagrams were used to compare the number of common genes between DEG lists. Further to the clustering analysis, this allowed for informative comparisons between the different tissues for each compound to be made. To apply biological meaning to the data and generate hypotheses on toxic mechanisms, functional analysis was used to enrich DEG lists to pathways and gene annotations (section 2.2.6.7). Functional analysis was performed using Ingenuity Pathway analysis (IPA) and Database for Annotation Visualisation and Integrated Discovery (DAVID).

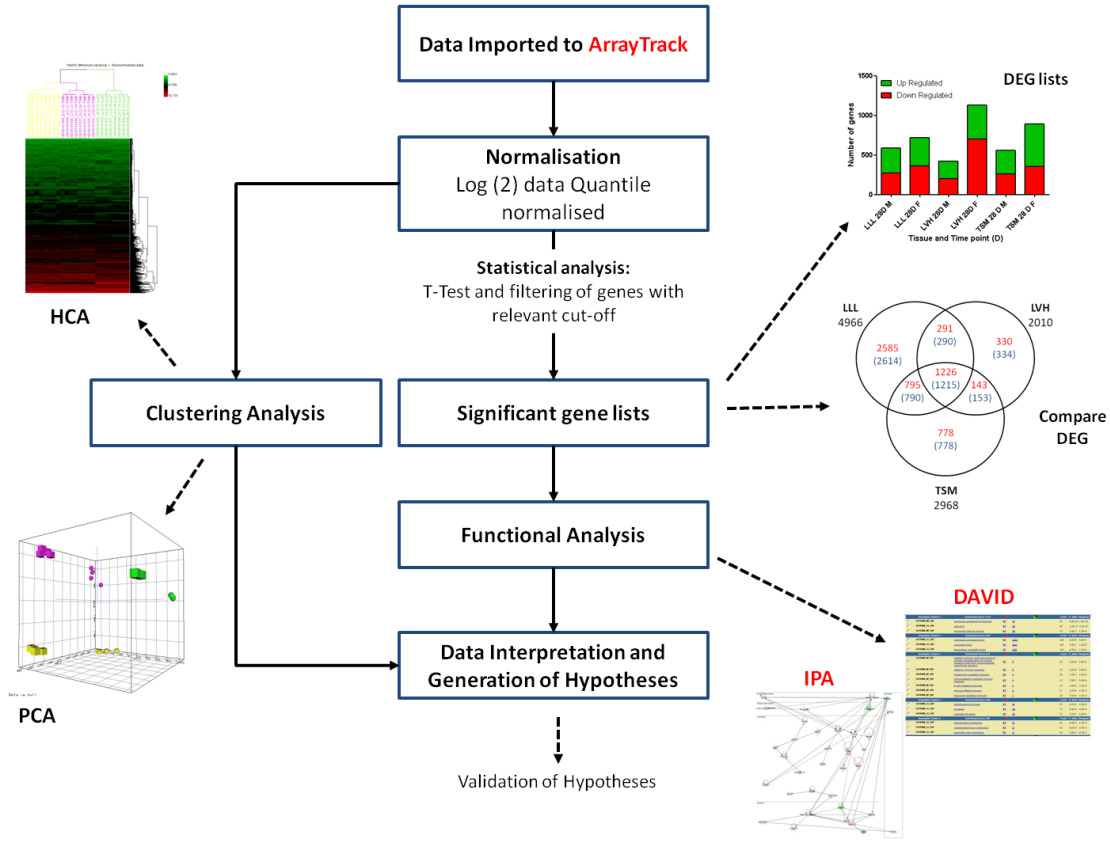

Key:

⟶ Direct line of data analysis

- - - ▶ Example of data analysis outputs

Red Packages used in data analysis

Figure 3.1 Summary of work flow for transcriptional data analysis. Data were normalised in ArrayTrack™ using quantile normalisation. HCA and PCA clustering analysis were carried out to group samples based on the similarity of their gene expression profiles. Lists of differentially expressed genes were identified using a two sample t-test. As cut-off for significance P<0.05 was chosen and if it was possible, an FDR-adjusted P<0.05. Gene lists were compared using Venn diagrams to identify common genes. Functional analysis was carried out using various tools to generate hypotheses on possible mechanisms of toxicity. Abbreviations: DEG = Differentially expressed genes. HCA = Hierarchical clustering analysis; PCA = Principal component analysis; IPA = Ingenuity Pathway analysis and DAVID = Database for Annotation Visualisation and Integrated Discovery.

3.4 Results

3.4.1 Microarray Gene expression profiles and quality control

In this study, gene expression profiles of the LLL, LVH and TSM of female rats treated for 28 days with 150ppm of SI compounds (triazoles; 177, 197 and phenyl; 907) were determined. All gene expression profiles were determined by whole genome wide gene expression microarray analysis (Illumina RatRef-12 Expression BeadChips, 21, 510 genes). There were four biological replicates for control and treated groups. To assess the quality and reproducibility of the microarray data and identify potential outlier's, pair-wise $\log_2$ intensity Pearson's correlation coefficients were calculated for each tissue (table3.2).

Tissue	Mean Coefficient	Coefficient Range
LLL	0.954	0.995- 0.706
LVH	0.965	0.995-0.878
TSM	0.952	0.994-0.695

Table 3.2 The mean and range of correlation coefficients for each tissue within each treatment group. Pearson's correlation coefficient of pair-wise log2 intensity correlation was calculated between samples in each tissue group. No specific cut-off was applied and the intensity of the whole rat genome was used.

The mean correlations were all above 0.9, indicating the data from the arrays were highly reproducible. However, the coefficient ranges for LLL and TSM were large, indicating a high level of variability within these groups. Further analysis of these groups revealed that individual samples in each group had particularly low correlations and so were skewing the data (figure 3.2). The control samples; 907 female LLL (3016 K) and 907 female TSM (3016 H) had coefficients <0.75, and so these outlier arrays were excluded from further data analysis.

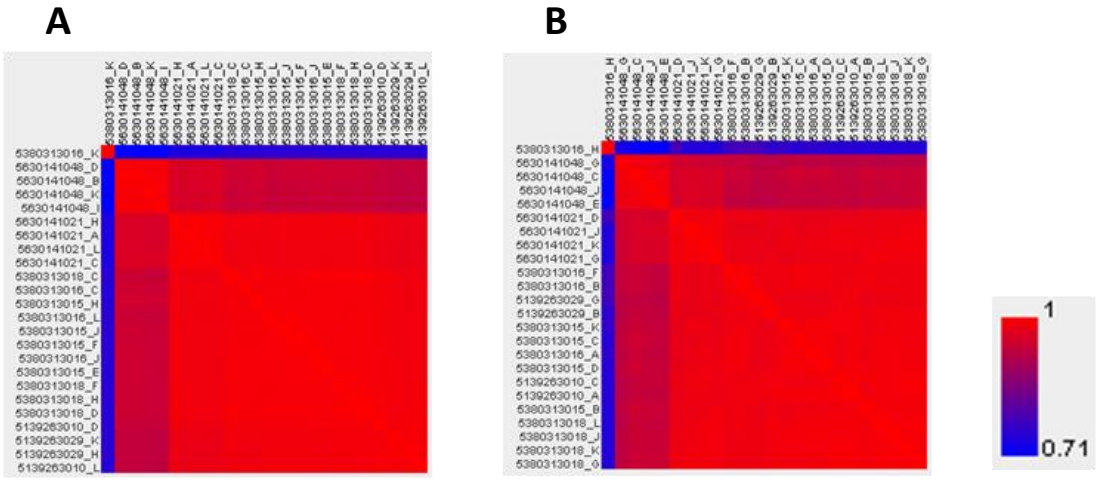

Figure 3.2 The pair-wise log2 intensity correlation matrix heat maps for outlier samples. No specific cut-off was applied and the intensity of the whole rat genome was used. The key represents the R value for Pearson's correlation coefficient. **(A)** 177, 197 and 907 28 D LLL sample correlations. **(B)** 177, 197 and 907 28 D TSM sample correlations. The two outlier samples identified; 907 female LLL (3016 K) and 907 TSM (3016 H) controls had average coefficients of 0.739 and 0.737 respectively. These outlier's were left out of further analysis.

3.4.2 Clustering analysis

Cluster analysis was used to organise gene expression data into groups that share related gene expression profiles. Two forms of clustering were used in this study; hierarchical clustering analysis (HCA) and principal component analysis (PCA). PCA is a multivariate analysis that identifies directions termed 'principal components' along which the variation in data is maximal (Ringner, 2008). PCA provides a means to view multidimensional gene expression data in 3-dimensional space to reveal clusters in the experimental data. This allows for the examination of the relationship among samples, with samples closer together having a more similar gene expression profile. Conversely, HCA groups datasets that have a similar gene expression profile. This is represented in a dendogram tree, in which the length of the branch represents the degree of similarity between values. In this study, the entire dataset, accounting for 22,519 probes, without a specific cut off, was applied for PCA and HCA, using the tools available within ArrayTrack, as detailed in section 2.2.6.3. The relative variances (% of total variance) for each PCA analysis are detailed in figure S1 (additional file 3, addenda).

3.4.3 Effect of 28 day SI treatment on LLL, LVH and TSM gene expression

PCA and HCA were used to determine the effect on the gene expression of LLL, LVH and TSM samples after 28 day treatment with 150ppm of 177, 197 and 907 in female Han Wistar rats. Previous studies have shown that gene expression differences between tissues and treatments can be clearly identified using unsupervised clustering analysis (Chen *et al*., 2006; Mei *et al*., 2007; Han *et al*., 2006). For PCA of all three compounds, the first component (PC 1) accounted for over 65% of the total variance. The second and third componenets represented a lower percentage of the sample variability, and were selected based on their ability to cluster samples of interest.

PCA and HCA results demonstrated that samples from the same tissue clustered together, with clear separation between LLL, LVH and TSM evident for all three compound treatments (figure 3.3). PCA indicated that LVH and TSM samples were separated by PC2, which accounted for <20% of the total variability, while they were separated from LLL along PC1, which represented >65% of the sample variance. HCA also showed that LVH and TSM were linked by shorter length branches in the dendogram, than they were to LLL. Thus, LVH and TSM samples were more closely clustered to one another than to LLL, indicating they shared a similarity in gene expression distinct from LLL. This is expected, since tissues having similar composition and function, like heart and skeletal muscle, tend to cluster more closely compared to other tissues (Son *et al.*, 2005). Samples were also grouped according to treatment with the SI compounds, although the extent of the clustering was different for each compound. There was a clear separation between control and treated samples in all tissues for 197, demonstrating that 197 had a dramatic effect on LLL, LVH and TSM gene expression (figure 3.3 C andD). However, the clustering of control and treated samples was not so distinct with 177 and 907. HCA was unable to cluster control and treated samples for these two compounds (figures 3.3). Using PCA, it took careful selection of principal components to find the direction of variability able distinguish control and treated samples . With 177 (figure 3.3 A and B), PCA showed a subtle, but not complete, clustering of control and treated samples in LVH and TSM, suggesting a treatment related effect in gene expression in these tissues.

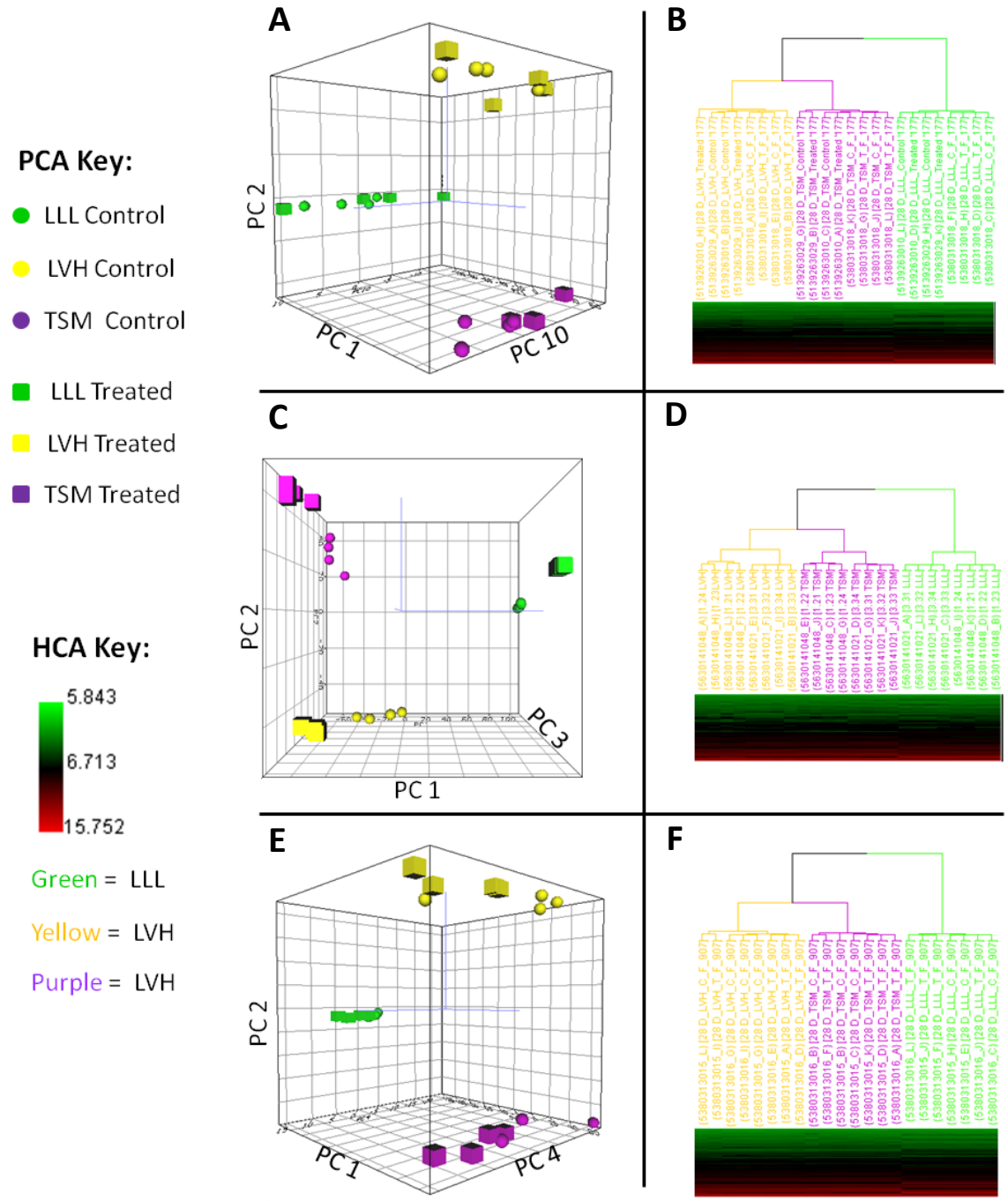

Figure 3.3 Principal component analysis (PCA) and Hierarchical analysis grouped samples according to the tissues and SI treatment. PCA and HCA of expression profiles for control and treated samples of LLL (green), LVH (yellow) and TSM (purple) from female Han Wistar rats treated with 150ppm, 177 (A and B), 197 (C and D) and 907 (E and F) for 28 days. The normalized log(2) intensity of the entire dataset, with no specific cut off, was used for PCA and HCA within ArrayTrack. PCA data was pre-processed using centre scaling and Ward's Minimum Variance method was used for HCA. Groups are presented by columns, and genes in rows. Expression values were colour coded with a red green scale. Green, transcript levels below the median; black, equal to the median and red, greater than median.

Conversely, the effects of 177 treatment on the gene expression of the LLL appears less dramatic, with less separation between control and treated samples.
The 907 control and treated samples of LVH and TSM are slightly separated, as with 177, although the clustering with LVH is clearer (figure 3.3 E and F). The 907 LLL control and treated samples are more tightly clustered than LVH and TSM, although not seperated to the same extent. Clearly, treatment with 197 had the largest effect on the gene expression in all tissues, while 177 and 907 treatment had more subtle and more tissue specific effects on gene expression. Taken together, unsupervised clustering analysis was able to identify clear differences in gene expression between the SI compounds themselves and between LLL, LVH and TSM tissue responses to SI treatment.

3.4.4 Identification of differentially expressed genes between control and treated SI samples

While the PCA and HCA shows that there were differences in the gene expression patterns in the parameters measured (SI compound sensitivities and tissue sensitivities), it does not reveal how many genes and what kind of genes were modulated and what the differences between the parameters actually are. To this end, a t-test was used to determine significant differentially expressed genes (DEG) between control and treated samples in each group. Significant DEG were selected based on the criteria of $P \leq 0.05$ for 177 and 907, and an $FDR \leq 0.05$ for 197. Further fold change (FC) cut-offs were applied to the gene lists. The results for each SI treatment, time point and gender are illustrated in figure 3.4.

3.4.4.1 DEG lists for LLL, LVH and TSM from female rats treated with 28 day treatment of with SI compounds

Treatment with 197 resulted in the most significant (FDR<0.05) DEG in all tissues, with 4966 in LLL, 2010 in LVH and 2968 in TSM (figure 3.4 A). In the LLL, a majority of the genes were down-regulated (2963), whereas in the LVH, most of the genes were up-regulated (1545). The levels of up and down regulated DEG were equivalent in the TSM. With increasing FC cut-off, the proportion of up-regulated DEG increased in all tissues, suggesting that the most affected genes were up-regulated.

As informed by the PCA and HCA, the gene expression changes following 177 (4 and 28 days) and 907 (28 days) treatment were subtle and as a result multiple testing correction (with a FDR $\leq$0.05) resulted in no DEG (data not shown). Therefore, a P<0.05 cut-off was considered acceptable to provide comparative analysis of the compounds and hypothesise on mechanisms associated with these treatments. Interestingly, the most DEG following 907 treatment were in the LVH (2051), followed by LLL (1756) and TSM (1266), with most genes up-regulated in LVH and equivalent levels of up and down- regulated genes evident in LLL and TSM (figure 3.4 B). A FC cut-off >1.5 resulted in a loss of ~95% of DEG in all tissues, implying only modest changes in gene expression.

Treatment with 177 (28 day female) resulted in the least amount of DEG between the SI compounds in all tissues; with LLL (721) and TSM (894) having the least and LVH having the highest (1133) amount of DEG (figure 3.4 C). Application of a >1.5 FC cut-off eliminated >95% of genes in all tissues, with LVH maintaining the highest number of DEG (60). As with 907, this further implies that only small, yet significant, changes were detectable following 28 day 177 treatment in females.

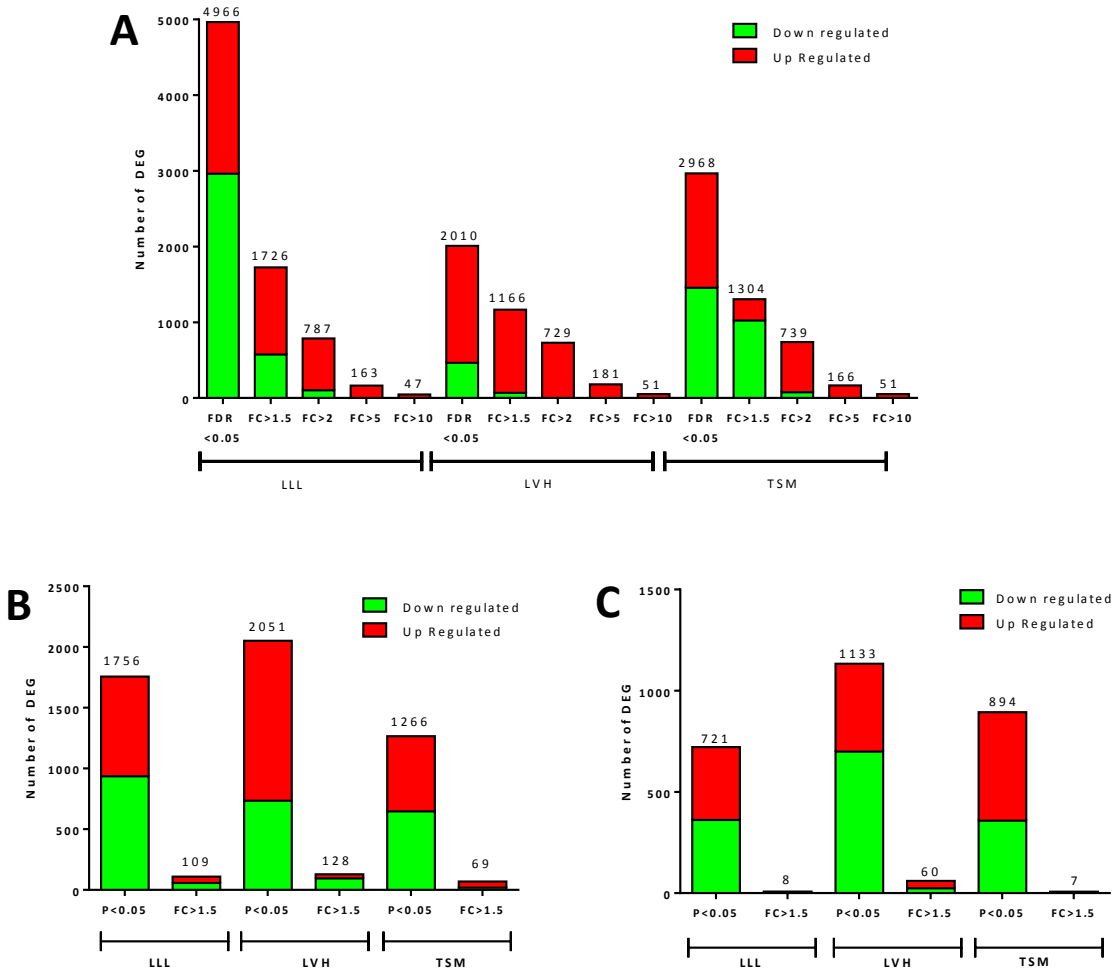

Figure 3.4 Number of significant differentially expressed genes (DEG) following SI treatment. The significantly up (red) and down (green) regulated genes were calculated for Han Wistar rat LLL, LVH and TSM following; (A) 28 day 197 treatment of female rats, using an FDR $\leq$0.05 or FDR$\leq$0.05 with various fold change (FC) cut-offs, (B) 28 day 907 treatment of female rats and (C) 28 day treatment of female rats with 177, using a P<0.05 or P<0.05 with a FC >1.5.

3.4.4.2 Venn analysis of LLL, LVH and TSM from female rats treated for 28 days with SI compounds

Venn analyses was performed with the significant 177 (P<0.05), 907 (P<0.05) and 197 (FDR<0.05) LLL, LVH and TSM DEG to identify those DEG that were common between the tissues (figure 3.5). The number of DEG common to all tissues following 28 days of 177 and 907 was negligible, with only 4 and 14 genes overlapping respectively. This implied that 28 day treatment with 177 and 907 resulted in a tissue specific response to treatment. On the contrary, there was a considerable number of DEG (1226) common between LLL, LVH and TSM following 28 days of 197 treatment. Interestingly,

this overlap accounted for over half of the LVH DEG (2010), about a third of the TSM DEG (2968) and a fifth of the LLL DEG. Moreover, nearly all of the common DEG (1215) were regulated in the same direction (i.e. the same genes were up and down regulated), with most being up regulated (1065). These results suggest there was a specific, up-regulated transcriptional response common to all tissues following 28 days of 197 treatment.

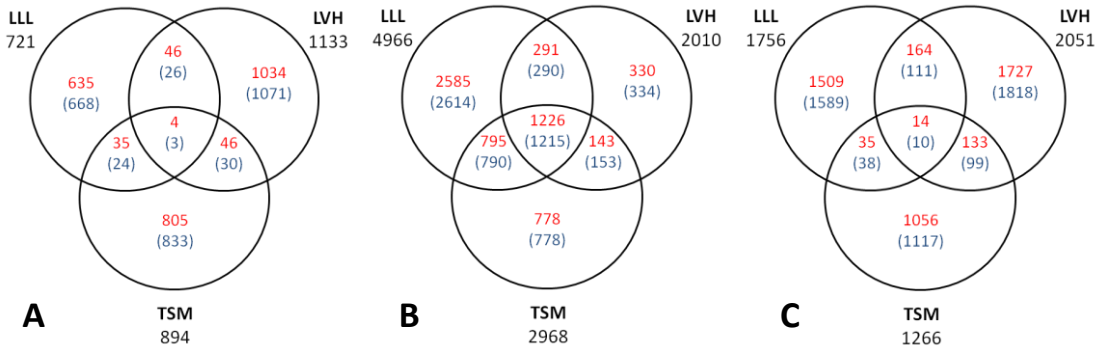

Figure 3.5 Venn analyses of LLL, LVH and TSM significant DEG following 28 day treatment with 177, 197 and 907 in female rats. Venn diagram illustrating DEG in common between LLL, LVH and TSM for each 177 (A), 197 (B) and 907 (C) compound. The DEG 'not considering fold change direction' are illustrated in red and the DEG 'considering fold change direction' are presented in brackets below in blue. The total DEG for each tissue is shown in black.

3.4.5 Functional analysis of SI DEG

The DEG were analysed using a bioinformatics pipeline to understand the functional role of the genes and to provide hypotheses on the potential toxic mechanisms of the SI compounds. A flow-chart of the bioinformatics approach is provided in figure 3.6. Multiple bioinformatics tools (IPA and DAVID) were integrated into the pipeline to provide a cohesive view of the biological functions and pathways associated with the DEG. Moreover, the use of multiple bioinformatics tools is important since no single resource provides information about all available biological pathways (Huang *et al*., 2009).

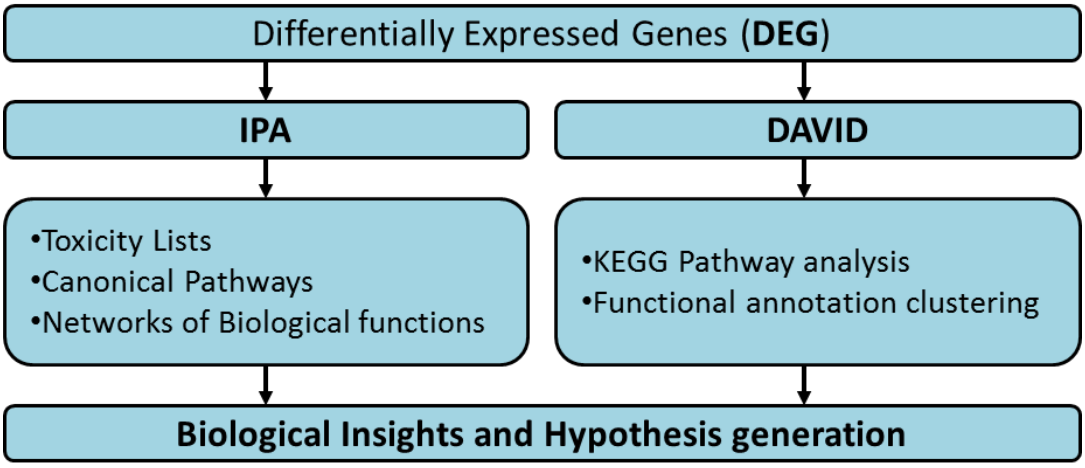

Figure 3.6 Bioinformatics pipeline used for the biological interpretation of DEG and to allow hypotheses on the toxic mechanism of action to be made.

IPA provides the ability to map DEG to fixed canonical pathways, toxicity lists and networks of biological functions. Canonical pathways can be used to gain an overview of the most affected metabolic and signaling pathways in response to xenobiotic treatment. Toxicity lists are gene sets based on critical biological processes and key toxicological responses that enable understanding of mechansistic responses to a xenobiotic insult. IPA also uses the Ingenutiy Pathway Knowledge database (IPKB) to identify networks of biological functions that are significantly enriched by the gene expression data. Right-tailed Fisher's exact test is applied to determine the level of significance for each network, pathway and toxicity list and the p-value is displayed as a score, which is the negative log of that p-value. Only canonical pathways and toxicity lists with a score of $\geq$1.3, which equated to a P-value $\leq$0.05, were consisdered

significant. For network analysis, a score of ≥3 (P ≤0.001) was considered significant and, as a default setting in IPA, only the top 25 significant networks were reported. The Genbank accession IDs, fold changes and P-values for the DEG were used for IPA analysis.

DAVID analysis was used to enrich DEG with KEGG pathways and functional annotation clustering. The significance of KEGG pathway enrichment was assessed using a modified Fisher Exact Test, which generated an enrichment probability score (P-value). Any pathway with a P value ≤0.05 was considered significant. Functional annotation clustering grouped functionally similar annotations built from 40 annotation databases (e.g., GO terms, protein-protein interactions, bio-pathways and literature) (Huang *et al*., 2007). An enrichment score was calculated by averaging unadjusted P-values (determined by Fisher's Exact Test) of the annotations within the cluster. In this study, annotations with a p-value (EASE score) ≤0.1 were considered and a default setting of ≥medium classification stringency was applied to calculate an enrichment score. An enrichment score of ≥1.3, equivalent to P<0.05, was used as the cut-off. The same DEG used in IPA were analysed in DAVID using GenBank Accession ID, and the entire annotated Illumina RatRef array was used as background.

Functional analysis was performed on the tissues that were toxic targets of each SI compound, as informed by the animal studies. For 177 and 197, this included the LLL, LVH and TSM and for 907 this included only the LLL. The primary focus with 177 and 197 was the mechanism of striated muscle (LVH and TSM) toxicity. The LLL analysis was included since this tissue also developed toxicity related to triazole treatment and consequently provided additional mechanistic insight.

3.4.6 Fucntional analysis of 177 LLL, LVH and TSM

Functional analysis was carried out using LLL, LVH and TSM significant DEG (P<0.05) from female rats treated with 150ppm 177 for 28 days (figure 3.4 C).

3.4.6.1 177 IPA enrichment analysis

The top 10 canonical pathways and toxicity lists for each tissue (LLL, LVH and TSM) are listed in table 3.3. The complete results for the toxicity lists, canonical pathways and functional networks for LLL, LVH and TSM are reported in the addenda (additional files 4-6). The results of the IPA analysis for each tissue are summarized as follows:

177 LLL: The most significantly enriched canonical pathways and toxicity lists associated with LLL response to 177 related to; xenobiotic metabolism (glutathione-mediated, AhR signaling), response to oxidative stress (NRF-2-mediated oxidative stress response, glutathione depletion, AhR signaling), inflammatory response (FC-epsilon RI signaling, autoimmune thyroid disease signaling), mitochondrial dysfunction (swelling of mitochondria) and stress response signalling (ERK/MAPK, VEGF family Ligand-Receptor interactions). The top functions associated with the LLL networks included cell cycle control, 'DNA replication, recombination and repair', cell death and survival, inflammatory response, xenobiotic metabolism, energy production and protein synthesis (additional file 4, addenda).

177 LVH: A majority of the canonical pathways enriched by the LVH DEG were involved with an inflammatory response (8 of the top 10 pathways). This inflammatory response related to pathological findings in the enriched toxicity lists; cardiac fibrosis and cardiac necrosis/cell death. Taken together, these results suggest gross cytotoxicity and inflammation at the transcriptional level, that could possibly mask the underlying toxic mechanism in LVH. In spite of this, the remaining toxicity lists provided evidence for antioxidant defence response (NRF-2 mediated oxidative stress response, glutathione depletion, RAR activation, AhR signaling) mitochondrial dysfunction and response to xenobiotic stimulus (AhR signaling). The top functions enriched by the LVH networks were concerned with effects on energy production, glutathione depletion in liver, cell cycle control, 'DNA replication, recombination and repair' and cardiovascular system development (additional file 5, addenda).

LLL			
Toxicity Lists	**-log (P-V)**	**Canonical Pathways**	**-Log (P-V)**
Glutathione Depletion - Phase II Reactions	2.94	Glutathione-mediated Detoxification	2.38
NRF2-mediated Oxidative Stress Response	2.41	Fc Epsilon RI Signaling	2.34
Aryl Hydrocarbon Receptor (AhR) Signaling	1.44	Autoimmune Thyroid Disease Signaling	2.29
Swelling of Mitochondria	1.31	ERK/MAPK Signaling	2.28
Increases Liver Steatosis	1.24	Synaptic Long Term Depression	2.21
Biogenesis of Mitochondria	1.09	VEGF Family Ligand-Receptor Interactions	2.02
Increases Transmembrane Potential of Mitochondria and Mitochondrial Membrane	0.93	Phospholipases	1.97
Cytochrome P450 Panel - Substrate is a Vitamin (Human)	0.86	Sphingomyelin Metabolism	1.96
Oxidative Stress	0.80	NRF2-mediated Oxidative Stress Response	1.94
Cytochrome P450 Panel - Substrate is a Vitamin (Mouse)	0.80	NGF Signaling	1.87
LVH			
Toxicity Lists	**-log (P-V)**	**Canonical Pathways**	**-Log (P-V)**
Cardiac Fibrosis	2.94	Type I Diabetes Mellitus Signaling	4.67
NRF2-mediated Oxidative Stress Response	2.31	Graft-versus-Host Disease Signaling	4.19
Glutathione Depletion - Phase II Reactions	2.15	Dendritic Cell Maturation	4.17
RAR Activation	2.02	Antigen Presentation Pathway	4.11
Glutathione Depletion - CYP Induction and Reactive Metabolites	1.99	OX40 Signaling Pathway	3.92
Mitochondrial Dysfunction	1.68	NRF2-mediated Oxidative Stress Response	3.11
Cardiac Necrosis/Cell Death	1.45	Allograft Rejection Signaling	2.85
Aryl Hydrocarbon Receptor (AhR) Signaling	1.32	CD28 Signaling in T Helper Cells	2.68
Decreases Respiration of Mitochondria	1.25	IL-6 Signaling	2.68
Cardiac Hypertrophy	1.16	Autoimmune Thyroid Disease Signaling	2.64
TSM			
Toxicity Lists	**-log (P-V)**	**Canonical Pathways**	**-log (P-V)**
Mitochondrial Dysfunction	2.76	Mitochondrial Dysfunction	2.81
Mechanism of Gene Regulation by Peroxisome Proliferators via PPARα	1.30	Ascorbate Recycling (Cytosolic)	2.64
Increases Depolarization of Mitochondria and Mitochondrial Membrane	1.09	Arsenate Detoxification I (Glutaredoxin)	2.34
Glutathione Depletion - Phase II Reactions	0.97	Antioxidant Action of Vitamin C	2.29
Decreases Permeability Transition of Mitochondria and Mitochondrial Membrane	0.87	Thioredoxin Pathway	1.96
LPS/IL-1 Mediated Inhibition of RXR Function	0.81	Valine Degradation I	1.88
VDR/RXR Activation	0.75	Cell Cycle Regulation by BTG Family Proteins	1.79
Cytochrome P450 Panel - Substrate is a Vitamin (Mouse)	0.74	PPAR Signaling	1.79
Cytochrome P450 Panel - Substrate is a Vitamin (Rat)	0.74	2-amino-3-carboxymuconate Semialdehyde Degradation to Glutaryl-CoA	1.55
Oxidative Stress	0.66	Tumoricidal Function of Hepatic Natural Killer Cells	1.54

Table 3.3 IPA analysis of 177 LLL, LVH and TSM DEG. The top 10 enriched toxicity lists (left) and canonical pathways (right) of 177 LLL (green), LVH (yellow) and TSM (purple) DEG ($P<0.05$) are displayed. –log (P-V) = $-\log_{10}$ (P-value), which is known as a P-score. A P score of ≥ 1.3 was considered significant, which equates to a p vlaue of <0.05.

177 TSM: The most significantly enriched toxicty list and canonical pathway by the TSM DEG was mitochondrial dysfunction. In conjuction with mitochondrial dysfunction, there were four cannonical pathways associated with antioxidant defence (ascorbate recycling, arsenate detoxification (glutaredoxin), antioxidant action of vitamin C and thioredoxin pathway) and two pathways associated with energy metabolism (PPAR signaling and Valine degradation). In addition, two pathways concerned with cell cycle control were signficantly enriched (Cell Cycle Regulation by BTG Family Proteins and 2-amino-3-carboxymuconate Semialdehyde Degradation to Glutaryl-CoA). The most enriched functions in the TSM networks were cell growth and proliferation, cell death and survival, skeletal and muscular development, free radical scavenging, energy metabolsm, cell cycle control and RNA/DNA damage and repair (additional file 6, addenda).

3.4.6.2 177 DAVID enrichment analysis

The same 177 LLL, LVH and TSM DEG used for IPA analysis were used for DAVID analysis. The significantly enriched ($P<0.05$) KEGG pathways for each tissue are presented in table 3.4. The complete results for the LLL, LVH and TSM functional annotation clustering (DAVID) are reported in additional files 4-6 (addenda) due to the amount of material.

177 LLL: Functional annotation clustering identified 8 annotation clusters that were significantly enriched by the LLL DEG (additional file 4, addenda) These clusters were concerned with effects on fatty acid oxidation, phospholipase A2 activation, glutathione transferase activity, ribosomes and inflammatory mediators. Along with the KEGG pathway analysis (table 3.4), these results further highlighted the significance of glutathione metabolism, inflammation, proten synthesis (ribosomes) and xenobiotic metabolism in the LLL response to 177.

177 LVH: Functional annotation clustering with the LVH DEG significantly enriched 14 annotation clusters, which consisted of effects on inflammation (7 clusters) cell death (caspase-mediated apoptosis) and protein synthesis (additional file 5, addenda). Concurrently, KEGG pathway analysis enriched inflammatory effects most

significantly, accounting for 11 out of the 14 signficantly enriched pathways. The other KEGG pathways related to protein synthesis (Ribosomes) and stress signal responses (Wnt signaling and RNA degradation).

LLL		LVH	
Term	**P-Value**	**Term**	**P-Value**
Glutathione metabolism	0.005	NOD-like receptor signaling pathway	1.3E-04
Fc epsilon RI signaling pathway	0.011	Systemic lupus erythematosus	5.9E-03
Ribosome	0.019	Asthma	6.9E-03
Metabolism of xenobiotics by cytochrome P450	0.038	Cytosolic DNA-sensing pathway	7.7E-03
		RIG-I-like receptor signaling pathway	1.1E-02
		Type I diabetes mellitus	1.1E-02
TSM		Graft-versus-host disease	1.1E-02
Term	**P-Value**	Allograft rejection	1.6E-02
Oxidative phosphorylation	5.5E-04	Autoimmune thyroid disease	3.2E-02
Alzheimer's disease	5.3E-03	RNA degradation	3.2E-02
Parkinson's disease	7.4E-03	Wnt signaling pathway	3.3E-02
Huntington's disease	1.6E-02	Ribosome	4.0E-02
Proteasome	1.8E-02	Toll-like receptor signaling pathway	4.3E-02
Ubiquinone and other terpenoid-quinone biosynthesis	2.4E-02	Antigen processing and presentation	5.5E-02

Table 3.4 KEGG pathway analysis of 177 LLL, LVH and TSM. The significant KEGG pathways (P<0.05) for 177 LLL (green), LVH (yellow) and TSM (purple) DEG (P<0.05) are reported.

177 TSM: With the TSM DEG, functional annotation clustering significantly enriched 10 clusters, of which 7 related to effects on the mitochondria (additional file 6, addenda). These mitchondrial clusters included effects on oxidative phophorylation, mitochondrial inner membrane, electron transport chain, ubiquinone metabolic process and flavoprotein (FAD). The other clusters were concerned with cell death, proteosome activity (ubiquitin-protein ligase activity) and ribonucleotide metabolism. KEGG pathway analysis provided further confirmation of effects on mitochondrial (Oxidative phosphorylation and ubiquinone biosynthesis) and proteosomal pathways (table 3.4). The remaining KEGG pathways related to neurological (Alzheimer's, Parkinson's and Huntington's) diseases, whose pathogenesis has been strongly linked to oxidative stress and mitochondrial dysfunction (Yan *et al.*, 2013; Chen, 2011).

3.4.7 Functional analysis of 197 LLL, LVH and TSM

3.4.7.1 197 IPA enrichment analysis

IPA analysis was carried out using the LLL, LVH and TSM significantly DEG (FDR<0.05) from female rats treated with 150ppm 197 for 28 days (figure3.4 A). The top 10 toxicity lists and canonical pathways are reported in table 3.5. Complete details of the analysis and associated genes are reported in additional files 7-9 (addenda).

197 LLL: Among the top significantly enriched canonical pathways and toxicity lists, most pertained to effects on xenobiotic metabolism (AhR signaling), energy metabolism (PPARα activation, fatty acid metabolism), mitochondrial dysfunction, oxidative stress (NRF-2 mediated oxidative stress response), stress response signaling (PTEN, eiF2 and HIF- signaling), inflammatory response signaling (acute phase response signaling) and protein homeostasis (protein ubiquitination pathway and eiF2 signaling). The top functions associated with the LLL networks were concerned with cell cycle control, cell signaling, xenobiotic metabolism, protein synthesis, 'DNA replication, recombination and repair', energy production and inflammatory response (additional file 7, addenda).

197 LVH: As with LLL, the most significantly enriched toxicity lists and pathways alluded to effects on mitochondrial dysfunction, oxidative stress, energy metabolism (PPARα/RXRα Activation, fatty acid β-oxidation I) and protein homeostasis (eiF2, protein ubiquitination, tRNA charging and regulation of eIF4 and p70S6K Signaling). Additionally, DNA damage responses (G1/S and G2/M DNA damage checkpoint) and cardiac development (telomerase signaling, tight junction signaling, and ERK5 signaling) were significantly enriched in LVH. The top functions enriched in the LVH DEG included cell death and survival, 'DNA recombination and repair', cell cycle, drug metabolism, energy metabolism, gene expression, protein synthesis and cardiovascular system dvelopment and function (additional file 8, addenda).

LLL			
Toxicity lists	**-log (PV)**	**Canonical Pathways**	**-log (PV)**
Xenobiotic Metabolism Signaling	9.51	Protein Ubiquitination Pathway	10.8
NRF2-mediated Oxidative Stress Response	8.58	Acute Phase Response Signaling	10.4
PPARα/RXRα Activation	7.95	NGF Signaling	9.55
Mechanism of Gene Regulation by Peroxisome Proliferators via PPARα	7.58	B Cell Receptor Signaling	8.77
Mitochondrial Dysfunction	6.43	PPARα/RXRα Activation	8.53
LPS/IL-1 Mediated Inhibition of RXR Function	5.95	Xenobiotic Metabolism Signaling	8.49
Fatty Acid Metabolism	5.70	Production of Nitric Oxide and Reactive Oxygen Species in Macrophages	8.36
Aryl Hydrocarbon Receptor (AhR) Signaling	5.14	eiF2 Signaling	8.20
Liver Necrosis/Cell Death	4.52	IL-15 Signaling	8.13
Hypoxia-Inducible Factor (HIF) Signaling	4.29	PTEN Signaling	7.98
LVH			
Toxicity Lists	**-log (PV)**	**Canonical Pathways**	**-log (PV)**
Mitochondrial Dysfunction	3.17	eiF2 Signaling	9.96
Oxidative Stress	2.73	Protein Ubiquitination Pathway	7.57
Cell Cycle: G2/M DNA Damage Checkpoint Regulation	2.30	Mitochondrial Dysfunction	3.26
Increases Transmembrane Potential of Mitochondria and Mitochondrial Membrane	2.12	Regulation of eIF4 and p70S6K Signaling	3.19
Fatty Acid Metabolism	2.02	Fatty Acid β-oxidation I	3.06
Cell Cycle: G1/S Checkpoint Regulation	1.91	tRNA Charging	2.97
Mechanism of Gene Regulation by Peroxisome Proliferators via PPARα	1.46	Tight Junction Signaling	2.60
PPARα/RXRα Activation	1.31	Cell Cycle: G2/M DNA Damage Checkpoint Regulation	2.57
Cardiac Necrosis/Cell Death	1.09	ERK5 Signaling	2.37
Swelling of Mitochondria	1.07	Telomerase Signaling	2.37
TSM			
Toxicity Lists	**-log (PV)**	**Canonical Pathways**	**-log (PV)**
RAR Activation	4.21	Protein Ubiquitination Pathway	13.7
Hypoxia-Inducible Factor (HIF) Signaling	3.60	eiF2 Signaling	10.8
Mechanism of Gene Regulation by Peroxisome Proliferators via PPARα	2.36	tRNA Charging	5.52
Mitochondrial Dysfunction	2.03	Regulation of eIF4 and p70S6K Signaling	5.13
Cholesterol Biosynthesis	1.68	Estrogen Receptor Signaling	4.79
PPARα/RXRα Activation	1.67	RAR Activation	4.32
Cell Cycle: G2/M DNA Damage Checkpoint Regulation	1.65	PTEN Signaling	4.05
Oxidative Stress	1.47	Hypoxia Signaling in the Cardiovascular System	3.52
NRF2-mediated Oxidative Stress Response	1.34	IGF-1 Signaling	3.00
TGF-β Signaling	1.19	Mitotic Roles of Polo-Like Kinase	2.88

Table 3.5 IPA analysis of 197 LLL, LVH and TSM DEG. The top 10 enriched toxicity lists (left) and canonical pathways (right) of 197 LLL (green), LVH (yellow) and TSM (purple) DEG (FDR<0.05) are displayed. –log (P-V) = $-\log_{10}$ (P-value), which is known as a P-score. A P score of $\geq$1.3 was considered significant, which equates to a p vlaue of <0.05.

197 TSM: Consistent with LLL and LVH, toxicity lists and pathways enriched by TSM DEG related to effects on protein homeostasis (Protein ubiquitination pathway, tRNA charging, eiF2, eIF4 and p70S6K signaling), stress response signalling (HIF, PTEN, eiF2, eIF4 and p70S6K signlaing), energy metabolism (PPARα), mitochondrial dysfunction and oxidative stress (NRF-2 mediated oxidative stress response). As with LVH, there was a toxicity list referring to a DNA damage response (Cell Cycle: G2/M DNA Damage Checkpoint Regulation). Among the most significantly enriched toxicity lists and pathways was RAR activation, which has down stream effects related to apoptosis and cell proliferation. The top functions identifed by the TSM networks were concerned with energy production, DNA replication, recombination and repair, gene expression, cell cycle, protein synthesis/degradation and post-translational modification (additional file 9, addenda).

3.4.7.2 197 DAVID enrichment analysis

DAVID analysis was carried out using the LLL, LVH and TSM significantly DEG (FDR<0.05) from female rats treated with 150ppm 197 for 28 days, as used with IPA. The significantly enriched KEGG pathways for each tissue are presented in table 3.6. However, for functional annotation clustering, the DEG limit was 3000 genes. Since LLL FDR<0.05 DEG consisted of 4966 genes, an additional fold change cut-off of $\geq$1.5 was applied, providing a total of 1726 DEG for analysis. The results for the LLL, LVH and TSM functional annotation clustering (DAVID) are reported in additional files 7-9 (addenda) due to the amount of material.

197 LLL: Functional annotation clustering identified 45 clusters that were significantly enriched by the 197 LLL DEG (FDR<0.05, FC>1.5). The most significant clusters related to effects on protein homeostatsis (8 clusters in total), which included both ribosomal and proteosomal components. Other significantly enriched clusters were associated with inflammation (7 clusters), energy metabolism (4 clusters), mitochondria (3 clusters) and apoptotic cell death (3 clusters) (additional file 7, addenda). In total there were 51 KEGG pathways significantly (FDR<0.05) enriched by the 197 LLL DEG, although only pathways corrected for multiple testing with Benjamini-Hochberg FDR corrected P-value were included in the analysis (table 3.6).

LLL		TSM	
Term	**P –Value Benjamani**	**Term**	**P –Value**
Ribosome	4.28E-12	Ribosome	8.75E-23
Proteosome	9.72E-04	Spliceosome	4.46E-07
Huntington's disease	1.18E-03	Proteasome	4.91E-06
Alzheimer's disease	1.44E-03	RNA degradation	1.14E-05
Splicesome	1.51E-03	Ubiquitin mediated proteolysis	2.74E-05
Parkinson's disease	1.61E-03	Aminoacyl-tRNA biosynthesis	2.44E-04
Fc gamma R-mediated phagocytosis	2.57E-03	Cell cycle	8.88E-04
Complement and coagulation cascades	2.79E-03	Oxidative phosphorylation	0.00344
Oxidative phosphorylation	3.53E-03	Huntington's disease	0.00469
Chronic myeloid leukaemia	7.13E-03	Parkinson's disease	0.00589
Lysosome	7.49E-03	Basal transcription factors	0.00778
Endocytosis	2.39E-02	Alzheimer's disease	0.0144
RNA degradation	2.90E-02	Glycolysis / Gluconeogenesis	0.01677
Drug metabolism	2.91E-02	Nucleotide excision repair	0.03974
LVH		TGF-beta signaling pathway	0.04065
Term	**P -Value**	Other glycan degradation	0.04317
Ribosome	4.80E-25	SNARE interactions in vesicular transport	0.04479
Spliceosome	1.83E-07		
Huntington's disease	3.55E-04		
Proteasome	3.55E-04		
Oxidative phosphorylation	4.60E-04		
Alzheimer's disease	6.85E-04		
Parkinson's disease	7.99E-04		
Fatty acid metabolism	9.39E-04		
Aminoacyl-tRNA biosynthesis	0.008015		
RNA degradation	0.011732		
Glycolysis / Gluconeogenesis	0.017301		
PPAR signaling pathway	0.02391		

Table 3.6 KEGG pathway analysis of 197 LLL, LVH and TSM. KEGG pathways significantly enriched with a Benjamani-Hochberg-P-value $\leq$ 0.05 are reported for 197 LLL (green) and with a P-value $\leq$0.05 for 197 LVH (yellow) and TSM (purple) DEG (FDR<0.05) .

Similarly to previous 197 LLL analysis, KEGG pathways significantly enriched ribosome, proteosome and splicesome pathways, highlighting the effect on transcriptional and translational regulation. Additionally, KEGG pathways pertaining to xenobiotic metabolism, inflammation and oxidative phosphorylation were significantly enriched. As seen with 177 TSM KEGG analysis (table 3.4), the neurological disease pathways,

Alzheimer's, Parkinson's and Huntington's, were significantly enriched, which, as previously suggested for 177 TSM, implicates the role of oxidative stress and mitochondrial dysfunction in 197 toxicity.

197 LVH: There were 46 significantly enriched clusters by the LVH DEG, with a majority concerned with protein homeostasis (10 clusters) and gene expression (9 clusters). There were also a significant number of clusters relating to mitochondria (3 clusters), regulation of apoptosis (4 clusters) energy metabolism (4 clusters) and cell cycle (additional file 8, addenda). The KEGG pathways were confirmation of significant effects on protein homeostasis (ribsome, proteosome) and gene expression (splicesome), energy metabolism (PPAR signaling, Fatty acid metabolism, glycolysis) and mitochondrial dysfunction. With respect to mitochondrial dysfunction, oxidative phosphorylation was highly significant, as well as the neurological diseases (Alzheimer's, Parkinson's and Huntington's).

197 TSM: A total of 17 functional annotation clusters were significantly enriched by TSM DEG, which related to protein homeostasis, cell death (regulation of apoptosis), gene expression (RNA splicing) and mitochondria (additional file 9, addenda). As with LLL and LVH, KEGG pathways were concerned with protein homeostasis (ribosome, proteosome, Ubiquitin mediated proteolysis), gene expression (splicesome, RNA degradation, basal transcription factors), energy metabolism (glycolysis) and mitochondrial dysfunction (oxidative phosphorylation, neurological diseases). In addition, pathways involved with a DNA damage response (nucleotide excision repair, cell cycle) were significantly enriched.

3.4.8 Identification of a specific stress response to 197 in all tissues

Venn analysis revealed a significant amount of overlap in DEG between 197 LLL, LVH and TSM (FDR<0.05) suggesting a common and specific response to 197 in all tissues after 28 day treatment (figure 3.5 B). Functional analysis (with IPA and DAVID) was carried out with the common DEG list, in which 1215 DEG were regulated in the same direction (figure 3.5 B). The full results of both analytical tools is detailed in additional file 10, addenda).

Ingenuity Toxicity Lists	-log (pv)	Ingenuity Canonical Pathways	-log (pv)
Renal Necrosis/Cell Death	1.96	eiF2 Signaling	12.7
Cell Cycle: G1/S Checkpoint Regulation	1.94	Protein Ubiquitination Pathway	10
Hypoxia-Inducible Factor (HIF) Signaling	1.71	Regulation of eIF4 and p70S6K Signaling	5.27
Mechanism of Gene Regulation by Peroxisome Proliferators via PPARα	1.48	tRNA Charging	3.22
Cell Cycle: G2/M DNA Damage Checkpoint Regulation	1.44	Telomerase Signaling	2.73
Fatty Acid Metabolism	1.37	p70S6K Signaling	2.61
PPARα/RXRα Activation	1.30	Antiproliferative Role of TOB in T Cell Signaling	2.52
Increases Depolarization of Mitochondria and Mitochondrial Membrane	0.848	PI3K/AKT Signaling	2.49
Hepatic Stellate Cell Activation	0.805	mTOR Signaling	2.45
Biogenesis of Mitochondria	0.736	Fatty Acid β-oxidation III (Unsaturated, Odd Number)	2.35

KEGG pathway	P Value
Ribosome	2.5E-28
Spliceosome	2.3E-08
Proteasome	5.0E-06
Parkinson's disease	1.8E-03
Alzheimer's disease	2.4E-03
RNA degradation	4.4E-03
Oxidative phosphorylation	4.5E-03
Fatty acid metabolism	6.6E-03
Huntington's disease	7.0E-03
Glycolysis / Gluconeogenesis	1.8E-02
Aminoacyl-tRNA biosynthesis	2.1E-02

Table 3.7 IPA and KEGG analysis of 197 commonly regulated DEG. Top: IPA analysis of the top 10 enriched toxicity lists and canonical pathways of 197 commonly regulated DEG (FDR<0.05) are displayed. –log (P-V) = -$\log_{10}$ (P-value), which is known as a P-score. A P score of $\geq$1.3 was considered significant, which equates to a p vlaue of <0.05. **Bottom:** KEGG pathways significantly enriched with an P<0.05 are are reported for 197 commonly regulated DEG (FDR<0.05).

3.4.8.1 IPA analysis

Unsurprisingly, IPA identified a number of toxicity lists and canonical pathways evident in the LLL, LVH and TSM individual analysis (table 3.7). These alluded to effects on cell death, stress response signaling (HIF, eiF2, P13K/AKT eIF4, p70S6K and mTOR signaling), DNA damage checkpoints (Cell cycle: G1/S and G2/M checkpoint regulation), protein homeostasis (eiF2 eIF4, p70S6K signaling, protein Ubiquitination pathway and tRNA charging) and energy metabolism (gene regulation by PPARα, Fatty Acid β-oxidation III). The top functions associated with the common 197 DEG were

gene expression, protein synthesis, RNA post-translational modification, energy production (lipid and carbohydrate metabolism), cell death and survival, 'DNA replication, recombination and repair' and cell growth and proliferation (additional file 10, addenda).

3.4.8.2 DAVID analysis

Functional analysis with DAVID identified 29 significant clusters, with most relating to protein homeostasis (11 clusters) and gene expression regulation (5 clusters). Additionally, a number of clusters were concerned with mitochondrial effects (3 clusters), apoptotic cell death (3 clusters) and energy metabolism (additional file 10, addenda). KEGG pathways enriched related to protein homeostasis (Ribosome and proteasome), gene expression (splicesome and RNA degradation), mitochondria (oxidative phosphorylation and neurological diseases) and energy metabolism (Fatty acid metabolism and Glycolysis) (table 3.7).

3.4.9 Functional analysis of 907 LLL

The LLL DEG (FDR<0.05) from female rats treated with 907 for 28 days was used for IPA and DAVID functional analysis. The complete results for these analyses are presented in additional file 11, addenda. The top 10 toxicity lists and canonical pathways and the signficant KEGG pathways (P<0.05) are presented in table 3.8.

3.4.9.1 907 IPA analysis

A number of the most significantly enriched canonical pathways and toxicity lists were associated with cholesterol biosynthesis (i.e. Cholesterol Biosynthesis I, II &III, zymosterol biosynthesis and FXR/RXR activation). The remaining pathways and lists were enriched for effects on xenobiotic metabolism (glutathione depletion, cytochrome P450 and AhR signaling), stress response signalling (HIF and JAK/STAT signalling), inflammation (acute phase response siganling) and liver cell death and proliferation. The top functions enriched by LLL networks corresponded to cell morphology, drug metabolism, glutathione depletion in the liver, gene expression, cell cycle, 'DNA replication, recombination and repair', lipid metabolism, inflammatory response and amino acid metabolism (additional file 11, addenda).

LLL			
Toxicity Lists	**-log(p-value)**	**Canonical Pathways**	**-log(p-value)**
Hypoxia-Inducible Factor (HIF) Signaling	2.86	Cholesterol Biosynthesis I	5.31
Cholesterol Biosynthesis	2.61	Cholesterol Biosynthesis II (via 24,25-dihydrolanosterol)	5.31
Liver Necrosis/Cell Death	2.46	Cholesterol Biosynthesis III (via Desmosterol)	5.31
Glutathione Depletion - Phase II Reactions	2.15	Superpathway of Cholesterol Biosynthesis	5.18
Liver Proliferation	2.03	Colanic Acid Building Blocks Biosynthesis	3.91
Cytochrome P450 Panel - Substrate is a Sterol (Human)	2.02	Zymosterol Biosynthesis	3.66
Cytochrome P450 Panel - Substrate is a Sterol (Mouse)	2.02	JAK/Stat Signaling	3.0
Cytochrome P450 Panel - Substrate is a Sterol (Rat)	2.02	Acute Phase Response Signaling	2.65
FXR/RXR Activation	1.70	Methylglyoxal Degradation III	2.61
Aryl Hydrocarbon Receptor Signaling	1.64	IL-10 Signaling	2.46

LLL	
KEGG Pathways	**P-Value**
Steroid biosynthesis	8.04E-04
Pyruvate metabolism	0.002
Propanoate metabolism	0.006
Pancreatic cancer	0.018
Amino sugar and nucleotide sugar metabolism	0.029
SNARE interactions in vesicular transport	0.038
Adherens junction	0.046

Table 3.8 IPA and KEGG analysis of 907 LLL DEG. Top: IPA analysis of the top 10 enriched toxicity lists and canonical pathways of 907 LLL DEG (P<0.05) are displayed. – log (P-V) = -$\log_{10}$ (P-value), which is known as a P-score. A P score of $\geq$1.3 was considered significant, which equates to a p vlaue of <0.05. **Bottom:** KEGG pathways significantly enriched with a P<0.05 are are reported for 907 LLL DEG.

3.4.9.2 907 DAVID analysis

A total of 35 clusters were enriched by 907 LLL DEG, with the most significant cluster being steroid/cholesterol biosynthesis. The other clusters related to protein homeostasis, energy metabolism, inflammation and xenobiotic metabolism (additional file 11, addenda). Complementary to functional clustering and IPA analysis, the most significant KEGG pathway was steroid biosynthesis (table 3.8). Other notable significantly enriched pathways were involved in energy metabolism (pyruvate, propanoate, amino acid and nucleotide sugar metabolism).

3.5 Discussion

The aim of this chapter was to investigate the gene expression profiles of rat LLL, LVH and TSM in response to treatment with SI compounds and to generate hypotheses on the mechanisms of their target organ toxicity. Toxicogenomics was used to generate gene expression profiles of LLL, LVH and TSM from female rats treated daily for a sub-chronic (28 day) time course with a subtoxic (150ppm) concentration of two triazoles (177 and 197) and one phenyl (907) SI compound. Functional analysis, using IPA and DAVID, was then carried out with the 177, 197 and 907 gene signatures to generate hypotheses on their mechanisms of toxicity.

3.5.1 Quality control of microarray data- addressing the issue of outliers using Pearson's Rank Correlation

Microarray experiments are complicated processes involving multiple steps. There are a range of factors, involved in manufacturing of the arrays to data acquisition by scanning of arrays, which can lead to unwanted random or systematic variation in the data (Kauffman and Huber, 2010). A majority of the statistical tests used for differential gene expression analysis, such as t-test and ANOVA, rely upon accurate estimation of sample variance (Yang *et al*., 2006). So any data points that greatly affect this variance can add noise and impair statistical and biological significance of analysis (Kauffman and Huber, 2010). Therefore, assessment of data quality is an essential part of microarray analysis to ensure that unreliable data points, outliers, are excluded from subsequent analysis. Outlier detection is a process to search for samples that do not obey the general rules of the majority portion of the data in the same analysis group (Leung *et al*., 2012). In this study, the statistical diagnostic for flagging potential outlying samples was comparison of the arrays using Pearson's correlation coefficient for a given group of microarrays (using all probes on the array). Correlation analysis has been successfully implemented for identification of outliers in a range of microarray studies and removing these outliers strengthens the power of detecting DEG (Yang *et al.*, 2006; Oldham *et al*., 2008). This unbiased method identified 2 arrays, 907 female LLL (3016 K) and 907 female TSM (3016 H), that had considerably lower coefficients (<0.75) than arrays in the same group (average >0.9). There is no formal

threshold to reject an array, so thresholds are set empirically, taking into account the nature of the experiment and the samples (Yang *et al*., 2006). In this case, the two samples were control samples, each from different (tissue) groups of samples and so did not represent a variation resulting from treatment. Furthermore, HCA and PCA analysis illustrated that the pattern of gene expression of these two samples was distinct from all other control and treated samples within each respective group (data not shown). Taking into account that these two arrays were one control sample out of four biological repeats, and differed considerably in their gene expression from the other arrays, it was logical to filter them out from subsequent analysis. Potential reasons for the difference in gene expression of these outliers were not investigated, but could be attributable to any range of factors, including; sample quality, mislabelling of samples, array manufacture error and scanning error. The problem of potential outliers highlights the importance of biological replicates to ensure robust statistical analysis. Aside from identifying outliers, Pearson's correlation coefficient indicated the high quality and reproducibility of the microarray data that were obtained in this study.

3.5.2 Clustering analysis to determine the effect of SI treatment on gene expression

Clustering analysis is used to gain an unbiased visual assessment of the similarities and differences between samples and determine whether samples can be grouped (Ringer, 2008). Once outliers were removed from the dataset, clustering analysis, using PCA and HCA, was carried out using the whole rat genome (22,519 probes). This revealed that samples could be grouped based on their tissue of origin and SI treatment. Treatment of female rats for 28 days with subtoxic doses of SI compounds resulted in separate clustering of control and treated samples in LLL, LVH and TSM. The extent of the separation of control and treated samples differed between the compounds; 197 resulted in a distinct and homogeneous clustering of control and treated samples, whereas 177 and 907 clustering was more modest and less homogeneous in all tissues. Separate clustering of samples is indicative of variation in gene expression, which can arise due to biological differences or technical errors (Zakharkin *et al.,* 2005). The quality and reproducibility of the microarrays, identified

by correlation analysis (section 3.4.1), indicated that biological differences and not technical error were the cause of these clustering effects. Thus, these results can be interpreted as evidence for the biological similarity within each group and biological differences between control and treated groups. Given the fact that all of the genes on the array were used for cluster analysis, these results can be considered highly significant (Han *et al*., 2006). Overall, clustering analysis determined that the effects of SI compound treatment in female rats could be determined by gene expression profiling. The results are confirmation that gene expression changes were present before overt histopathological changes, demonstrating the utility of these gene expression studies for mechanistic studies (Foster *et al*, 2007). As well as confirmation that sub toxic doses of SI compounds induced biologically relevant changes in female rats, these results are further confirmation of the high quality and reproducibility of the microarray data. Therefore, the effects of SI compounds were investigated by differential gene expression (section 3.4.4) and functional analysis (section 3.4.5).

3.5.3 Statistical analysis - multiple testing correction and p-values for identification of significant differentially expressed genes (DEG)

Differential gene expression analysis of microarray data involves multiple testing (of thousands of transcripts), which is likely to produce false positives (Type 1 errors) if arbitrary p-value thresholds (i.e. 0.05) are applied. Therefore, multiple testing correction is applied to adjust statistical confidence measures based on the number of tests performed (Pounds, 2005). Traditionally, biologists used family-wise error rates (FWER), such as Bonferroni, to limit false positives. However, minimising the FWER is considered too conservative and results in false negatives (type II error) (Allison *et al.*, 2006). Therefore, false discovery rate (FDR), which accepts that a small proportion, i.e. 5% will be wrong, has been successfully employed for microarray analysis and is calculated using the Benjamani-Hochberg procedure (Benjamani and Hochberg, 1995).

In this study, a t-test was used to identify significant differentially expressed genes (DEG) between control and treated 177, 197 and 907 samples. A p-value of <0.05 ($p<0.05$) was applied as a cut-off and FDR was used to control for multiple correction testing. The 197 DEG lists were the most statistically robust with an FDR<0.05 resulting

in ideal size gene lists with all tissues for downstream analysis. However, FDR correction resulted in no significant DEG with 177 and 907 gene lists. The reason for this is likely because 28 day treatment of a subtoxic dose of 177 and 907 only induced modest changes to gene expression relative to the noise inherent with microarray technology (Subramanian *et al*., 2005). Therefore, an arbitrary cut-off of $p<0.05$ for all 177 and 907 (LLL, LVH and TSM) DEG lists was used for subsequent analysis. Despite not correcting for multiple testing, an arbitrary cut off was considered acceptable, since type I and type II errors are inversely related, with decreases in false positives (type I) being associated with increases in false negatives (type II) (Pedra *et al*., 2004). There are numerous examples in the literature where an arbitrary p-value has been successfully used and validated for investigation of biological processes (Smeianov *et al*., 2007; Juretic *et al*., 2007). Also, the importance of the statistical robustness of a DEG list is dependent on the downstream analysis. The primary aim of this toxicogenomics study was to identify potential mechanisms of toxicity through functional analysis. The more generous statistical power of functional analysis (pathway and annotation term analysis) can reveal significant changes that are not apparent at the single gene level, providing hypotheses for follow up analysis (Subramanian *et al.,* 2005). Therefore, while there may be false positives at the level of individual gene targets, biologically meaningful patterns of functional enrichments can be identified (Carl *et al*., 2013).

3.5.4 Comparison of gene expression profiles and their relationship to pathology SI compound differences

Comparing SI compound DEG lists, it was evident that 197 resulted in a much greater amount of statistically robust DEG than 177 and 907 in all tissues. As identified with clustering analysis, this was likely because 28 day treatment with 177 and 907 only resulted in modest effects on gene expression. The difference between 197 and 907 was not surprising, given that 197 was identified as more potently toxic than 907 after 28 days (table 1.7). In this respect, 197 induced a greater amount of histopathological changes in the liver than 907 at equivalent toxic doses. However, the disparity between 177 and 197 gene expression at 28 days was unexpected as there was a similar level of histopathological findings at this time point in all tissues. What is more,

the 7 day studies identified 177 as potently more toxic to striated muscle, inducing a higher amount of histopathological changes than 197, at equivalent concentrations. The difference in potency identified by the 7 day studies and the difference in magnitude of gene expression changes at 28 day would suggest that the timing at which each triazole elicited a gene expression response would have been different. Research carried out by Chechik and Koller (2009) into the timing properties of gene expression responses to toxins may shed some light onto the differences seen with the SI compounds in this study. They proposed an 'impulse model', illustrated in figure 3.7, in which there is a two phase response to xenobiotic stress; the first phase is a sharp increase or decrease in gene expression, which is followed by a second phase, in which the cell achieves a new homeostasis in its new environment, transitioning to a 'steady state' (Chechik and Koller, 2009). Fitting the results of the SI compounds to the 'impulse model' is not straight forward since we have no time course for the compounds. Therefore, it is only possible to hypothesise on what phase each SI compound would fit in the model, based on the magnitude of gene expression change, the pathological findings and the functional analysis.

The magnitude of gene expression changes elicited by 197 would suggest that in all tissues gene expression is at or near the peak amplitude (h_1), where a maximal gene expression response is occurring. This phase of the response is characterised by transcriptional and translational changes that respond to stress to promote survival of the organism (Chechik and Koller, 2009). Functional analysis of the 197 common DEG lists supported these responses, with significant up regulation of transcriptional (*splicesome*), translational (*ribosome* and *proteasome*) and stress signalling (*HIF, eiF2, P13K/AKT eIF4, p70S6K and mTOR signaling)* processes.

Based on the fact 177 was determined more potent than 197, we can hypothesise that the first phase stress response had already been elicited by 28 days and gene expression had reached the second, 'steady state' phase (h_2). This 'steady state' is different from the original 'resting state' (h_0), suggesting that even if the first phase of gene expression change was missed, informative mechanistically-relevant gene expression changes can be found. The functional changes in the 177 LLL and LVH were

indicative of late stage, adaptive gene expression responses, with inflammatory and adaptive responses (such as cardiac fibrosis) being significantly enriched.

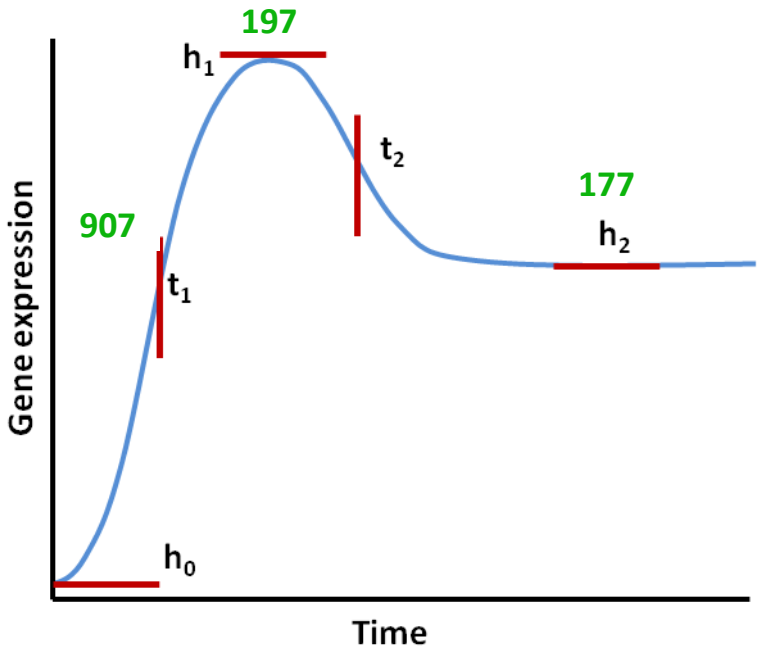

Figure 3.7. The Impulse model. There are five parameters of the impulse model; h_0 = Initial amplitude ('resting state'), t_1 = time of first transition, h_1 = peak amplitude, t_2 = time of second transition and h_2 = steady state amplitude. The hypothesised position of each SI compound is displayed on the graph (green); 907 is in t_1 transition, 197 is in h_1 peak amplitude and 177 is in h_2 steady state (adapted from Chechik and Koller, 2009).

The triazoles were determined as more potently toxic than the phenyl, 907, so we can hypothesise that 907 gene expression changes would have been between h_0 and h_1, in the t_1 phase. As with 177, this transition stage provides significant and informative gene expression changes from which we can draw conclusions on the mechanisms of toxicity.

3.5.5 SI triazole and phenyl tissue comparisons

As well as variation in gene expression between the SI compounds, there was considerable variation in DEG changes between the tissues with each SI compound treatment.

Treatment with 177 resulted in more DEG in striated muscle (LVH, 1133 DEG and TSM, 894 DEG) than in the liver (LLL, 721 DEG). These gene expression changes correlated with the 7 day study, which identified striated muscle as the primary target organ of triazole treatment. The doses used in the 7 study, however, were over ten times greater (~1500ppm) than used at 28 days. For ethical reasons, higher concentrations than 150ppm could not be used at 28 days. After 28 days with the subtoxic (150ppm) dose of 177, there were limited, inconclusive histopathological changes in all tissues, making it difficult to determine differential organ toxicity. However, while no histopathological changes were evident in the heart, there was an increase of cardiac troponin T (cTnT) detected in the serum of the rats (section 1.5.2.2). cTnT is considered to be a highly sensitive and specific biomarker for the detection of myocardial damage in the rat (Wallace *et al*., 2004). Numerous studies have been carried out to investigate the utility of cTnT to detect early myocardial damage and assess its relationship with histopathological findings (York *et al*., 2007; Bertinchant *et al*., 2000). By carrying out time-course experiments with Isoproterenol (ISO), a well characterised cardiotoxic compound, these studies showed that cTnT levels increased prior to the onset of histopathological lesions. For example, York *et al* (2007) showed that following a single toxic dose of ISO, cTnT levels were increased by 1 hour, peaking at 2 hours, while histopathologic lesions were not detected until 4 hours. Therefore, we can hypothesise that the increase in DEG number coupled with the increase in cTnT would be predictive of histopathologic lesions in the LVH at higher concentrations.

The magnitude of gene expression differed significantly between 197 treated tissues, with nearly twice as many DEG in the liver (4966) than in the striated muscles (LVH, 2010 and TSM, 2968) at FDR<0.05. Since subtoxic doses were used here, we are assuming that these changes are predictive of what would happen at more toxic doses or after a longer time course. Therefore, to put these DEG differences into context, the histopathological changes of female rats treated with higher, more toxic doses of 197 were considered (section 1.5.2.1). These results indicated that higher doses (1500ppm and 5000ppm) resulted in slightly more histopathological changes in the liver than the heart and skeletal muscle after 28 day treatment. Thus, the increased

amount of DEG in the LLL at the subtoxic dose (150ppm) may be a reflection of the increased histopathological changes in the liver at higher doses.

Unlike the triazoles, 907 treatment did not cause toxicity to striated muscle (heart and skeletal muscle), but it was toxic to the liver (section 1.5.2.3). Comparison between the numbers of 907 treated LLL (1756), LVH (2051) and TSM (1266) DEG revealed that the magnitude of gene expression change did not correlate with the target organ of toxicity, the liver. For example, 907 induced higher numbers of DEG in the LVH than in the LLL, despite the absence of any pathology in the heart (at higher, toxic doses) (section 3.4.4). This is contrary to findings by Auman *et al* (2007), who determined that there were a higher amount of DEG in the target tissue (liver) than there were in the nontarget tissue (kidney), following treatment of rats with the hepatotoxicant methpyriline (Auman *et* al., 2007). However, Foster *et al* (2007) found that the magnitude of gene expression change did not always associate with histopathological findings (Foster *et al*., 2007). Coupled with the fact that the gene expression changes in 907 tissues were only modest (p value <0.05), it was not possible to accurately interpret the meaning of these tissue DEG differences.

These studies highlight the importance of anchoring the gene expression changes to traditional endpoints (i.e. histopathology and clinical chemistry) for accurate interpretation of results. However, to accurately interpret the differences in the magnitude and significance of DEG between the SI compounds and tissues a series of time and dose response experiments would need to be carried out. Interestingly, research carried out by Foster *et al* (2007), on a number of compounds, concluded that it was not possible to determine whether in response to equivalent xenobiotic exposures some tissues (e.g. the liver) are on average more transcriptionally responsive than others (e.g. the skeletal muscle).

3.5.6 Functional analysis to identify potential mechanisms of SI toxicity

3.5.6.1 Differential gene list selection for functional analysis

The decision on the size of the gene lists and the various fold change cut-offs to apply to the gene lists was largely influenced by the experimental design. We were

interested in enrichment analysis of genes rather than individual genes themselves, and to perform this analysis it is important to have a gene list that was the right size (Huang *et al*., 2009). Currently there is no good systematic way to quantitatively estimate the quality of the gene list before functional analysis is carried out. Huang *et al* (2009) suggest that the gene list should contain a relatively large amount of genes (ranging from hundreds to thousands) since this provides greater statistical power resulting in increased sensitivity to slightly enriched terms (Huang *et al.,* 2009). Therefore, in this study, to provide large enough gene lists for enrichment analysis a statistical threshold ($P<0.05$ for 177, 907 and $FDR<0.05$ for 197) without fold change cut-offs was used. The use of fold change cut-offs assumes that genes with large regulations (fold changes) are contributing more to the biology. In real biology, however, this is not always the case and small changes of some signal transduction genes can result in larger down-stream consequences (Huang *et al*., 2009). In this respect, a modest increase (e.g. 20%) in a number of genes encoding the members of a metabolism pathway may dramatically alter the flux through the pathway and may be more important than a significant increase (e.g. 20-fold) in a single gene (Subramanian *et al.,* 2005). Thus, it was just as important to include the mildly changed genes as well as the larger changing genes in this analysis.

3.5.6.2 A bioinformatics pipeline to investigate mechanisms of triazole and phenyl SI compound toxicity

IPA and DAVID analysis were carried out to provide a high level functional overview of the LLL, LVH and TSM gene expression response to subchronic (28 day) SI exposure. It was highly advantageous to use multiple tools, which even offer similar analytic capability, in order to obtain maximum satisfactory analytic results (Rhee *et al.*, 2008). Integration of the results from the IPA and DAVID analytical tools took advantage of the different focus and strength of each software package, making the overall biological picture assembled on the basis of a given DEG list more comprehensive and detailed. There are a number of gene expression profiling studies that have effectively used a combination of IPA and DAVID to understand the functional role of DEG (Masud *et al*., 2012; Monaco *et al*., 2012; Piantoni *et al*., 2010). Perhaps the biggest challenge of functional analysis was the interpretation of the canonical pathways,

toxicity lists, biological functions, KEGG pathways and functional annotation clusters into clearly defined mechanisms of toxicity. The beauty of the 'toxicity lists' tool in IPA was that it delivered a focused toxicity interpretation, revealing biological mechanisms that were related to the toxicity on a molecular, cellular and biochemical level. However, to evaluate the remaining analytical tools in a relevant toxicity context required an in-depth literature curation, using resources such as PubMed. In doing this, the canonical pathways, functional annotation clusters, biological functions and toxicity lists were classified into biological processes that had toxicity context (i.e. 'toxicity pathways'), such as inflammatory response, mitochondrial dysfunction and energy metabolism, to name a few. This allowed for comparison between the compounds and tissues on the basis of similar biological processes perturbed, even if the exact pathways, annotation terms, toxicity lists and functions contributing to them were not identical.

3.5.6.3 Functional analysis identified clear class differences and confirmed the quality of input gene lists

Functional analysis revealed distinct differences in the biological processes perturbed by the SI triazoles and phenyl compounds. The triazoles, 177 and 197, had a considerable amount of overlap of biological processes between LLL, LVH and TSM, suggesting a common mechanism of toxicity across all tissues. Although, there were distinct processes that took place in each tissue, such as xenobiotic metabolism in the LLL, that reflected the specific functions of each tissue. More strikingly, there was considerable overlap of biological processes between the triazoles, suggesting a common triazole mechanism of toxicity. These commonly enriched biological processes alluded to effects on mitochondrial dysfunction, oxidative stress, energy metabolism, cell death and survival signaling, protein regulation and cell cycle/DNA damage response. Although only phenyl LLL was analysed, the biological processes enriched were different to the triazoles, with cholesterol biosynthesis the most highly ranked process. From this toxicogenomic study we can hypothesise that the difference in mechanism of toxicity between the triazoles and phenyls may account for the difference in primary target organ toxicities identified by the traditional endpoints.

As discussed previously, the quality of the input gene lists could not be properly assessed until functional analysis had been carried out. One of the hallmarks of a good quality gene list is the ability of a given gene list to enrich certain interesting and biologically relevant processes, rather than enriching random biological processes (Huang *et al*., 2009). In this study, there was consistency between the biological process enriched within individual triazole (LLL, LVH and TSM) and phenyl (LLL) DEG lists. Importantly, the types of biological processes affected in each tissue were relevant to that specific tissue – such as enrichment of *xenobiotic metabolism* in the LLL and *skeletal muscle development* in the TSM. Furthermore, in the case of 177 and 197, there was a consistency of the biological processes affected between the compounds. Thus, these results confirm the high quality of the input gene lists, even for the gene lists with the arbitrary p-value cut-offs.

3.5.6.4 Biological processes affected by triazoles 177 and 197 – potential mechanisms of toxicity

Despite the differences in the magnitude and significance of gene expression between 177 and 197, there were a number of biological processes that were commonly affected, which may constitute a common triazole mechanism of toxicity. Figure 3.8 illustrates the systematic process that was used to identify the common and specific processes affected by each tissue and compound. The common biological processes ('toxicity pathways') between 177 and 197 tissues were mitochondrial dysfunction, oxidative stress, altered energy metabolism, stress response signalling - cell death and survival, protein regulation and cell cycle/DNA damage response, which will be discussed in more detail.

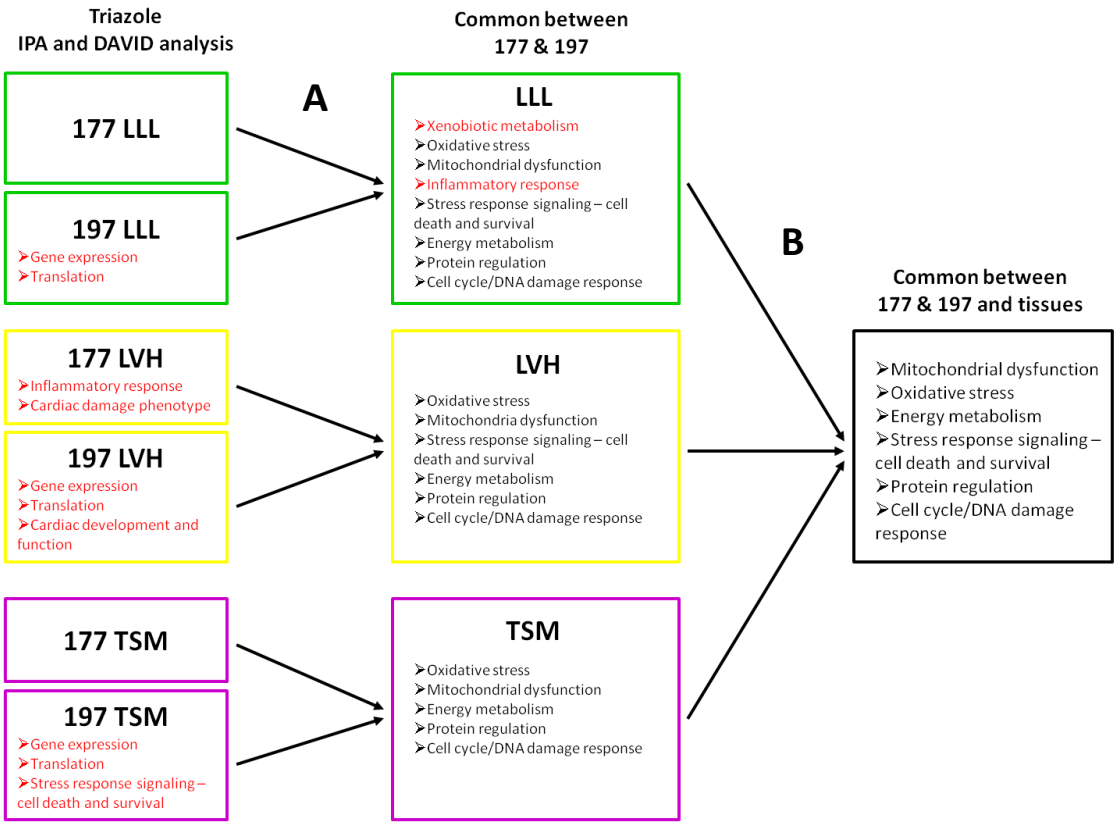

Figure 3.8 Identification of commonly affected biological processes between triazoles 177 and 197. (A) A systematic process was used to indentify commonly affected biological processes between 177 ($p<0.05$) and 197 (FDR<0.05) LLL, LVH and TSM. (B) Biological processes that were commonly affected by triazoles in the LLL, LVH and TSM were identified. The biological processes that were not common between the compounds or tissues are highlighted in red.

3.5.6.5 Commonly affected triazole biological processes

Mitochondrial Dysfunction

Mitochondria are vital organelles that make approximately 90% of the cell's ATP utilizing oxidative phosphorylation (OXPHOS) (Dykens and Will, 2007). Mitochondria also play a crucial role in apoptosis, fatty acid oxidation, heme synthesis and steroid synthesis (Nadanaciva *et al*., 2007). Dysfunction of mitochondria can result in a decline in energy production, increased generation of reactive oxygen species (ROS) and induction of stress-induced apoptosis (Subramaniam and Chesselet, 2013). A number of processes relating to mitochondrial dysfunction were significantly enriched by all tissues from 177 and 197 treated rats. Significantly, the toxicity list *mitochondrial dysfunction* was enriched by 177 LVH and TSM and all 197 tissues. Although 177 LLL did not enrich the term *mitochondrial dysfunction* specifically, the toxicity term

swelling of mitochondria was significantly enriched, which is indicative of mitochondrial dysfunction. Mitochondrial swelling is characterised by an increase in the mitochondrial volume and can result from a range of dysfunctions, including mitochondrial depolarization, mitochondrial calcium overload and opening of the permeability transition pore (Kaasik *et al*., 2007). Mitochondrial swelling is not only a manifestation of mitochondria injury, but is also a mechanism by which cytochrome c and apoptosis inducing factors (AIF) are released (Petit *et al.*, 1998). Therefore, enrichment of *mitochondrial swelling* is indicative of a potential connection between mitochondria and apoptosis following 177 treatment.

Mitochondrial dysfunction is a broad term which encompasses a range of mitochondrial toxicity targets, including; uncoupling of electron transport from ATP synthesis (Non-steroidal anti-inflammatory drugs (NSAIDs), redox-cycling (quinones), opening of mitochondrial permeability transition pore, depletion of mtDNA (nucleoside reverse transcriptase inhibitors (NRTIs), inhibition of the Krebs cycle (fluoroacetate), inhibition of β fatty acid oxidation (NSAIDs) and inhibition of the oxidative phosphorylation complexes (Dykens and Will, 2007; Nadanaciva *et al*., 2007). With respect to 177, mitochondrial dysfunction effects were enriched most prominently in TSM, which provided a greater insight into the type of mitochondrial perturbations induced by 177. KEGG pathway analysis of 177 TSM significantly enriched *'oxidative phosphorylation'* and '*ubiquinone and other terpenoid-quinone biosynthesis'*. Similarly, DAVID functional clustering significantly enriched clusters associated with *mitochondrial inner membrane, electron transport chain* and *ubiquinone metabolic process.* The oxidative phosphorylation (OXPHOS) system is embedded in the mitochondrial inner membrane and is composed of an electron transport chain (ETC), which coordinates the transport of electrons and protons, culminating in the production of ATP (Smeitink *et al*., 2001). Ubiquinone (coenzyme Q) is one of two electron carriers that transports electrons between the complexes of the electron transport chain, which is essential to establishing the proton-motive force used to drive ATP synthesis by ATP synthase (Crane, 2001). Therefore, the TSM analysis indicated that 177 treatment resulted in a significant effect on OXPHOS. These effects on OXPHOS may explain the enrichment of *swelling of mitochondria* by 177

LLL, since studies have shown that loss of mitochondrial membrane potential leads to mitochondrial swelling (Safiulina *et al*., 2006).

In concordance with 177 findings, functional analysis of 197 resulted in enrichment of a range of terms and pathways associated with OXPHOS. KEGG analysis of all 197 tissues significantly enriched *oxidative phosphorylation* and functional clustering analysis of 197 LLL and LVH significantly enriched clusters concerned with *mitochondrial envelope* and *mitochondrial inner membrane*. There was also evidence of protective mechanisms against mitochondrial dysfunction, as revealed by enrichment of *Increases Transmembrane Potential of Mitochondria and Mitochondrial Membrane* by 197 in LVH. Mitochondrial membrane potential is coupled with OXPHOS to drive ATP synthesis and studies have shown that an increase in mitochondrial membrane potential confers a protective effect by enhancing mitochondrial function, through enhanced ATP and antioxidant levels (Li *et al*., 2009b; Kim *et al*., 2003; Seo *et al*., 1999).

Taken together, these results indicate that the mitochondria, and more specifically OXPHOS, is a possible target for triazole toxicity in LLL, LVH and TSM. The liver, heart and skeletal muscle are particularly vulnerable to mitochondrial toxicities since they are amongst the most metabolically active tissues and so have the largest amount of mitochondria (Neustadt and Pieczenik, 2008). Mitochondrial toxicity has been identified as a primary 'off-target' effect of a range of xenobiotics, including troglitazone, doxorubicin (DOX) and statins (Dykens and Will, 2007). Notably, gene expression studies, utilising microarray technology, have been used to investigate mitochondrial toxicants. For example, Pointon *et al* (2010) investigated the effects of (DOX) in rat cardiotoxicity using transcriptomics, and found that 'oxidative phosphorylation' was the most significantly affected pathway (using KEGG pathway analysis). These findings were further validated through gene expression studies carried out by Zhang *et al*. (2012), who identified significant transcriptome effects on 'mitochondrial dysfunction' and 'oxidative phosphorylation', using IPA, following DOX treatment of mice (Zhang *et al*., 2012). Given the fact DOX is a well characterised

mitochondrial toxicant, these studies support the utility of microarray gene expression to accurately detect xenobiotic-induced mitochondrial dysfunction.

Oxidative Stress

Oxidative stress occurs when the levels of reactive oxygen species (ROS) exceed the capacity of antioxidant defence systems, resulting in damage to DNA, protein and lipid (Scandalios, 2002). In response to oxidative stress, cells function to counteract the resulting oxidant effects and restore redox balance, largely through modulation of transcription factor activities that effect changes in the pattern of gene expression (Martindale and Holbrook, 2002). In this study, a range of processes relating to oxidative stress were significantly enriched by both triazoles in all tissues. The enrichment of the toxicity list *oxidative stress* by 197 in LVH and TSM, and canonical pathway *Production of Nitric Oxide and Reactive Oxygen Species in Macrophages* by 197 in LLL provided convincing evidence for the role of oxidative stress in 197 triazole toxicity. The expression of genes involved with antioxidant defences further supported the role of oxidative stress in triazole toxicity. The most commonly enriched antioxidant defence mechanism by 177 and 197 was *NRF-2 mediated oxidative stress response*, which was significantly enriched by 177 LLL, 177 LVH and 197 LLL, TSM and LVH (although it was not in the top 10 toxicity lists for 197 LVH). Nrf2 (nuclear erythroid 2-related factor 2) is a basic region leucine-zipper transcription factor, which is activated in response to xenobiotic and radiation induced electrophilic and oxidative stress (Jaiswal, 2004). Notably, the Nrf2 pathway is regarded as the most important in the cell to protect against oxidative stress (Copple *et al*., 2008). In basal conditions, Nrf2 is bound to the endogenous inhibitor Keap1, but once activated it translocates to the nucleus where it binds to antioxidant response elements (ARE) (Jaiswal, 2004). Nrf2-ARE binding regulates the expression of a battery of defensive genes encoding proteins involved in the detoxification and elimination of reactive oxidants and electrophilic agents through conjugative reactions and by enhancing cellular antioxidant capacity (Nguyen *et al*., 2009). These include phase 2 detoxification enzymes (e.g. NAD(P)H:quinone oxidoreductase), enzymes which are necessary for glutathione biosynthesis (e.g. glutathione S-transferase (GST) and glutamate cysteine

ligase (GCL)), extracellular superoxide dismutase, glutamate-6-phosphatedehydrogenase, heat shock proteins and ferritin (Petri *et al*., 2012). One of the key targets of Nrf2, the antioxidant glutathione pathway, was signicantly affected following 177 treatment, as shown by enrichment of *glutathione phase II reactions* by 177 LLL, LVH and TSM (although significance was not reached in TSM). The enrichment of *Arsenate Detoxification I (Glutaredoxin)* by 177 TSM was further evidence for glutathione antioxidant activity, since glutaredoxins catalyze the formation and reduction of mixed disulfides between protein thiols and glutathione, thus protecting against oxidative stress (Berndt *et al*., 2007). As well as Glutaredoxin, in TSM, 177 enriched a coordinated set of antioxidant systems, including; *Thioredoxin pathway, Antioxidant action of vitamin C and Ascorbate recycling,* which was further confirmed by the enrichment of *free radical scavenging* function in IPA. Thioredoxin forms part of the redoxin system with glutaredoxin and exerts most of its antioxidant defence through thioredoxin peroxidase, which scavenges ROS such as H_2O_2 (Yamawaki and Berk, 2005). Significantly, research in rats has shown that the thioredoxin system is regulated via the Nrf2 pathway (Tanito *et al*., 2007). Vitamin C (ascorbic acid (AA)) is an electron donor, which reduces reactive free radicals (such as superoxide), becoming oxidized itself to dehydroascorbate (DHA), a less reactive oxidant, making it an ideal free radical scavenger (Padayatty *et al*., 2003). During periods of oxidative stress, the levels of AA are maintained through recycling of DHA to AA, a process which is largely glutathione dependent (May *et al*., 1995).

Overall, these results suggest there was an Nrf2-coordinated antioxidant response to oxidative stress induced by both triazole compounds in all tissues. In addition, the enrichment of *glutathione depletion* by 177 LLL, LVH and TSM (although not significant with TSM), suggests that a reduction in the glutathione levels may have contributed to oxidative stress due to 177. Glutathione depletion is particularly significant in mitochondria, because they do not have catalase and rely on glutathione to detoxify hydrogen peroxide (H_2O_2) (Mari *et al*., 2009). Thus, depletion of glutathione below a critical level favours H_2O_2 accumulation, which can trigger mitochondrial dysfunction, and eventually cell death (Begriche *et al*., 2011).

From the data it was not possible to hypothesise the precise mechanism of ROS generation by the triazole compounds. Xenobiotics induce ROS production through a variety of different mechanisms, including inhibition of the mitochondrial ETC, redox cycling and CYP uncoupling. Mitochondria are considered one of the main sources of ROS, where superoxide ($O_2^{\bullet-}$**)** is a byproduct of normal OXPHOS, primarily from complex I and III (Murphy, 2009). Moreover, mitochondrial DNA is a major target for ROS-induced cellular injury because it lacks protective structural proteins and also the DNA repair mechanism is less efficient in this organelle (Kumar *et al*., 2009). Thus, whatever the source of ROS, oxidative damage to mtDNA may result in alterations in ETC complexes, leading to further increase in the production of ROS, perpetuating the cycle of oxidative damage to mitochondria (Van Houten *et al*., 2006). Therefore, the enrichment of processes involved in oxidative stress and mitochondrial dysfunction by the triazoles are intrinsically linked, whether the mitochondria are the direct source of ROS, or a target for ROS. There are numerous examples of xenobiotics that induce both oxidative stress and mitochondrial dysfunction in a variety of tissues. For example, acetaminophen (APAP) toxicity results from the formation of a reactive metabolite (NADPQI), which damages cell structures, depletes glutathione leading to oxidative stress and inhibits mitochondrial functions. Significantly, APAP activates Nrf2 in rodent models and Nrf2 knockout mice have demonstrated that NRf2-mediated antioxidant proteins/enzymes are critical for protection against APAP-induced hepatotoxicity (Chan *et al.*, 2001).

The hypothesis that triazoles increase ROS levels and/or modifies antioxidant capacity provides a possible explanation for the difference in sensitivity of cardiac muscle, skeletal muscle and liver to triazole toxicity. It is well established that the antioxidant capacity of tissues differs and the intracellular concentrations of antioxidants can modify tissue susceptibility to toxicity. In rats, the order of antioxidant capacity has been determined as liver > heart > muscle (Venditti *et al*., 1998; Masuda *et al*., 2003; Katalinic *et al*., 2004), while susceptibility to oxidative stress is heart >muscle >liver (Venditti *et al*., 1998). Therefore, we can hypothesise that the increased antioxidant capacity of the liver makes it more resilient to triazoles-induced oxidative stress induced than striated muscle.

Altered energy metabolism

In response to triazole treatment, there was a profound enrichment of pathways relating to energy metabolism in all tissues. These changes were consistent with the effects on mitochondria, since in a majority of mammalian cells, mitochondria provide most of the energy necessary for cell homeostasis. Mitochondrial ATP synthesis is possible thanks to the oxidative degradation of endogenous substrates, such as , glucose, fatty acids (FA), and amino acids (Begriche *et al*, 2011). FA are oxidized in the mitochondrial matrix by the process of FA β-oxidation (FAO), whereas pyruvate (generated from glycolysis), is oxidized by the pyruvate-dehydrogenase (PDH) complex, localised in the inner mitochondrial membrane. Acetyl-CoA, derived from both pathways, enters the TCA cycle to produce reducing equivalents $FADH_2$ and NADH, which enter the ETC to drive the synthesis of ATP (figure 1.4). Treatment with 177 resulted in significant enrichment of the functional annotation term *fatty acid oxidation* by the LLL and the canonical pathway *valine degradation* by the TSM. Valine is degraded (metabolized) in the mitochondria, resulting in the production of succinyl-CoA, which is an important intermediate of the TCA cycle, thereby stimulating ATP production. There was enrichment of a number of energy metabolism related pathways and functional terms by 197 treated LLL (*fatty acid metabolism, fatty acid oxidation, response to glucose stimulus, glycolysis*), LVH (*fatty acid metabolism and β-oxidation I and glycolysis)* and TSM (*fatty acid metabolism, glycolysis / Gluconeogenesis, fatty acid β-oxidation*). Energy metabolism is tightly regulated by numerous regulatory systems, including the transcription factors peroxisome proliferator-activated receptors (PPARs) (Lefebvre *et al*., 2006). PPARα is the best characterised PPAR and has been shown to regulate lipid, amino acid and glucose metabolism in the liver, heart and skeletal muscle (Wang, 2010). PPARα achieves this by heterodimerizing with retinoid X receptors (RXR) and binding to the PPAR response elements to coordinate the expression of genes (Rakhshandehroo *et al*., 2010). IPA analysis highlighted the prominent role of PPAR signaling in response to triazole treatment, significantly enriching *PPAR signaling* in 177 TSM and *PPARα/RXRα activation* and *mechanism of gene regulation by PPARα* in all three 197 tissues. These results suggest that in response to 177 and 197 treatment, there was regulation of energy metabolism through PPARα coordinated transcriptional regulation. The

activation of PPARα is also a key player in the transcriptional regulation of mitochondrial biogenesis following mitochondrial damage. Peroxisome proliferator-activated receptor gamma co-activator (PGC-1α) is a transcriptional co-activator that is considered the master regulator in mitochondrial biogenesis (Ventura-Clapier *et al*., 2008). PGC-1 is enriched in tissues with high oxidative activity, like the heart and skeletal muscle, and functions to control the expression of genes involved in FAO, OXPHOS and antioxidant defences through a number of transcription factors, including PPARα, Nrf1, Nrf2 and ERRα (Scarpulla, 2008). PGC-1α cooperates with PPARα to regulate expression of mitochondrial FAO enzymes and transport proteins, thereby increasing the FAO pathway to coordinate with mitochondrial biogenesis. Nrf2 transcriptional activation not only plays an important role in antioxidant defence, as previously highlighted, but also regulates the expression of genes involved in mitochondrial bioenergetics (Kelly and Scarpulla, 2004). Additionally, Nrf2 regulates the mitochondrial transcription factor, Tfam, allowing coordination between mitochondrial and nuclear activation during mitochondrial biogenesis (Ventura-Clapier *et al*., 2008). In the same way Nrf-2 acts to coordinate both mitochondrial biogenesis and antioxidant defence, research has also shown the importance of PPARα in increasing antioxidant defence. For example Ibarra-Lara *et al* (2012) demonstrated how clofibrate-induced PPARα stimulation promotes an antioxidant environment, decreasing oxidative stress and preserves normal cardiac function despite myocardial infarction. Thus, the regulation of genes involved in PPARα and Nrf2 transcriptional responses suggests a concurrent regulation of energy metabolism, mitochondrial biogenesis and antioxidant defences to promote cell survival following mitochondrial dysfunction induced by 177 and 197 triazole treatment.

Cell cycle/DNA damage checkpoint

In all triazole treated tissues IPA analysis ranked the functions *cell cycle control* and *DNA replication, recombination and repair* as highly significant. Furthermore, there were a number of cell cycle and DNA damage related pathways and toxicity lists enriched by both triazoles. In 177 TSM the pathway *cell cycle regulation by BTG family proteins* was significantly enriched, which is a protein family that has been implicated in the G2/M DNA damage checkpoint (Doidge *et al*., 2012). Concurrently, the toxicity

list *cell cycle: G2/M DNA damage checkpoint regulation* was significantly enriched in both 197 LVH and TSM. In addition, the toxicity list *cell cycle: G1/S DNA damage checkpoint regulation* was significantly enriched in 197 LVH. Thus, these results strongly implicate DNA damage and cell cycle arrest in the toxicity of triazoles. One of the principal causes of DNA damage is ROS (Houtgraaf *et al*., 2006) and so we can hypothesise that oxidative stress induced by triazole treatment contributed to DNA damage in the tissues. DNA damage in terminally differentiated cells (such as skeletal muscle myotubes and cardiac myocytes) gives rise to DNA repair to ensure the integrity of the transcribed genome, whereas the induction of DNA damage in proliferating cells (such as skeletal muscle myoblasts and hepatocytes) results in the activation of cell cycle checkpoints. These checkpoints halt proliferation in order to give time to the DNA damage repair machinery to do its work (Latella *et al*., 2004). There are a number of DNA repair mechanisms, including base excision repair, nucleotide excision repair, mismatch repair and recombinational repair, whose activation is dependent on the type of DNA lesion (Houtgraaf *et al*., 2006). Indeed, the KEGG pathway *nucleotide excision repair* was significantly enriched in 197 TSM, which is the most important repair system to remove DNA lesions caused by ROS. Notably, this DNA repair mechanism is very active in terminally differentiated cardiac myocytes after DNA injury induced by irradiation (L'Ecuyer *et al*., 2006).

Protein Regulation

The most significant canonical and KEGG pathways enriched by 197 treatment in all tissues were related to protein regulation (homeostasis). Protein homeostasis refers to the equilibrium between translation of proteins, maintaining protein conformations, refolding misfolded proteins and removing damaged proteins (Conn and Qian, 2011). The canonical pathways *protein ubiquitination* and *eiF2 signaling* were highly significant in all 197 tissues. These pathways made up the top 2 pathways for LVH and TSM, which also significantly enriched *regulation of eiF4 and* p70S6K and *tRNA charging.* Complementary to this, the KEGG pathways *ribosome* and *proteasome* were significantly enriched by all 197 tissues and *aminoacyl-tRNA biosynthesis* by LVH and TSM. Similarly, KEGG analysis identified changes in protein homeostasis in response to 177, as shown by enrichment of *ribosome* by LLL and LVH and

proteasome by TSM. Overall, there was significant effects on pathways associated with translation of proteins (*eiF2 signaling, regulation of eiF4 and* p70S6K, *ribosome, aminoacyl-tRNA biosynthesis*) and removal of damaged proteins (*protein ubiquitination pathway* and *proteasome*) in response to both triazoles.

A central mechanism for translational control involves phosphorylation of the α subunit of eukaryotic initiation factor (eiF2) (eIF2~P), which represses the initiation phase of protein synthesis, allowing cells to conserve energy resources. Selective translation of a subset of mRNAs continues, however, constituting the integrated stress response (ISR), which is adopted to prevent stress damage (Baird and Wek, 2012). The phosphorylation of eiF2 is accomplished by 4 different kinases that each monitor different exogenous and endogenous stresses. These include PKR-like endoplasmic reticulum kinase (PERK), which responds to perturbations in the endoplasmic reticulum (ER) (ER stress); GCN2, an eIF2a kinase induced in response to nutritional stresses; protein kinase R (PKR), which participates in an antiviral defence pathway involving interferon and heme-regulated eIF2a kinase (HRI) , which is activated by heme deprivation in erythroid cells and oxidative stress (Baird and Wek, 2012). Significantly, studies have demonstrated that arsenite mediates phosphorylation of eIF2 through HRI in erythroid cells and that HRI is activated by arsenite-induced ROS (oxidative stress) (Lu *et al*., 2001). Scrutiny of the genes affected in the eiF2 pathway by 197, identified that HRI was activated, whereas the other eiF2 kinases were unaffected. Thus, we can hypothesise that 197, like arsenite, phosphorylated eiF2 through an oxidative stress-induced HRI mechanism. Research by Tan *et al* (2001) has also demonstrated that eiF2 is a critical regulatory factor in response to oxidative stress through the control of the major intracellular antioxidant, GSH.

Two other pathways that play critical roles in translational regulation are p70S6K and eiF4, which were both enriched by 197 LVH and TSM. In contrast to eiF2, these regulators are involved in translation initiation (Sun *et al*., 2005). p70S6K regulates protein synthesis by activating 40S ribosomal protein S6, leading to an increased rate of translation of the class of 5'TOP mRNA transcripts, which encode for ribosomal

proteins and elongation-factor-1 thereby contributing to ribosomal biogenesis (Kawasome *et al*., 1998). This may explain why there was a significant enrichment of the ribosome pathways in the triazole gene lists. Since the p70S6k pathway is critical in the control of protein synthesis, it is essential in the development of cardiac and skeletal muscle hypertrophy (Bodine *et al.*, 2001; Boluyt *et al*., 2004). Given the important role of hypertrophy following cardiac and skeletal muscle damage, it is unsurprising that *regulation of eiF4 and p70S6K signalling* was significantly enriched by 197 LVH and TSM.

Protein homeostasis is not only regulated through protein synthesis, but also by protein degradation. Protein degradation is crucial because it prevents the accumulation of potentially toxic damaged or abnormal proteins. In response to triazole treatment *protein ubiquitination* and *proteasome* pathways were significantly enriched, which implicates activation of the ubiquitin-proteasome pathway (UPP) in response to damaged proteins. The UPP involves covalent attachment of ubiquitin to protein substrates followed by degradation of ubiquitin-tagged protein by the 26S proteasome (Glickman and Ciechanover, 2002). One of the major causes of protein damage is oxidation by ROS and it is well documented that the UPP selectively degrades oxidatively modified proteins (Shang and Taylor, 2011). This therefore supports the ongoing hypothesis that oxidative stress plays an important role in the toxicity of triazoles.

Stress response signaling pathways, cell survival and cell death

In conditions of stress, cells mount protective responses to counteract the effect of stress on cellular processes. If the stress remains unresolved, eventual death ensues. Treatment with the triazoles resulted in clear stress responses relating to oxidative stress (Nrf-2 antioxidant defence), energy metabolism (PPARα signaling), mitochondrial dysfunction (PPARα and Nrf2 mitochondrial biogenesis), DNA damage (DNA repair and cell cycle arrest) and protein regulation (protein synthesis and degradation). In addition, there were a number of stress response signaling pathways enriched by the triazoles, including *Wnt signaling (*177 LVH), *VEGF signaling* (177 LLL), *ERK/MAPK signaling (*177 LLL), *PTEN signaling* (197 LLL and TSM), *HIF signaling* (197

LLL and TSM). Enrichment of these pathways provides further evidence for the mechanistic hypotheses of triazole toxicity. For example, the Wnt pathway plays a pivotal role in cardiac remodelling and hypertrophy (Bergmann, 2010) and VEGF signaling is important in coordinating mitochondrial biogenesis through activation of the serine/threonine kinase Akt3 (Wright *et al*., 2008). Notably, there was a considerably greater stress response by 197 than 177, which was highlighted by the 'common 197 genes' canonical pathways; *mTOR signaling, P13K/AKT signaling*, *HIF signaling, Regulation of eiF4 and p70S6k signaling* and *eiF2 signaling*. Of these pathways, the P13/AKT/mTOR pathway plays a central role in regulating critical processes such as cell survival and growth. One of the most established roles of this pathway is the control of translation and hypertrophy, which it does by mediating the eiF4 and p70S6K pathways (Nader *et al*., 2005). This pathway also plays an important role in a number of other processes, including autophagy, lipid synthesis, mitochondrial metabolism and mitochondrial biogenesis (Dowling *et al*., 2010). In this respect, the PI3K/Akt/mTOR/p70S6K pathways also play a major role in the protection against oxidative stress-induced apoptosis (Faghiri and Bazan, 2010).

The outcome of these stress responses is in the balance between cell survival and cell death, which is dependent on the level and mode of stress and the prosurvival strategies that are mounted (Fulda *et al*, 2010). Since the concentrations of 177 and 197 used in this study were relatively non-toxic (in terms of histopathology), the stress responses here tip in the balance of prosurvival. However, there was enrichment of cell death related functional annotation terms in 177 LVH (*caspase-mediated apoptosis*) and 197 TSM and LVH (*programmed cell death, apoptosis, regulation of apoptosis*). From this we can hypothesise that the cell death endpoint of triazole treatment is possibly a caspase-mediated apoptotic form of programmed cell death. There are two main apoptotic pathways; the extrinsic or death receptor pathway and the intrinsic or mitochondrial pathway (Elmore, 2007). Although we cannot we cannot discern the exact pathway of apoptosis from this data, given the level mitochondrial dysfunction enrichment, we can speculate on the intrinsic/mitochondrial pathway being the key apoptotic pathway mediating triazole toxicity. Specifically, the enrichment of the toxicity list *mitochondrial swelling* by 177 LLL provided evidence for

the intrinsic pathway. Mitochondrial swelling is a mechanism by which cytochrome c and apoptosis inducing factors (AIF) are released, which are both hallmarks of the intrinsic/mitochondrial apoptotic pathway (Petit *et al.*, 1998).

Neurodegenerative disease enrichment – providing an insight into triazole mechanisms

The enrichment of neurological diseases (*Alzheimer's, Parkinson's and Huntington's disease*) by KEGG analysis of 177 TSM and 197 LLL, LVH and TSM provided further evidence for triazole-induced mitochondrial dysfunction and oxidative stress. These neurological diseases are characterised by prominent neurodegeneration in selective neural systems and there is substantial evidence that mitochondrial dysfunction plays a key role in their pathogenesis (Schon and Przedborski, 2011). Defects in almost all aspects of mitochondrial function have been implicated in these neurodegenerative diseases, including changes to; mitochondrial DNA, mitochondrial dynamics, Ca^{2+} homeostasis, ROS production and mitochondrial bioenergetics (OXPHOS) (Yan *et al*., 2013; Subramaniam and Chesselet, 2013).

3.5.6.6 Potential mechanisms of SI phenyl (907) toxicity

Functional analysis was only carried out on the LLL DEG list because there was no striated muscle toxicity observed with 907 treatment. The effects of 907 on LLL gene expression related to cholesterol biosynthesis, amino acid metabolism, xenobiotic metabolism and stress response signaling. The most significantly enriched pathway was cholesterol biosynthesis, which accounted for the top 5 canonical pathways (*Cholesterol biosynthesis I, II, III, superpathway of cholesterol biosynthesis and zymosterol biosynthesis*), the top KEGG pathway (*steroid biosynthesis*) and the top functional clusters (*steroid/cholesterol biosynthesis*). Cholesterol plays several structural (e.g. major component of plasma membrane) and metabolic (e.g. precursor for bile acids, steroids) roles that are vital for biology and so deregulation of cholesterol homeostasis is likely to manifest unwanted toxicity (Trapani *et al*., 2012). Significantly, the liver is the principal site of cholesterol maintenance and a range of compounds are known to cause hepatotoxicity through cholesterol perturbation, including, perfluorinated chemicals (Martin *et al*., 2007), anticonvulsants (Lee *et al*.,

2006), 5-HT6 receptor antagonists (Suter *et al*., 2003) and statins (MacDonald and Halleck, 2004). Perhaps the best example is the statins, whose pharmacological mechanism is to inhibit the production of cholesterol by targeting the enzyme HMG CoA reductases, the rate-limiting step in the biosynthesis of cholesterol (MacDonald and Halleck, 2004). The adverse toxicity of statins is thought to derive as an exaggeration of the desired pharmacological mechanism. By inhibiting HMG CoA reductases, statins deplete secondary metabolic intermediates formed during cholesterol synthesis. For example, the enzyme ubiquinone, which assists in oxidative phosphorylation, becomes deficient following statin treatment, resulting in mitochondrial dysfunction (Jamal, 2004). As well as hepatotoxicity, two other adverse effects are common to statins; hyperplasia, hyperkeratosis and submucosal edema in the squamous epithelium of the non-glandular stomach and testicular changes (MacDonald and Halleck, 2004). Along with liver hypertrophy and necrosis, both of these were adverse affects of 907 treatment (at the highest concentrations) (section 1.5.2.3). Significantly, cholesterol and liver biomarkers ALT, AST and GLDH were increased in the serum of 907 treated rats, further implicating adverse liver and cholesterol functions. Therefore, based on both the toxicogenomic and pathology data we can hypothesise that deregulation of cholesterol homeostasis is a key toxicity mechanism of 907.

3.5.6.7 Potential effects of absorption, distribution, metabolism and excretion (ADME) properties on SI compound toxicity

Amongst the most significantly enriched processes in the 177, 197 and 907 LLL DEG lists was xenobiotic metabolism. Xenobiotic metabolism is required for the metabolism, elimination and/or detoxification of xenobiotics (Xu *et al*., 2005). This is achieved by a number of xenobiotic metabolizing enzymes (XMEs), which include phase I (oxidation, reduction and hydrolysis reactions) and Phase II (conjugation reactions) metabolizing enzymes, as well as phase III transporters (Omiecinski *et al*., 2011). In response to SI compound treatment there was enrichment of a number of xenobiotic metabolism pathways in the LLL, including glutathione phase II reactions (177, 197, 907) and Phase I CYP450 (177, 197, 907), as well as the transcription factor *aryl hydrocarbon receptor (AhR) signaling*. The enrichment of this transcription factor

is important since it coordinates the regulation of a set of xenobiotic-metabolising enzymes, termed the AhR battery (Kohle and Bock, 2007). Although the general purpose of xenobiotic metabolism is detoxification, metabolites with a higher potential for toxicity than the parent compound can be formed, in a process termed bioactivation (Dekant, 2009). It is therefore possible that metabolism, whether it was phase I or phase II reactions, could have either detoxified or bioactivated the SI compounds. If the compounds were bioactivated, then it may have been reactive metabolites that were responsible for their toxicity. For instance, glutathione conjugation of the triazole compounds could have produced a reactive metabolite that inhibits the ETC, resulting in mitochondrial dysfunction. Although the liver has the greatest capacity to metabolize compounds, extrahepatic tissues, such as the heart and skeletal muscle, also have the capacity to metabolise xenobiotics. In this way, extrahepatic metabolism may determine local exposure to xenobiotics/reactive metabolites and thus influence their resultant toxicological effects in peripheral tissues (Pavek and Dvorak, 2008). In this study, there was evidence of extrahepatic xenobiotic metabolism, with enrichment of *glutathione phase II reactions* and *AhR signaling* in the 177 LVH (although glutathione enrichment could have been related to antioxidant effects). Thus, the ADME properties of each compound in the whole body and each tissue may have be an important factor in the target organ of toxicity and the severity of the toxicity of each compound. For example, the stomach toxicity witnessed after high doses of 907 may have been due to the high local concentration of the compound in the stomach since gavage was the method of administration. Equally, the mechanism of action of each compound may be important in the determination of the target organ of toxicity. For example, we hypothesise that mitochondrial dysfunction plays a major role in triazole toxicity and given that cardiac and skeletal muscle are amongst the most metabolically active tissues, they have a large amount of mitochondria, making them particularly vulnerable to mitochondrial toxicants (Neustadt and Pieczenik, 2008). This may therefore explain why striated muscles were particularly sensitive to triazole treatment.

3.6 Conclusions

- Pearson's rank correlation and clustering analysis demonstrated that high quality and reproducible gene expression profiles were obtained for LLL, LVH and TSM tissues from female rats treated with 177, 197 and 907 for 28 days.

- The magnitude of gene expression changes found with 177, 197 and 907 in the LLL, LVH and TSM did not always correlate with the observed changes found with traditional endpoints (i.e. histopathology and blood chemistry), which may have been because:
  - Timing of gene expression changes were different for 177, 197 and 907 after 28 days repeat dose treatment.
  - The magnitude of transcriptional response of tissues may differ.
  - Treatment of sub-toxic doses of 177 and 907 after 28 days resulted in modest gene expression changes.

- Functional analysis provided hypotheses on the mechanisms of 177, 197 and 907 toxicity:
  - The results suggest that deregulation of cholesterol homeostasis was the key toxicity mechanism of 907, which correlated well with the observed histopathology.
  - The triazoles, 177 and 197, had a considerable amount of overlap of biological processes between LLL, LVH and TSM, suggesting a common non-tissue specific mechanism of toxicity. These biological processes included mitochondrial dysfunction, oxidative stress, altered energy metabolism, cell death and survival (stress response) signalling, protein regulation and cell cycle/DNA damage response.
  - Mechanistic analysis was therefore able to differentiate the triazoles and phenyl compounds based on the differential biological processes effected. In addition, it provided hypotheses on the reasons for differential tissue toxicity.

CHAPTER FOUR

Assessment of the translation of SI compound toxicity from an *in vivo* to an *in vitro* model

Chapter 4: Assessment of the translation of SI compound toxicity from an *in vivo* to an *in vitro* model

4.1 Introduction

In chapter 3, toxicogenomics identified clear class differences between the mechanisms of toxic action of SI triazoles and the SI phenyl. The triazoles (177 and 197) both induced a similar toxicity profile in all three tissues (LLL, LVH and TSM) indicative of a common non-tissue specific mechanism of toxicity. The traditional endpoints (histopathology and clinical chemistry) did, however, identify striated muscle as more sensitive than the liver to triazole toxicity, making cardiac and skeletal muscle the primary toxicity targets. The hypothesised triazole toxicity mechanisms consisted of; mitochondrial dysfunction, oxidative stress, altered energy metabolism, cell cycle arrest, hypertrophy (protein homeostasis) and apoptosis (cell death signalling). In contrast, the phenyl compound (907) was toxic to liver, stomach and testes, but not to striated muscle (as shown by histopathology and clinical chemistry) and the hypothesised mechanism of liver toxicity was related to deregulation of cholesterol homeostasis.

4.1.1 A shift in the toxicity testing paradigm from *in vivo*-centred to *in vitro* testing

Despite the success of *in vivo* toxicogenomics for identification of toxicity mechanisms, the *in vivo* model is low-throughput, costly, requires a lot of resources and relies on animal testing. Therefore, there has been a shift in the testing paradigm towards high-throughput predictive *in vitro* models that accurately mimic the effects *in vivo* and allow for detection of potential toxicities early in the R&D process. Although not designed as an "alternative to animal testing," *in vitro* toxicity testing would provide the toxicity data to prioritize compound selection for *in vivo* testing, thereby reducing the use of animals in research (Andersen and Krewski, 2009). Amongst the many important areas for concern in R&D of xenobiotics is the potential for toxicities of the major organ systems. Although hepatotoxicity and cardiotoxicity are the main causes of xenobiotic attrition (MacDonald and Robertson, 2009), skeletal muscle toxicity has become an area of interest given the propensity of xenobiotics to induce such toxicities. In the pharmaceutical industry, the potential for skeletal muscle toxicity was

highlighted by the withdrawal of Cerivastatin in 2001, due to rhabdomyolysis, a potentially fatal deleterious injury to skeletal muscle (Charaten, 2001). Consequently, there has been an increased effort in toxicology to develop and validate new approaches to risk assessment.

4.1.2 Approaches to *in vitro* toxicity testing

The current *in vitro* approaches in toxicity testing consist of assays for general or cell-type-specific cytotoxicity, genotoxicity, biochemical endpoints (e.g. ion channel block), and metabolite mediated toxicity (Kramer *et al*., 2007). Of these, cytotoxicity assays are the earliest to be conducted and consist of measurement of xenobiotic effects on cell cultures using either single or multiple endpoints (Lin and Will, 2012). One approach has been the use of organ-specific cell lines to predict *in vivo* organ toxicities. In this respect, it may be that variations in the antioxidant capacity, mitochondrial capacity or expression of enzymes/proteins of different tissue cell-types may determine differential susceptibility to certain compounds. In recent years, a number of studies have investigated the feasibility of organ-specific cell lines to predict cardio-, hepato- and nephro-toxicities (Inoue *et al*., 2007; Li *et al*., 2004; Zhang *et al*., 2007; Xia *et al*., 2008, Lin and Will, 2012). For example, Xia *et al* (2008) tested 1408 compounds in 13 human and rodent cell lines from six common targets of xenobiotic toxicity (liver, blood, kidney, nerve, lung and skin) and found that some compounds were cytotoxic to all cells at similar concentrations, whereas others exhibited cell type specific cytotoxicity. To date, most of the progress with predictive *in vitro* testing has been with hepatotoxicity (Dere *et al*., 2006; O'Brien *et al*., 2006; Kienhuis *et al*., 2009), with more limited efforts towards cardiotoxicity (Zhang *et al.,*2007; Lin and Will, 2012) and none towards skeletal muscle toxicity. Notably, the author has not found any studies that have investigated the utility of skeletal muscle cell lines for *in vitro* skeletal muscle toxicity testing.

4.1.3 Validation of *in vitro* systems to accurately predict *in vivo* outcomes

One of the most important scientific challenges of *in vitro* toxicity testing is extrapolation of *in vitro* results to the *in vivo* situation. It is therefore important that *in vitro* models are well validated for accurate prediction of *in vivo* outcomes. To address

the issue of validation, toxicogenomics technology has been employed to assess the ability of *in vitro* models to accurately mimic certain *in vivo* responses (Kienhuis *et al*., 2006; Blomme *et al*., 2009). As detailed in chapter 3, toxicogenomics has been successfully applied to identify toxicant-induced perturbations of cellular pathways (toxicity pathways) that are indicative of the mechanism of toxicity of a xenobiotic both *in vivo* and *in vitro*. Since the incorporation of this technology for mechanistic studies, a number of studies have compared *in vitro* and *in vivo* toxicant-induced toxicogenomics responses to assess the correlation between the two systems (Kienhuis *et al*., 2006 and 2009; Dere *et al*., 2006; Boess *et al*., 2007; Jo *et al*., 2012). The overall conclusion from these studies was that comparison at the level of pathway analysis is more effective than single gene analysis. This is the same logic that was employed to compare toxicity pathways between the different SI compounds in chapter 3 and is based on the idea that even though individual differentially expressed genes may differ, they may share a similar biology. Thus, pathway analysis allows translation of these genes to a common and therefore easy to compare vocabulary (Kienhuis *et al*., 2009). A majority of these studies have been carried out for assessment of *in vitro* hepatotoxicity. For example, Kienhuis *et al* (2009) compared rat hepatocytes *in vitro* and rats *in vivo* treated with acetaminophen (APAP) using toxicogenomics. They found that six biological pathways and processes were enriched by both models, which related to effects on energy metabolism and mitochondrial dysfunction, which support the hypothesis on APAP hepatotoxicity (Kienhuis *et al*., 2009). Another study, by Boess *et al* (2007) compared the effects of two 5-HT6 receptor antagonists between rats *in vivo* and rat hepatocytes *in vitro* using gene expression and biochemical endpoints. Their results showed that the hepatotoxic potential of the two compounds could be assessed *in vitro* using biochemical endpoints as well as toxicogenomics.

Overall, the results of these studies suggest that the comparison between *in vivo* and *in vitro* models can be determined by comparison of cellular biochemical processes, without the need for toxicogenomics in both systems. We therefore propose to validate the utility of an *in vitro* skeletal muscle system to detect *in vivo* responses by investigating key cellular processes that were highlighted *in vivo*, by toxicogenomics,

in vitro, using cytotoxic endpoints. This method bypasses the need to carry out toxicogenomics studies *in vitro* and also validates the findings of the *in vivo* toxicogenomics study.

4.2 Overall aim and hypothesis

The overall aim of this chapter was to compare the toxicity pathways of SI triazoles, identified using *in vivo* rat toxicogenomics, with responses to SI triazoles in a skeletal muscle *in vitro* model. It was hypothesised that the toxicity pathways identified by *in vivo* gene expression analysis would extrapolate to the *in vitro* model, thereby validating the *in vitro* model to predict *in vivo* outcomes.

Specific aims

- To determine the utility of cardiac muscle (H9c2), skeletal muscle (L6) and liver (HepG2) cell lines to detect SI compound target organ toxicities. Given the prior knowledge on SI compound organ toxicities, it was hypothesised that triazole toxicity would be detected more sensitively by L6 and H9c2 cells, whereas 907 toxicity would be more sensitively detected by HepG2 cell lines.

- To investigate the translation of the *in vivo* triazole toxicity pathways, identified by *in vivo* toxicogenomics, into the L6 *in vitro* model. In doing this, we are both validating the L6 *in vitro* model to predict *in vivo* outcomes and validating the findings of the *in vivo* toxicogenomics data. Specifically, the following toxicity pathways will be assessed in L6 skeletal muscle cells:
    - Mitochondrial function
    - Mitochondrial and cytosolic superoxide generation (oxidative stress)
    - Cell death
    - Cell cycle analysis
    - Hypertrophy

4.3 Experimental Approach

4.3.1 Cell culture

L6, H9c2 and HepG2 cell lines were cultured in DMEM containing 25mM glucose (high glucose), 1mM sodium pyruvate, supplemented with 5mM HEPES, 10% FBS, and penicillin-streptomycin and kept in 5% CO_2 at 37^{o}C (section 2.2.7.1). Cells were maintained in T.75 flasks and were subcultured at 70% confluence by trypsinization. Cell counts were performed using a haemocytometer and cells were seeded onto 96-well and 6-well plates for experiments (section 2.2.7.2). L6, H9c2 and HepG2 cell lines were used between passages 6-23, 10-30 and 1-30, respectively. All experiments were performed in 5% CO_2 at 37^{o}C, unless otherwise stated.

4.3.2 Compound preparation

All commercially available compounds were prepared in their respective solvents and stored as indicated in section 2.2.7.2. The SI compounds were soluble in DMSO and so stock concentrations of 100mM were made and stored at -20^{o}C. Fresh stocks were made every two months to account for potential degradation of the compounds. Since the SI compounds had not been used in cell culture preparations before, the maximum soluble concentration in culture media was first determined. Doubling dilutions were made from starting concentrations of 1mM 177, 197 and 907 in 96-well (200µl) and 6-well (2000µl) plates and incubated for 24 hours at 37^{o}C. Solubility was assessed by microscopy as precipitation of the compounds, in crystalline form, in the media. The maximum soluble concentration of 907, 197 and 177 in a 96-well plate was 100, 200 and 500µM and in a 6-well was 100, 100 and 500 µM, respectively.

4.3.3 Cell Viability Assays

Two assays were carried out to assess cell viability; CCK-8 assay and ATP determination kit, as described in section 2.2.8. For the CCK-8 assay, clear 96-well plates were seeded at a density of $5x10^3$ cells/well for L6, $7.5x10^3$ cells/well for H9c2 and $2x10^4$ cells/well for HepG2. For the ATP assay, white 96-well microplates with clear bases were seeded at a density of $1x10^4$ cells/well for L6, $7.5x10^3$ cells/well for

H9c2 and $1x10^4$ cells/well for HepG2. The cells were incubated for 24 hours, by which point the cells were ~70-80% confluent and ready for treatments:

Dose responses for SI compounds: Stock concentrations for each compound were prepared in DMSO at 100x highest aqueous soluble treatment concentration for each SI compound, equating to 50mM (500µM), 20mM (200µM) and 10mM (100µM) for 177, 197 and 907, respectively. In a clear 96-well plate (compound plate), 8 doses of each compound were prepared using a 2-fold dilution scheme. For 177, the doubling dilutions were made from 40mM so the concentrations were comparable with 197 and 907, although an additional treatment of 500µM was prepared from a 50mM stock. A 1:100 dilution for each compound was made in a high-glucose-containing growth media to obtain 1 x compound dilutions for the immediate treatment of cells. The media was removed from the cell plates and 100µl of compound/media mixture was dispensed into each well. This method ensured an equal volume of DMSO in each well, resulting in a final DMSO concentration of 1%. DMSO titrations were performed at 5, 4, 3, 2, 1, 0.5 and 0.1% concentrations. DMSO at $\leq$2% did not affect viability of L6 or H9c2 (data not shown). The final compound concentration ranges were 500µM - 6.25µM, 200µM –1.56 µM and 100µM-0.78µM for 177, 197 and 907, respectively. The cells were incubated for 24 hours and the CCK-8 and ATP assays were carried out as described in section 2.2.8.

Time courses for L6 treatment with triazoles: A time course was carried out with the highest soluble concentration of 177 and 197 alongside a positive control, Antimycin A, in L6 cells. Cells were treated with 500µM 177, 200µM 197 or 100nM Antimycin A for 2, 4, 16 and 24 hours and analysed with the CCK-8 and ATP assays, as detailed in section 2.2.8.

Antioxidant experiments using NAC in L6 cultures: With L6 cells, an NAC dose response was carried out with 8 doses in a 2-fold dilution scheme ranging from 5-0.03mM for 24 hours. Cell viability was assessed using the ATP assay as described in section 2.2.8.2. Pre-treatments with 0.625, 1.25 and 2.5mM NAC were made 3 hours

prior to treatments with 177 (400, 200, 100 and 50µM) and 197 (200, 100, 50 and 25µM) in L6 cells for 24 hours.

4.3.4 Measurement of cell death

4.3.4.1 Annexin V/PI assay

To assess apoptosis quantitatively, an annexin V/PI staining assay was performed with flow cytometry as described in section 2.2.9.1. L6 cells were seeded at $2x10^5$ cells/well in 6-well plates and incubated for 24 hours, by which point the cells were ~70-80% confluent. The cells were treated for 24 hours with 177 (50, 100, 200, 400 and 500µM), 197 (12.5, 25, 50 and 100µM) and positive controls staurosporine (250nM) and H_2O_2 (2mM). Cells were determined as viable (annexin V and PI negative), early apoptotic (annexin V positive and PI negative) or late apoptotic (annexin V and PI positive) as illustrated in figure 4.1. The apoptotic rate was calculated as the percentage of early and late apoptotic cells.

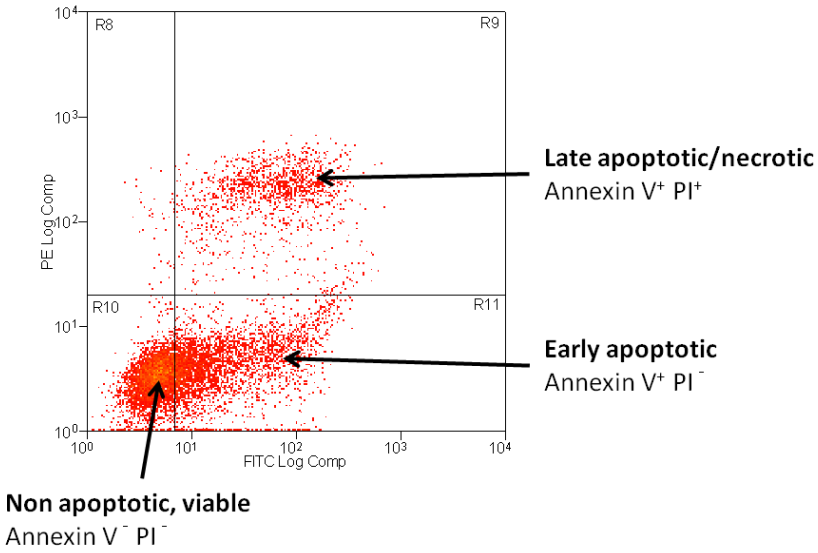

Figure 4.1 Example of flow cytometric scatter-gram of Annexin V/PI stained L6 cells. L6 cells were treated with Staurosporine (250nM), an apoptosis inducer, for 24 hours at 37°C. The quadrant can be divided into three distinct cell populations marked as: annexin V and PI negative corresponding to viable, non apoptotic cells (bottom left quadrant), annexin V positive PI negative corresponding to early apoptotic (bottom right quadrant) and annexin V and PI positive corresponding to late apoptotic/necrotic (top right quadrant). The position of the quadrant gate on the X-axis was based on the position of the control population, in which 95% of the control population was included in the bottom left (non-apoptotic quadrant). The position of the quadrant on the Y-axis was determined by the position of the early apoptotic population, dividing the transition between the early and late apoptotic populations.

4.3.4.2 Caspase 3/7 activity

Caspase 3/7 activation in L6 cells was assessed to determine the induction of apoptosis signaling pathways following treatment with 177 and 197, using the Caspase-Glo® 3/7 assay. Cells were seeded at $1x10^4$ cells/well in white 96-well microplates with clear bases and incubated for 24 hours to ~70-80% confluence. Cells were treated with a concentration range of 177 (500, 250, 125 and 62.5µM) and 197 (200, 100, 50 and 25µM) for 2, 4, 16 and 24 hours. Staurosporine (250nM) was included as a positive control for caspase3/7-induced apoptosis. The caspase 3/7 assay was carried out as described in section 2.2.9.2.

4.3.5 Cell cycle analysis

To analyse the cell cycle, DNA content was measured using PI staining. In this protocol, ethanol (EtOH) was used to fix and permeabilize the cells to make them accessible to PI. L6 cells were seeded at $2x10^5$ cells/well in 6-well plates and incubated for 24 hours to ~70-80% confluence. Cells were treated with 177 (100 and 200µM), 197 (50 and 100µM) and H_2O_2 (250 and 500µM) for 24 hours. To assess if the cell cycle was progressing, the cells were co-treated with nocodazole (132nM) 4 hours following initiating treatment with SI triazoles and controls (20 hours nocodazole exposure). Flow cytometric cell cycle analysis was then performed as described in section 2.2.10.

4.3.6 Measurement of cell size - hypertrophy

L6 cells were seeded with $2x10^5$ cells/well in 6-well plates and incubated for 24 hours to grow cells to ~70-80% confluence. Cells were treated with 177 (100 and 200µM) and 197 (50 and 100µM) for 24 hours and analysed by flow cytometry as detailed in section 2.2.11. Cell size was determined by the forward light scatter of cell populations gated on the G1 cell population. It was important to gate on the G1 population of cells since the mean size of cells changes throughout the cell cycle, increasing as cells progress to G2 (Monkawa *et al*., 2002).

4.3.7 ROS measurements – MitoSox and Dihydroethidium (DHE) detection of mitochondrial and cytosolic superoxide in L6 cells

Intracellular cytosolic- and mitochondrial- derived superoxide production was determined using DHE and MitoSox, respectively. L6 cells were seeded with $2x10^5$ cells/well in 6-well plates and incubated for 24 hours. Treatments with 177 (200 and 400µM), 197 (50 and 100µM) and Antimycin A (100µM) were for 1 and 24 hours and MitoSox and DHE fluorescence was detected by flow cytometry, as described in section 2.2.12. Further MitoSox dose responses were carried out with 177 (50, 100, 200, 400 and 500µM) and 197 (6.25, 12.5, 25, 50 and 100 µM) for 24 hours and analysed as detailed in section 2.2.12. Pre-treatments with NAC were carried out for 3 hours prior to 24 hour co- treatment with 177 (100, 200 and 400µM) and 197 (100µM) and analysis was carried out with MitoSox, as described in section 2.2.12.

4.4 Results

4.4.1 Effect of SI compounds on cell viability

4.4.1.1 Detection of SI triazole and phenyl target organ toxicities using organ-specific cell lines

Three cell lines of different target tissue origin, namely HepG2 (human hepatocellular carcinoma), H9c2 (rat embryonic myocardium) and L6 (rat skeletal muscle myoblast) were utilized to investigate SI compound cytotoxicity. Because of the observed toxicities of triazoles and phenyls towards striated muscle and liver, it was suggested that L6 and H9c2 cells might be more suitable for detecting triazole toxicity and conversely, HepG2 cells might be more suitable for detecting phenyl toxicity. Each cell type was treated with a range of concentrations of each SI compound for 24 hours and cell viability was evaluated using the CCK-8 assay. The highest concentration employed for each SI compound was determined by the maximum concentration that each compound was soluble in culture media. The CCK-8 assay was used as a general marker of cell viability and is based on the reduction of WST-8 by dehydrogenase activity, in the presence of an electron carrier, to an orange formazan product. The ability of cells to reduce WST-8 can be interpreted as a measure of cell number, proliferation, viability and/or cytotoxicity depending on the design of the experiment.

As shown in figure 4.2, the triazoles (177 and 197) dose-dependently decreased cell viability in all three cell lines. However, L6 and H9c2 cell viability was decreased significantly more than HepG2 cell viability at concentrations of 177 $\geq$ 200µM and 197$\geq$100µM (figure 4.2 D and E). Triazoles reduced L6 cell viability to a greater extent than H9c2 cells, suggesting L6 was the more sensitive to 177 and 197. However, this difference did not reach statistical significance. At concentrations $\geq$50µM, 197 reduced L6 and H9c2 cell viability significantly more than 177, indicating 197 was the more potent of the two triazoles (figure 4.2 A and B). In contrast to the triazoles, 907 had no significant effect on L6 and H9c2 cell viability, but significantly decreased HepG2 cell viability at concentrations $\geq$ 12.5µM (figure 4.2 F). Consequently, 177 and 197 reduced L6 and H9c2 cell viability more significantly than 907 at concentrations $\geq$50µM (figure 4.2 A and B). All three compounds had similar effects on HepG2 cell viability, although

at concentrations of 12.5, 25 and 50µM, 197 and 907 reduced cell viability significantly more than 177 (figure 4.2 C).

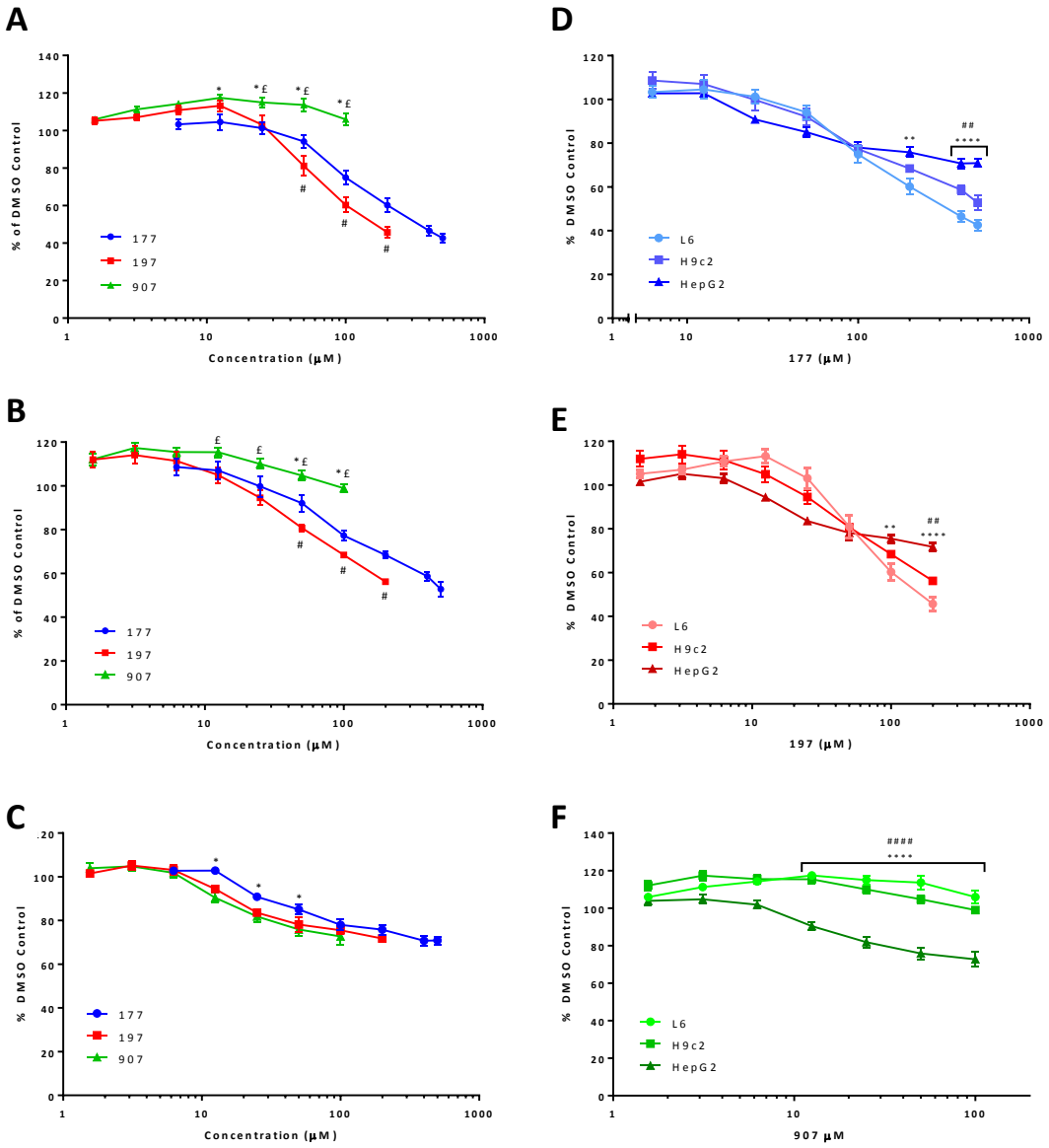

Figure 4.2 Effect of SI compounds on L6, H9c2 and HepG2 cell viability. (A-C) The L6 **(A)**, H9c2 **(B)** and HepG2 **(C)** cell lines were treated with a range of 177, 197 and 907 concentrations for 24 hours. Cell viability was determined with the CCK-8 assay relative to the DMSO control group. Results represent the mean ±SEM; n=5-7 (*P<0.05 177 vs. 907, #P<0.05 177 vs. 197 and £P<0.05 197 vs. 907). **D-E,** The effects of 177 **(D)**, 197 **(E)** and 907 **(F)** on L6, H9c2 and HepG2 cell viability were compared. (**P<0.01, ****P<0.0001 L6 vs. HepG2; ##P<0.01, ####P<0.0001 H9c2 vs. HepG2).

Due to the solubility of the compounds, it was not possible to produce a complete dose response and calculate absolute IC50 values. However, a nonlinear regression

could be fit to the 177 and 197 data, providing an estimated IC50 value (table 4.1). The estimated IC50 values provided further evidence for the differential sensitivities of the cell lines and the triazole compounds. In all three cell lines 197 had a lower IC50 than 177 and L6 and H9c2 cells had lower IC50 values than HepG2 cells with both triazoles. Previous studies have suggested that the difference between IC50 values of cell lines is a good measure of a compounds target organ toxicity (Inoue *et al*., 2007). The difference between the IC50 values of each cell line were calculated as an IC50 ratio to provide a quantitative comparison. The triazole IC50 ratios of HepG2 to L6 and H9c2 were >2, while the ratio of H9c2 to L6 was <1.5.

	IC50 (µM)			IC50 Ratio		
	L6	**H9c2**	**HepG2**	**H9c2:L6**	**HepG2:L6**	**HepG2:H9c2**
177	320.8	487.4	1622	1.5	5.05	3.32
197	149	204.6	541.6	1.3	3.6	2.65

Table 4.1 IC50 values for 177 and 197 in L6, H9c2 and HepG2 cell lines. A nonlinear regression was fit to the 177 and 197 dose response curves in L6, H9c2 and HepG2 cell lines. Maximum (DMSO control) and minimum values (total cell kill) were fixed. The IC50 ratio between cell lines was calculated; H9c2/L6, HepG2/L6 and HepG2/H9c2.

4.4.2 Effect of SI triazoles on mitochondrial function

Toxicogenomics analysis identified pathways relating to mitochondrial dysfunction as amongst the most affected following triazole treatment *in vivo* (section 3.5.6.5). Therefore, a simple, high-throughput assay was employed to address this hypothesis *in vitro*. The quantitation of ATP is commonly used as an index of cell proliferation and viability. However, when used in conjunction with another marker of cell viability, ATP content can be used to assess the effects of treatment on cellular bioenergetics and mitochondrial function. ATP synthesis is tightly regulated in a mammalian cell and so any compound that produces specific mitochondrial toxicity will reduce ATP concentrations before a loss of cell viability or induction of cytotoxicity is detected (Tirmenstein *et al*., 2002; Mingatto *et al*., 2002).

In this study, the effects on CCK-8 (cell viability) and ATP content were compared to assess mitochondrial function following treatment. Initial experiments were carried out with a classic mitochondrial toxin, antimycin A (AMA), to assess the utility of the CCK-8/ATP assay to detect mitochondrial dysfunction in L6, HepG2 and H9c2 cells. AMA is a mitochondrial toxin that inhibits complex III of the electron transport chain, thereby inhibiting the production of mitochondrial-derived ATP (Midzak *et al*., 2011). Previous studies have demonstrated that the depletion of ATP by AMA precedes the loss of cell viability (de Graaf *et al*., 2002). L6, H9c2 and HepG2 cells were treated with a range of AMA concentrations for 24 hours and cell viability (CCK-8 assay) and ATP content were assessed. In all three cell lines, AMA dose-dependently decreased cellular ATP concentrations, but had no significant effect on cell viability at this time point (figure 4.3).

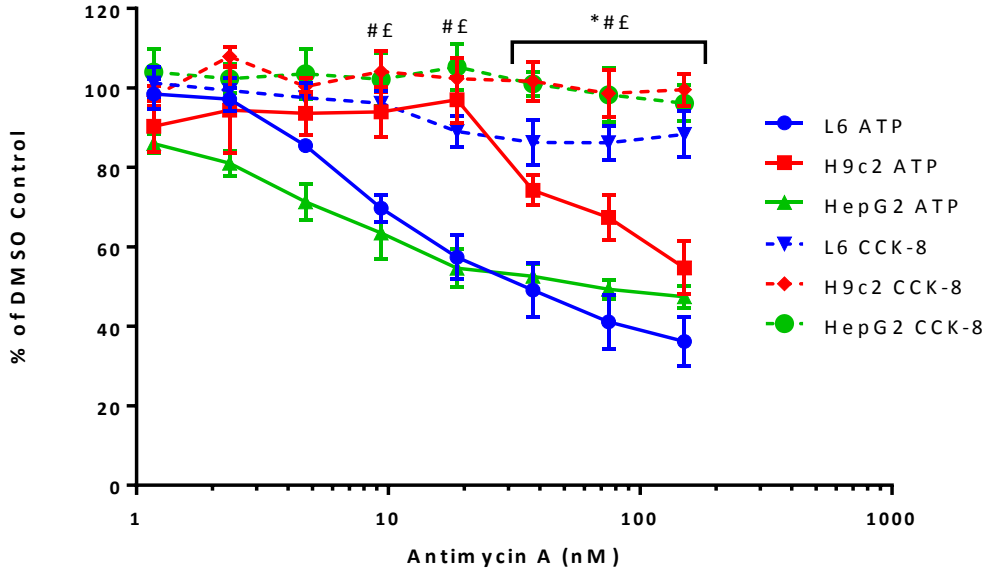

Figure 4.3 Effect of Antimycin A on cell viability (CCK-8) and ATP content. The L6 (blue), H9c2 (red) and HepG2 (green) cells were treated with a dose range of antimycin A for 24 hours and assessed for cell viability with CCK-8 (dotted lines) and ATP content (solid lines). ATP content was depleted to a greater extent than cell viability, becoming significant at $\geq$ 9nM for L6 and HepG2 and $\geq$ 37.5nM for H9c2. Results represent the mean ±SEM; n=3 (*P<0.001 H9c2 ATP vs. CCK-8; #P<0.001 L6 ATP vs. CCK-8; £P<0.001 HepG2 ATP vs. CCK-8).

The lack of significant changes in cell viability is confirmation that ATP depletion was the result of AMA mitochondrial toxicity and not the result of a loss in cell viability or

induction of cytotoxicity. These results confirmed previous studies and demonstrated the utility of the CCK-8/ATP assay combination to detect xenobiotic-induced effects on L6, H9c2 and HepG2 mitochondrial function. This assay was therefore used to determine the effects of the SI triazoles on mitochondrial function.

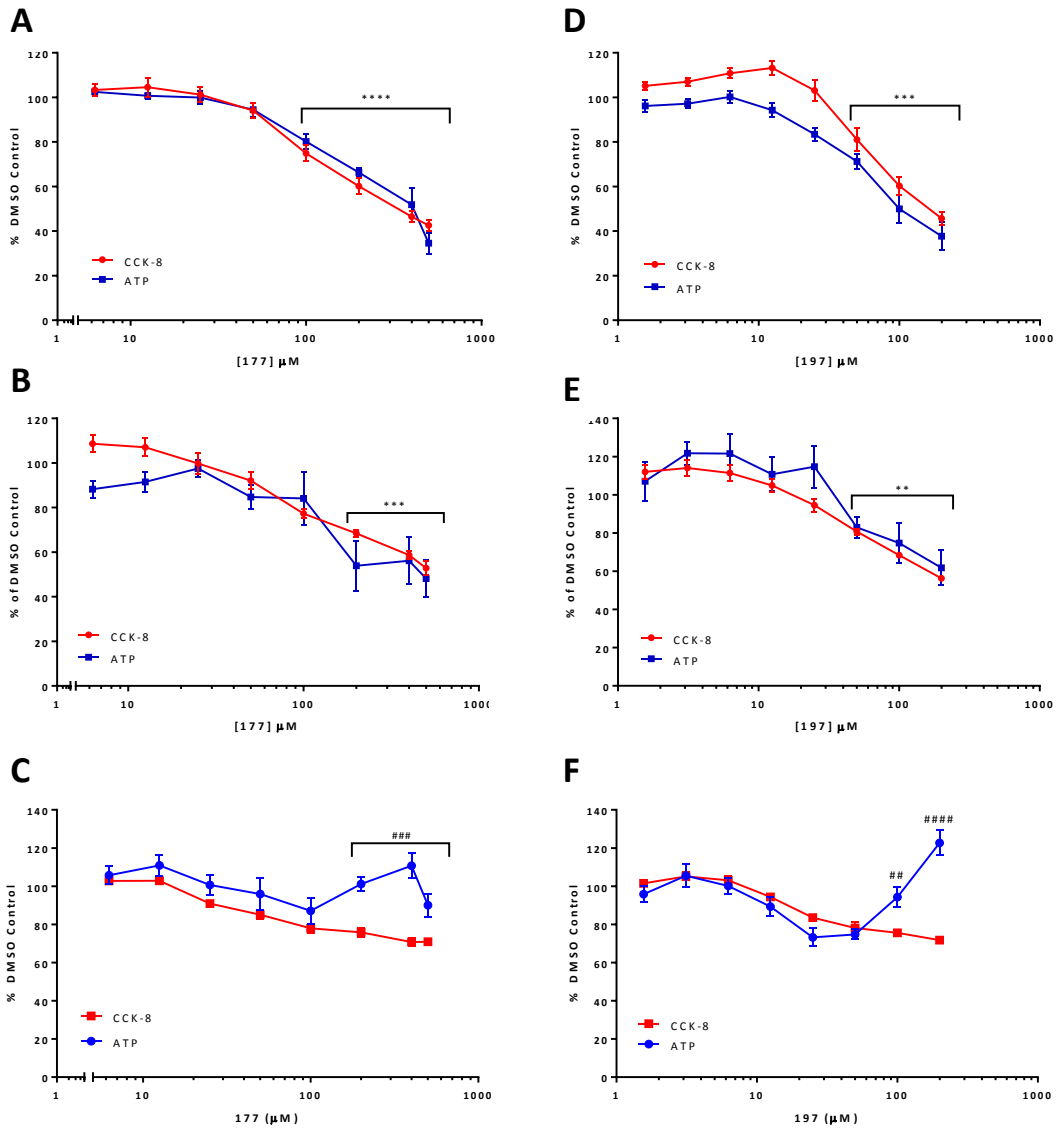

Figure 4.4 Effect of 24 hour SI triazoles treatment on cell viability and ATP content. L6, H9c2 and HepG2 cells were treated with a range of 177 and 197 concentrations for 24 hours and ATP content was assessed. The ATP content results were compared with the CCK-8 assay results to assess effects on cellular bioenergetics. **A, B and C,** represent 177 dose responses in L6, H9c2 and HepG2, respectively. **D, E and F,** represent 197 dose responses in L6, H9c2 and HepG2, respectively. Results represent the mean ±SEM; n=5-7 (**P<0.01, ***P<0.001, ****P<0.0001 Control vs. Treated; ##P<0.01, ###P<0.001, ####P<0.0001 CCK-8 vs. ATP).

L6, H9c2 and HepG2 cells were treated with the same concentrations of 177 and 197 for the same time point (24 hours) as used for the CCK-8 assay, and ATP content was determined. ATP content and cell viability (CCK-8) were plotted on the same graph to allow for comparison between the two parameters (figure 4.4). In L6 and H9c2 cells, 24 hour treatment with 177 and 197 induced a dose-dependent decrease in ATP content that was proportionate with the decrease in cell viability (CCK-8) (figures 4.4 A, B, D and E). In contrast, 177 and 197 increased ATP production in HepG2 cells at concentrations >100µM and >50µM, respectively (figure 4.4 C and F). Taken together, these results provide no evidence that triazoles target mitochondria as a principle mechanism of toxicity. The results did confirm the CCK-8 assay results, demonstrating that; the L6 cell line was the most sensitive to triazole treatment, while the HepG2 was the least sensitive, 197 was more potent than 177 and the HepG2 response to triazole treatment was distinct from the L6 and H9c2 responses. Since we were interested in the validation of a skeletal muscle *in vitro* model system, the L6 cells were used for the remainder of the experiments.

In the previous experiment, only one time point (24 hours) was used to assess ATP content following triazole treatment. However, since mitochondrial-specific reductions in ATP are time-dependent, they may be temporally distinct from reductions in cell viability. Therefore, a time course with CCK-8 and ATP was carried out with triazoles, along with AMA as a positive control. L6 cells were treated with 500µM 177, 200µM 197 and 100nM AMA for 2, 4, 16 and 24 hours and cell viability and ATP content were determined. There was a time-dependent decrease in cell viability and ATP content following 177, 197 and AMA treatment (figure 4.5). However, the decrease in ATP content preceded the decrease in cell viability following treatment with both triazoles and AMA. After only 2 hours treatment with 177, 197 and AMA, ATP levels were decreased to ~67%, ~44% and ~33% of DMSO control, respectively, whereas cell viability remained ~100% for all treatments. This pattern was maintained over the time course with AMA, with ATP levels at ~34% , while cell viability dropped to ~86% (figure 4.5 C). These results were consistent with the 24 hour dose response (figure 4.3) and confirmed the mitochondrial toxicity of AMA in L6 cells. As with AMA, 197 reduced ATP levels rapidly and by 4 hours ATP depletion was

maximal at ~38%, remaining at this level to 24 hours (figure 4.5 B). With 177 treatment however, the ATP levels continued to decrease over the time course declining from 67% at 2 hours to 34% at 24 hours (figure 4.5 A). The levels of ATP were significantly lower than cell viability after 2, 4 and 16 hours treatment with 177 and 197. By 24 hours, however, cell viability was decreased to the same extent as ATP, which is in agreement with the 24 hour dose responses (figure 4.4 A and D). Overall, these results suggest that 177 and 197 both have deleterious effects on mitochondrial function and cellular bioenergetics, with 197 being the more potently toxic of the two triazoles. Since ATP depletion occurred early (2 hours) and preceded the loss of cell viability, we can hypothesise that mitochondrial impairment was a primary contributor of triazole toxicity rather than a secondary reflection of other deleterious pathways.

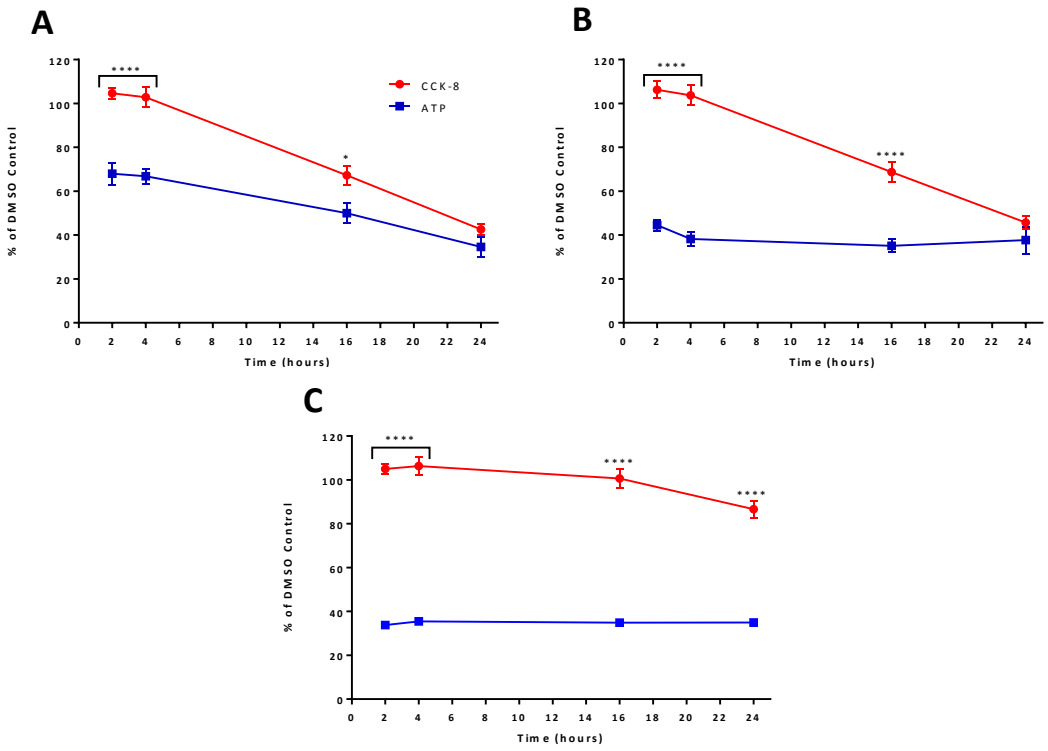

Figure 4.5 Time course of L6 cell viability and ATP content. L6 cells were treated with **(A)** 500µM 177, **(B)** 200µM 197 and **(C)** 100nM Antimycin A for 2, 4, 16 and 24 hours and cell viability (CCK-8) (red) and ATP (blue) content were assessed. There was a clear time-dependent decrease in ATP content following triazole and antimycin A treatment, which preceded the loss of cell viability. Results represent the mean ±SEM; n=3 (****P<0.0001 CCK-8 vs. ATP).

4.4.3 Effect of SI triazoles on cytosolic and mitochondrial superoxide generation in L6 cells

Based on the *in vivo* toxicogenomic analysis, oxidative stress was hypothesised to play an important role in mediating the toxicological effects of triazoles 177 and 197. Therefore, the ability of the triazoles to induce cytosolic and mitochondrial derived superoxide generation was assessed using the fluoroprobes DHE and MitoSox, respectively. The MitoSox probe is a membrane permeant derivative of DHE, which allows for the highly selective detection of superoxide in the mitochondria of live cells (Koppers *et al*., 2008). The oxidation of both probes by superoxide leads to the fluorescent product 2-hydroxy-ethidium, which is excitable at 480nm, with emission at 567nm (Mukhopadhyay *et al*., 2007). To ensure that 177 and 197 did not emit a fluorescence (due to autofluorescence) that would interfere with the fluoroprobes, cells were treated with the highest concentrations of 177 and 197 and analysed without the addition of either fluoroprobe. The fluorescence intensities of 100µM 197 and 400µM 177, after 1 and 24 hour incubation, were analogous to control cells not loaded with either probe, thereby indicating that neither compound produced a fluorescence that would interfere with MitoSox or DHE fluorescence signal (figure 4.6 A and figure 4.7 A).

The generation of superoxide was assessed after 1 and 24 hour treatment with 177, 197 and AMA, as a positive control. Treatment with AMA (100µM) for 1 hour significantly increased MitoSox and DHE intensity, although the fold increase in MitoSox intensity (5.4 fold) was significantly higher than DHE (2.4 fold) (figure 4.6 B). Both triazoles dose-dependently increased MitoSox and DHE intensity after 1 hour treatment (figure 4.6 A), although, in a similar manner to AMA, the fold increase in MitoSox intensity was significantly higher than DHE intensity (figure 4.6 B and C). At the highest concentration of 177 (400µM) and 197 (100µM) there was only a small increase in DHE intensity, with a 1.4 and 1.6 fold increase, respectively. The increase in MitoSox intensity was significantly higher than DHE at 400µM 177, 50µM 197 and 100µM 197, with a 2.3, 2 and 3.7 fold increase, respectively. The higher potency of 197 was again displayed, with 100µM 197 able to induce a greater increase in MitoSox intensity than 400µM 177.

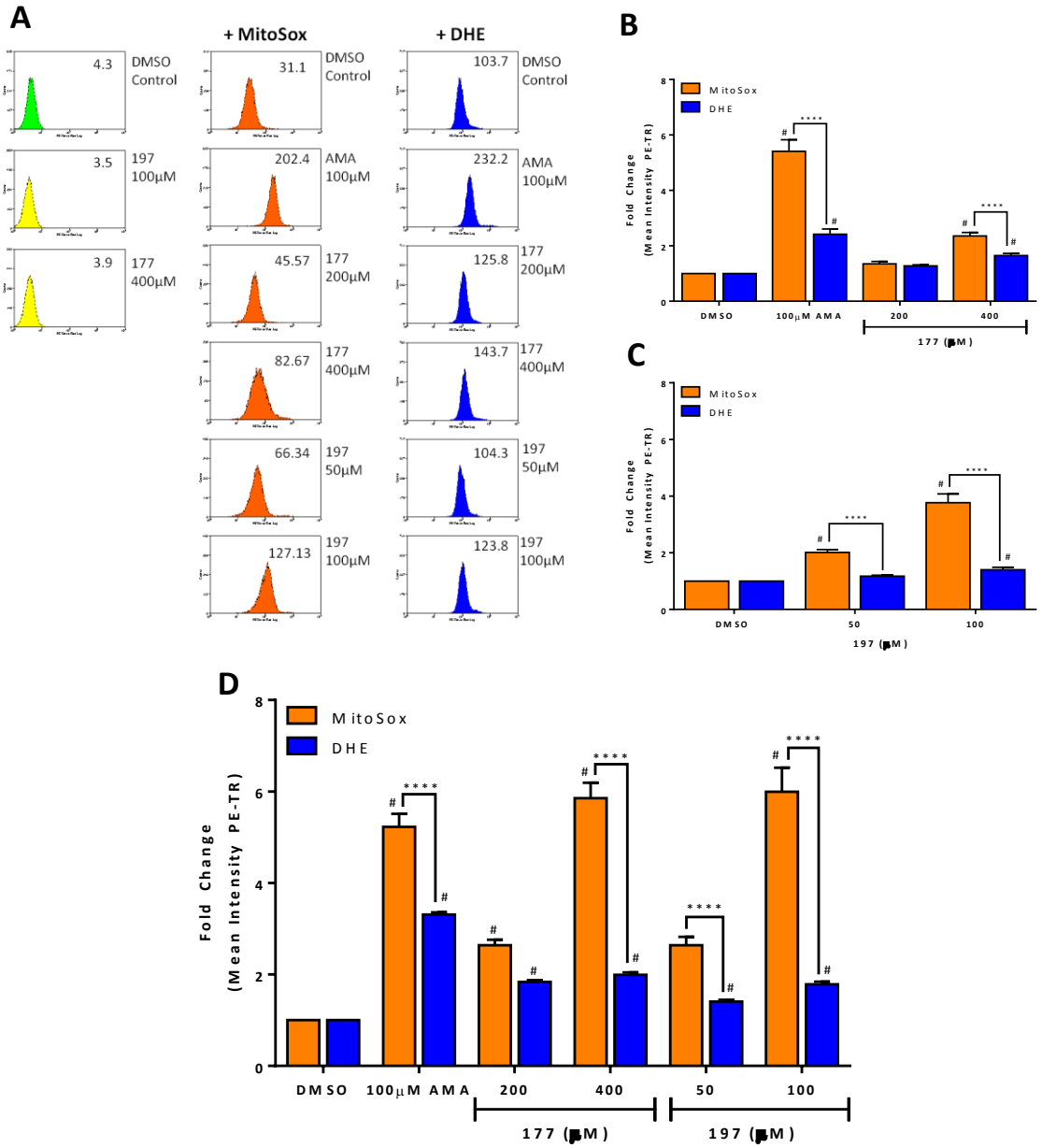

Figure 4.6 Triazoles dose- and time- dependently increase cystolic and mitochondrial superoxide formation in L6 cells. Cells were treated with 177, 197 and AMA for 1 and 24 hours and analysed with or without MitoSox and DHE using flow cytometry. **(A)** Representative histograms demonstrating dose-dependent increase in the mean fluorescence intensity (PE-Texas Red(PE-TR)) of oxidized DHE (blue) and MitoSox (orange) following 1 hour AMA, 177 and 197 treatment as indicated. **(B) and (C)** Quantitative data expressing increase in mean fluorescence intensity of oxidized DHE and MitoSox following 1 hour AMA, 177 **(B)** and 197 **(C)** treatment. **(D)** Quantitative data expressing increase in mean fluorescent intensity of oxidized DHE and MitoSox following 24 hour AMA, 177 and 197 treatment. Results represent the mean +SEM; n=3 (****P<0.0001 DHE vs. MitoSox, #P<0.05 treated vs. respective fluoroprobe control).

After 24 hour treatment with AMA, the MitoSox intensity did not change significantly from 1 hour, yet the intensity of DHE increased to 3.3 fold (up from 2.4 fold at 1 hour) (figure 4.6 D). Unlike with AMA, 24 hour treatment with 177 and 197 resulted in a considerable increase in MitoSox intensity compared with 1 hour, but only a very small increase in DHE intensity (figure 4.6 D). Treatment with 50µM and 100µM 197 increased MitoSox intensity by 2.6 and 5.9 fold (up from 2 and 3.7 fold at 1 hour), while only increasing DHE intensity by 1.4 and 1.7 fold (up from 1.1 and 1.4 at 1 hour), respectively. A similar response was induced by 177, with 200 and 400µM increasing MitoSox intensity by 2.6 and 5.8-fold (up from 1.3 and 2.3 fold at 1 hour), while only increasing DHE intensity by 1.8 and 1.9 fold (up from 1.2 and 1.6 at 1 hour), respectively. Consequently, the increase in MitoSox intensity was significantly higher than DHE with 400µM 177, 50µM 197 and 100µM 197. Notably, after 24 hour treatment the MitoSox intensities of 400µM 177 and 100µM 197 were analogous to the increase by 100µM AMA. Taken together, these results indicate that 177 and 197 dose- and time-dependently increased cytosolic and mitochondrial derived superoxide generation. However, the fold increase in cytosolic derived superoxide was significantly lower than that of mitochondrial derived superoxide after both 1 and 24 hour, suggesting that the mitochondria were the primary source of superoxide following triazole treatment. Moreover, after 24 hours, the increase in mitochondrial superoxide by the triazoles was analogous to AMA, a mitochondrial-specific inhibitor, implying that 177 and 197 had a potent effect on mitochondrial function.

To further characterise the generation of mitochondrial superoxide by the triazoles, a dose response with 177 and 197 was carried out for 24 hours and analysed with MitoSox. Representative histograms showed a marked increase of mean MitoSox fluorescence intensity with increasing concentrations of 177 and 197 (figure 4.7 A). Quantitative measurements demonstrated that statistically significant increases in MitoSox intensity were achieved with 177 at $\geq$200µM and 197 $\geq$50µM (figure 4.7 B). At equivalent concentrations (both 50 and 100µM), 197 proved more potent, inducing a greater intensity of MitoSox fluorescence than 177. These results further confirmed the dose-dependent manner by which 177 and 197 increased the production of mitochondrial superoxide.

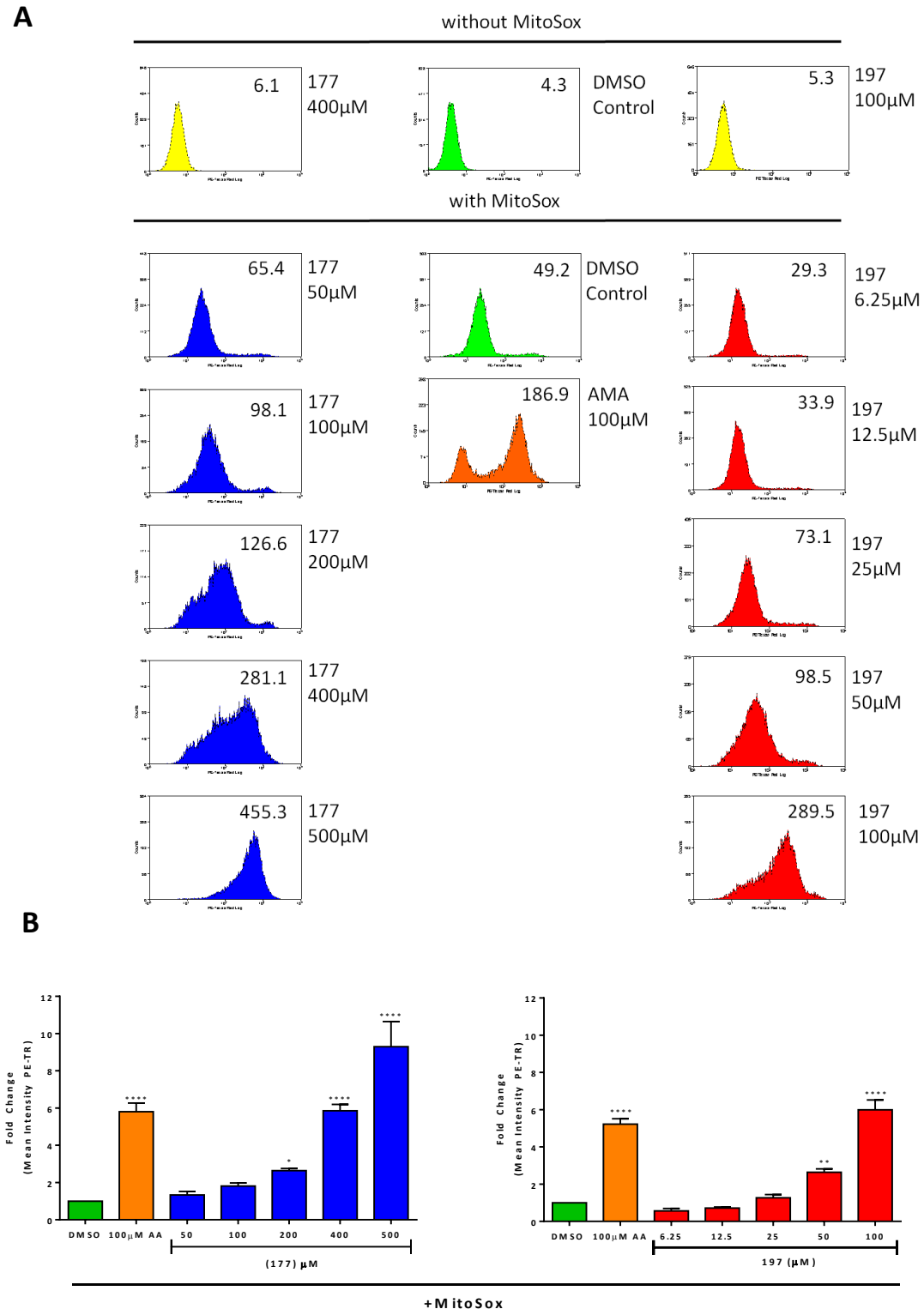

Figure 4.7 Triazoles increase mitochondrial superoxide generation in L6 cells. Cells were treated with 177 and 197 for 24 hours and analysed with or without MitoSox using flow cytometry. **(A)** Representative histograms demonstrating dose-dependent increase in mean fluorescent intensity (PE-Texas Red (PE-TR)) of oxidized MitoSox following 24 hour AMA, 177 and 197 treatment. **(B)** Quantitative data expressing increase in mean fluorescent intensity of oxidized DHE and MitoSox following 24 hour AMA, 177 and 197 treatment. Results represent the mean +SEM; n=3 (*P<0.05, **P<0.01, ****P<0.0001 control vs. treated).

4.4.4 Inhibition of triazole-induced mitochondrial superoxide generation and ATP depletion by the antioxidant NAC in L6 cells

The antioxidant, N-acetylcysteine (NAC), was used to confirm that the triazole-induced increase in MitoSox intensity was the result of mitochondrial superoxide generation. In addition, NAC was used to assess the involvement of mitochondrial superoxide in triazole induced ATP-depletion. NAC is a very effective antioxidant, which it accomplishes by serving as a glutathione precursor, ROS scavenging and through direct covalent coupling to redox cycling organic chemicals, such as quinones (Xiao, *et al*., 2003). However, there is a balance between the antioxidant and pro-oxidant activity of NAC, with lower concentrations protecting against GSH depletion and oxidative stress, whereas high concentrations enhance generation of ROS and result in carbonylation and glutathionylation of cellular proteins (Mukherjee *et al*., 2007). Therefore, preliminary experiments were carried out to determine the optimum NAC concentration that would not adversely affect L6 cell viability.

Cells were treated with an NAC concentration range for 27 hours (3 hour pre-treatment and a 24 hour co-treatment) and ATP content was used to assess the effects on cell viability (figure 4.8).

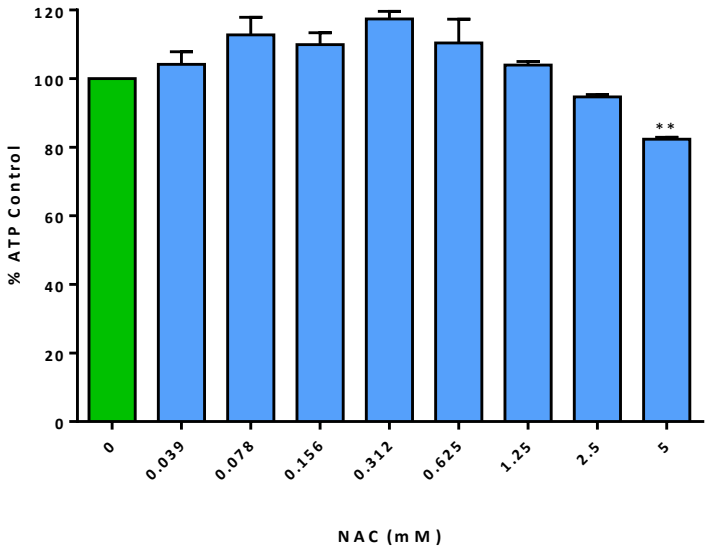

Figure 4.8 Effects of NAC on ATP content of L6 cells. Cells were treated with an NAC dose range for 27 hours and ATP content was assessed. Bars are mean + SEM; n=3 (**P<0.01).

There was an initial trend towards stimulation of ATP content at low concentrations of NAC, peaking with a 17% increase at 0.325mM NAC, but this did not reach statistical significance. Above this concentration, however, the ATP levels began to deplete in a concentration dependent manner, which became significant at 5mM NAC, with an 18% depletion in ATP relative to control. Therefore, the optimal NAC concentration for the antioxidant experiments was chosen as 2.5mM.

4.4.4.1 Effect of NAC on triazole-induced mitochondrial superoxide generation in L6 cells

The ability of NAC to protect against triazole-induced MitoSox fluorescence increase was investigated. A study by Estany *et al* (2007) determined that a combination of pre- and co- treatment with NAC was most the most effective treatment method to optimise antioxidant activity. Therefore, in this study cells were pre-treated with NAC for 3 hours followed by co-treatment with 177 and 197 for 24 hours. As illustrated by representative histograms in figure 4.9 A and B, 2.5mM NAC decreased the mean MitoSox fluorescence intensity induced by 400µM 177 (figure 4.9 A) and 100µM 197 (figure 4.9 B). Quantitative measurements demonstrated that NAC dose-dependently inhibited the generation of MitoSox fluorescence intensity by 177 and 197 (figure 4.9 C and D). The treatment of NAC alone resulted in no effect on MitoSox intensity, thereby confirming that the NAC concentrations used were sub-cytotoxic.

With both triazoles, 2.5mM NAC had a greater inhibitory effect on MitoSox fluorescence intensity production than 1.25mM NAC. In this respect, 1.25mM and 2.5mM NAC decreased the MitoSox intensity induced by 400µM 177 from 5.9 to 3.9 and 2.6, respectively. Similarly, 1.25 and 2.5mM NAC were able to decrease 100µM 197 MitoSox intensity from 6.1 to 3.1 and 2.3, respectively. The ability of NAC to reduce the triazole-induced increase in MitoSox intensity was further confirmation that the triazoles increased mitochondrial superoxide generation.

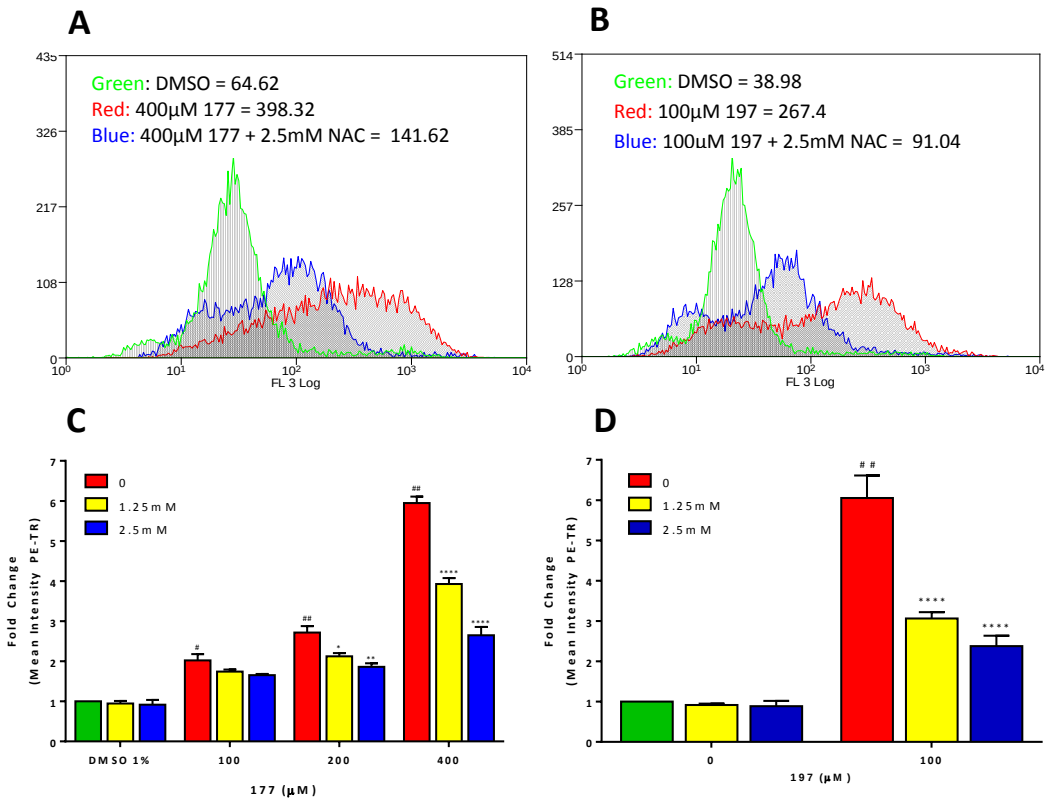

Figure 4.9 Inhibition of triazole-induced mitochondrial superoxide by NAC in L6 cells. Cells were pre-treated for 3 hours with NAC and then co-treated with NAC and 177 or 197 for a further 24 hours. Following treatment, mitochondrial superoxide generation was determined with MitoSox using flow cytometry. **(A, B)** Representative histograms demonstrating a decrease in MitoSox mean fluorescence intensity induced by **(A)** 177 and **(B)** 197 treated cells following pre-treatment with NAC. **(C, D)** Quantitative data expressing a dose-dependent decrease in MitoSox mean fluorescent intensity induced by **(C)** 177 and **(D)** 197 following pre-treatment with NAC. Bars represent mean +SEM; n=3 (#P<0.05, ##P<0.0001 control vs. treated; *P<0.05, **P<0.01, ****P<0.0001 treated vs. treated + NAC).

4.4.4.2 Effect of NAC on triazole-induced ATP depletion in L6 cells

To assess if mitochondrial superoxide production played an important role in triazole-induced ATP depletion, the effect of NAC on the ATP content of triazole treated L6 cells was determined. As shown in figure 4.10, both triazoles again showed a dose-dependent decrease in cellular ATP levels in agreement with previous data. NAC dose-dependently inhibited triazole-induced ATP depletion. Significantly, 2.5mM NAC was able to completely inhibit the ATP depletion induced by 50, 100 and 200µM 177 (figure 4.10 A). Treatment with 197 showed a similar trend, with 2.5mM NAC able to maintain ATP levels close to control for 25, 50 and 100µM 197 treated cells (figure 4.10 B).

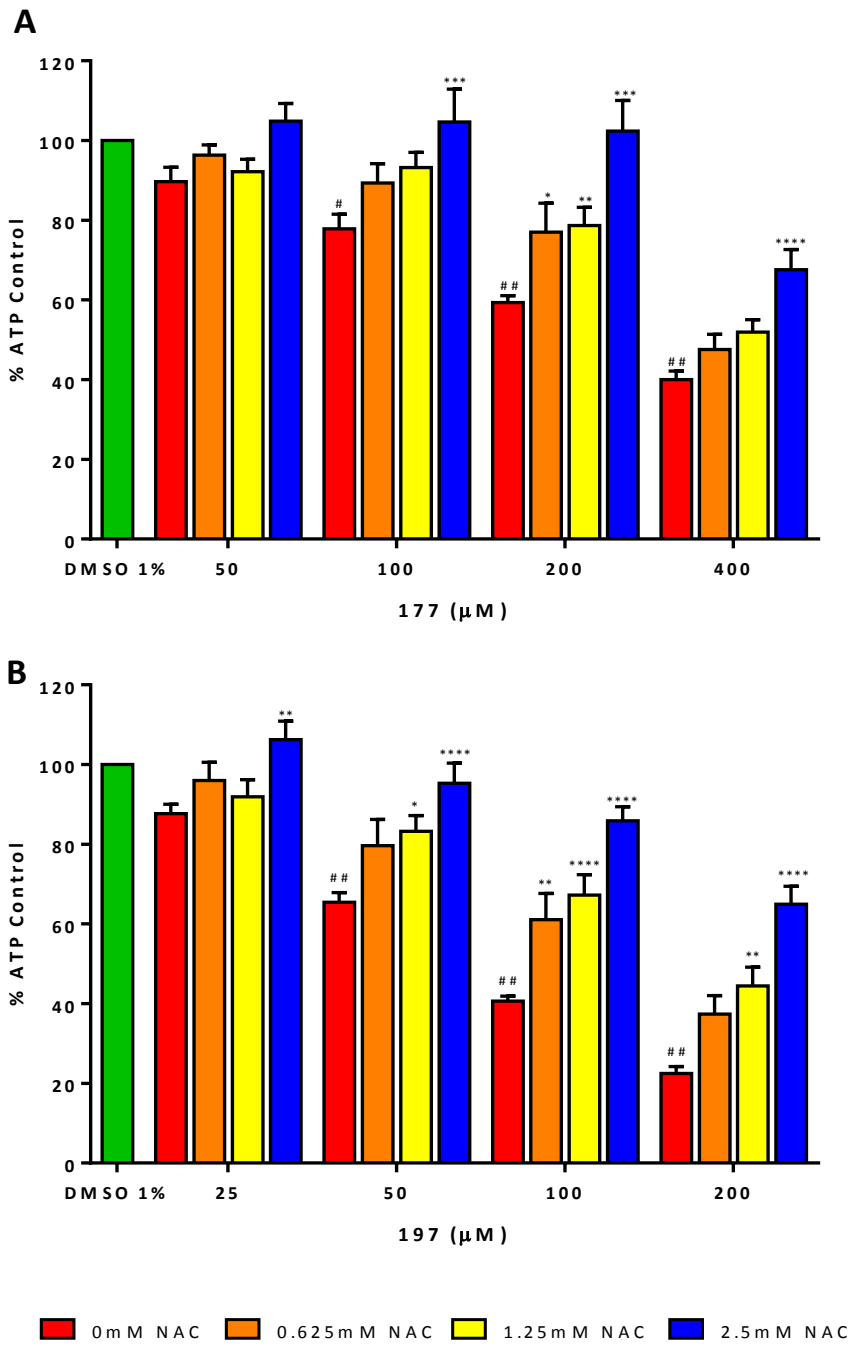

Figure 4.10 Inhibition of triazole-induced ATP depletion by NAC in L6 cells. Cells were pre-treated for 3 hours with 0mM (red), 0.625mM (orange), 1.25mM (yellow) and 2.5mM (blue) NAC and then co-treated with NAC and a concentration range of **(A)** 177 and **(B)** 197 for a further 24 hours. Following treatment, ATP content was determined. NAC dose-dependently reduced the 177 and 197-induced ATP depletion. Bars represent mean +SEM; n=3 (#P<0.05, ##P<0.0001 control vs. treated; *P<0.05, **P<0.01, ***P<0.001, ****P<0.0001 treated vs. treated + NAC).

At the highest concentrations of 177 (400µM) and 197 (200µM), 2.5mM NAC significantly increased ATP content from 40% to 67% and 22% to 64%, respectively.

This suggests that high triazole concentrations crossed a threshold level where 2.5mM NAC was only able to exert partial protection. This is in concert with the dose-dependent protection conferred by NAC, with lower concentrations, 0.625mM and 1.25mM, only able to provide partial protection against triazole-induced ATP depletion. The ability of NAC to significantly inhibit triazole-induced ATP depletion and superoxide production was evidence for the involvement of mitochondrial superoxide in triazole toxicity. These results also imply that mitochondrial superoxide production occurred upstream of ATP depletion, making it an early and deleterious effect of triazole treatment.

4.4.5 SI triazoles induced apoptosis in L6 cells

The toxicogenomics study indicated that the triazoles potentially induced cell death by apoptosis through a caspase-dependent pathway (section 3.5.6.5). In addition, the CCK-8 and ATP assays (figures 4.2 and 4.4) showed that the triazoles dose and time dependently decreased cell viability, which could be attributable to cell death, cell cycle arrest or a combination of both. Therefore, the ability of triazoles to induce apoptosis in L6 cells was investigated. Apoptosis occurs via a complex signaling cascade, involving either a death receptor (extrinsic) or mitochondrial (intrinsic) mediated pathway, and both converge at the point of an execution phase, characterised by the activation of execution caspases (Elmore, 2007). There are many features of apoptosis and necrosis that can overlap so it is crucial to employ at least two distinct assays to confirm cell death is occurring via apoptosis. The two methods employed to measure apoptosis following triazole treatment were; caspase 3/7 (executioner caspase) activity and externalisation of phosphatidylserine residues, which occurs downstream of caspase activity as an end-point of the executioner phase.

4.4.5.1 Annexin V-FITC/PI staining of L6 cells following 177 and 197 treatment

To measure externalisation of phosphatidylserine residues on the outer membrane of apoptotic cells, FITC-labelled Annexin V was used. Cultured cells undergoing apoptosis will eventually undergo secondary necrosis, so to demonstrate integrity of

phosphatidylserine-positive cells, the membrane-impermeant nucleic acid dye PI was used in conjunction with Annexin V-FITC.

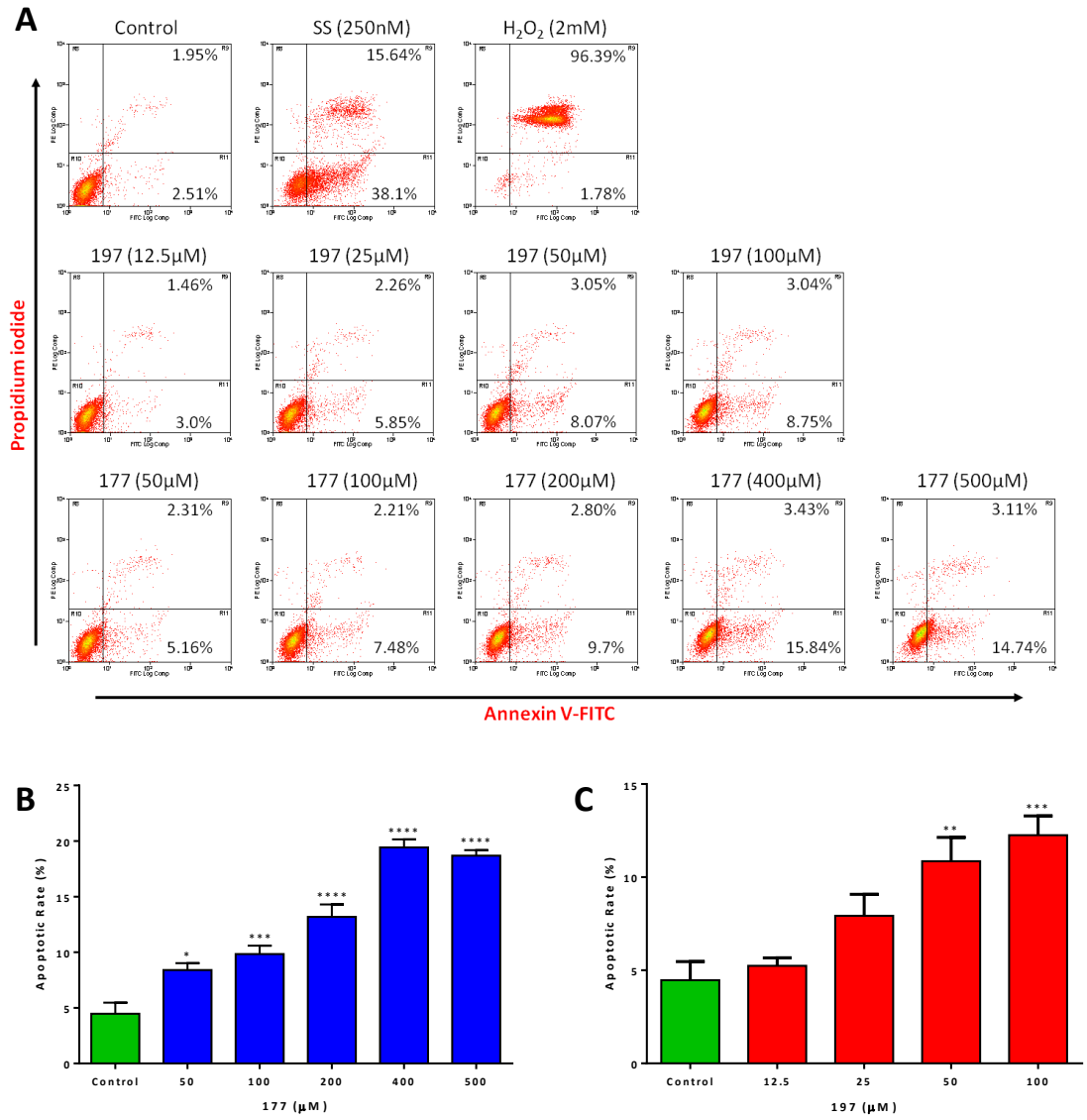

Figure 4.11 Annexin V/PI staining to assess triazole-induced apoptosis in L6 cells. Cells were treated with a range of 177 and 197 concentrations, along with staurosporine and H_2O_2 positive controls, for 24 hours. Annexin V/PI staining was used to assess apoptosis using FACS analysis. **(A)** Scatter plots representative of each treatment showing the gating of the cell populations. The quadrant can be divided into three distinct cell population: annexin V and PI negative corresponding to viable, non apoptotic cells (bottom left quadrant), annexin V positive PI negative corresponding to early apoptotic (bottom right quadrant) and annexin V and PI positive corresponding to late apoptotic /secondary necrosis (top right quadrant). The apoptotic rate for 177 **(B)** and 197 **(C)** was calculated as the percentage of cells in early (annexin V positive) and late apoptosis (annexin V positive and PI positive). Bars represent the mean +SEM; n=3 (*P<0.05, **P<0.01, ***P<0.001, ****P<0.0001 control vs. treated).

L6 cells were treated with a range of 177 and 197 concentrations, as well as positive controls staurosporine, for early apoptosis, and H_2O_2, for necrosis, for 24 hours. Representative scatter plots for each treatment are illustrated in figure 4.11 A and the apoptotic rates for 177 and 197 are presented in figure 4.11 B and C. The apoptotic rate of 177 and 197 treated cells increased in a dose-dependent manner. All concentrations of 177 significantly increased the amount of apoptosis, reaching a maximum apoptotic rate of 19.4% at 400µM, which decreased to 18.7% at the highest concentration, 500µM (figure 4.11 B). The two highest 197 concentrations, 50 and 100µM, significantly increased the apoptotic rate by 10.8% and 12.3%, respectively (figure 4.11 C). Comparison of these 197 values with the equivalent 177 50µM (8.4%) and 100µM (9.8%) concentrations demonstrated that 197 was more potent and induced a greater amount of apoptosis. However, this difference did not reach statistical significance. Importantly, the scatter plots (figure 4.11 A) illustrate that the increase in triazole apoptotic rate was primarily attributable to an increase in the number of cells in early apoptosis. This is confirmation that the cells were undergoing apoptosis and not progressing immediately to secondary necrosis ($FITC^+$ and PI^+), which would be indicative of a necrotic pathway of cell death.

4.4.5.2 Effect of triazoles on caspase 3/7 activation

The activation of caspases is only transient (Elmore, 2007) and so it was important to measure the temporal expression of caspase activity in response to triazole treatment. To this end, L6 cells were treated with a range of 177 and 197 concentrations for 2, 4, 16 and 24 hours and caspase 3/7 activity measured using the luminescent protease assay. Treatment with both triazoles resulted in a time and dose-dependent increase in caspase activity (figure 4.12). After 2 and 4 hours, there was no significant induction of caspase-3/7 activity with either 177 or 197. This was in accordance with the CCK-8 time response, in which there was no significant loss in cell viability following 2 and 4 hours triazole treatment. By 16 and 24 hours, both triazoles produced a significant increase in caspase activity at all concentrations investigated. The peak 177 caspase 3/7 activity was a 1.9 fold increase at 250µM after 24 hours, which significantly decreased to 1.3 fold at 500µM (figure 4.12 B). These results are consistent with the annexin V/PI data, in which there was a decrease in apoptotic rate at 500 µM 177

compared to 400µM 177. The peak 197 caspase-3/7 activity was a 2.3 fold increase at 100µM after 24 hours, which correlated with the peak apoptotic rate observed with the annexin V/PI assay (figure 4.12 A). At 200µM 197, the caspase-3/7 activity significantly decreased to a 1.6 fold change at 24 hours, analogous with the decrease evident at the highest 177 concentration (500µM).

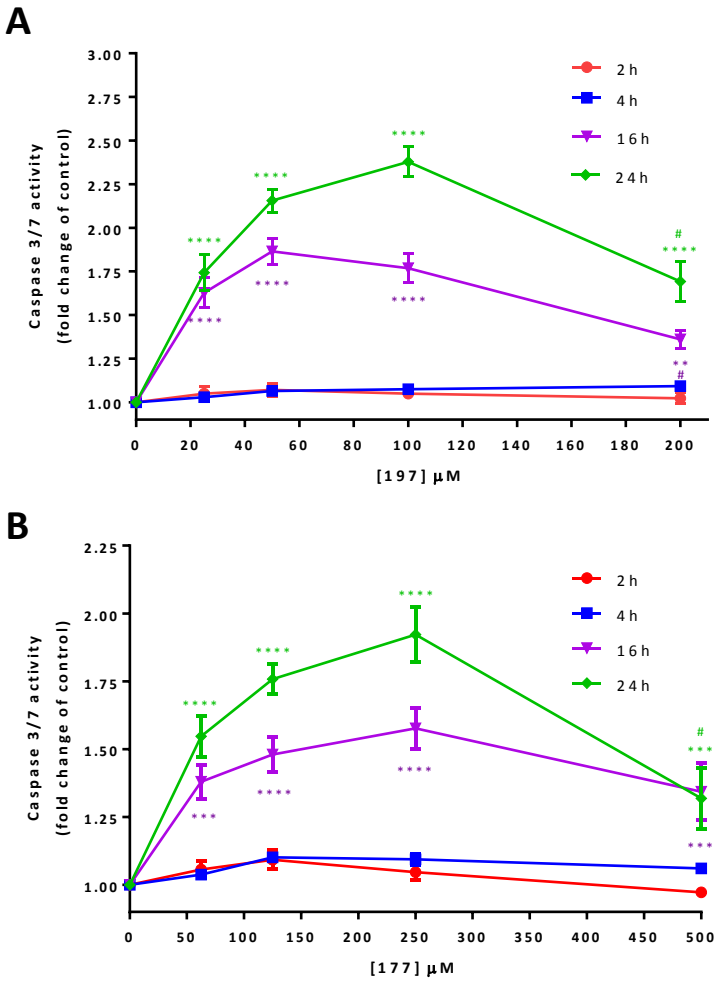

Figure 4.12 Time course of caspase-3/7 activity following treatment with triazoles in L6 cells. Cells were treated with a dose range of 197 **(A)** and 177 **(B)** for 2 (red), 4 (blue), 16 (purple) and 24 (green) hours. Luminescence values were recorded 1 hour following the addition of the Caspase 3/7 reagent and values are represented as a fold change relative to DMSO control. Results represent mean ±SEM; n=3 (***P<0.001, ****P<0.0001 control vs. treated; 197 #P<0.01 200µM vs. 100µM; 177 #P<0.01 500µM vs. 250µM).

Due to solubility issues, 200µM 197 was not investigated with the annexin V/PI assay. However, based on the 177 data, we can speculate that the decrease in caspase 3/7

activity at 200µM 197 would correlate with a decrease in the annexin V/PI determined apoptotic rate of 200µM treated cells relative to 100µM.

4.4.6 Effect of SI triazoles on cell cycle progression

The toxicogenomics study identified the cell cycle as a potential pathway adversely affected by the triazoles. The current data supports this cell cycle arrest hypothesis, since the amount of apoptosis induced by the triazoles does not account for the magnitude of decrease in cell viability. For example, treatment of L6 cells with 400µM 177 reduced cell viability by 54% (figure 4.2), but only increased apoptosis by 15% (figure 4.11 B). This discrepancy suggests that triazole treatment severely diminished the cells ability to proliferate, indicative of cell cycle arrest. Therefore, the effect of triazoles on cell cycle was assessed.

To determine distribution of the cell cycle, DNA content of L6 cells was measured using PI staining of fixed cells and analysed on the flow cytometer. To assess the cell cycle was progressing, control cells were treated (for 24 hours) with nocodazole, which prevents progression through mitosis by inhibiting microtubule polymerisation (Blajeski *et al*., 2002). There was a significant increase in the number of cells in G_2/M compared to control (from 22% to 61%), signifying a G_2/M arrest and thereby demonstrating the L6 cell cycle was progressing (figure 4.13 A). This was accompanied by a decrease in G_0/G_1. Treatment with 177 and 197 for 24 hours resulted in a significant G_0/G_1 cell cycle arrest (figure 4.13 A). Following treatment with 100 and 200µM 177, the number of cells in G_1 phase increased significantly from 65.2% (control) to 80.7 and 80.9% ($P<0.0001$), respectively, and there was a concomitant significant decrease ($P<0.0001$) in the number of cells in S and G_2/M phase (figure 4.13 A and B). Similarly, 50 and 100µM 197 significantly increased the number of cells in G_1 to 76% and 79%, respectively, and simultaneously decreased the numbers of cells in S and G_2M phase (figure 4.13 A and C).

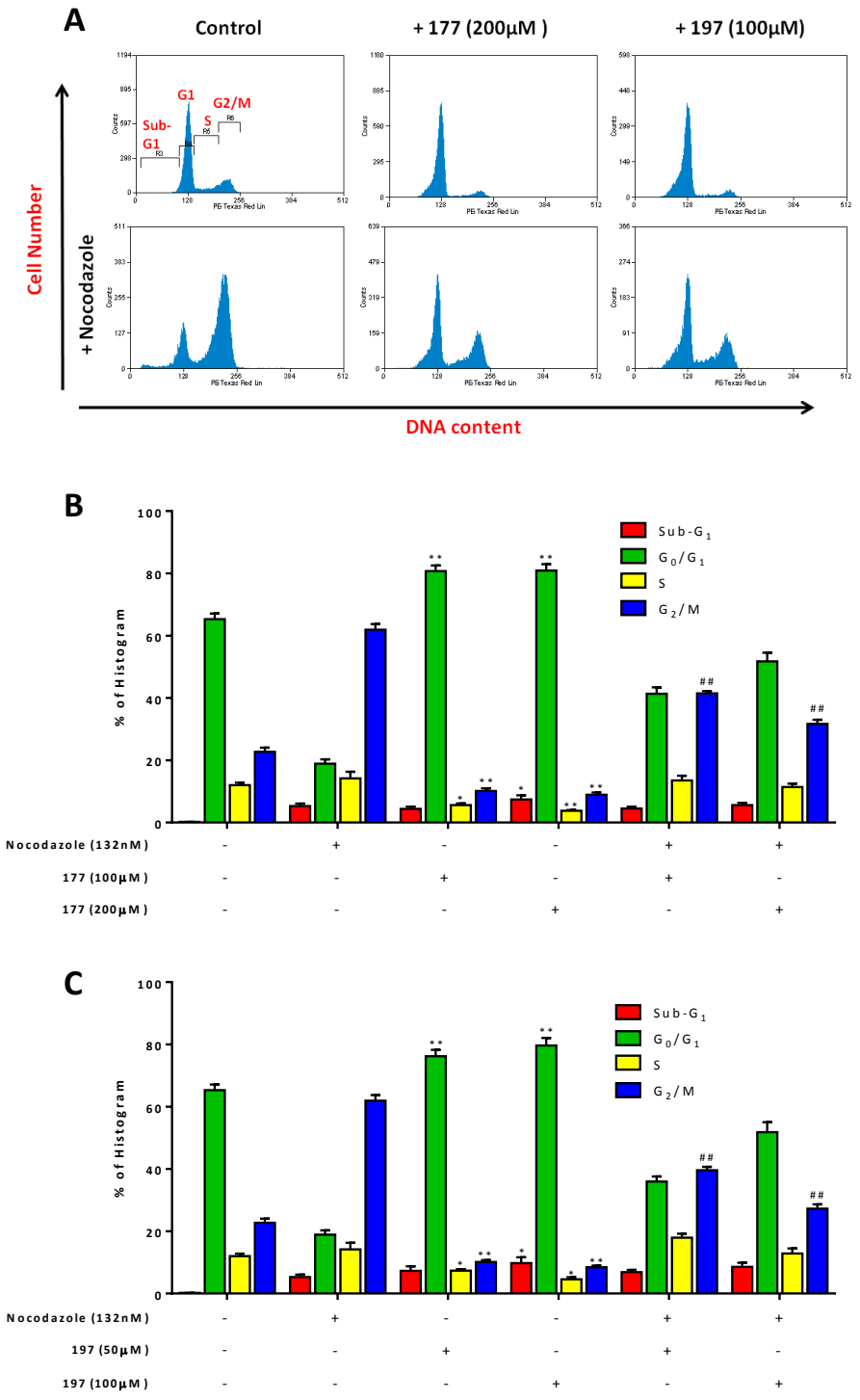

Figure 4.13 G_0/G_1 cell cycle arrest induced by 177 and 197 treatment in L6 cells . Cells were treated with 177 and 197 for 24 hours. To assess if the cell cycle was progressing following treatment, the cells were co-treated with Nocodazole 4 hours following triazole treatment (20 hours in total). To analyse the cell cycle, DNA content was measured with PI staining and analysed on the flow cytometer. **(A)** Representative histograms of the treatments, with the control sample labelled with the different phases of the cell cycle. Quantitative analysis displaying the percentage of cells in each phase for 177 **(B)** and 197 **(C)**. Bars represent mean +SEM; n= 5 (*P<0.05,**P<0.0001 control vs. treated; ##P<0.0001 Nocodazole G_2 vs. triazole treated G_2).

To confirm 177 and 197 G_0/G_1 cell cycle arrest, cells were co-treated with nocodazole 4 hours post-triazole treatment. The triazoles dose-dependently reduced the amount of cells progressing to G_2/M when co-treated with nocodazole. Nocodazole treatment alone resulted in 61% of cells in G_2M, but when co-treated with 100 and 200µM 177, the number of cells in G_2M reduced significantly to 41% and 31%, respectively (figure 4.13 B). The same pattern occurred following 50 and 100µM 197, in which the cells in G_2M decreased to 39% and 27%, respectively (figure 4.13 C). With both triazoles the number of cells in G_0/G_1 proportionally increased as the cells were blocked from progressing to G_2/M. As evident with previous assays, 197 was the more potent of the two compounds and arrested cells in G_0/G_1 to a greater extent than 177 at equivalent concentrations (100µM). The nocodazole co-treatment not only confirmed that the triazoles dose-dependently arrested the cells in G_0/G_1, but also indicated that the arrest was induced within 4 hours of 177 and 197 treatment. This acute effect on the cell cycle follows the same trend as the ATP time course data, in which ATP levels were depleted after only 2 hours (figure 4.5).

Apoptosis was also detectable using cell cycle analysis, since apoptotic cells have a fractional DNA content due to the loss of fragmented (low molecular weight) DNA during the staining procedure. The end result is a level of DNA staining below that of G_0/G_1, and so apoptotic cells are represented as a sub-G_1 cell population (figure 4.13 A, B and C). There was a significant increase in the sub-G1 cell population following 200µM 177 (~7%) and 100µM 197 (~9%), suggesting triazole-induced apoptosis. This compliments the annexin V/PI (figure 4.11) and caspase-3/7 assay (figure 4.12) findings, thereby confirming apoptosis as the principle mechanism of triazole-induced cell death.

4.4.7 SI triazoles induced hypertrophy of L6 cells

In vivo toxicogenomic analysis revealed that protein homeostasis was affected by triazole treatment. Specifically, pathways relating to hypertrophy were significantly enriched. To test this hypothesis, L6 cell size was determined following 24 hour 177 and 197 treatment. Cell size was measured using the G_0/G_1 cell population since the triazoles arrested the cells in this phase of the cell cycle. The relative increase in cell

size was determined by gating control cells such that 10% of the total cell population was in a 'large-cell' region (figure 4.14 A).

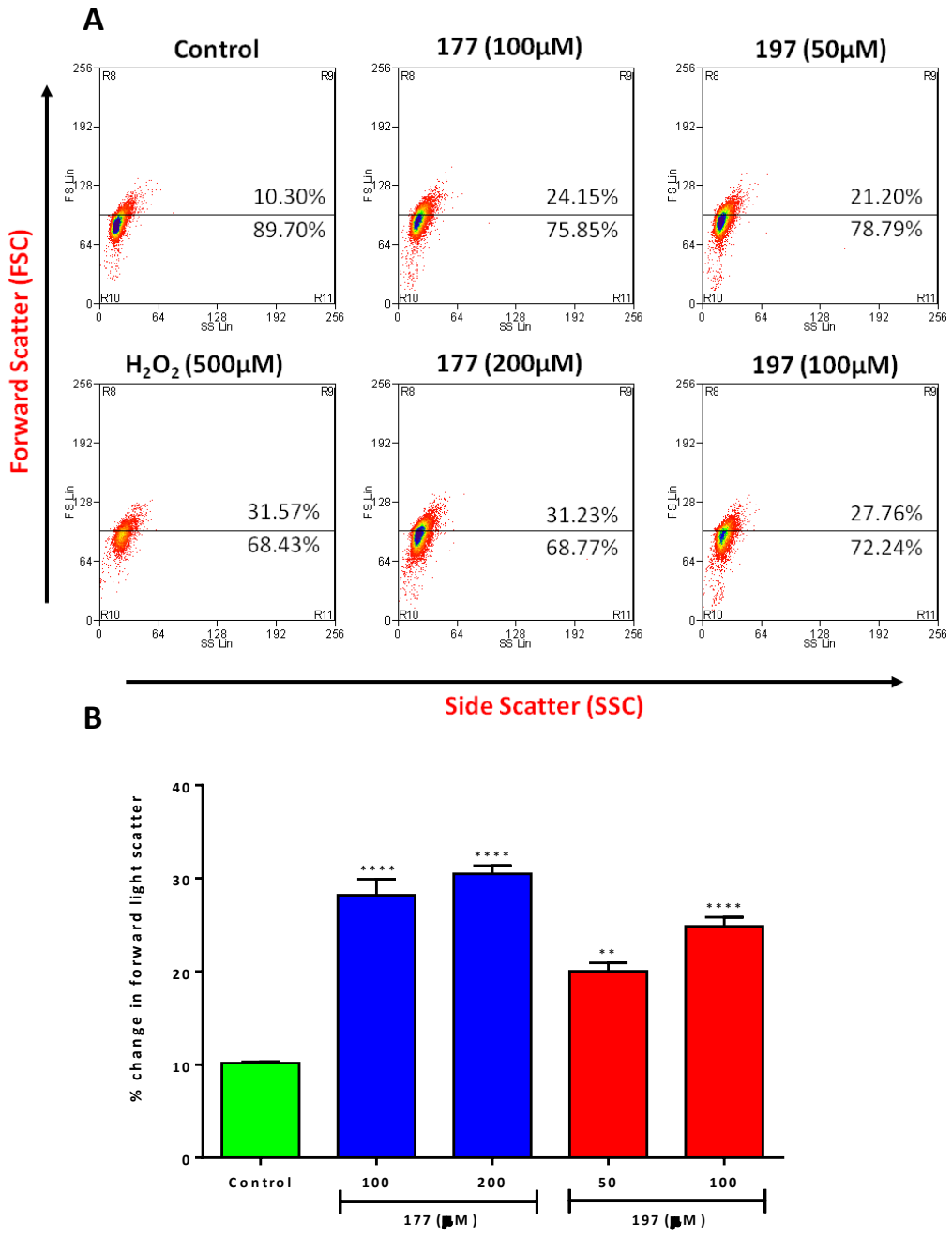

Figure 4.14 Effect of triazoles on L6 cell size. Cell size was determined by measuring the forward light scatter of the G_0G_1 population following treatment with 177 and 197 for 24 hours. **(A)** Representative FSC vs. SSC scatter plots of all treatments. The control cells were gated such that an arbitrary 10% of the cells were presumed to represent large-sized cells in a given population. H_2O_2 was used as a positive control. **(B)** The percentage increase in forward light scatter from control of 177 and 197 treated cells. Bars represent mean +SEM; n=5 (**P<0.01, ****P<0.0001 control vs. treated).

Both triazoles increased cell size in a dose-dependent manner following 24 hour treatment, indicative of a hypertrophy response (figure 4.14 B). The percentage of cells in the large-region was significantly increased to 28% and 30% following 100 and 200µM 177 and to 20% and 24% following 50 and 100µM 197.

4.5 Discussion

The overall aim of this chapter was to investigate the ability of an *in vitro* skeletal muscle model to effectively mimic the triazole-induced toxicity effects *in vivo*. To this end, the translation of the of the SI triazole toxicity pathways, identified using *in vivo* toxicogenomics, into an L6 skeletal muscle *in vitro* model was investigated. In doing this, we aimed to validate the L6 *in vitro* model to predict *in vivo* skeletal muscle outcomes, as well as validate the findings of the *in vivo* toxicogenomics data.

4.5.1 Detection of SI triazole and phenyl target organ toxicities using organ-specific cell lines

In recent years, there has been an increased effort in toxicology to improve predictive *in vitro* toxicity models to identify organ toxicities early in R&D. One approach has been the use of organ-specific cell lines to predict target organ toxicities. Given the differential organ toxicities of the two SI compound classes, the ability of organ-specific cell lines to accurately detect SI triazole and phenyl target organ toxicities was investigated.

As determined by *in vivo* repeat dose studies, the triazoles were primarily toxic to cardiac and skeletal muscle, and to a lesser extent the liver, whereas the phenyl did not induce any striated muscle toxicity but was toxic to the liver, albeit less potently than the triazoles (section 1.5.2.4). Based on this *in* vivo data, it was hypothesised that 177 and 197 toxicity would be detected more sensitively with skeletal (L6) and cardiac (H9c2) muscle cell lines, whereas 907 toxicity would be detected more sensitively with a liver (HepG2) cell line. The results of the study support this hypothesis, with the organ-specific cell lines accurately reflecting the *in vivo* target organ toxicity profiles of the SI compounds, as summarised in table 4.2. Thus, the results of this experiment support the potential of organ-specific cell lines to investigate target organ toxicities.

	Triazole organ toxicities	Phenyl Organ toxicities
In vivo	Skeletal muscle **>** Heart **>** Liver	Liver **>** Heart & Skeletal muscle
In vitro	L6 **>** H9c2 **>** HepG2	HepG2 **>** H9c2 & L6

Table 4.2. *In vivo* and *in vitro* SI compound organ toxicity profiles. > = 'more sensitive than'

These findings are in concert with a number of other studies that have investigated the feasibility of organ specific cell lines to accurately predict cardio-, hepato- and nephro- toxicity (Inoue *et al*., 2007; Li *et al*., 2004; Zhang *et al*., 2007). For example, Inoue *et al* (2007), used rat heart cells and rat hepatocytes to predict cardio- and hepato- toxicity with four cardiotoxins and five hepatotoxicants. Using the LDH cytotoxicity assay, they found that the cardiotoxic compounds were more toxic to the rat heart cells than the rat hepatocytes and the hepatotoxicants, with the exception of acetaminophen, were more toxic to hepatocytes than heart cells. In this study, the authors suggested that taking a ratio of one cell line over the other would be predictive of possible organ toxicity. They judged that a 2-fold difference between cell lines was a good measure of a compounds target organ toxicity. In this study it was not possible to accurately calculate the IC50 for each SI compound because solubility prevented higher concentrations being tested, resulting in incomplete dose responses. To generate a more complete dose response, a longer time course could have been implemented, although, for this study, we were only interested in analysing the effects on cell viability at 24 hours. However, with 177 and 197, an IC50 could be estimated based on the available data points, so a ratio of L6 over HepG2 and H9c2 over HepG2 was calculated. With 177, this resulted in an IC50 ratio of more than 5 (L6/HepG2) and 3 (H9c2/HepG2) for skeletal and cardiac muscle cell lines, respectively. Similarly, 197 produced an IC50 ratio of more than 3 (L6/HepG2) and 2 (L6/HepG2) for skeletal and cardiac muscle cell lines, respectively. Based on the Inoue *et al* (2007) criteria then, the L6 and H9c2 cell lines are confirmed as more sensitive to triazoles treatment, reflecting the *in vivo* data that striated muscle was the principle target organs of triazoles. Given that 907 had no effect on either L6 or H9c2, we can only speculate that an IC50 ratio would determine that HepG2 were >2 fold more

sensitive to 907 that the other cell lines, thereby confirming that 907 targeted the liver but not striated muscle.

Other studies have concluded that while organ-specific *in vitro* systems could potentially predict target organ toxicity, in some cases toxicokinetic and ADME properties would need to be considered (Zhang *et al*., 2007; Lin and Will, 2012). For example, Zhang *et al* (2007) included an S9 hepatic mixture to account for metabolism and potential bioactivation of compounds, and found that this increased toxicity for 2/6 compounds tested. Given the correlation between the 177, 197 and 907 *in vivo* and *in vitro* responses, it is more likely that cell type sensitivity and exposure to the compounds, rather than metabolism and bioactivation, were the determining factors in SI compound target organ toxicity. However, xenobiotic metabolism was one of the most highly enriched processes in the toxicogenomics analysis of 177, 197 and 907 liver samples, highlighting a role for metabolism in the overall toxicity of these compounds. Since the parent compounds demonstrated considerable effects on cell viability, it is likely that changes in genes relating to xenobiotic metabolism pathways related to detoxification and excretion of the SI compounds rather than bioactivation. In this respect, the ability of HepG2 cell lines to metabolise and detoxify 177 and 197 more effectively than 907 may have accounted for the differential sensitivity of the cell lines. However, most views are that HepG2 cells are not metabolically competent, lacking the relevant enzymes, such as cytochrome P-450 enzymatic activity (Westerink and Schoonen, 2007; Zhang *et al*., 2007). Thus, the differential sensitivity of the cell lines to SI compounds could have been due to differences in uptake of each compound or the differences in toxicity mechanisms of each class of compound.

Overall, these results showed that SI compound target organ toxicities could be replicated *in vitro*, thereby confirming other studies that organ specific cell lines have the potential to predict target organ toxicities *in vivo*. Notably, this is the first study to consider the utility of a skeletal muscle cell line in a multi-organ *in vitro* system for prediction of skeletal muscle toxicity. This study was carried out with relatively uncharacterised compounds and so further experiments using characterised reference compounds would be needed to further validate this *in vitro* organ-toxicity system. In

addition, the HepG2 cell line is human derived, and so species differences may have contributed to the differences seen between this cell line and the rat-derived L6 and H9c2 cell lines. Therefore, for future experiments, it would be preferable to use organ cell lines derived from the same species. It would also be useful to investigate species differences in response to xenobiotic-induced toxicity between species-specific skeletal muscle cell lines.

These results also determined that, *in vitro*, 197 was more toxic than 177 at equivalent doses, which is contrary to the *in vivo* histopathology data. These differences are likely attributable to ADME effects *in vivo* and highlight the potential shortfalls of a simple *in vitro* approach to organ specific toxicity testing.

4.5.2 Comparison of SI triazole-induced toxicity between L6 skeletal muscle cells and rats *in vivo*

The validation of *in vitro* models to accurately mimic *in vivo* outcomes remains an important challenge for the successful implementation of *in vitro* assays to the decision making process in early R&D (Kienhuis *et al*., 2006). Toxicogenomics provides the ideal platform for comparing the similarity between *in vivo* and *in vitro* systems. In this study, the triazole toxicity pathways (biological processes) identified by *in vivo* toxicogenomics were investigated in an *in vitro* rat skeletal muscle cell line (L6). These toxicity pathways included mitochondrial dysfunction, oxidative stress, cell death, cell cycle arrest and hypertrophy and are discussed in detail below.

4.5.2.1 SI triazoles induced mitochondrial dysfunction

In vivo toxicogenomics identified mitochondrial dysfunction as a potential mechanism mediating the toxic effects of SI triazoles. Specifically, a number of toxicity pathways enriched by both 177 and 197 related to effects on OXPHOS (section 3.5.6.5). Mitochondria utilize OXPHOS to generate ATP, and so any compounds that affect OXPHOS function will have a serious effect on ATP generation (Marroquin *et al*., 2007). To determine that reductions in ATP were not a result of cytostatic or cytotoxic effects, ATP levels were measured in conjunction with cell viability (CCK-8 assay). This is a standard technique for determining mitochondrial dysfunction, with a decrease in

ATP prior to a loss of cell viability indicative of mitochondrial dysfunction (Li *et al*., 2012).

Initial experiments carried out with the mitochondrial complex III inhibitor, AMA, resulted in a dose-dependent decrease in ATP without a loss of cell viability in L6, H9c2 and HepG2 cells after 24 hour treatment. These experiments were consistent with previous AMA findings (de Graaf *et al*., 2002; Im *et al*., 2012) and confirmed the utility of this assay to detect mitochondrial dysfunction in L6, H9c2 and HepG2 cells. There was a difference in cell-type sensitivity to AMA treatment, with L6 and HepG2 cells more sensitive to AMA-induced ATP depletion than H9c2 cells. This may have been because the threshold inhibition for complex III was higher in H9c2 cells than L6 and HepG2 cells, which would mean a higher amount of complex III inhibition, and hence a greater concentration of AMA, was required to decrease ATP production in H9c2 cells. This cell type variation could in part be due to different excess of enzyme activity that could be correlated to variations in the amount of complex and/or to the presence of isoforms of nuclear origin differing in their regulatory properties (Rossignol *et al.*, 1999).

Treatment with 177 and 197 for 24 hours resulted in a dose-dependent decrease in ATP content that was proportional to the loss of cell viability in L6 and H9c2 cells. Given the correlation between the decrease in ATP content and cell viability, these results provided no evidence that mitochondria were a primary target of 177 and 197 toxicity. Interestingly, with HepG2 cells, there was an increase in ATP content at the higher concentrations of 177 and 197, despite a decrease in cell viability. The concentrations at which HepG2 ATP content increased (177: 125µM and 197: 100µM) coincided with the concentrations where L6 and H9c2 cell viability levels were significantly decreased compared to HepG2 cell viability levels (figure 4.4). This suggests that the increase in HepG2 ATP levels may have conferred a protective effect against 177 and 197 toxicity effects, thereby reducing the loss of cell viability compared to L6 and H9c2 cells. This increase in ATP content may have been a consequence of either an enhanced ATP production or a decreased ATP consumption. The rise in ATP production may result from an increased glycolysis or from a more active or efficient mitochondrial respiration (Sánchez-Alcázar *et al*., 1997).

Since mitochondrial-dependent reductions in ATP levels are time-dependent and not just concentration dependent (Mingatto *et al*., 2002), it was possible that the triazole-induced ATP depletion may have been temporally distinct from a reduction in cell viability. A time course with the highest concentrations of 177 and 197 in L6 cells revealed that ATP depletion preceded the loss of cell viability. Both 177 and 197 significantly depleted levels of ATP after only 2 hours (to 67% and 44% of control, respectively), while cell viability remained unaffected. Since ATP depletion is an early event of mitochondrial dysfunction, these results suggest that the SI triazoles target the mitochondria as a primary mode of toxicity. The time dependent nature of mitochondrial ATP depletion was confirmed with AMA, which, in a similar way to 197, decreased ATP maximally by 4 hours. The difference in target organ-cell line toxicity of AMA and the triazoles suggests that 177 and 197 disrupt mitochondrial function in a mechanism distinct from AMA complex III inhibition. In addition, 177 and 197 had significant effects on cell viability after 24 hour treatment, whereas AMA did not, further supporting the notion for a differential mechanism of mitochondrial impairment. Overall, the rank order for mitochondrial dysfunction in L6 cells is AMA>197>177, which is expected given that AMA is the most potent inhibitor of the mitochondrial electron transport chain (Huang *et al*., 2005).

Following 197 and AMA treatment, maximum ATP depletion (~35-40%) was achieved by 4 hours and remained at a steady level through to 24 hours. This ATP depletion threshold was also reached with 177 (~34%), but only after 24 hours. This suggests that following mitochondrial impairment, ATP depletion reached a threshold level in L6 cells (~35%) at which ATP levels were sustained through the alternative ATP source, glycolysis. In the case of AMA, this level of ATP was enough to prevent mitochondrial dysfunction from reducing cell viability. For most cells, glucose is an excellent glycolytic substrate that is able to compensate for mitochondrial impairment by producing requisite ATP via increased glycolytic flux (Dykens *et al*., 2008). This metabolic adaptability was amplified in these experiments by the use of supraphysiological glucose conditions of 25mM in cell culture media. Although glycolysis is inefficient, flux rates through the glycolytic pathway can be dramatically

accelerated so that inefficiency is offset by abundance of substrate (Marroquin *et al*., 2007). In this respect, cell models that more faithfully report mitochondrial physiology have been developed by replacing glucose in the media with galactose and glutamine as the only oxidizable substrates (Rossignol *et al*., 2004). Since cells cultured in galactose are unable to generate sufficient ATP from glycolysis they are forced to rely on mitochondrial oxidative phosphorylation for ATP generation and consequently are more sensitive to mitochondrial perturbation than cells grown in glucose (Robinson *et al*, 1992). Previous studies have demonstrated that this model is better suited to reveal the effects of xenobiotic-induced mitochondrial dysfunction on ATP content in HepG2 and H9c2 cells (Marroquin *et al*., 2007; Rana *et al*., 2011). Therefore, in chapter 5, the utility of L6 cells to adapt to galactose and exacerbate detection of triazole-induced mitochondrial dysfunction was investigated. This model was also used to investigate whether the increase in HepG2 ATP was a result of glycolytic flux or increased mitochondrial respiratory rate. In addition, further studies were carried out in Chapter 5 with the extracellular flux analyser to simultaneously measure the effects of 177 and 197 on OXPHOS and glycolysis to confirm and further characterise triazole-induced mitochondrial dysfunction.

When a mitochondrial toxicant causes uncoupling of mitochondrial OXPHOS, glycolytic substrates by themselves will not protect against cell cytotoxicity. This is because uncoupling OXPHOS stimulates mitochondrial ATPase (complex V), causing hydrolysis of ATP generated by glycolysis and loss of glycolytic protection (Wang *et al*., 2001). Since the triazoles did not completely deplete ATP in the presence of excess glucose substrate in the media (in a similar manner to AMA) we can hypothesise that the triazole compounds did not induce mitochondrial impairment through uncoupling OXPHOS. Again, this hypothesis was addressed in Chapter 5 using the extracellular flux analyzer.

4.5.2.2 SI triazoles increased mitochondrial superoxide generation in L6 cells

Oxidative stress was hypothesised to play an important role in triazole toxicity based on the *in vivo* toxicogenomic analysis (section 3.5.6.5). Oxidative stress occurs when there is an imbalance between the production of ROS (prooxidants) and the presence

of antioxidants, in favour of prooxidants, resulting in damage to DNA, protein and lipids (Scandalios, 2002). Xenobiotics can dramatically enhance intracellular ROS production in both the cytosol (e.g. by NAD(P)H-cytochrome P450 reductase-mediated redox cycling or CYP uncoupling) and mitochondria (e.g. by inhibition of the ETC and redox cycling) (Turrens *et al*., 2003; Fussell *et al*., 2011).

In this study, the fluoroprobes DHE and MitoSox were used to detect the relative increase in cytosolic and mitochondrial-derived superoxide ($O_2^{\bullet-}$), respectively. Importantly, experiments carried out with 177 and 197 alone (without either probe) demonstrated that the triazoles did not produce an autofluorescence that would interfere with the fluorescence produced by the fluoroprobes. This is a problem with some compounds, such as doxorubicin, which autofluoresces at a similar wavelength to DHE and MitoSox, and therefore has the potential to yield false positive signals at high concentrations (Mukhopadhayay *et al*., 2007).

The specificity of each probe for detecting cytosolic and mitochondrial derived $O_2^{\bullet-}$ is an important consideration. MitoSox is comprised of DHE conjugated to a triphenylphophonium (TPP^+) group, which facilitates accumulation into the mitochondria in response to negative membrane potential (Mukhopadhyay *et al*., 2007). Given that DHE probes are relatively large hydrophobic molecules that are able to readily enter the mitochondrial matrix, they can potentially detect $O_2^{\bullet-}$ in the mitochondrial matrix. However, a study in skeletal muscle mitochondria has determined that DHE is unable to detect $O_2^{\bullet-}$ in the mitochondrial matrix (Muller, *et al*., 2004). The authors speculated that while DHE is able to reach the mitochondrial matrix, it is vastly outcompeted for reacting with $O_2^{\bullet-}$ by MnSOD (~10µM). Thus, DHE is able to detect $O_2^{\bullet-}$ extramitochondrially, but not $O_2^{\bullet-}$ in the mitochondrial matrix (Muller, *et al*., 2004). In contrast, the rate constant between $O_2^{\bullet-}$ and MitoSox ($7x10^7 M^{-1}s^{-1}$) is much higher than with DHE ($10^5 M^{-1}s^{-1}$), and so it is able to detect $O_2^{\bullet-}$ in the mitochondria by efficiently competing with MnSOD (Janes *et al*., 2004). In addition, MitoSox is concentrated in the mitochondria up to 1000-fold compared to the medium, meaning high intramitochondrial concentrations allow MitoSox to compete with MnSOD for $O_2^{\bullet-}$ (Robinson *et al*., 2006).

Since the relative fraction of $O_2^{\bullet-}$ reacting with SOD is unknown, detection of $O_2^{\bullet-}$ with DHE and MitoSox is only a semiquantitive technique (Robinson *et al*., 2006). In addition, due to differences in the accumulation of DHE and MitoSox, it is not possible to directly assess $O_2^{\bullet-}$ production in each compartment by comparing the fluorescence intensities between the two probes (Robinson *et al*., 2006). Indeed, in this study, DHE had a higher basal level of fluorescence than MitoSox. Therefore, to ascertain a semiquantitive and relative increase in $O_2^{\bullet-}$ in the cytosol and mitochondria, the data were normalised to control cells loaded with DHE and MitoSox. By comparing the relative increase in fluorescence from control, an estimate on the increase in $O_2^{\bullet-}$ in the cytosol and mitochondria following treatment could be made.

Treatment with 177 and 197 resulted in a time- and concentration- dependent increase in both MitoSox and DHE fluorescence, although the relative increase in MitoSox fluorescence was significantly higher than DHE after 1 and 24 hours. Importantly, from 1 to 24 hours, the level of MitoSox increased dramatically with 177 and 197, while there was only a very small increase in DHE fluorescence. These results suggest that 177 and 197 both induced $O_2^{\bullet-}$ production in L6 cells, and that the induction of $O_2^{\bullet-}$ generation is an early consequence of triazole treatment. Furthermore, the significant increase in MitoSox relative to DHE suggests that the mitochondria is the primary source of triazole-induced $O_2^{\bullet-}$ generation. The rapid generation (1 hour) of a significant quantity of mitochondrial-derived $O_2^{\bullet-}$ production is consistent with mitochondrial dysfunction (ATP depletion) after only 2 hours treatment with 177 and 197. However, from this data, it was not possible to deduce if $O_2^{\bullet-}$ production occurred prior to or in parallel with ATP depletion. In addition, 197 induced more $O_2^{\bullet-}$ than 177 at equivalent concentrations, which may explain why 197 was more potent at depleting ATP and cell viability levels than 177. There are two potential mechanisms by which 177 and 197 could increase the rate of mitochondrial $O_2^{\bullet-}$ production. The first is inhibition of the electron transport chain, which would increase the reduction level of carriers located upstream of the inhibition site. For example, rotenone inhibits the CoQ-binding site in complex I, which leads to a back up

of electrons onto FMN resulting in production of $O_2^{\bullet-}$ (Murphy, 2009). The second mechanism is redox cycling, where xenobiotics may accept an electron from a respiratory chain carrier and transfer it to O_2, stimulating $O_2^{\bullet-}$ formation without inhibiting the respiratory chain (Turrens, 2003). Whatever the mechanism of mitochondrial-derived $O_2^{\bullet-}$, these results are consistent with ATP depletion and the role of mitochondrial dysfunction in triazole toxicity.

After 24 hour treatment, 177 and 197 induced a slightly greater amount of mitochondrial-derived $O_2^{\bullet-}$ than AMA, although the level of DHE fluorescence induced by AMA was significantly greater than with 177 and 197. The large increase in AMA-induced cytosolic derived $O_2^{\bullet-}$ is expected because AMA inhibits complex III of the ETC, which releases $O_2^{\bullet-}$ to both sides of the inner mitochondrial membrane (Han *et al*., 2003; Muller *et al*., 2004). Since 177 and 197 induced a similar amount of MitoSox fluorescence as AMA, without the subsequent equivocal increase in DHE, we can hypothesise that inhibition of complex III is not the mechanism of triazole-induced mitochondrial $O_2^{\bullet-}$. In contrast to complex III, $O_2^{\bullet-}$ produced at complex I of the ETC is released exclusively into the mitochondrial matrix and no detectable levels escape intact mitochondria (Muller *et al.*, 2004). It is therefore possible that complex I is the site of triazole-induced $O_2^{\bullet-}$ in the mitochondria, which is plausible given the potential for complex I to produce a large amount of $O_2^{\bullet-}$ (Murphy, 2009).

4.5.2.3 NAC inhibited triazole-induced superoxide production and ATP depletion

The antioxidant NAC dose-dependently decreased the production of MitoSox fluorescence induced by 177 and 197 treatment. Although NAC was unable to completely prevent an increase in MitoSox fluorescence, it was able to significantly reduce it by ~4 fold at the highest 177 and 197 concentrations. The ability of NAC to reduce triazole-induced MitoSox fluorescence was confirmation that the triazoles increased mitochondrial $O_2^{\bullet-}$ production. Previous studies have demonstrated the ability of NAC to protect against mitochondrial $O_2^{\bullet-}$ (as measured by MitoSox) induced by mitochondrial toxicants (Yang and Hekimi, 2010; Kuznetsov *et al*., 2011). For example, NAC was able to prevent MitoSox fluorescence increase by paraquat treatment (Yang and Hekimi, 2010), which generates mitochondrial $O_2^{\bullet-}$ by redox

cycling at complex I of the mitochondrial inner membrane (Cocheme and Murphy, 2008). The antioxidant effect of NAC is achieved through numerous mechanisms. NAC has a thiol (SH)- group, which enables it to directly scavenge ROS, such as $O_2^{\bullet-}$ and H_2O_2 (Winterburn and Metodiewa, 1999; Benrahmoune *et al*., 2000) and studies have shown that it has an equivalent efficacy to SOD at reducing $O_2^{\bullet-}$ (Luo *et al*., 2009). Deacteylation of NAC also leads to the formation of cysteine, which is a precursor for glutathione (GSH) synthesis. GSH itself is one of the most important antioxidants, able to directly scavenge free radicals and provide reducing equivalents for activity of the antioxidant enzyme, GSH peroxidise (Gibson *et al*., 2009). NAC and GSH are both able to detoxify redox cycling organic chemicals, such as quinones, by direct covalent binding (Xiao *et al*., 2003; Li *et al*., 2009a). In addition to these effects, NAC has been shown to activate nuclear transcription factor kB (NFkB) and thereby enhance the expression of manganese superoxide dismutase (MnSOD) (Murley *et al*., 2001; Barreiro *et al*., 2005). This is significant for mitochondrial superoxide production, since MnSOD is a mitochondrial specific antioxidant that catalyses dismutation of $O_2^{\bullet-}$.

The role of mitochondrial $O_2^{\bullet-}$ in triazole-induced ATP depletion was investigated using NAC. The results showed that NAC was able to prevent ATP depletion induced by 177 and 197, which indicates that ATP depletion was the result of mitochondrial $O_2^{\bullet-}$ production. Thus, mitochondrial $O_2^{\bullet-}$ is the principal factor contributing to triazole-induced mitochondrial dysfunction. Experiments with ETC inhibitors (such as AMA) have shown that NAC is able to protect against mitochondrial derived $O_2^{\bullet-}$ production, but not against ATP depletion (Watabe and Nakaki, 2007). This implies that the triazoles did not inhibit the mitochondrial ETC to induce $O_2^{\bullet-}$, otherwise ATP would have depleted regardless of the antioxidant effect of NAC. Therefore, we can hypothesise that the triazole compounds redox cycle to generate $O_2^{\bullet-}$ and that this redox cycling takes place in the mitochondria. The specificity of triazoles to induce mitochondrial $O_2^{\bullet-}$ production may be because these compounds accumulate within mitochondria. Since triazole-induced $O_2^{\bullet-}$ production was primarily limited to the mitochondrial matrix, it is possible that the reduction site for redox cycling would be complex I of the mitochondrial membrane. In addition, the inhibitory effects of NAC

on triazole ATP depletion could have been attributable to NAC covalently binding to redox cycling 177 and 197, thereby limiting their ability to induce mitochondrial superoxide. Whatever the exact contributions to the antioxidant effect, NAC is able to interfere with $O_2^{\bullet-}$ generation and prevent ATP depletion following triazole treatment.

4.5.2.4 SI triazoles induced apoptosis in L6 cells

Based on the *in vivo* toxicogenomics data, it was hypothesised that the cell death endpoint of triazole treatment was a caspase-mediated apoptotic form of programmed cell death. The evidence of increased mitochondrial ROS production and subsequent mitochondrial dysfunction coupled with the decrease in cell viability add weight to this hypothesis, strongly implicating apoptotic cell death in triazole treated L6 cells. ROS production by mitochondria results in oxidative damage to mitochondrial proteins, membrane and DNA, impairing the ability of the mitochondria to synthesize ATP and carry out a range of metabolic functions, such as the TCA cycle and fatty acid metabolism (Murphy, 2009). Considerable mitochondrial oxidative damage can cause opening of the mitochondrial permeability transition pore (MPTP), loss of mitochondrial membrane potential and release of pro-apoptotic proteins, cytochrome c and AIF into the cytosol, resulting in caspase activation and DNA fragmentation (Elmore, 2007).

Treatment with 177 and 197 resulted in a dose-dependent increase in apoptosis as demonstrated by caspase 3/7 activation, phosphatidylserine (PS) externalisation and DNA fragmentation (sub-G1 peak). The dose dependent increase in PS externalisation ($FITC^+$) was coupled with a negligible increase in necrosis staining (PI^+) indicating that the cells were progressing through apoptosis rather than straight to necrosis following 177 and 197 treatment. In addition, there was a time and dose dependent increase in caspase 3/7 activation, which correlated well, temporally with the progression of apoptosis (PS externalisation).

At the highest concentration of 177 (500µM) the level of early apoptosis ($FITC^+$) decreased compared to 400µM 177 and the level of caspase-3/7 activity significantly decreased (at 16 and 24 hours) compared with 250µM. Similarly, caspase-3/7 activity

significantly decreased from 100µM to 200 µM 197. Research indicates that caspase-3 is involved in the regulation of PS externalisation on oxidatively stressed erythrocytes (Mandal *et al*., 2002). This explains why there was a good correlation between the activity of caspase-3 and the level of PS externalisation in response to triazole treatment, which is particularly emphasised at the highest concentration of 177, where a decrease in $FITC^+$ staining (PS externalisation) correlated with a decrease in level of caspase-3/7 activity. Research has shown that caspase activity is affected by both ATP and ROS levels (Hampton and Orrenius, 1997; Hampton *et al*., 2002; Nicotera and Melino, 2004). ATP is essential for energy requiring steps of the apoptotic program, one of which is the formation of the protein complex between Apaf-1, cytochrome c and pro-caspases (Nicotera and Melino, 2004; Jaeschke and Bajt, 2005). Therefore, a lack of ATP at this step prevents caspase-3 activation and subsequent PS externalization. Since ATP levels were severely depleted at the highest concentrations of 177 and 197 (~35% of control), it is possible that there was insufficient ATP to activate caspase-3/7, resulting in a decrease in the apoptotic rate. Caspase activity is also sensitive to ROS levels due to an active cysteine site present in certain caspases, such as caspase-3 (Hampton *et al*., 2002). Research has demonstrated that H_2O_2 is able to inhibit caspase activity (IC50 of 7µM), by oxidation of the cysteine site (Hampton and Orrenius, 1997; Hampton *et al*., 2002). Given that 177 and 197 induced a large amount of mitochondrial $O_2^{\bullet-}$, it is possible that the level of oxidative stress inactivated caspase 3/7-activity. The reduction in caspase 3/7-activity following a high concentration of 177 and 197 could therefore be a result of ATP depletion and/or an increase in mitochondrial $O_2^{\bullet-}$ level. A decrease in caspase activity, due to either oxidation or ATP depletion correlates with a switch from apoptotic to necrotic death (Hampton and Orrenius, 1997; Nicotera and Melino, 2004). Thus, the reduction in caspase activity and apoptotic rate at the highest triazole concentrations may represent a switch from apoptosis to necrosis .

4.5.2.5 SI triazoles induced G_1 cell cycle arrest and hypertrophy in L6 cells

Cell cycle arrest and hypertrophy were two pathways hypothesised to contribute to the toxic effects of SI triazoles following *in vivo* toxicogenomics. The cell viability and apoptosis results add weight to the cell cycle arrest hypothesis given that the amount

of apoptosis (~20% at 400µM 177) did not correlate with the magnitude of decrease in cell viability (~50% reduction with 400µM 177). The results of this study confirmed these hypotheses, with 177 and 197 treatment inducing G_1 cell cycle arrest, with a concomitant increase in cellular hypertrophy. As determined through nocodazole co-treatment, 177 and 197 dose-dependently increased the number of cells that arrested in the G_0/G_1 phase of the cell cycle. The co-treatment with nocodazole also indicated that the effect of triazole treatment on cell cycle was relatively rapid, occurring within 4 hours of treatment.

Cellular hypertrophy was observed clearly after 24 hours triazole treatment, with cell size increasing in a concentration-dependent fashion. Hypertrophy occurs in cardiac and skeletal muscle as a fundamental adaptive process in response to physiological or toxicological stimulation (Hlaing *et al*., 2002). A number of studies have demonstrated the involvement of the cell cycle machinery in the development of hypertrophy in cardiac and skeletal muscle hypertrophy both *in vivo* and *in vitro* (Brooks *et al*., 1998; Hlaing *et al*., 2002; Oyama *et al*., 2011; Choi *et al*., 2011). Research using a mouse muscle cell line (C2C12) showed that during skeletal muscle hypertrophy, the G_1 cell cycle machinery was recruited to regulate the hypertrophic response (Hlaing *et al*., 2002). Similarly, Brooks *et al* (1998) have shown that for cardiac hypertrophic growth to occur, the cell must proceed through G_1 to synthesise the relevant proteins. Therefore, it is probable that the triazole-induced G_1 cell cycle arrest was related to the development of cellular hypertrophy.

Previous studies have shown that ROS play an important role in mediating cell cycle arrest (Shackelford *et al*., 2000; Oyama *et al*., 2011; Panieri *et al*., 2013). Among the various ROS, H_2O_2 is most stable and can reach molecular targets distant from its site of generation, enabling it to modulate/trigger signal transduction pathways. In this study, we showed the triazoles generated a significant amount of mitochondrial-derived $O_2^{\bullet-}$, which would have been converted to H_2O_2 either spontaneously or through a reaction catalysed by mitochondrial MnSOD (Turrens, 2003). DNA is particularly sensitive to H_2O_2, as oxidative damage can result in single and double-strand breaks and base adducts (Houtgraaf *et* al., 2006). Research in male Wistar rats

has shown that DNA damage induced by oxidative stress is able to increase expression of p53 and arrest cells at the G1/S checkpoint or induce apoptosis (Kumar *et al*., 2009). Previous studies have also determined that cell cycle arrest precedes the development of hypertrophy following an oxidative stress insult (Oyama *et al*., 2011). Interestingly, Panieri *et al* (2013) have demonstrated that the site of ROS generation is an important determinant for cell fate. They found that mitochondrial derived H_2O_2 resulted in G_1 cell cycle arrest, whereas exogenously generated H_2O_2 resulted in G_2/M –phase arrest. Therefore, it is probable that through mitochondrial H_2O_2 generation, the triazoles were able to mediate oxidative stress effects in the cytosol and nuclear compartments and thereby signal G_1 cell cycle arrest and subsequent hypertrophy. The acute generation of mitochondrial $O_2^{\bullet-}$ (1 hour) and early cell cycle arrest (4 hours) induced by 177 and 197 supports this hypothesis. The decision of the L6 cells to undergo either cell cycle arrest and hypertrophy, or cell death through either apoptosis or necrosis following triazole treatment was attributable to the amount of ROS produced and the availability of ATP. The reason some cells may undergo cell cycle arrest, while others proceed to apoptosis could be due to heterogeneous antioxidant levels within a given population of cells (Chen *et al.*, 2000).

4.6 Conclusions

- The organ-specific cell lines accurately reflected the *in vivo* target organ toxicity profiles of the SI compounds, thereby confirming other studies that organ specific cell lines have the potential to predict target organ toxicities *in vivo*. These results also highlight the importance of testing in organ-specific cell lines to achieve maximal sensitivity to compounds eliciting organ-specific toxicities.

- The parent SI compounds were toxic to their target-organ cell lines suggesting that metabolic bioactivation is not required for them to elicit a toxic response. This is an important consideration when using *in vitro* models, as certain compounds require expression of specific metabolism genes to elicit a toxic response.

- The toxicity pathways identified using *in vivo* toxicogenomics translated into the *in vitro* model system accurately (table 4.3), providing further validation that these models may be useful to predict skeletal muscle toxicity. Concomitantly, these results provide validation for the *in vivo* toxicogenomics data. This data also provides convincing evidence that mitochondrial dysfunction is likely the primary toxicity target of SI triazoles 177 and 197.

***In vivo* hypotheses on triazole toxicity**	**Effect of the triazoles on an *in vitro* skeletal muscle model (L6)**
Mitochondrial Dysfunction	>177 and 197 depleted ATP prior to a decrease in cell number, which is indicative of mitochondrial dysfunction.
Oxidative stress	>177 and 197 induced mitochondrial $O_2^{\bullet-}$ production after only 1 hour treatment, which was significantly reduced by addition of the antioxidant, NAC. >NAC was able to significantly reduce 177 and 197-induced ATP depletion suggesting that mitochondrial $O_2^{\bullet-}$ played a key role in triazole-induced mitochondrial dysfunction.
Cell death (apoptosis)	>177 and 197 resulted in a caspase-mediated apoptotic cell death.
Cell Cycle	>177 and 197 induced a G_1 cell cycle arrest within 4 hours of treatment.
Hypertrophy	>177 and 197 significantly increased cell size after 24 hours.

Table 4.3 Concordance between the pathways effected *in vivo* and *in vitro* in skeletal muscle.

CHAPTER FIVE

Development of an *in vitro* skeletal muscle model that more sensitively detects mitochondrial toxicity

Chapter 5: Development of an *in vitro* skeletal muscle model that more sensitively detects mitochondrial toxicity

5.1 Introduction

Using *in vivo* toxicogenomics analysis (chapter 3), mitochondrial dysfunction and oxidative stress pathways were hypothesised as potential mechanisms of SI triazole toxicity. These hypotheses were investigated with an L6 skeletal muscle cell line (chapter 4), which confirmed the findings *in vivo*. *In vitro,* the triazoles increased the production of mitochondrial-derived $O_2^{\bullet-}$ and depleted ATP production in a time and concentration-dependent fashion. Experiments with the antioxidant NAC demonstrated that mitochondrial $O_2^{\bullet-}$ generation was responsible for the depletion of ATP, thereby substantiating mitochondrial $O_2^{\bullet-}$ and presumed oxidative stress as the principal factor in triazole-induced mitochondrial dysfunction. However, the L6 cell model system used for these experiments was cultured in supraphysiological glucose conditions (25mM), thereby facilitating flux through the glycolytic pathway to produce requisite ATP following impairment of the mitochondria. As a consequence, the glucose cultured cells were probably more resistant to mitochondrial toxicity. Therefore, in this chapter, a skeletal muscle *in vitro* model system that more sensitively detected mitochondrial toxicity was developed and validated.

5.1.1 Xenobiotic-induced mitochondrial toxicity

In most mammalian cells, mitochondria generate all of the required ATP required by the cell to perform 'work'. Consequently, compounds that undermine mitochondrial function will correspondingly impair cell viability, and, depending on the severity, lead to deleterious injury of organ systems. Recently, xenobiotic-induced mitochondrial toxicity has been recognized to contribute to toxicities of many organs, such as the liver (Marroquin *et al*., 2007; Dykens *et al*., 2008), heart (Pointon *et al,* 2010) and skeletal muscle (Bouitbir *et al*., 2011). Indeed, research has indicated that mitochondrial dysfunction played a role in the toxicity that forced the withdrawal of a range of compounds, including troglitazone (hepatotoxicity) and cerivastatin (skeletal muscle toxicity) (Charaten, 2001; Dykens and Will, 2007; Lauer *et al*, 2009). Skeletal

muscle systems are particularly susceptible to mitochondrial toxicity, due to their high metabolic activity and mitochondrial content (Neustadt and Pieczenik, 2008), as well as a reduced antioxidant capacity (compared to the liver and heart) (Vendetti *et al*., 2001; Bouitbir *et al*., 2011). Many different classes of xenobiotics can exhibit skeletal muscle toxicity through mitochondrial dysfunction, including NRTIs and statins (Scruggs and Naylor, 2008; Bouitbir *et al*., 2011). It is therefore important that compounds with mitochondrial liabilities, particularly to organ systems like skeletal muscle and the liver, are identified early in the R&D process.

5.1.2 Mitochondrial toxicity testing: replacing glucose with galactose in the media increases susceptibility to mitochondrial toxicants

One model that has been developed to improve detection of mitochondrial toxicants early in the R&D process utilizes cells grown in two types of media, one supplemented with high glucose (25mM) and the other with galactose (glucose/galactose model) (Marroquin *et al*., 2007; Dykens *et al*., 2008; Rana *et al*., 2011). Cells grown in high glucose media are able to compensate for mitochondrial impairment by utilizing glycolysis for ATP generation, and therefore, are more resistant to mitochondrial toxicities. Although glycolysis is inefficient, capturing as ATP only 5-6% of potential energy in the glucose substrate when fully oxidized via OXPHOS, the rate of flux through the pathway can be dramatically accelerated so inefficiency of substrate is offset by an abundance of substrate (Robinson *et al*., 1992; Marroquin *et al*., 2007). In contrast, cells grown in galactose as the sole sugar are forced to rely on mitochondrial oxidative phosphorylation (OXPHOS) to meet their energy requirements (Robinson *et al*., 1992; Gohil *et al*., 2010). This is due to the slow metabolism of galactose to glucose-1-phosphate, which means that cells grown in galactose derive 98% of their ATP from glutamine (Reitzer *et al*., 1979; Wagner *et al*., 1991). Indeed, many types of cells (e.g. cancer cells, fibroblasts, and myotubes) grown in galactose have a significantly increased oxygen consumption rate and decreased glycolysis compared to cells cultured in high glucose (Rossignol *et al*., 2004; Marroquin *et al*, 2007; Aguer *et al*., 2011, Domenis *et al*., 2012). Since galactose grown cells (supplemented with glutamine) rely mostly on OXPHOS to produce their ATP, they become more sensitive to mitochondrial toxicants than cells grown in high glucose (Marroquin *et al*., 2007;

Dykens *et al*., 2008). Conversely, if compounds are more toxic to high glucose than galactose grown cells, they are thought to adversely affect the glycolytic pathway (Gohil *et al*., 2010). The glucose/galactose model has been successfully implemented with liver (HepG2) and cardiac (H9c2) cell lines to identify mitochondrial toxicants (Marroquin *et al*., 2007; Dykens *et al*., 2008; Rana *et al*, 2011). However, to date, this model has not been applied to a skeletal muscle cell line to assess mitochondrial toxicity. Given that certain compounds exhibit organ-specific sensitivities, including the triazoles (chapter 4), it would be valuable to have a high-throughput, *in vitro* skeletal muscle screen for mitochondrial toxicants.

Previous studies have been carried out with human primary skeletal muscle cells to investigate the utility of the galactose model for studying metabolic disorders like type 2 diabetes (Aguer *et al*., 2011; Kase *et al*., 2013). These studies demonstrated that, like HepG2 and H9c2 cells, primary skeletal muscle cells are able to adapt to galactose and provide a useful cell model for metabolic studies related to disorders involving mitochondrial impairments. Although primary muscle cells are a good model for studying mitochondrial impairment, they are low-throughput, costly and require the use of animals. Therefore, a skeletal muscle cell line that accurately reflects the *in vivo* situation would constitute an excellent model to identify compounds that have deleterious effects on skeletal muscle mitochondrial function. Since the L6 skeletal muscle cell line accurately reflected the mitochondrial *in vivo* toxicity profile (of the triazole compounds, chapter 4), this cell line represents a suitable model for mitochondrial toxicity testing.

5.2 Aims and Hypothesis

The overall aim of this chapter was to develop an *in vitro* skeletal model system that more sensitively reports mitochondrial toxicity. It was hypothesised that replacing glucose with galactose in the culture media of L6 skeletal muscle cells would increase their reliance on mitochondrial OXPHOS, thereby making them more sensitive to mitochondrial toxicants.

Specific aims

- To establish whether L6 cells can tolerate a switch to galactose as an oxidizable substrate. To assess if L6 cells have truly adapted to galactose the cells will be evaluated with known mitochondrial toxicants (rotenone and antimycin A).

- To characterise the cellular bioenergetic function of L6 cells cultured in galactose and glucose media. The effects of each media type on oxygen consumption rate (OCR) and extracellular acidification rate (ECAR) will be measured to assess mitochondrial function and glycolysis, respectively.

- To determine the toxicity of the SI triazole compounds in glucose and galactose cultured L6 cells to confirm their mitochondrial toxicity.

- To further investigate the mechanism of SI triazole mitochondrial toxicity by assessing the effects of 197 on the cellular bioenergetic function (OCR and ECAR) of L6 cells cultured in glucose and galactose media.

5.3 Experimental Approach

5.3.1 Cell culture

5.3.1.1 High-glucose media

L6, H9c2 and HepG2 cell lines were grown in DMEM containing 25mM glucose (high glucose), 1mM sodium pyruvate, supplemented with 5mM HEPES, 10%FBS, and penicillin-streptomycin and kept in 5% CO_2 at 37^{o}C (section 2.2.7.1). Cells were maintained in T.75 flasks and were subcultured at 70% confluence by trypsinization for experiments, as described in section 2.2.7.1.

5.3.1.2 Galactose adaptation

L6, H9c2 and HepG2 cell lines were cultured in DMEM containing 10mM galactose, 1mM sodium pryruvate, supplemented with 2mM glutamine (6mM final), 5mM HEPES, 10%FBS and penicillin-streptomycin and kept in 5% CO_2 at 37^{o}C. Cells were maintained in T.75 flasks and allowed to adapt to galactose media for a minimum of 7 days before experiments. To evaluate if the cells had adapted to galactose, they were treated with mitochondrial toxicants, antimycin A and rotenone and toxicity in galactose compared with the toxicity in glucose.

5.3.1.3 Cell counting

CPD and DT were calculated to assess cell growth in glucose and galactose media. Once the cells had reached 70% confluence and still in the exponential phase of growth, the cells were trypsinised (section 2.2.7.1) and counted using a haemocytometer. CPD and DT were calculated for L6, H9c2 and HepG2 as described in section 2.2.7.1.

L6 cells cultured in glucose and galactose were seeded at 5x10^{5} cells/T.75 flasks and allowed to adhere overnight. After 24 and 48 hours, cells were counted using a haemocytometer (section 2.2.7.1).

5.3.2 Compound preparation

All commercially available compounds were prepared in their respective solvents and stored as previously described in section 2.2.7.2. SI compounds were made up in 100mM DMSO stocks and stored at -20^{o}C.

5.3.3 Measurement of cellular ATP content

To determine the ATP content of L6 cells cultured in glucose and galactose media, cells were seeded into white 96-well microplates with clear bases at a density of $2x10^4$ cells/well and allowed to adhere for 4 hours. ATP content was determined using the ATP determination kit as described in section 2.2.8.2.

5.3.4 Treatment with mitochondrial toxicants

Cells cultured in either glucose or galactose were seeded in white 96-well microplates with clear bases at a density of $1x10^4$ cells/well for L6, $7.5x10^3$ cells/well for H9c2 and $1x10^4$ cells/well for HepG2 and incubated for 24 hours, by which point the cells were ~70-80% confluent. Cellular treatments were made as follows:

Evaluate galactose adaptation: Cells were treated with 150nM antimycin A or 500nM rotenone for 24 hours in 100µL media. The final concentration of DMSO in the culture media was 1%. ATP content was determined using the ATP determination kit as detailed in section 2.2.8.2).

Dose responses: Stock compounds were prepared in DMSO at 100x treatment concentration for each compound tested. The highest aqueous soluble concentration for each SI compound, equated to 50mM (500µM), 20mM (200µM) and 10mM (100µM) for 177, 197 and 907, respectively. The stock concentration of troglitazone and antimycin A were 30mM and 150µM, respectively. In a clear 96-well plate (compound plate), 8 doses of each compound were prepared using a 2-fold dilution scheme. For 177, the doubling dilutions were made from 40mM so the concentrations were comparable with 197 and 907, although an additional treatment of 500µM was prepared from a 50mM stock. A 1:100 dilution for each compound was made in high glucose or galactose growth media to obtain 1 x compound dilutions for the

immediate treatment of cells. Media was removed from the cell plates and 100µl of compound/media mixture was dispensed into each well. The final DMSO concentration in each well was 1%. The concentration ranges were 500µM - 6.25µM, 200µM –1.56 µM, 100µM-0.78µM, 150nM-1.1nM and 300µM-2.3µM for 177, 197, 907, AMA and troglitazone, respectively.

5.3.5 Measurement of mitochondrial superoxide production

L6 cells cultured in either glucose or galactose media were seeded at $2x10^5$ cells/well in 6-well plates and incubated for 24 hours. Mitochondrial $O_2^{\bullet -}$ levels were determined using MitoSox as described in section 2.2.12. For assessment of mitochondrial toxicity, cells were treated with 197 (50 and 100µM) and AMA (50 and 100µM) for 1 hour before MitoSox measurement.

5.3.6 Measurement of the mitochondrial membrane potential

L6 cells cultured in either glucose or galactose media were seeded at $2x10^5$ cells/well in 6-well plates and incubated for 24 hours. Mitochondrial membrane potential was determined using MitoTracker Red CMXRos, as described in section 2.2.13.

5.3.7 Protein content of L6 glucose and galactose cultured cells

L6 cells cultured in either glucose or galactose media were aliquoted into a clear 96-well with 4 cell densities in a 2-fold dilution scheme ranging from $1.6x10^5$ to $4x10^4$ cells/well. The cells were centrifuged for 5 minutes at 450xg, washed with PBS, centrifuged for a further 5 minutes at 450xg, the supernatant discarded and the cells were lysed as detailed in section 2.2.15. Relative protein content was measured using the Bradford Reagent as detailed in section 2.2.16. Bradford reagent (245µl) was added to a clear 96-well plate and 5µl of each sample was added was mixed at a medium speed on a shaker for 30 seconds. Absorbance was measured at 595nm after 30 minutes and the absorbance values of glucose- and galactose-cultured cells were plotted for comparison.

5.3.8 XF Seahorse extracellular flux analysis

Rates of glycolysis and mitochondrial respiration (OXPHOS) were determined by measuring proton release (extracellular acidification rate (ECAR)) and oxygen consumption rate (OCR) using an XF24 extracellular flux analyser. The XF24 creates a transient, 7µl chamber in specialized microplates and uses fluorescent sensors to measure extracellular oxygen consumption (OCR) and extracellular acid release (ECAR) in real time (Ferrick *et al*., 2008). Thus, the rate of oxygen consumption and proton production can be measured across several samples at a time.

5.3.8.1 XF24 assay

The XF24 assay was carried out as described in section 2.2.14.1. Cells were seeded in XF24 cell culture plates using a 2-step seeding process to ensure an even monolayer, and incubated for 16 hours in 5% CO_2 at 37^{o}C. The sensor cartridge was prepared the night before the experiments. Measurements of extracellular flux were made in unbuffered media, supplemented with either 25mM glucose or 10mM galactose. For these experiments, media was changed 30 minutes prior to the start of the assay and the cells incubated at 37^{o}C without CO_2. While the cell culture plate was equilibrating in unbuffered media, the compounds for the mitochondrial stress kit were prepared to 10 x concentrated stocks and loaded into the correct ports in the XF sensor cartridge. The final treatment concentrations for oligomycin, FCCP and AMA were 800nM, 800nM and 200nM, respectively. The XF sensor was equilibrated to 37^{o}C (without CO_2) for 10 minutes and loaded into the XF24 extracellular flux analyzer to calibrate. After calibration, the utility plate was replaced with the cell culture plate and the measurement program implemented. The mix/wait/measure cycle for L6 cells was 2 min/2 min/3 min (figure 5.2).

Normalization to total protein content

Normalization to total protein content in the well following the experiment was used to control for variation in cell number between glucose and galactose cultured cells. At the completion of the XF assay, the cell plate was immediately removed and the media carefully aspirated. The cells were lysed as detailed in section 2.2.15 and protein content measured using the Bradford Reagent as detailed in section 2.2.16.

The protein concentration (mg/ml) was input into the XF analysis software, which automatically normalized the data to protein concentration. OCR was presented as pmoles/min/mg protein and ECAR as mpH/min/mg protein.

5.3.8.2 XF assay treatment protocols

The treatment protocols used in this study are outlined in figure 5.1. A dose response with AMA was carried out using 10, 20, 40 and 80nM AMA (as part of the mitochondrial stress test) in L6 cells cultured in glucose or galactose (figure 5.1 A).

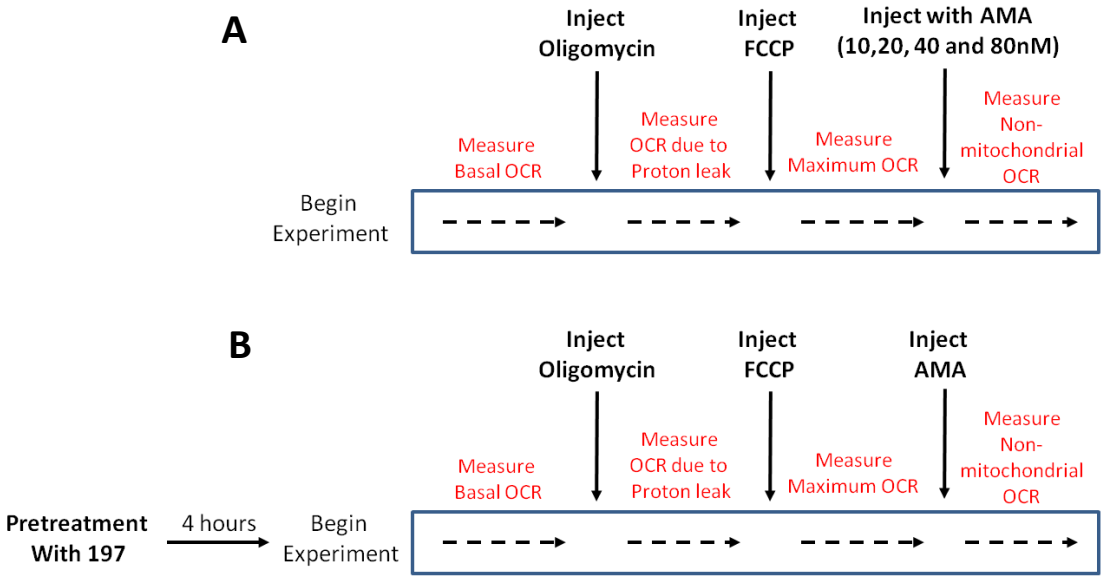

Figure 5.1 (A) Protocol for antimycin A dose response in L6 glucose and galactose cells. Basal OCR and ECAR were measured and then mitochondrial function was assessed using the mitochondrial stress test, with 800nM oligomycin, 800nM FCCP and an AMA dose response (10, 20, 40 and 80nM). **(B) Protocol of 197 treatment and mitochondrial stress test**. L6 cells were treated with 197 (50, 100 and 200 µM) for 4 hours outside the instrument. Basal OCR and ECAR were measured and then mitochondrial function was assessed using the mitochondrial stress test (800nM oligomycin, 800nM FCCP and 200nM AMA).

L6 cells cultured in glucose or galactose were treated with 197 (50, 100 and 200µM) in 250µl media for 4 hours before the XF assay was carried out. Final DMSO concentration in the wells was 0.2% DMSO (figure 5.1 B).

5.3.8.3 Analysis of mitochondrial function

The mitochondrial stress test was used to dissect processes that were contributing to overall mitochondrial oxygen consumption. This technique uses selected mitochondrial inhibitors which allow for determination of six main parameters that describe key aspects of mitochondrial function in a cellular context: basal OCR, ATP-linked OCR, proton leak OCR, maximal OCR, reserve capacity, and non-mitochondrial OCR (figure 5.2). These parameters were determined by measuring OCR after the sequential injection of oligomycin (to inhibit the ATP synthase), FCCP (introduces a high artificial conductance into the mitochondrial inner membrane, allowing for maximum electron flux through the ETC and uncoupling electron flow from OXPHOS), and AMA (to inhibit complex III) at the indicated time points, as illustrated in figure 5.2. The area under curve (AUC) was calculated using three data points for: OCR at basal level, oligomycin-insensitive OCR (proton leak), OCR following addition of FCCP (maximal OCR) and OCR after addition of AMA (non-mitochondrial OCR). From these AUC values, the mitochondrial function parameters were calculated as detailed in figure 5.2.

Normalised ratios of mitochondrial function

State apparent is used to determine the apparent respiratory state of the cells. In isolated mitochondrial preparations, when saturating concentrations of substrate are in maximal turnover, and ADP is present, the protonmotive force (pmf) decreases, electron transport accelerates and ATP synthase function is maximal, the mitochondria are in state 3 respiration. When ADP decreases (ATP/ADP ratio reaches equilibrium), pmf increases, proton re-entry through synthase stops, respiration slows and mitochondria are said to be in state 4 (Brand and Nicholls, 2011). As suggested by other studies, it is unlikely that either of these extremes exists for mitochondria in cells and instead some intermediate turnover state, assigned as State 3.5 (the $State_{apparent}$) occurs in the cellular context (Dranka *et al*., 2011). In these experiments, the assumption was made that state 3 respiration was equivalent to the rate measured after addition of FCCP ('state 3_{FCCP}' or 'state 3u') and state 4 was the rate measured after addition of oligomycin ('state $4_{oligomycin}$' or 'state 4o). These

assumptions allow for calculation of the apparent respiratory state of the cells under basal conditions.

The $State_{apparent}$ was calculated from the following equation:

$$State_{apparent} = 4 - \frac{(Basal - Oligo)}{(FCCP - Oligo)}$$

where Basal represents the basal OCR, Oligo represents the oligomycin-insensitive OCR and FCCP represents the FCCP-stimulated OCR. This calculation yields an estimate of relative mitochondrial work being used by the cell under basal condition. The $State_{apparent}$ allows for an index of where cells fall on the scale between State 3 and State 4.

Using the same assumptions regarding the relative state 3 and state 4 respiration, the **respiratory control ratio (RCR)** can be calculated as the state 3u rate divided by state 4o rate. Thus, the RCR is the ratio of the uncoupled rate (FCCP) ('state 3u') to the rate with oligomycin present ('state 4o) (maximal OCR/oligomycin-insensitive OCR).

Coupling efficiency is determined from the change in basal respiration rate on addition of oligomycin and was calculated as the fraction of basal mitochondrial OCR used for ATP synthesis (ATP-linked OCR/Basal OCR).

The fraction of respiration *vs.* the maximal OCR that is used under routine conditions to produce ATP (**Phosphorylating respiration**) was estimated as the ratio between ATP-linked OCR and maximal OCR (FCCP) (ATP-linked OCR/Maximal (OCR).

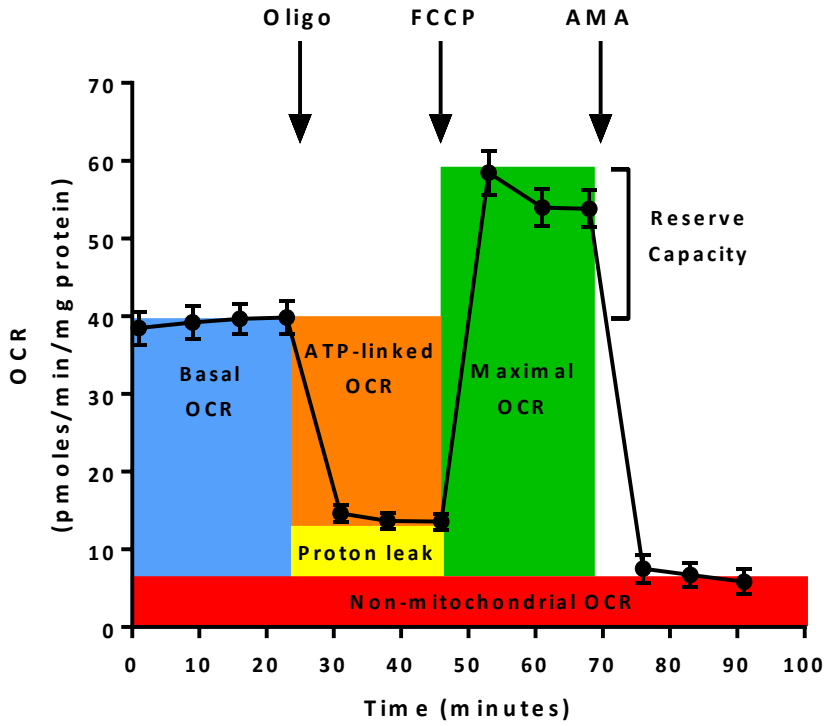

Figure 5.2 A typical L6 glucose grown cell profile of the mitochondrial stress test to assess mitochondrial function. The example is from control L6 cells cultured in glucose. Baseline OCR was measured 3 times for 3 min each separated by a 2min wait and 2 min mix. Following the measurement of basal respiration, oligomycin (800nM) was injected into each well, followed by 3 cycles of; 2 min mix, 2 min wait and 3 min measurement to determine O_2 consumption resulting from proton leak. The difference between the basal OCR and the oligomycin-insensitive OCR yields the amount of O_2 consumption that is ATP-linked. The balance of the basal OCR is comprised of O_2 consumption due to proton leak and non-mitochondrial sources. Then, FCCP (800nM) was injected into each well, followed by 3 cycles of 2 min mix, 2 min wait and 3 min measurement to determine the maximal O_2 consumption that is possible at complex IV. The difference between FCCP rate and basal OCR yields an estimate of the reserve capacity of the cells. Finally, antimycin A (200nM) was injected into each well, followed by 3 cycles of: 2 min mix, 2 min wait and 3 min measurement to determine the rate of O_2 consumption from non-mitochondrial sites.

5.4 Results

5.4.1 Effect of replacing glucose with galactose on cell growth and ATP content

H9c2 and HepG2 cells have previously been shown to successfully adapt to galactose media (Marroquin *et al*., 2007, Rana *et al*., 2011) and so were used in conjunction with L6 cells as positive control cell lines. In addition, they were used to further investigate the SI triazole organ-specific cell line effects in the context of mitochondrial toxicity testing.

Frozen L6, H9c2 and HepG2 cells previously grown in high glucose media were thawed and grown for a minimum of 7 days in either high glucose (25mM) or galactose (10mM) media. The media was changed every 2 days, and the cells subcultured once they had reached 70% confluence. A number of studies have demonstrated that 7 days is sufficient for cells to adapt to galactose media and consequently adjust their cellular bioenergetics (i.e. an increase in OXPHOS) (Gohil *et al*., 2010; Aguer *et al*., 2010; Domenis *et al*., 2012). No significant change in cell morphology or cell death rate was observed in L6, H9c2 or HepG2 cells grown in galactose compared with glucose. Cumulative population doublings were measured over 24, 11 and 13 days for L6, H9c2 and HepG2 cells, respectively and the doubling time (DT) was calculated (figure 5.3 A, B and C). In all three cell lines, growth rates were higher in glucose than galactose media. In glucose, the DT of L6, H9c2 and HepG2 cells was approximately 18, 55 and 39 hours, respectively. In galactose media the DT was longer, taking about 20, 63 and 45 hours for L6, H9c2 and HepG2 cells, respectively (Figure 5.3 D). Consequently, there was a significantly greater number of high glucose than galactose cultured L6 cells after 24 and 48 hours growth (figure 5.3 E).

Previous studies have demonstrated that HepG2 and H9c2 cells both maintain equivalent levels of ATP content when cultured in glucose or galactose media (Marroquin *et al*., 2007; Rana *et al*., 2011). Similarly, no significant difference was found in ATP content between L6 cells grown in glucose or galactose media (figure 5.3 F).

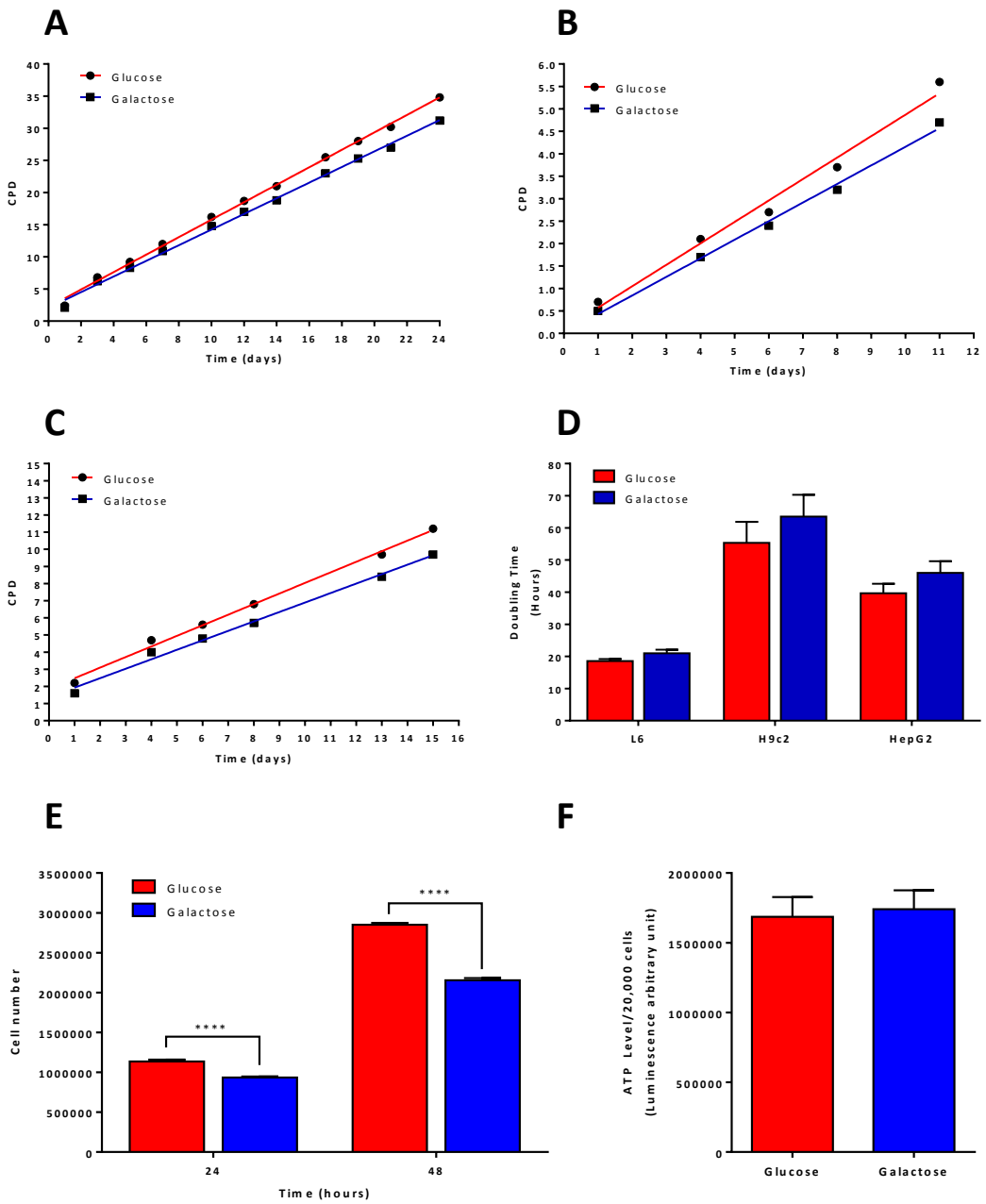

Figure 5.3 Effect of replacing glucose with galactose on cell growth and ATP content. Growth curves of L6 **(A)**, H9c2 **(B)** and HepG2 **(C)** cells cultured in glucose (red) and galactose (blue). **(D)** Doubling time of L6, H9c2 and HepG2 cells cultured in glucose and galactose media. Bars represent the mean +SEM; L6 n=11, H9c2 n=5, HepG2 n=6. **(E)** L6 cells cultured in glucose and galactose media were seeded at a density of $5x10^5$ cells/T.75 flask and cell proliferation was determined after 24 and 48 hours. **(F)** ATP content of L6 cells cultured in glucose and galactose media was compared. Bars represent the mean +SEM; n=3 (****P<0.0001 glucose vs. galactose).

Effect of mitochondrial inhibitors on cells cultured in glucose and galactose

To test that the cells had adapted to galactose media and were consequently more susceptible to mitochondrial insult, both glucose and galactose-grown L6, H9c2 and

HepG2 cells were treated with classical inhibitors of the mitochondria. L6, H9c2 and HepG2 cells were cultured in either glucose or galactose media for a minimum of 7 days and then treated with 150nM AMA (complex III inhibitor) for 24 hours and ATP content was determined (figure 5.4 A).

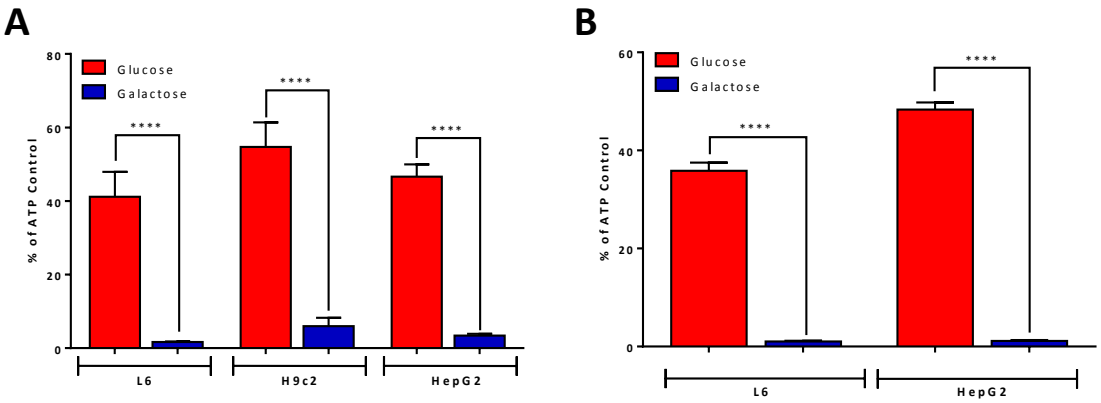

Figure 5.4 Effect of classical inhibitors of mitochondrial function on glucose and galactose-cultured cells. (A) L6, H9c2 and HepG2 cells cultured in either glucose (red) or galactose (blue) media for a minimum of 7 days were treated with 150nM AMA for 24 hours and ATP content was assessed. **(B)** L6 and HepG2 cells cultured in glucose or galactose media for a minimum of 7 days were treated with 500nM rotenone for 24 hours and ATP content was assessed. Results represent mean +SEM; n=3-5 (****P<0.0001 glucose vs. galactose).

In glucose-cultured cells, L6, H9c2 and HepG2 cellular ATP concentrations were reduced to approximately 40, 55 and 45 % of control, respectively. In contrast, cells grown in galactose were highly susceptible and L6, H9c2 and HepG2 ATP levels were depleted to 1.5, 6.0 and 3.5% of control, respectively. As further confirmation that the L6 cells had adapted, L6 cells (and HepG2 cells as a positive control) cultured in glucose or galactose media were treated for 24 hours with rotenone (complex I inhibitor) and ATP content was determined (figure 5.4 B). Similarly to AMA, rotenone reduced ATP levels of L6 and HepG2 glucose-grown cells to 35 and 48% of control and galactose grown cells to 1.0 and 1.1% of control. Taken together, these results provide evidence that L6, H9c2 and HepG2 cells are able to adapt to galactose after 7 days in culture and are subsequently more susceptible to mitochondrial toxicants. Previous groups have referred to the method of culturing cells in glucose and galactose media to identify mitochondrial liabilities as a 'model' system (Marroquin *et al.*, 2007;

Dykens *et al*., 2008) and so for the remainder of this chapter, this model will be referred to as the 'glucose/galactose' cell model.

5.4.2 Effect of galactose on L6 cellular bioenergetic function

To assess the effects of galactose on L6 cellular bioenergetics, extracellular flux (XF) 24 analysis was used to determine the rates of glycolysis and mitochondrial respiration (OXPHOS) by measuring proton release (extracellular acidification rate (ECAR)) and oxygen consumption rate (OCR) (Ferrick *et al*., 2008).

5.4.2.1 Optimization of L6 glucose and galactose cells for XF24 analysis

In the first series of experiments, the optimal number of L6 glucose and galactose cultured cells needed to obtain a measureable OCR and ECAR was established (Figure 5.5 A and B).

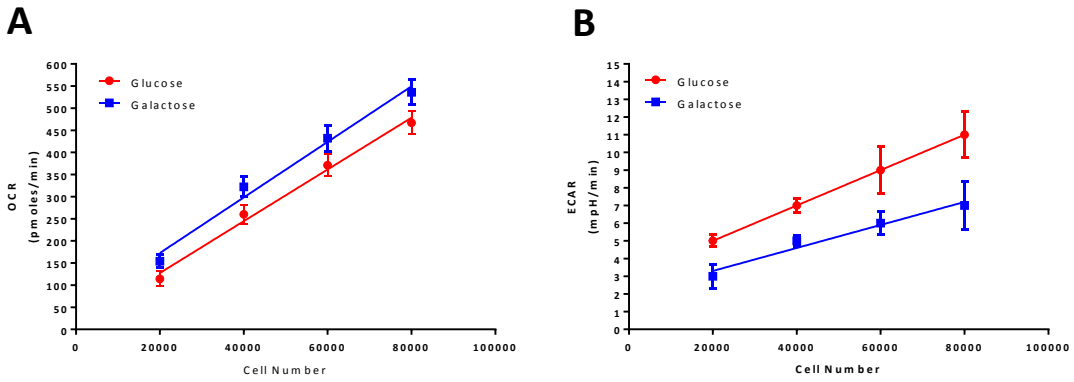

Figure 5.5 Optimization of L6 glucose and galactose-grown cell seeding density for XF24 analysis. XF24 cell culture plates were seeded with L6 cells cultured in either glucose or galactose media for a minimum of 7 days (20,000, 40,000, 60,000 & 80,000 cells/well) and allowed to grow for 16 hours before measurement of (A) OCR and (B) ECAR. Results represent the mean ±SD; n=5 from one experiment.

In both glucose and galactose media, L6 cells displayed a linear response with regard to cell density from 20, 000-80,000 cells per well both in measured OCR and ECAR. For subsequent experiments a seeding density of 60,000 cells per well was selected to allow for optimal detection of changes in OCR and ECAR in L6 cells cultured in glucose and galactose.

Since there was a difference in the growth rate between L6 cells cultured in glucose and galactose media (figure 5.3 A, D and E), it was important to control for variation in cell number. Therefore, normalization to total protein was used to account for variation in cell number for the XF experiments. To ascertain if this was a feasible method for normalization, the total protein content of L6 cells grown in glucose and galactose media was compared using the Bradford reagent. As shown in figure 5.6, there was no significant difference in total protein content between glucose and galactose-grown L6 cells over a range of seeding densities. Thus, for subsequent experiments, the data was normalized to total protein content.

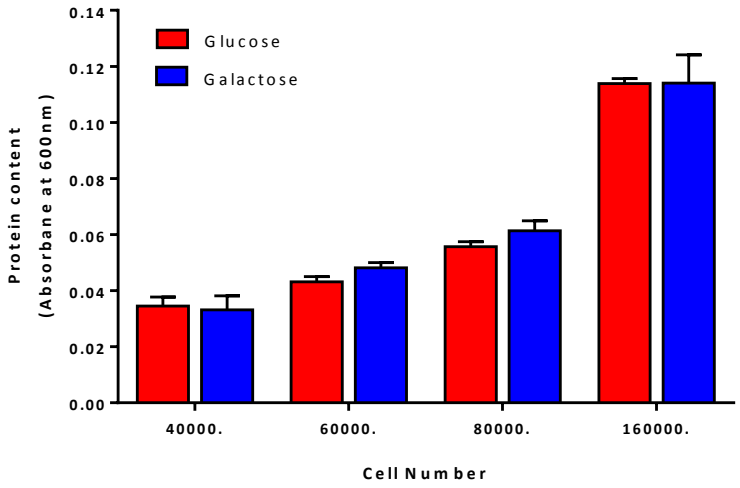

Figure 5.6 Total protein content of L6 cells cultured in glucose and galactose. L6 cells were cultured in glucose and galactose for a minimum of 7 days and total protein content was assessed over a range of cell densities (40,000-160,000 cells). Results represent the mean +SEM; n=3.

5.4.2.2 Effect of galactose on OCR and ECAR in L6 cells

L6 cells cultured in galactose for a minimum of 7 days had increased levels of OXPHOS (Figure 5.7 A) with basal mitochondrial OCR ~50% higher than cells cultured in glucose media (Figure 5.7 B). Conversely, ECAR activity in galactose cells was ~25% lower than in glucose cultured cells, although this did not reach significance (Figure 5.7 B and D). The residual ECAR of galactose cells may be derived from a small 'proton leak' from the respiring mitochondria (Robinson *et al*., 2012). This was confirmed by the differential response of glucose and galactose cells to mitochondrial toxicants (figure

5.7 C). Addition of oligomycin and FCCP to glucose cells increased ECAR, which is attributable to the increased requirement for glycolysis for ATP production. In contrast, addition of oligomycin had no effect on ECAR of galactose cells, although FCCP resulted in a sharp increase (figure 5.7 C). The FCCP-induced increase in ECAR could be due to an increase in the 'proton leak' from the cells following uncoupling of the mitochondrial inner membrane. This was confirmed by addition of AMA, which inhibited the FCCP-induced ECAR stimulation of galactose cells.

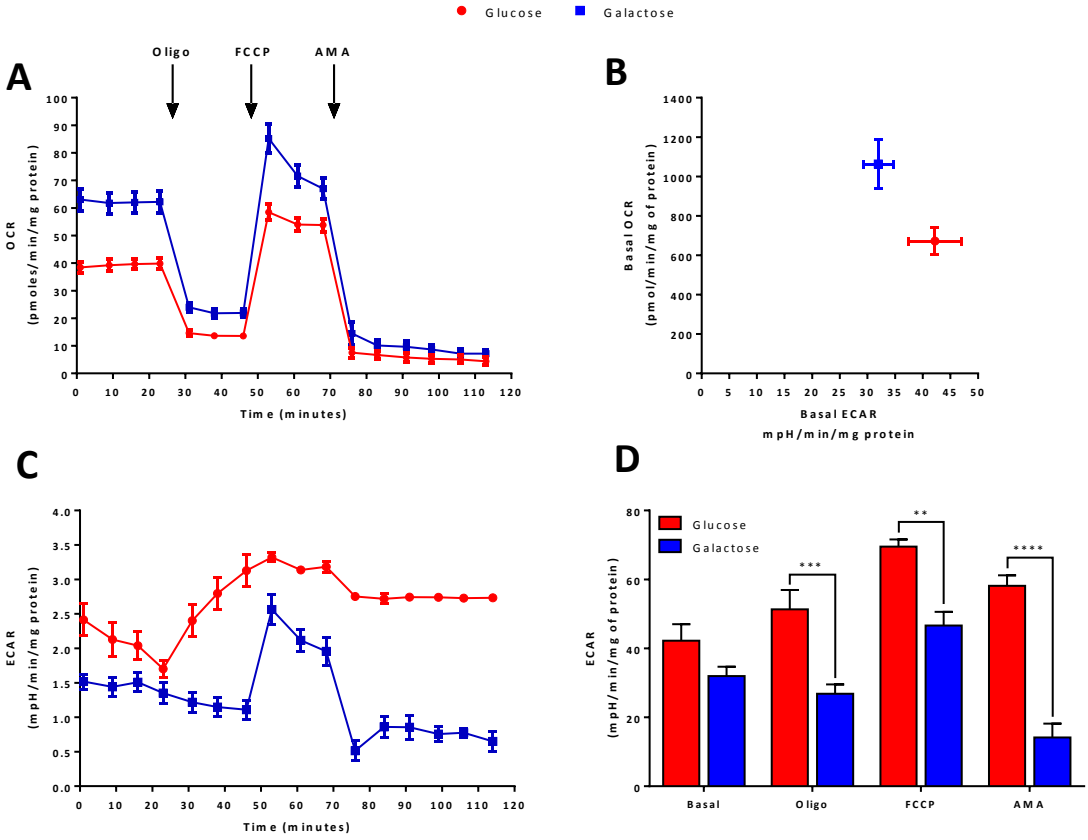

Figure 5.7 Cellular bioenergetics of L6 cells cultured in glucose and galactose using the XF24 analyzer. L6 cells were cultured for a minimum of 7 days in either glucose (25mM) or galactose media (10mM). Real time measurements (mean ± SEM., n=5) of OCR **(A)** and ECAR **(C)** were measured and oligomycin (800nM), FCCP (800nM) and AMA (200nM) injected sequentially as shown **(A, C)**. **(B)** Basal OCR and ECAR values of glucose and galactose cells were plotted to illustrate the difference in metabolic profile (mean ± SEM., n=5). **(D)** Quantitative ECAR analysis of glucose and galactose cells following treatment with the mitochondrial inhibitors. Bars represent mean ± SEM., n=5 (**P<0.01, ***P<0.001, ****P<0.0001 glucose vs. galactose).

Addition of AMA also slightly decreased the ECAR of glucose cells, which may have represented the proportion of 'proton leak' contributing to the ECAR of glucose cells.

As shown in figure 5.7 D, basal ECAR levels of glucose and galactose cells were not significantly different, although following addition of mitochondrial toxicants, ECAR of glucose cells was significantly higher than galactose cells. These results demonstrate that glucose cells were able to up regulate glycolysis to maintain ATP levels following mitochondrial stress, whereas galactose cells could not. Consequently, in galactose cultured L6 cells, there was a higher OCR/ECAR ratio, demonstrating a metabolic dependency on mitochondrial OXPHOS (figure 5.7 B).

5.4.2.3 Effect of galactose on mitochondrial function in L6 cells

The mitochondrial stress test was used to define the mitochondrial function of L6 cells cultured in glucose and galactose media. After basal OCR was established, glucose and galactose cells were exposed to oligomycin, FCCP and AMA at the timepoints indicated (figure 5.8 A).The measurements taken after each injection were used to calculate area under the curve (AUC) values for the mitochondrial function parameters; basal OCR, ATP-linked OCR, proton leak, maximal OCR, reserve capacity and non-mitochondrial OCR (figure 5.8 A and B). As shown in figure 5.8 B, basal OCR, proton leak, ATP-linked OCR and maximal OCR were significantly higher in galactose than in glucose cultured cells. In contrast, the reserve capacity of glucose cells was significantly greater than galactose cultured cells. Figure 5.7 A shows that galactose cells were unable to maintain maximal OCR levels following the addition of FCCP, with the OCR level decreasing to basal OCR levels prior to AMA treatment (15 minutes). This implies that at basal levels, the galactose cells were operating at close to maximal OCR capacity and any increase was unsustainable, resulting in a lower reserve capacity. There was also a trend for a higher non mitochondrial OCR in galactose cells compared to glucose cells, but this did not reach statistical significance (figure 5.8 B).

The mitochondrial function parameters were used to derive normalized respiratory flux control ratios; coupling efficiency, respiratory control ratio (RCR), $State_{apparent}$ and phosphorylating respiration (table 5.1). The advantage of the flux control ratios is that they are internally normalised allowing for accurate comparison between glucose and galactose cultured cells.

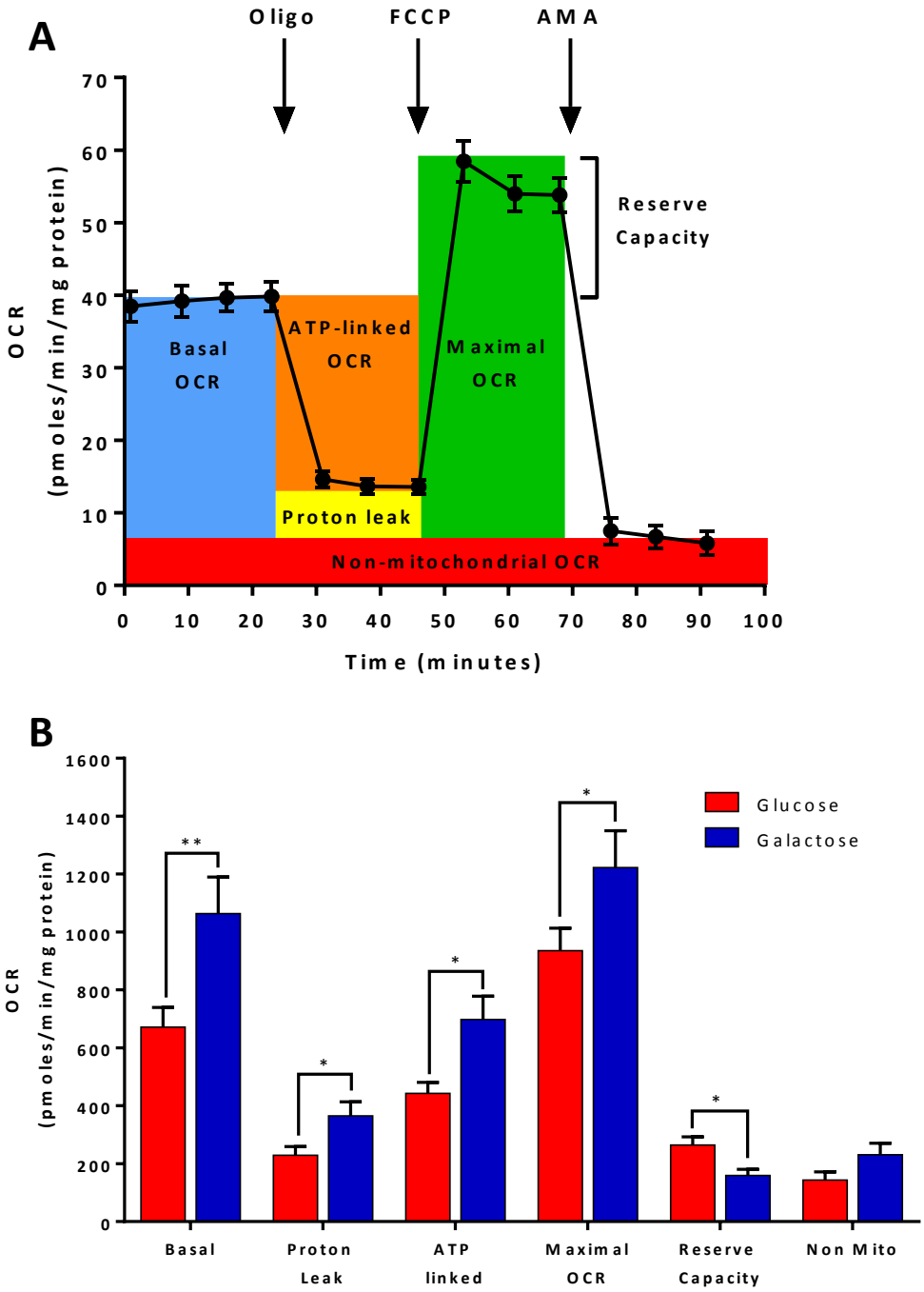

Figure 5.8 Measurement of mitochondrial function in L6 cells cultured in glucose and galactose. (A) Representative profile of the mitochondrial stress test using L6 cells cultured in glucose, showing time course for measurement of OCR under basal conditions followed by sequential addition of oligomycin (800nM), FCCP (800nM) and AMA (200nM). The profile is annotated to show the relative contribution of basal OCR, ATP-linked OCR, proton leak OCR, maximal OCR, reserve capacity, and non-mitochondrial (Non Mito) OCR. **(B)** The AUC for each mitochondrial function parameter was calculated for L6 cells cultured in glucose and galactose cells for a minimum of 7 days and is derived from the from data in figure 5.7 A. Bars represent mean + SEM; n=5 (*P<0.05, **P<0.01 glucose vs. galactose).

Table 5.1 shows that there was no significant difference in coupling efficiency between glucose and galactose cultured cells, indicating that substrate change had no effect on the efficiency of mitochondrial respiration. In both glucose and galactose media, ~66% of cellular OCR was related to ATP synthesis. An equivalent coupling efficiency also demonstrated that the change in proton leak in glucose and galactose cultured cells was proportional to the change in ATP-linked OCR. Thus, proton leak accounted for ~34% of total cellular OCR in both glucose and galactose media cells.

RCR was significantly greater in glucose than galactose cultured cells, which means the mitochondria of glucose cells have a higher capacity (reserve capacity) for substrate oxidation and ATP turnover than galactose cells (Brand and Nicholls, 2011). In addition, a higher RCR in glucose cells correlated with a lower proton leak (Brand and Nicholls, 2011). As with reserve capacity, the lower galactose cell RCR is attributable to the fact that the galactose cell basal OCR level is close to the maximal OCR capacity of the cells.

	L6 cells	
Normalised respiratory flux control ratios	**Glucose**	**Galactose**
Respiratory Control Ratio (RCR)	4.33 ± 0.36	3.43 ± 0.19 **
Coupling Efficiency	0.66 ± 0.02	0.66 ± 0.02
$State_{apparent}$	3.37 ± 0.03	3.19 ± 0.03 *
Phosphorylating respiration	0.47 ± 0.01	0.57 ± 0.02 *

Table 5.1 Normalized respiratory flux control ratios of L6 cells cultured in glucose and galactose. The respiratory control ratio (RCR), coupling efficiency, $State_{apparent}$ and phosphorylating respiration were derived from the mitochondrial parameters shown in figure 5.8 B. Data represents mean ± SEM; n=5 (*P<0.05, **P<0.01 glucose vs. galactose).

$State_{apparent}$ was calculated to determine the apparent respiratory rate in glucose and galactose cells to provide an estimate of the relative mitochondrial work being used by the cells under basal conditions. The galactose cells $State_{apparent}$ (3.19) was significantly closer to state 3 than glucose cells (3.37) were, indicating that galactose cells had an increased mitochondrial workload compared to glucose cells. In addition, the phosphorylating respiration of galactose cells (0.57) was significantly higher than glucose cells (0.47; $p<0.05$). This demonstrates that galactose cells use a greater

proportion of the maximal respiratory capacity (maximal OCR) for ATP production than glucose cells under basal conditions.

Taken together, these results show that culturing cells in galactose media decreased the ECAR levels and increased the OCR levels. Consequently, the mitochondria of galactose cells were operating at a higher level of respiration than glucose cells and so were closer to 'state 3' configuration than glucose cells. This was not due to an increased efficiency of the mitochondrial ETC however, implying OXPHOS complex synthesis or activity regulation. Although at basal levels there was no significant difference between glucose and galactose cells ECAR, under mitochondrial stress, the galactose cells were unable to increase ECAR to account for ATP demand like the glucose cells could.

5.4.3 Effect of galactose on mitochondrial membrane potential and mitochondrial superoxide production

The major component of the mitochondrial electrochemical potential gradient of protons is the mitochondrial membrane potential (ΔΨm), and hence it is an important measure of how the mitochondria are functioning (Serviddio and Sastre, 2010). The ΔΨm of L6 cells cultured in glucose and galactose media was assessed using MitoTracker Red CMXRos. Briefly, MitoTracker Red CMXRos is a fluorescent probe that passively diffuses through the plasma membrane of viable cells and is selectively sequestered in mitochondria with an active ΔΨm and permits the examination of the ΔΨm in adherent cells (Isenberg and Klaunig, 2000). As shown in figure 5.9 A, the ΔΨm of L6 cells cultured in galactose media was ~10% lower than cells cultured in glucose media. The ΔΨm functions as a regulator of mitochondrial reactive oxygen species (ROS) production (Serviddio and Sastre, 2010) and so the effect of culturing L6 cells in glucose and galactose media on mitochondrial $O_2^{\bullet-}$ production was assessed using MitoSox. Under basal conditions, glucose-cultured cells produced a significantly greater amount of mitochondrial $O_2^{\bullet-}$ (~18% greater) than galactose cells (figure 5.9 B).

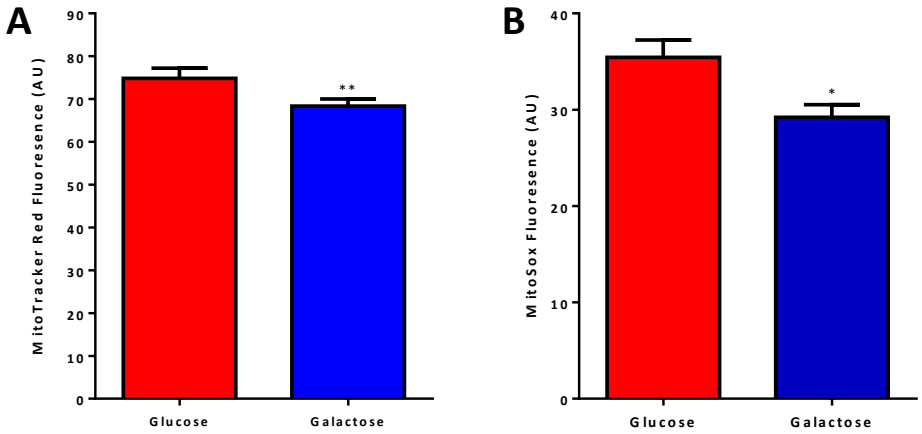

Figure 5.9 Effect of galactose on mitochondrial membrane potential and mitochondrial superoxide production. L6 cells were cultured in glucose (red) or galactose (blue) media for a minimum of 7 days and mitochondrial membrane potential **(A)** and mitochondrial superoxide production **(B)** were determined at basal conditions. Bars represent mean ± SEM; n=3 (*P<0.05, **P<0.01 glucose vs. galactose).

5.4.4 Using the 'glucose/galactose' model to assess the mitochondrial toxicity of SI triazoles

L6, H9c2 and HepG2 cells lines are all able to adapt to galactose media and consequently are more susceptible to mitochondrial insult, as shown in this study (figure 5.4) and previous studies, using classical mitochondrial toxicants (AMA and rotenone) (Marroquin *et al*., 2007; Rana *et al*., 2011). Therefore, the 'glucose/galactose' model was used to further investigate the mitochondrial toxicity of the SI triazole compounds. L6, H9c2 and HepG2 cells were cultured in glucose and galactose media for a minimum of 7 days and treated with a concentration range of 177, 197 and AMA (as a positive control) for 24 hours. L6 cells were also treated with troglitazone as an additional mitochondrial toxicant positive control.

L6 cells cultured in galactose media were significantly more sensitive to the positive controls, AMA and troglitazone, than cells grown in glucose, at concentrations $\geq$4.6nM and $\geq$150µM, respectively (figure 5.10 A and B). The IC50 ratios show that galactose grown cells were 5.9 and 1.8-fold more sensitive to AMA and troglitazone, respectively, compared to cells grown in glucose (Table 5.2). L6 cells also showed a significantly greater sensitivity to 177 ($\geq$200µM) and 197 ($\geq$50 µM) in galactose media

than in glucose media (figure 5.10 C and D). Comparison of the glucose and galactose IC50 ratios demonstrated that galactose cells were 2.1 and 2.6-fold more sensitive to 177 and 197, respectively (Table 5.2).

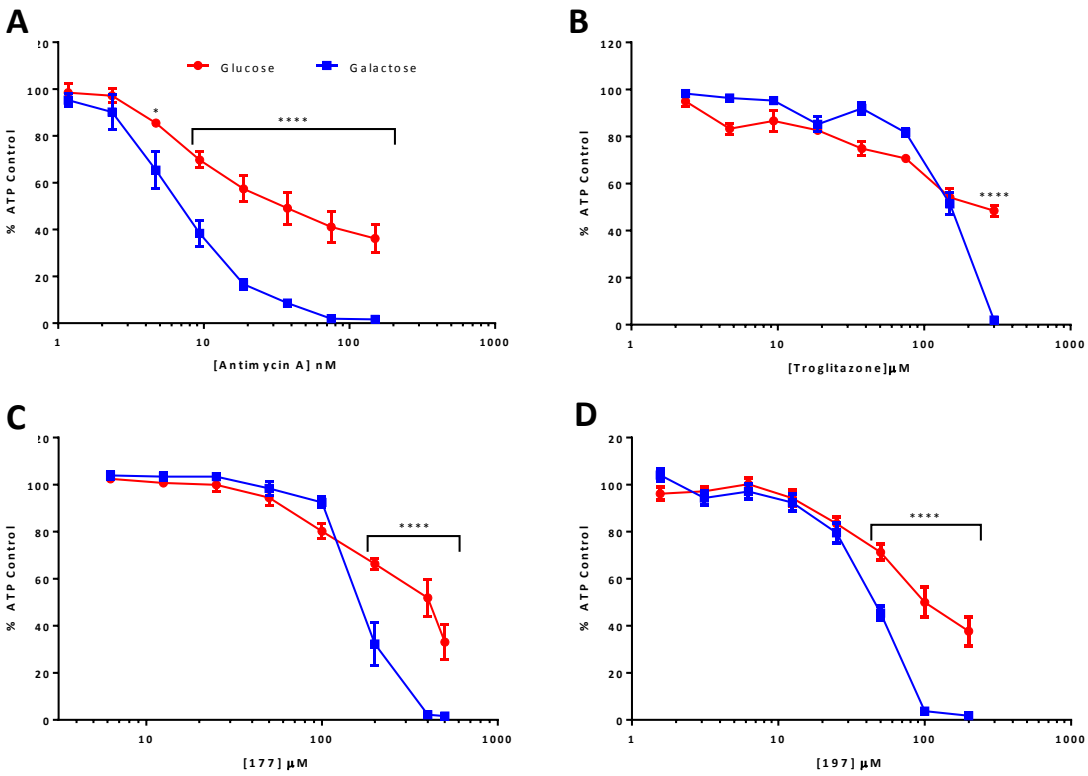

Figure 5.10 Dose responses for high-glucose-grown (25mM) (red line) and galactose-grown (10mM) (blue line) L6 cells treated with **(A)** Antimycin A, **(B)** troglitazone, **(C)** 177 and **(D)** 197. After 24 hours treatment the ATP content was assessed. Data are mean ±SEM; n=3 (*P<0.05, ****P<0.0001 glucose vs. galactose).

	IC50 (µM)		IC50 Ratio
Compound	**Glucose**	**Galactose**	**Fold difference**
AMA (nM)	42.1	7.1	5.9
Troglitazone (µM)	262.7	139.6	1.8
177 (µM)	350.8	170.1	2.1
197 (µM)	112.1	43.5	2.6

Table 5.2 IC50 values of AMA, troglitazone, 177 and 197 in L6 cells cultured in glucose and galactose media. A nonlinear regression was fit to the dose response curves from figure 5.10. Maximum (DMSO control) and minimum values (total cell kill) were fixed. The IC50 ratio between glucose and galactose media was calculated.

Like with L6 cells, H9c2 and HepG2 cells cultured in galactose media were significantly more sensitive to AMA ≥18.75nM and ≥4.68nM, respectively, than cells grown in

glucose (figure 5.11 A and D). These results supported the findings in chapter 4 (figure 4.3) that L6 and HepG2 cells were more sensitive to AMA than H9c2 cells. The IC50 ratios indicate that H9c2 and HepG2 cells grown in galactose were 10.7 and 17.7-fold more sensitive to AMA, respectively, compared to cells grown in glucose (table 5.3).

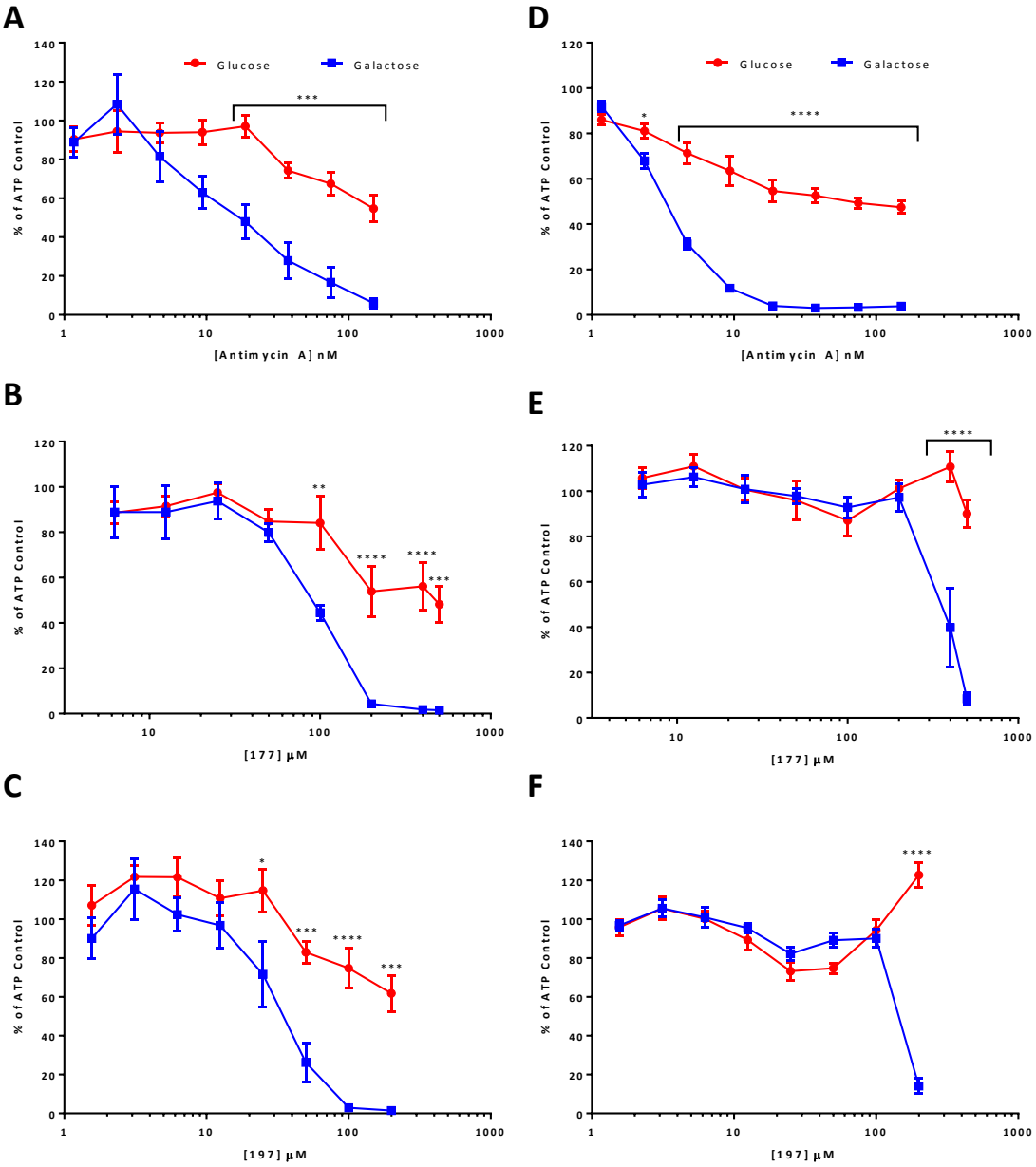

Figure 5.11 (A-C) Dose responses for glucose (25mM) (red line) and galactose-grown (10mM) (blue line) H9c2 cells treated with **(A)** Antimycin A, **(B)** 177 and **(C)** 197. **(D-F)** Dose responses for glucose (red line) and galactose-grown (blue line) HepG2 cells treated with **(D)** Antimycin A, **(E)** 177 and **(F)** 197. After 24 hours treatment ATP content was assessed. Data are mean ±SEM; n=4-5 (*P<0.05, **P<0.01, ***P<0.001, ****P<0.0001 glucose vs. galactose).

H9c2 cells cultured in galactose were significantly more sensitive to 177 and 197 ≥100µM and ≥25µM, respectively, than cells grown in glucose (figure 5.11 B and C). Comparison between the glucose and galactose IC50's show that H9c2 cells grown in galactose were 4.9 and 7-fold more sensitive to 177 and 197, respectively (Table 5.3). Notably, H9c2 cells proved more sensitive to 177 and 197 than L6 cells in galactose media, despite L6 cells being more sensitive in glucose media (Table 5.3).

In glucose media, 177 and 197 did not deplete HepG2 ATP levels, and in fact increased the production of ATP at concentrations >100 µM and >12.5µM, respectively. Conversely, HepG2 cells cultured in galactose media were significantly more sensitive to 177 and 197, with ATP levels depleting to ~8% and ~14% of control at 400µM and 200µM of 177 and 197, respectively (figure 5.11 E and F). Since 177 and 197 IC50 values could not be calculated for HepG2 cells cultured in glucose media, it was not possible to ascertain an IC50 ratio. However, HepG2 cells cultured in galactose media had an IC50 of 380.9µM and 144.4µM with 177 and 197, respectively (Table 5.3). Thus, in galactose media, HepG2 cells had an increased susceptibility to 177 and 197 mitochondrial toxicity, although were still less sensitive than L6 and H9c2 cells.

		IC50		IC50 Ratio
Cell line	**Compound**	**Glucose**	**Galactose**	**Glucose / Galactose**
H9c2	**AMA (nM)**	176.5	16.5	10.7
	177 (µM)	427.6	85.8	4.9
	197 (µM)	241	34.2	7
HepG2	**AMA (nM)**	58.1	3.3	17.7
	177 (µM)	>500	380.9	-
	197 (µM)	>200	144.4	-

Table 5.3 IC50 values of AMA, troglitazone, 177 and 197 in H9c2 and HepG2 cells cultured in glucose and galactose media. A nonlinear regression was fit to the dose response curves from figure 5.11. Maximum (DMSO control) and minimum values (total cell kill) were fixed. The IC50 ratio between glucose and galactose media was calculated.

5.4.5 Antimycin A OCR dose response in L6 cells cultured in glucose and galactose media

To assess if there was a difference in the sensitivity of L6 cells cultured in glucose and galactose media to complex III inhibition, a dose and time response with AMA was

carried out. In these experiments, a mitochondrial stress test was performed on glucose and galactose cells with a range of AMA concentrations to assess the threshold of OCR inhibition with each media type (figure 5.12). The results are presented as a percentage of baseline and since glucose cells were able to maintain an increased OCR following FCCP treatment, the glucose control (DMSO) value is greater than galactose when compared to baseline values. At all concentrations tested, the effects of AMA were identical in each media type, suggesting that the threshold for complex III inhibition was not different between L6 cells cultured in glucose and galactose media.

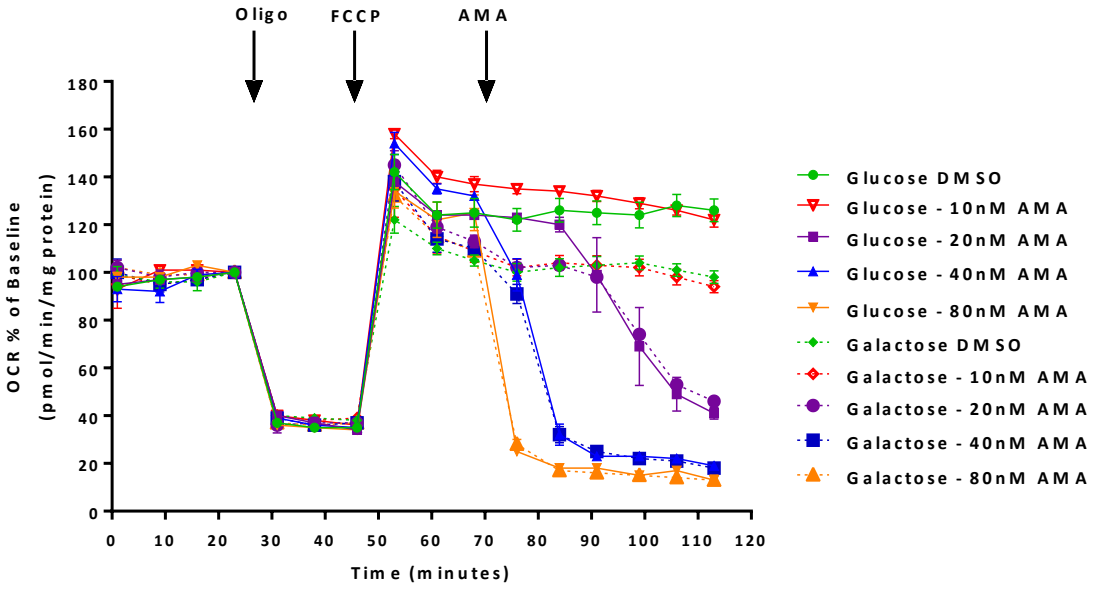

Figure 5.12 AMA OCR dose and time response in glucose and galactose cultured L6 cells. L6 cells were cultured for a minimum of 7 days in glucose (solid line) or galactose (dashed line) media. Real time measurements of OCR were made and oligomycin (800nM), FCCP (800nM) and a dose response of AMA (10, 20, 40 and 80nM) were injected sequentially as shown. The resulting effects on OCR are plotted as a percentage of the baseline measurement for glucose and galactose cultured L6 cells. Results represent mean ±SD; n=10 from two independent experiments of n=5.

5.4.6 Effect of 197 on the bioenergetics of L6 cells cultured in glucose and galactose media

L6 cells cultured in glucose and galactose media for a minimum of 7 days were treated with a range of 197 concentrations (50, 100 and 200µM) for 4 hours. Baseline measurements of OCR and ECAR were then made and mitochondrial function was

assessed by sequential injection of oligomycin, FCCP and AMA, as shown in figure 5.13. The individual mitochondrial function parameters were derived as detailed in figure 5.8 A and the AUC was calculated for each parameter (figure 5.14).

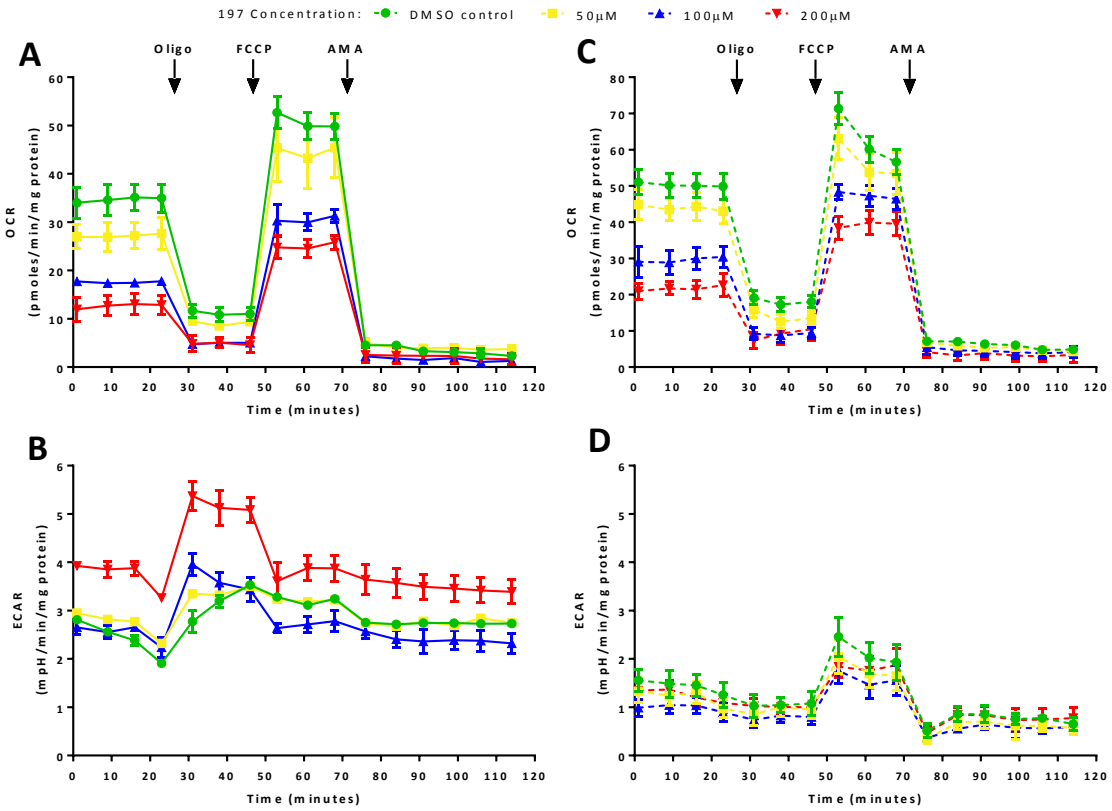

Figure 5.13 Effect of 197 on the OCR and ECAR of L6 cells cultured in glucose and galactose media. L6 cells were cultured in glucose (solid line) and galactose(dashed line) media for a minimum of 7 days. Cells were treated with 50µM (yellow), 100µM (blue) and 200µM (red) of 197 for 4 hours. Basal OCR and ECAR of glucose **(A and B)** and galactose **(C and D)** cells were then measured followed by sequential injection of oligomycin (800nM), FCCP (800nM) and AMA (200nM) at the times indicated. Data represent mean ±SEM; n=3.

As shown in figure 5.14 A and B, 197 concentration-dependently decreased the level of OCR in glucose and galactose cultured L6 cells. Although OCR was reduced to a greater extent in glucose cells following treatment with 197 (figure 5.13 A and C), the decrease in OCR was proportional to the control OCR levels in both glucose and galactose (figure 5.14 A and B). In both media types, 50µM 197 had no significant effect on any mitochondrial function parameters after 4 hours treatment (figure 5.14 A and B). However, 100 µM and 200µM 197 significantly reduced basal OCR by 68%

and 45% in glucose cells (figure 5.14 A) and 66% and 50% in galactose cells (figure 5.14 B), respectively. Interestingly, 200µM 197 reduced basal OCR of glucose grown cells (~45%) to a greater extent than galactose grown cells (~50%), although this difference was not significant.

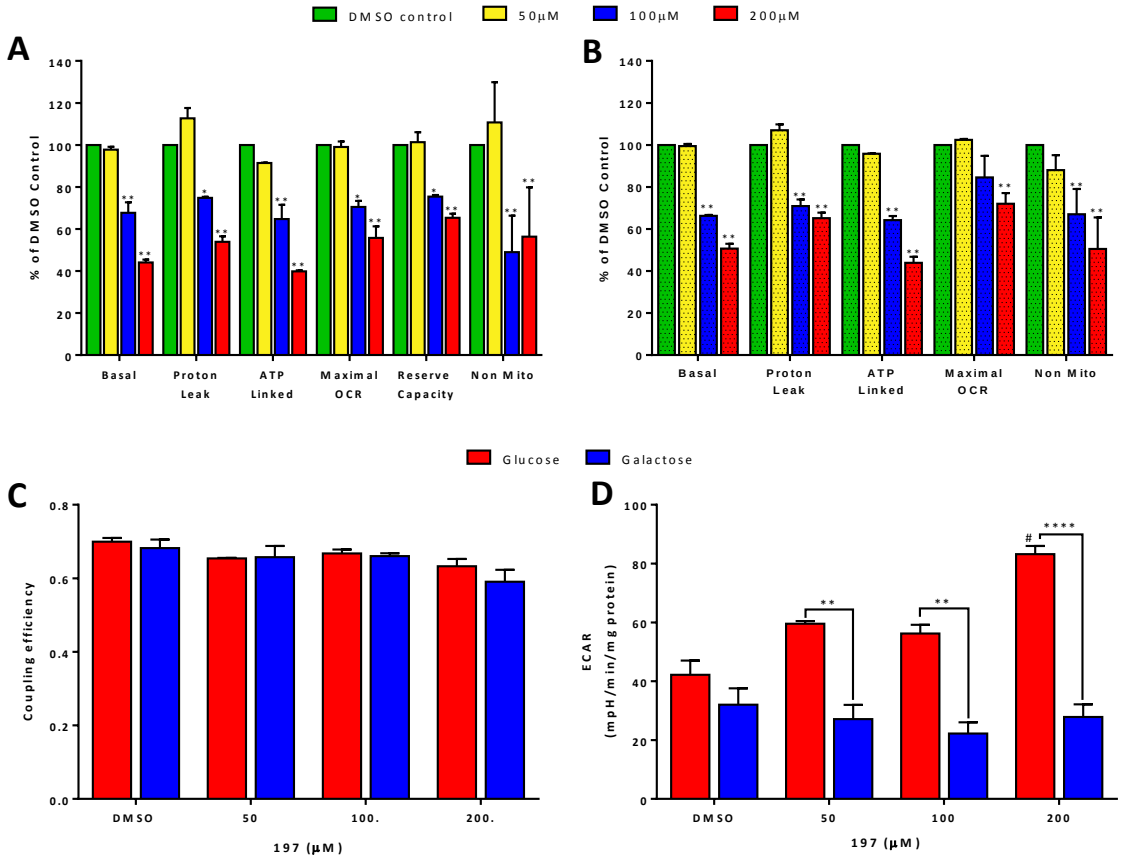

Figure 5.14 Effect of 197 on mitochondrial function and glycolysis in glucose and galactose cultured L6 cells. (A, B) The mitochondrial function parameters of glucose **(A)** and galactose **(B)** cultured L6 cells were derived from figure 5.13 A and C as detailed in figure5.8. The AUC for each parameter was calculated and presented as a percentage of respective media-type control for internal normalization. Results represent mean + SEM; n=3 (*P<0.05, **P<0.01 control vs. treated). **(C)** Coupling efficiency was calculated by dividing ATP-linked OCR by basal OCR to determine fraction of basal OCR used for ATP synthesis in glucose and galactose cells following 197 treatment. Results represent mean + SEM; n=3 **(D)** AUC for basal ECAR activity was calculated from figure 5.13 in glucose and galactose cells following 197 treatment. Results represent mean +SEM; n=3 (**P<0.01, ****P<0.0001 glucose vs. galactose).

In both glucose and galactose grown L6 cells, proton leak, ATP-linked OCR, maximal OCR and non-mitochondrial OCR were reduced in a concentration-dependent fashion following 197 treatment. There was no significant difference in the coupling efficiency

between DMSO control and treated cells cultured in glucose or galactose media (figure 5.14 C). This means there was a proportional decrease in proton leak and ATP-linked OCR following 197 treatment of glucose and galactose grown L6 cells.

In L6 cells cultured in glucose, 197 decreased the mitochondrial reserve capacity in a concentration-dependent fashion (figure 5.14 A). In contrast, reserve capacity increased in a concentration-dependent fashion in galactose grown cells. This result was not included, however, since it represents a false positive increase because galactose cells are operating at close to maximum OCR at basal levels and so only have a small reserve capacity. Therefore, when the overall basal OCR levels were decreased by 197, the galactose cells had the scope to increase OCR following FCCP treatment, and thus there was an increase in the reserve capacity.

There was no significant change in the ECAR activity of galactose grown cells following 197 treatment (figure5.13 D and 5.14 D). In contrast, there was a concentration-dependent increase in ECAR activity in glucose cultured cells, with 200µM 197 increasing activity significantly by ~2-fold compared to control (figure 5.13 B and 5.14D). At all concentrations of 197, the activity of ECAR was significantly higher in glucose than in galactose cultured cells (figure5.14 D).

5.4.7 Effect of 197 on mitochondrial superoxide production of L6 cells cultured in glucose and galactose

In the previous chapter (section 4.4.3) it was established that 197 and AMA significantly increased mitochondrial $O_2^{\bullet-}$ generation in L6 cells cultured in glucose media. In this chapter, it was found that culturing L6 cells in galactose media increased mitochondrial respiration and subsequently decreased basal levels of mitochondrial $O_2^{\bullet-}$ production. It was therefore investigated if culturing L6 cells in galactose affected mitochondrial $O_2^{\bullet-}$ generation induced by 197 and AMA . As shown in figure 5.15, treatment with 197 and AMA resulted in a significant increase in mitochondrial $O_2^{\bullet-}$ generation in both glucose and galactose grown cells. However, a significantly greater amount of mitochondrial $O_2^{\bullet-}$ was produced in galactose grown cells than in glucose grown cells following 100µM AMA and 50µM and 100µM 197 treatment. Following

treatment with 100µM AMA, galactose grown cells induced ~40% more mitochondrial $O_2^{\bullet-}$ generation than glucose grown cells. Treatment of galactose grown cells with 50µM and 100µM 197 resulted in a 2.7-fold and 3.8-fold increase in mitochondrial $O_2^{\bullet-}$, respectively. In glucose grown cells, there was significantly less mitochondrial $O_2^{\bullet-}$ generation following treatment with 50 µM and 100µM 197, with a 2-fold and 2.8-fold increase, respectively.

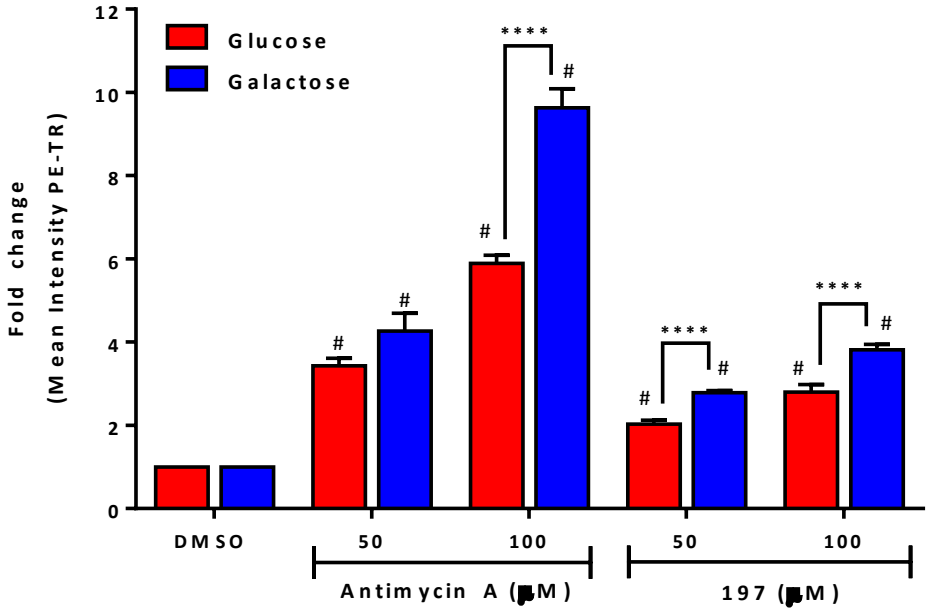

Figure 5.15 Effect of 197 on mitochondrial superoxide production in L6 cells cultured in glucose and galactose media. L6 cells were cultured in glucose and galactose media for a minimum of 7 days and treated for 1 hour with AMA (50 and 100µM) and 197 (50 and 100 µM) for 1 hour. Mitochondrial superoxide was assessed using MitoSox with flow cytometry. Results represent the mean +SEM; n=3 (#P<0.01 treated vs. respective media-type control, ****P<0.0001 glucose vs. galactose).

5.5 Discussion

The overall aim of this chapter was to investigate whether substituting galactose for glucose in the media of L6 skeletal muscle cells would increase their reliance on mitochondrial OXPHOS and thereby increase their susceptibility to mitochondrial toxicants. Importantly, the L6 'glucose/galactose' cell model was then used to further investigate the mitochondrial toxicity of the SI triazoles.

5.5.1 Adaptation of L6 cells to galactose media

5.5.1.1 Effect of galactose on L6 cell growth and ATP content

To determine if L6 cells were able to adapt to growth in galactose media, they were grown in either high-glucose (25mM) or galactose (10mM) media for a minimum of 7 days. In cells cultured in galactose media, there is a residual glucose concentration (~0.28mM) from the FBS, although this is rapidly metabolised within 5 hours of cell culture (Robinson *et al*., 2012). Thus, there would be negligible input from this glucose source in galactose grown L6 cells. HepG2 and H9c2 cells lines were included in this study since they have previously been shown to successfully adapt to galactose media (Domenis *et al*., 2010; Rana *et al*., 2011), and, because cell-line specific sensitivities were investigated, for detection of mitochondrial toxicities using the 'glucose/galactose' model.

All three cell lines adapted to growth in galactose media with no change in morphology or cell death rate, as has previously been determined with HepG2 and H9c2 cells (Rossignol *et al*., 2004; Marroquin *et al*., 2007; Domenis *et al*., 2010; Rana *et al*., 2011). L6 cells maintained similar ATP levels in glucose and galactose media, as has been shown with HepG2 and H9c2 cells in other studies (Marroquin *et al*, 2007; Rana *et al*., 2011). In addition, a study with primary skeletal muscle cells has shown no difference in the ATP content between myotubes cultured in high glucose and galactose, in which the authors concluded that replacing glucose with galactose has no negative effect on cellular physiology and metabolism (Aguer *et al*., 2011).

The rate of cell growth was found to be slower in L6, H9c2 and HepG2 cells cultured in galactose media compared to glucose media. A slower growth rate in galactose media has been demonstrated with HepG2 cells previously (Davit-spraul *et al*., 1994; Domenis *et al*., 2010), as well as with a range of other cell lines, including skin fibroblasts (Gohil *et al*., 2010) and Hela cells (Rossignol *et al*., 2004). The slower growth rate is not attributable to differences in ATP content, but instead relates to the differences in the flux kinetics between glucose and galactose in the cell. Galactose is taken up and metabolised to a much lower extent than glucose, despite the fact they are both hexoses and are taken up by the same transporters, GLUT1 and GLUT4, in skeletal muscle (Kase *et al*., 2013). The difference in uptake of each hexose is due to the fact that both transporters have a higher affinity for glucose than galactose (Wagner *et al*., 1991; Kase *et al*., 2013). Galactose is also metabolized at about an 8-fold slower specific rate than glucose (Wagner *et al*., 1991). This is because galactokinase, the rate-limiting step in galactose metabolism, is considerably less active than hexokinase, the first enzyme and rate-limiting step in the oxidation of glucose (Wagner *et al*., 1991). As a consequence, the levels of glucose-6-phosphate production are lower in galactose compared to glucose media (Davit-Spraul *et al*., 1994). Glucose-6-phosphate is an important substrate essential for cell proliferation via the pentose phosphate pathway (PPP) (Wamelink and Jakobs, 2008). Therefore, in galactose media, the key PPP intermediates, NADPH and ribose, are formed at a lower rate than in glucose media and thus the growth rate is slower (Wagner *et al*., 1991).

Glucose-6-phosphate is also a key substrate for glycolysis and so the flux rate through glycolysis is much higher with glucose than galactose media (Bustamante and Pedersen, 1977). Consequently, when cells are grown in galactose medium, glutamine provides >98% of total ATP content (Reitzer *et al*., 1979). Although glycolysis only provides 2 ATP/glucose molecule, the flux rates can be accelerated to maintain sufficient ATP levels when cells are cultured in high glucose (Davit-Spraul, *et al*., 1994). The ability of glucose grown cells to adapt cellular metabolism to maintain ATP levels following mitochondrial insult, while galactose grown cells cannot, is the premise for the ‘glucose/galactose’ cell mitochondrial toxicity testing model. The reason a glucose

vs. galactose model, and not a glucose vs. no-glucose model was used in this study was because galactose provides important substrates via the PPP.

5.5.1.2 Effect of mitochondrial inhibitors on L6 cells cultured in glucose and galactose

Once it was established that L6 cells were able to adapt to growth in galactose media, it was determined if the L6 cells grown in galactose were more susceptible to classical mitochondrial toxicants. This is considered the gold standard method for assessing if cells have adapted their metabolic profile to rely almost exclusively on mitochondrial OXPHOS in galactose media and are thus more susceptible to mitochondrial toxicity (Marroquin *et al*., 2007; Swiss and Will, 2011). L6, H9c2 and HepG2 cells cultured in galactose media for a minimum of 7 days (~2-3 passages) were significantly more sensitive to the complex III inhibitor, AMA, than cells cultured in glucose media. Further tests with the complex I inhibitor, rotenone, in L6 and HepG2 cells, confirmed the findings with AMA and in both instances glucose-grown cells were able to maintain their ATP levels between 40-60%, whereas the ATP levels of galactose cells were diminished to <5%. These results are analogous to results found with HepG2 and H9c2 cells in previous studies (Marroquin *et al*., 2007; Rana *et al*., 2011). Thus, it can be concluded that L6 skeletal muscle cells, like H9c2 and HepG2 cells, are able to detect mitochondrial toxicants more sensitively when cultured in galactose media.

5.5.1.3 Important considerations for galactose adaptation

It is essential that the cell line has the appropriate mitochondrial machinery and enzymatic capability in order to tolerate a switch to galactose growing conditions. Some cell lines, such as SH-SY5Y and CHO cells, have been shown not to be adaptable to galactose conditions (Jimenez *et al*., 2011; Swiss and Will, 2011). CHO cells, for example, are unable to survive in galactose as their sole carbon source due to lack of uptake (through GLUTs) and enzymes (galactokinase) required for its metabolism (Jimenez *et al*., 2011). Interestingly, CHO cell lines transfected with galactokinase were able to grow in the presence of galactose at a higher specific rate than control cells, with reduced levels of lactate produced (Jimenez *et al*., 2011). Research *in vivo* has shown that galactose metabolising enzymes (galactose-1-phophate, uridyltransferase

and galactokinase) are active in human skeletal muscle (Shin-Buehring *et al*., 1977) and that primary human skeletal muscle cells are able to adapt to galactose *in vitro* (Aguer *et al*., 2010). Information on rodents (specifically rats) is scarce, although it has been shown that the mouse skeletal muscle cell line, C2C12, is able to adapt to galactose or low glucose conditions (O'Hagan *et al*., 2009; Mailloux and Harper, 2010). Until this study, it was not known if the rat L6 skeletal muscle cell line is able to adapt to galactose. However, Liu *et al* (2012), have shown that L6 cells have the appropriate mitochondrial machinery and derive a bulk of their energy from mitochondrial OXPHOS (as judged by a high OCR to ECAR ratio) when cultured in high glucose (25mM). The duration of time it takes for cells to adapt to galactose media is also an important consideration. In this study, the L6 cells were allowed a minimum of 7 days to acclimate to galactose media, which was chosen based on findings in the literature (Gohil *et al*., 2010, Domenis *et al*., 2010; Swiss and Will, 2011). The fact that the L6 galactose cells were able to maintain ATP levels, proliferate (albeit at a slower rate than glucose cells) and respond to mitochondrial toxicants more sensitively, indicates that L6 cells, like HepG2 and H9c2 cells, are able to adapt to galactose media within 7 days. Importantly, this suggests that L6 cells have the correct complement of enzyme activity to metabolize galactose, as well as the appropriate mitochondrial machinery to rely on OXPHOS for energy. However, further research to investigate the expression of galactose metabolizing enzymes in L6 cells is required.

5.5.2 Effect of galactose on L6 cellular bioenergetics

Having determined that L6 cells were able to adapt to galactose media and were subsequently more susceptible to mitochondrial toxicants, the effects of galactose on L6 cellular bioenergetics were characterized. Using an XF24 analyzer, real-time measurements of mitochondrial OXPHOS and glycolysis were determined by measuring OCR and ECAR of L6 cells cultured in glucose and galactose media (Ferrick *et al*., 2008). As previously shown by others in different cell lines and primary cells (Rossignol *et al*., 2004; Aguer *et al*., 2010), replacing glucose with galactose in the media increased the mitochondrial OXPHOS of L6 cells. In galactose cultured cells, the rate of mitochondrial OXPHOS was ~50% higher than when cells were cultured in glucose. In accordance with the increase in mitochondrial OXPHOS, there was a

decrease in the rate of glycolysis when cells were cultured in galactose media. Although the basal levels of ECAR were not significantly different between glucose and galactose cells, addition of AMA showed that a majority of ECAR in galactose cells was attributable to 'proton leak' from the respiring mitochondria (Robinson *et al*., 2012). Conversely, addition of AMA had no deleterious effects on the ECAR of glucose cultured cells, indicating that glycolysis was active in glucose cultured cells, but not in galactose cultured cells. Furthermore, addition of mitochondrial inhibitors (oligomycin, FCCP) demonstrated that glucose cells were able to up regulate glycolysis in response to a decrease in mitochondrial OXPHOS, whereas galactose cells were not. These results are consistent with the fact that galactose metabolism is too slow to provide sufficient ATP via glycolysis, forcing the cells to rely almost exclusively on mitochondrial OXPHOS to produce ATP (Reitzer *et al*., 1979; Robinson *et al*., 1992; Rossignol *et al*., 2004).

In agreement with Liu *et al* (2012), L6 skeletal muscle cells cultured in high glucose media still derived a majority of their energy from mitochondrial OXPHOS, as demonstrated by the high OCR levels and relatively low ECAR levels. Notably, the cancer cell line Z138 (a mantle cell lymphoma cell line) has a basal ECAR level over 6-fold higher than L6 cells when cultured in high glucose concentrations (Robinson *et al*., 2012). Thus, L6 cells cultured in high glucose media are distinct from certain cell lines in that they do not derive most of the energy from aerobic glycolysis. Like with L6 cells, research has shown that HepG2 cells (a liver cancer cell line) are mainly sustained by mitochondrial OXHPOS (Piccoli *et al*., 2006). Given the high levels of glutamine (4mM) in the media of high glucose cells, the oxidation of this substrate through OXPHOS likely provides the bulk of ATP for glucose-derived cells. Indeed, research with a number of mammalian cells (e.g. Hela, CHO, BHK-21) has shown that even when cells are grown in glucose media, glutamine still provides ~70% of ATP (Reitzer *et al*., 1979; Neermann and Wagner, 1996). Glutamine is metabolized by two successive deaminations to yield α-ketoglutarate, a key intermediate of the tricarboxylic acid cycle (TCA cycle), and provides reductants, NADH and $FADH_2$, for mitochondrial OXPHOS (Reitzer *et al*., 1979). Thus, glutamine is considered the primary substrate for energy production through OXPHOS, while the primary function

of sugar is to provide vital intermediates, via the PPP, essential for biosynthesis and cell proliferation (Reitzer *et al*., 1979).

5.5.2.1 Effect of galactose on mitochondrial function in L6 cells

To further characterise the increased mitochondrial OXPHOS levels in galactose cells, mitochondrial function was investigated. In galactose cells, basal OCR, proton leak, ATP-linked OCR and maximal OCR were all significantly increased compared to glucose cells. There was no difference in coupling efficiency however, with both glucose and galactose cells coupling ~66% of cellular OCR to ATP synthesis. An equivalent coupling efficiency showed that the level of ATP-linked OCR was proportional to the level of proton leak in both glucose and galactose cells. Therefore, the increase in galactose OCR was not due to an increased efficiency of mitochondrial respiration. Importantly, proton leak was determined by inducing a state 4-like respiratory condition with oligomycin treatment, which inhibits phosphorylation and subsequently increases protonmotive force (Δp). The increased Δp results in higher proton leak through the mitochondrial membrane and thus the value determined for proton leak was overestimated and ATP-linked OCR was underestimated (Dranka *et al*., 2010). Consequently, such estimates yield artificially low coupling efficiencies, but the error is generally <10% (Divakaruni and Brand, 2011). The coupling efficiency of rat skeletal muscle has been shown to be ~65% (Rolfe *et al*., 1999), which is very similar to what was obtained with L6 cells cultured in glucose and galactose media (66%).

The calculated $State_{apparent}$ indicated that galactose cells were operating closer to state 3u (i.e. State 3 as determined by FCCP addition) respiration than glucose cells. In addition, the phosphorylating respiration ratio demonstrated that galactose cells use a greater proportion of the maximal respiratory capacity for ATP production than glucose cells under basal conditions. State 3u is characterised by a decrease in the Δp, an increase in proton leak and an acceleration of electron transport (Brand and Nicholls, 2011). The Δp describes the movement of protons against their electrochemical gradient into the mitochondrial inner membrane space, and has two components, ΔpH (the pH gradient across the inner membrane) and ΔΨm (mitochondrial membrane potential) (Divakaruni and Brand, 2011). As the dominant

component, ΔΨm contributes 80-85% to the Δp (Dzbek and Korzeniewski, 2008). Since galactose cells had a lower ΔΨm and a higher proton leak than glucose cells, this supports the fact that galactose cultured cells were operating closer to state 3u than glucose cultured cells. Net forward flux through each electron transport complex requires a thermodynamic disequilibrium, i.e. the free energy available from electron transfer must be greater than that required to pump protons across the membrane against the Δp (Brand and Nicholls, 2011). The electron transport chain thus responds to a drop in Δp, resulting from an increased proton re-entry through the ATP synthase or proton leak, with an increased flux (Brand and Nicholls, 2011). Therefore, in galactose grown cells, the decrease in Δp (as shown by the decrease in ΔΨm), increase in proton leak and increase in ATP-linked OCR compared to glucose grown cells, was indicative of an accelerated electron transport flux, and subsequent increase in ATP production via mitochondrial OXPHOS. Notably, the increase in respiration is linear to the fall in Δp until it plateaus at ~100mV, when the maximal respiration is attained (Brand and Nicholls, 2011). Although galactose cells had an increased maximal respiration compared to glucose cells, this was not sustainable, and reduced back to basal levels after ~15 minutes treatment with FCCP. This suggests that at basal respiration levels, galactose cells were operating close to the maximum OCR attainable, and any increase was restricted by respiration kinetics (i.e. substrate oxidation, Δp and proton leak).

Cells with an increased capacity for oxidative phosphorylation are also susceptible to increased mitochondrial $O_2^{\bullet-}$ production through increased leakage of single electrons from the electron transport chain (Brand and Nicholls, 2011). The function of proton leak is therefore to provide cells with a greater degree of protection from $O_2^{\bullet-}$ production via increased “mild uncoupling”. This results in a slight lowering in the Δp to prevent mitochondrial superoxide production without deleteriously lowering ATP synthesis (Divakaruni and Brand, 2011). As such, mitochondrial $O_2^{\bullet-}$ production is steeply dependent on Δp. The increased proton leak and subsequent decrease in ΔΨm of galactose cells compared to glucose cells therefore explains why galactose cells had a lower basal level of mitochondrial $O_2^{\bullet-}$ production than glucose cells. Indeed, high ΔΨm favours the production of $O_2^{\bullet-}$, particularly at complex III, which is thought to be

due to the slowed electron transport and the prolongation of $QH^{\bullet}$ occupancy in the complex (Zhang and Gutterman, 2006). A significant increase in proton leak might be explained by a difference in membrane composition or as a consequence of an increase in the expression of proteins involved in matrix return of protons. Basal proton conductance is primarily attributable to the abundance of adenine nucleotide translocase (ANT), although inducible proton conductance is catalysed by mitochondrial uncoupling proteins (UCPs) (Divakaruni and Brand, 2011). Notably, the mitochondrial anion carriers UCP2 and UCP3 have been shown to protect against oxidative damage by uncoupling when activated, thereby lowering Δp to reduce the original, causative $O_2^{\bullet-}$ production (Brand *et al*., 2004).

The reason for an increased mitochondrial OCR in L6 cells grown in galactose media compared to glucose media was not investigated in this study. It has been shown that substrate oxidation correlates with an increased respiratory flux and is thereby responsible for changes in state3u (Brand and Nicholls, 2011). Possible explanations for an increased substrate oxidation include a general increase in mitochondrial content (through mitochondrial biogenesis), an increased synthesis of electron-transport chain complexes, an increase in processing enzymes, an increased flux of glutamine oxidation through the TCA cycle and ETC or a combination of each. Previous studies have shown that HeLa cells, fibroblasts and primary skeletal muscle cells cultured in galactose do not increase their mitochondrial content through mitochondrial biogenesis to increase OCR levels (Rossignol *et al*., 2004; Palmfeldt *et al*., 2009; Aguer *et al*., 2010). Rossignol *et al* (2004) have demonstrated that HeLa and fibroblast cells cultured in galactose media increase the protein levels of respiratory chain complexes (Complex I, II, IV and V), the addition of which was accommodated in the mitochondria by increasing the amounts of cristal membrane rather than increasing the mass of mitochondria. A proteomic study with fibroblasts has also identified an increase in complex I and IV in galactose cultured cells (Palmfeldt *et al*., 2009). Similarly, Aguer *et al* (2010) found that primary muscle cells cultured in galactose increased activity of Complex IV by ~70%. Citrate synthase, a marker of TCA cycle activity, was found to be up-regulated in HeLa and fibroblast cells, but not in primary muscle cells (Rossignol *et al*., 2004; Palmfeldt *et al*., 2009; Aguer *et al*., 2010).

This may be because primary muscle cells derive more of their energy from glutamine metabolism (via the TCA cycle) than HeLa cells in glucose media, and so do not require an increased activity following a switch to galactose media. Indeed, when HeLa cells are grown in glucose, ~80% of the glucose is metabolised through glycolysis to lactic acid and only 4-5% of sugar carbon entered the TCA cycle (Reitzer *et al*., 1979). In contrast to the findings with HeLa cells, fibroblasts and primary muscle cells, it has been shown that HepG2 cells increase their mitochondrial content through mitochondrial biogenesis (increased PGC-1α activity) in response to galactose media (Domenis *et al*., 2012). Thus, each cell line/primary cell adapts mitochondrial and bioenergetic capabilities differently to galactose media and so further research would be required to understand the adaptations of L6 cells to galactose media.

5.5.3 Assessment of SI triazole compound mitochondrial toxicity using the 'glucose/galactose' cell model

In L6, H9c2 and HepG2 cells, dose-responses with the positive control AMA confirmed the initial mitochondrial toxicity tests (figure 5.4), with galactose cells being significantly more sensitive to treatment than glucose cells. The concentration at which AMA reduced HepG2 ATP content to <1% (~10nM) in galactose media was comparable to findings by Marroquin *et al* (2007). Interestingly, a previous study found that H9c2 cells were less sensitive (IC50 of 300nM) to AMA treatment than was demonstrated here (IC50 of 16nM) (Rana *et al*., 2011). This discrepancy highlights potential issues with attaining accurate, comparable and reproducible information from *in vitro* models. In this case, the study by Rana *et al* (2011) used cells seeded in 384-well plates, whereas 96-well plates were used here, and so potential differences in cell density may have altered the sensitivity of the cells to treatment. Indeed, a study by Riss and Moravec (2004) found that cells were more responsive to a toxin if they were seeded at lower numbers. It is likely that at higher cell densities the ratio of toxin to cell number is decreased, and so each individual cell is exposed to a lower concentration of compound.

Further tests with the positive control compound troglitazone were also carried out with L6 cells, which showed that galactose cultured cells were 100% non-viable at the

highest concentration whereas glucose-grown cells were able to maintain ATP levels to ~50%. These results confirm the notion that mitochondrial toxicity contributes to the idiosyncratic effects of troglitazone (Okuda *et al*., 2010; Rana *et al*., 2011) and that L6 cells are able to detect a range of mitochondrial toxicants using the 'glucose/galactose' model.

In all three cells lines the SI triazoles, 177 and 197, were much more toxic to galactose-grown cells than glucose grown cells. The increased susceptibility of galactose grown cells to 177 and 197 demonstrates that the mitochondria are the primary mode of toxicity for these compounds. These results therefore confirm the findings of the previous chapter (4), which showed that 177 and 197 depleted ATP prior to loss of cell viability (section 4.4.2) and induced mitochondrial $O_2^{\bullet -}$ production (section 4.4.3). Importantly, it was shown that treatment with an antioxidant (NAC) was able to reduce the mitochondrial $O_2^{\bullet -}$ production and prevent ATP depletion induced by 177 and 197, thereby implicating mitochondrial $O_2^{\bullet -}$ as the principle mechanism of triazole toxicity (section 4.4.4.2). Together with the bioinformatics data in chapter 1, these results are convincing evidence that 177 and 197 target mitochondria as a primary mechanism of toxicity.

The results of this study confirm previous studies that have illustrated the utility of the 'glucose/galactose' model system for identification of mitochondrial toxicants early in R&D (Marroquin *et al*.., 2007; Rana *et al*., 2011; Swiss and Will, 2011). In addition, these results highlight the use of organ-specific cell lines for more sensitive detection of mitochondrial toxicities. The L6 and H9c2 cell lines were more sensitive to 177 and 197 than HepG2 cells in both glucose and galactose media and so provide more sensitivity for detection of mitochondrial toxicity. This is in agreement with striated muscle (cardiac and skeletal muscle) being more sensitive to SI triazoles than the liver *in vivo* following acute (4 day) treatment (section 1.5.2.4). To date, this is the first study that has compared organ-specific cell lines for identification of mitochondrial toxicity. However, this study was done with relatively uncharacterised compounds and so to further validate the use of organ-specific cell lines for mitochondrial toxicity

testing, a large number of well characterised compounds would need to be tested in multiple organ-specific cell lines.

Previous studies have employed a ratio of glucose to galactose cell IC50 values to standardize the decision on whether a compound is a true mitochondrial toxicant (Swiss and Will, 2011; Rana *et al*., 2011). Swiss and Will (2011) and Rana *et al* (2011) consider a compound to be a true mitochondrial toxicant if the IC50 ratio of glucose to galactose is $\geq$3 for HepG2 cells and H9c2 cells, respectively. However, Swiss and Will (2011) do stipulate that this ratio is specific for these cell lines and may be different for other cell lines. In this study the IC50 ratio could not be determined for 177 and 197 with HepG2 cells as an IC50 could not be calculated for glucose cells. In H9c2 cells, the IC50 ratio for 177 and 197 was >3 (at 4.9 and 7-fold, respectively), which is in agreement with the classification of the previous studies, thereby providing convincing evidence that the compounds are true mitochondrial toxicants. However, in L6 cells, the IC50 ratio was <3 for 177 (2.06) and 197 (2.6). This is because L6 cells are more sensitive than H9c2 and HepG2 cells in glucose media, which decreased the ratio. In addition, the IC50 ratio of AMA for L6 cells (5.9) was lower than for H9c2 and HepG2 cells, again because L6 cells had a lower IC50 in glucose-cultured cells. Thus, L6 glucose-grown cells are more susceptible to mitochondrial toxicants than H9c2 and HepG2 cells, which may be because they rely primarily on mitochondrial-derived OCR for ATP and/or are less able to adapt to generating ATP via glycolysis than H9c2 and HepG2 cells. As a consequence, more research is required to ascertain a suitable IC50 ratio for identifying mitochondrial toxicants with L6 cells. It may be that an arbitrary cut-off of 3 is too high for L6 cells and could potentially yield false negative mitochondrial toxicity data. Certainly in this study there is convincing evidence that the mitochondria are a primary target for 177 and 197 toxicity.

In HepG2 cells, there was a stimulation in ATP at the highest concentrations of 177 and 197 in glucose-grown cells. In the previous chapter (4) this was hypothesised to result from either an increase in ATP production (as a stress response) or a decrease in ATP utilisation (section 4.5.2.1). Since the ATP was significantly depleted in galactose grown-cells at the concentrations where ATP was stimulated in glucose cells, the

stimulation of ATP could be attributed to an increase in glycolytic flux. Research in a number of cell lines has shown that an increased glycolytic flux is an adaptive response to oxidative stress that is regulated by activation of AMPK (Cidad *et al*., 2004; Wu *et al*., 2012). Activation of AMPK increases glycolytic flux and subsequently increases NADPH production via the PPP, which is a critical source of reducing equivalent, for example, contributing to the maintenance of glutathione regeneration (Wu *et al*., 2012). Thus, HepG2 cells grown in glucose may have conferred protection against triazole-induced oxidative stress by increasing glycolytic flux and thereby increasing ATP and NADPH levels.

5.5.4 Antimycin A dose response in L6 cells cultured in glucose and galactose

There was no difference in the rate of OCR inhibition induced by a concentration range of AMA in glucose and galactose cultured L6 cells. This result demonstrates that the threshold for AMA inhibition of complex III was the same in both glucose and galactose cultured L6 cells. This is in line with research in HeLa, fibroblasts and primary muscle cells that have shown no difference in the level of complex III in glucose and galactose cultured cells (Rossignol *et al*., 2004; Palmfeldt *et al*., 2009; Aguer *et al*., 2010). Rossignol *et al* (2004) suggest that high amounts of complex III in glucose cells are required even when there is little or no OXPHOS for other electron transport reactions or biosynthetic needs. Thus, if the levels of complex III were equivalent in glucose and galactose-grown L6 cells this would explain why the rate of AMA-induced OCR decrease was identical in both cell types. To date, the author could find no other studies comparing the inhibition of respiratory chain complexes in glucose and galactose cultured cells, so this is an area that needs exploring further.

5.5.5 Effect of 197 on the cellular bioenergetics of L6 cells cultured in glucose and galactose media

Treatment of glucose and galactose cultured L6 cells with 197 decreased the mitochondrial OCR in a concentration-dependent fashion, with 200µM reducing mitochondrial OCR by ~40-45%. Like with AMA, the decrease in OCR (compared to respective controls) was comparable in both glucose and galactose media following treatment with 50, 100 and 200µM 197. These results imply that the target of 197

mitochondrial toxicity remained unaffected by culture in galactose media. Furthermore, there was no difference in the coupling efficiency of glucose or galactose cells following 197 treatment, indicating that the decrease in ATP-linked OCR was proportional to the decrease in proton leak. Coupled with the fact glucose and galactose cells remained sensitive to both oligomycin and FCCP following 197 treatment, these results suggest that 197 does not inhibit the ATP synthase or uncouple the mitochondrial membrane. Additionally, 197 had much slower kinetics than canonical inhibitors that directly target the respiratory chain (AMA) or ATP synthase (oligomycin), since it took 200µM 197 ~4 hours to reduce basal OCR by ~50%, whereas for oligomycin (800nM) and AMA (80nM) it only took a matter of minutes to reduce it by 100%. The slow kinetics suggest that it takes time for 197 to accumulate in the mitochondria and/or that 197-induced mitochondrial $O_2^{\bullet -}$ takes time to reduce mitochondrial OCR. Notably, the kinetics of OCR decrease in L6 glucose grown cells correlated with the decrease in ATP after 4 hours (figure 4.5), suggesting that the decrease in ATP was a result of 197-induced reduction in mitochondrial OXPHOS activity. The maximal OCR of glucose and galactose L6 cells was also reduced by 197 in a concentration-dependent manner, suggesting that the overall capacity of mitochondrial OXPHOS was compromised by 197. In chapter 4, experiments with the antioxidant, NAC, demonstrated that mitochondrial $O_2^{\bullet -}$ significantly contributed to ATP depletion. However, from these results, it was not possible to determine if mitochondrial $O_2^{\bullet -}$ production was the sole mechanism for a decrease in OCR, or if there is another mechanism. To determine if mitochondrial $O_2^{\bullet -}$ generation was the primary factor contributing to a decrease in mitochondrial OXPHOS, experiments with NAC would have to be carried out with XF analysis. However, due to time constraints, it was not possible to carry out these experiments. We cannot exclude the possibility that that the triazoles, like many other compounds, hit multiple targets that impact cellular bioenergetics.

Consistent with previous studies, an inhibition of OXHPOS by 197 caused an increase in glycolysis of glucose cultured L6 cells (Gohil *et al*., 2010; Reily *et al*., 2012). In contrast, there was no increase in glycolysis of galactose cultured cells following 197 treatment. These results are consistent with the theory of the 'glucose/galactose'

model, in that L6 glucose cells were able to stimulate glycolysis to compensate for loss of mitochondrial ATP production, whereas galactose cells could not, resulting in a complete depletion of ATP in galactose cells (after 24 hours with 200μM 197).

5.5.6 Effect of 197 on mitochondrial superoxide production of L6 cells cultured in glucose and galactose

In chapter 4, it was shown that the SI triazoles increased mitochondrial $O_2^{\bullet-}$ production, which was responsible for triazole-induced ATP depletion in glucose cultured L6 cells (section 4.4.4.2). Since switching the media from glucose to galactose increased mitochondrial respiration, the effect of 197 and AMA (positive control) on mitochondrial $O_2^{\bullet-}$ production in galactose cultured L6 cells was investigated. Treatment with both 197 and AMA for 1 hour induced a significantly greater amount of mitochondrial $O_2^{\bullet-}$ in galactose cells than in glucose cells. The fact that galactose cells induced significantly more mitochondrial $O_2^{\bullet-}$ than glucose cells may provide further explanation for the increased sensitivity of galactose cells to certain mitochondrial toxicants. As such, the mechanism determining increased sensitivity of galactose cells to mitochondrial toxicants may not only depend on the cells inability to utilise glycolysis for ATP, but also on the induction of a greater amount of mitochondrial $O_2^{\bullet-}$ than in glucose cells.

At present there is no published literature comparing the induction of ROS in glucose and galactose cultured cells following mitochondrial insult. The potential reasons for an increased mitochondrial $O_2^{\bullet-}$ production in galactose cells likely relates to the changes in mitochondrial function. As detailed previously, galactose cultured cells are able to increase mitochondrial respiration by increasing TCA activity and/or increasing the quantity of electron carriers. An increase in the TCA activity of galactose grown cells, as demonstrated in primary muscle cells and fibroblasts (Rossignol *et al*., 2004; Palmfeldt *et al*., 2009; Aguer *et al*., 2010) increases NADH production. Indeed, Rossignol *et al* (2004) showed an increase in mitochondrial matrix NADH levels in HeLa cells cultured in galactose compared with high glucose. In terms of complex I, the proportion of fully reduced FMN (responsible for $O_2^{\bullet-}$ production) is thought to be set by the NADH/NAD^+ ratio and so inhibition or damage of the ETC would consequently

reduce the respiration rate, and increase the NADH/NAD^+ ratio leading to $O_2^{\bullet-}$ generation (Murphy, 2009). Therefore, galactose cells would likely have a higher NADH/NAD^+ ratio upon perturbation of complex I and hence induce a greater amount of $O_2^{\bullet-}$ production. Furthermore, an increased NADH/NAD^+ ratio would increase the production of $O_2^{\bullet-}$ induced by a compound that redox cycles at complex I (Cochemé and Murphy, 2008). Studies have also identified an increase in the concentration of complex I in galactose cells (Rossignol *et al*., 2004), which would increase the amount of complex I that can exist in a redox form able to react with O_2 to form $O_2^{\bullet-}$ (Murphy, 2009). In terms of $O_2^{\bullet-}$ production induced by AMA at complex III, it is possible that the increased respiration rate of galactose cells compared to glucose cells increases the reduced CoQ pool. Thus, when the Q_i site of complex III is inhibited by AMA, a larger amount of $O_2^{\bullet-}$ can be formed from the reaction of O_2 with ubisemiquinone bound to the Q_0 site in galactose cells (Murphy, 2009). An increase in the reduced CoQ pool would also favour a greater amount of $O_2^{\bullet-}$ production through reverse electron transport (RET) at complex I (Murphy, 2009).

Another reason for the increased generation of mitochondrial $O_2^{\bullet-}$ in galactose cells could be due to a reduced antioxidant capacity compared to glucose cells. To the author's knowledge, no published data have looked at the antioxidant capacity of cells cultured in glucose and galactose media. However, a study has shown that mouse skeletal muscle cells (C2C12) cultured with low glucose and high glucose media maintained equivalent levels of mitochondrial NADPH (Mailloux and Harper, 2010). NADPH is an important metabolite for mitochondrial homeostasis and functions as a directly and indirectly operating antioxidant (Kirsch and De Groot, 2001). Mailloux and Harper (2010) found that high glucose (glycolytic cells) maintained mitochondrial NADPH by glucose-6-phosphate dehydrogenase via the PPP, while low glucose (oxidative) cells were unable to maintain sufficient flux through the PPP, but compensated by activity of isocitrate dehydrogenase, an enzyme of the TCA cycle, to maintain mitochondrial NADPH levels. All together, it is likely that the adaptation of mitochondrial function to galactose media results in a greater potential for production of mitochondrial $O_2^{\bullet-}$. However, more research is required in this area to clarify the exact mechanism.

5.6 Conclusions

- L6 cells were able to adapt to growth in galactose media and maintain similar ATP levels to glucose cultured cells. In galactose cultured cells, the rate of mitochondrial OXPHOS was ~50% higher than when cells were cultured in glucose. In accordance with the increase in mitochondrial OXPHOS, there was a decrease in the rate of glycolysis in galactose cells. Addition of mitochondrial inhibitors demonstrated that glucose cells were able to up regulate glycolysis in response to a decrease in mitochondrial OXPHOS, whereas galactose cells were not.

- L6 cells cultured in galactose operated closer to state 3 respiration and used a greater proportion of the maximal respiratory capacity for ATP production than glucose cells under basal conditions. Consequently, galactose cells had a lower $\Delta\Psi m$ and basal level of mitochondrial $O_2^{\bullet-}$ than glucose cells.

- L6, H9c2 and HepG2 cells cultured in galactose media were significantly more sensitive to SI triazoles, 177 and 197, than glucose cultured cells. This data provides further evidence that 177 and 197 target mitochondria as a primary mechanism of toxicity.

- 197 dose-dependently decreased mitochondrial OXPHOS to the same extent in glucose and galactose cultured L6 cells. However, glucose cells were able to up regulate glycolysis to compensate, whereas galactose cells were not.

- 197 and AMA induced a significantly greater amount of mitochondrial $O_2^{\bullet-}$ generation in galactose than in glucose cultured L6 cells.

- Taken together, this data demonstrates that the L6 glucose/galactose model represents a sensitive model for detecting mitochondrial toxicity. Moreover, these results provide further evidence that the triazoles, 177 and 197, target the mitochondria as the primary mechanism of toxicity.

CHAPTER SIX

General discussion and future work

Chapter 6: General discussion and future work

The overall aim of this project was to investigate the extent of translation from an *in vivo* rat model to an *in vitro* skeletal muscle model, using a toxicogenomics approach. To this end, the mechanisms of toxicity of three novel SI herbicides (two triazole and one phenyl) developed by Syngenta were investigated *in vivo* and *in vitro*. Mechanistic toxicogenomics was carried out on liver (LLL), heart (LVH) and skeletal muscle (TSM) tissues from female rats treated with the SI triazoles and phenyl compounds for 28 days (Chapter 3). From this study, hypotheses on the toxic mechanisms of action of both classes of compounds were made. *In vitro* studies were then carried out to investigate the hypothesised mechanisms of triazole toxicity in an *in vitro* skeletal muscle model (Chapter 4). From this investigation, the ability of the *in vitro* skeletal muscle model to mimic the *in vivo* outcomes was assessed. As an extension of this work, an *in vitro* skeletal muscle model was developed and validated to more sensitively detect mitochondrial toxicities (Chapter 5).

6.1 *In vivo* mechanistic toxicogenomic analysis of SI compounds

6.1.1 Study design and analysis

The toxicogenomics studies in this project were carried out as an additional endpoint to the SI compound toxicity studies implemented by Syngenta as part of their safety R&D process. Therefore, the time point, dose, gender and species of the samples investigated were based on what was available and that would fit the experimental aims of this project. The advantage of this approach was the availability of traditional endpoints (e.g. histopathology and blood chemistry biomarkers) for a range of species and tissues, enabling a detailed overview on the toxic effects of the compounds. These studies identified clear class differences between the triazoles and phenyl. The primary toxicity observed with the triazole compounds was in cardiac and skeletal muscle and to a lesser extent the liver. In contrast, 907 was most toxic to the stomach, with toxicity in the liver and testes occurring at higher doses. Moreover, this approach ensured the toxicogenomics data was phenotypically anchored to the traditional endpoints, thereby reducing the over interpretation of transcriptional findings in the

absence of traditional endpoint data (Daston, 2008). Importantly, tissues from rats treated with a sub-toxic dose (150ppm) were chosen for all three compounds, which was advantageous since we could be sure that the differential gene expression changes were indicative of physiological changes and not of overt pathology (Heinloth *et al.,* 2004*;* Foster *et al*., 2007). However, it would have been ideal to track the gene expression changes in response to the SI compounds over a range of time points and doses. This would have allowed for sensitive detection of genes and pathways that displayed a temporal pattern of expression and were directly related to the progression of compound toxicity (Peddada *et al*., 2003). In addition, by only using a single time point, it was not possible to use these studies to investigate the predictability of genomic biomarkers relative to the time-course of appearance of toxicity.

In this study, the use of a single time point may explain the discrepancies between the magnitude of gene expression changes of the three SI compounds and the histopathological changes. For example, 197 induced more DEG than 177, despite histopathology identifying 177 as the more potent toxicant. In this respect, by only viewing a snapshot of gene expression at 28 days, the most significant gene expression changes following 177 treatment may have been missed (as they occurred at an earlier time point). Thus, the timing at which gene expression changes are measured may be critical (Chechik and Koller, 2008). However, a single dose and time point still enables mechanistic insight into the toxic mechanisms of action of a compound (Foster *et al*., 2007). Indeed, this study confirmed that a single time point (28 day) and dose (150ppm) were adequate to provide hypotheses on the toxic mechanism of action the SI compounds. In addition, by using tissues readily available from a previous study and not carrying out additional animal experiments, we were contributing to reduction, refinement and replacement (3R's) of animals in toxicity testing.

Functional analysis was performed using an integrated bioinformatics pipeline, which consisted of the two bioinformatics tools, IPA and DAVID. It is important to use multiple tools since they draw on different knowledge databases and so each may not

enrich the same gene lists to the same pathways (Huang *et al*., 2009; Monaco *et al*., 2012). However, there are limitations to using enrichment analysis. Among these, is the problem of comparing gene lists of different sizes (Huang *et al*., 2009). A larger gene list can have higher statistical power, resulting in higher sensitivity to slightly enriched terms, as well as to more specific terms, although the sensitivity is decreased towards largely enriched terms and broader terms (Huang *et al*., 2009). Thus, the size of the gene list can impact enrichment P-values, making it difficult to directly compare the absolute enrichment P-values across gene lists (Monaco *et al*., 2013). At present, there are no appropriate algorithms to facilitate these comparisons. Despite the limitations, enrichment analysis is still the most accepted method to uncover the most important "biological effect" contained in a gene list.

Functional analysis was able to identify clear class differences of SI compounds in terms of mechanisms of toxicity. The triazoles, 177 and 197, displayed considerable overlap of biological processes between LLL, LVH and TSM, suggesting a common non-tissue specific mechanism of triazole toxicity. These biological processes included mitochondrial dysfunction, oxidative stress, altered energy metabolism, cell death and survival (stress response) signalling, protein regulation and cell cycle/DNA damage response. The consistency between the biological processes enriched by the triazoles (in all tissues) confirmed the utility of this toxicogenomics approach and confirmed the quality of the DEG lists. Although only phenyl liver tissue was analysed for the phenyl 907, the biological processes enriched were different to the triazoles, with cholesterol biosynthesis the most highly ranked process. These results also highlighted the importance of including the phenyl compound as a comparison to the triazole compounds. By doing this, it provided the confidence that the toxicity pathways for each class were not just generic toxic responses, but actually reflected the class-specific responses. Therefore, from this toxicogenomic study we can hypothesise that the difference in mechanism of toxicity between the triazoles and phenyls may account for the difference in primary target organ toxicities identified by the traditional endpoints.

Despite the potential shortcomings of the study design (time and dose), hypotheses on the mechanisms of toxicity of the SI triazoles could be confidently made. The follow up *in vitro* studies in L6 cells confirmed these hypotheses, thereby validating the *in vivo* toxicogenomics approach for investigation of mechanisms of toxicity.

6.1.2 Alternative technologies for toxicogenomics

While microarrays are powerful tools for transcriptome analysis, there are several shortcomings (Graveley, 2008). First, they can only be used for organisms with known sequences. Second, the number of probes that fit on a microarray is limited, putting constraints on the minimum feasible genomic distance between the probes, and thus on the resolution at which a genome can be analysed. Finally, their limited specificity, sensitivity and dynamic range (the ratio of the smallest to the largest fluorescence signal) make it difficult to distinguish between highly similar mRNA sequences and to identify low abundance mRNAs. In recent years, the advent of next-generation sequencing (NGS) technologies has significantly accelerated genomic research and discovery. NGS technologies (such as pyrosequencing) provide cost-effective, rapid and highly parallel sequencing of transcripts at a whole-genome scale (termed RNA-seq), making it directly applicable to toxicogenomics studies (Roh *et al*., 2010). The single base resolution of NGS makes it a very sensitive technique, meaning a higher number of DEGs can be assessed than with microarrays (Su *et al*., 2011; Mutz *et al*., 2012). Moreover, unlike microarrays, RNA-Seq can evaluate absolute transcript levels of sequenced and unsequenced organisms, detect novel transcripts and isoforms, identify previously annotated 5' and 3' cDNA ends, map exon/intron boundaries, reveal sequence variations (e.g. SNPs) and splice variants and many more (Mutz *et al*., 2012). However, microarrays are still a valuable tool in research since it is a well established and validated technology allowing for routine study of selected targeted sequences (Wu *et al*., 2011).

6.1.3 Filling in the gaps of genomics

In this study, we took advantage of the power of genomics to understand the mechanisms underlying the toxic effect of the SI compounds. However, genomics does not reflect the complete effect of toxicants on the body. To obtain the complete

picture requires the implementation of the other 'omics technologies, particularly proteomics and metabolomics, in parallel, in a systems biology approach (Gatzidou *et al*., 2007). For example, mRNA transcriptional changes do not always result in translation and associated protein change. In addition, post-translational modifications, such as phosphorylation and glycosylation, that cause functional alterations in proteins do not appear as changes at the gene expression level.

In addition, there are a number of intermediate control points during the process by which protein is synthesised from a gene. One mechanism for post-transcriptional control of gene expression involves microRNAs (miRNAs). miRNAs are a family of evolutionary conserved, small (~ 22 nucleotides), endogenous non-coding RNA species that are transcribed from the genome, but are not translated to protein (Ambros, 2004). Instead they regulate gene expression at the post-transcriptional level by inhibiting translation or promoting mRNA degradation by base-pairing to complementary sequences within the 3' untranslated regions of regulatory target mRNAs (Chen *et al*., 2009). Since their discovery in *Caenorhabditis elegans*, thousands of miRNA genes have been identified in animal and plant genomes (Pasquinelli, 2012). Importantly, there is a subset of miRNAs that are specific or highly-enriched in cardiac and/or skeletal muscle (Chen *et al*., 2009). Studies have identified roles for miRNAs in skeletal muscle development (proliferation and differentiation), function (hypertrophy, atrophy and regeneration) as well as in skeletal muscle disease and dysfunction (Guller and Russell, 2010). There is also a growing body of research on the role of miRNAs in xenobiotic-induced toxicities, with examples in hepatotoxicity (Koufaris *et al*., 2012), neurotoxicity (Kaur *et al*., 2012) and cardiotoxicity (Horie *et al*., 2010). In this respect, miRNA profiles, like mRNA profiles, can provide mechanistic understanding on the toxicity of compounds and enable early prediction of toxic compounds (Koufaris *et al*., 2012). Circulating miRNA in plasma can also serve as a diagnostic biomarker of xenobiotic-induced toxicity (Yokoi and Nakajima, 2011). Notably, there is little research concerning xenobiotic-induced skeletal muscle toxicity and miRNAs, so this is an area that requires exploring further.

6.2 Extent of *in vivo* to *in vitro* translation in a skeletal muscle model

6.2.1 Study design and analysis

The future of toxicity testing envisions the use of predictive high-throughput toxicity screening assays that can be used to accurately predict *in vivo* responses. Ideally, high-throughput *in vitro* toxicity screens can be used to rank and prioritize compounds, as well as elucidate toxic mechanisms of action (Roggen, 2011). Although *in vitro* responses are assumed to reflect a subset of *in vivo* responses, few studies have completed a comprehensive and systematic comparison (Dere *et al*., 2006). Thus, the validation of *in vitro* cell-based models to reveal adequate *in vivo* functionality (i.e. express the relevant toxicity pathways of interest) remains an important challenge for the successful implementation of *in vitro* assays to the decision making process in early R&D (Kienhuis *et al*., 2006). Those studies that have compared *in vitro* and *in vivo* responses have been focused on hepatotoxicity and cardiotoxicity, with little focus on skeletal muscle toxicity. Therefore, in this study, the translation of the *in vivo* triazole toxicity pathways, identified by *in vivo* toxicogenomics, into the L6 skeletal muscle cell line was investigated. The advantage of using the triazole compounds to carry out this comparison, as opposed to a well characterised reference skeletal muscle toxicant, was that it avoided any potential bias. By using a well characterised skeletal muscle toxicant there would have been bias towards the toxicity pathways hypothesised from the *in vivo* toxicogenomics studies and those investigated in the *in vitro* studies.

Previous studies that have compared the responses of *in vivo* and *in vitro* models to toxicants have tended to compare the gene expression changes in both model systems (Dere *et al*., 2006; Kienhuis *et al.,* 2006; Boess *et al.,* 2009; Kienhuis *et al*., 2009). In these studies, it was shown that comparison at the level of perturbed pathways, as opposed to single gene analysis, was preferable and more informative. Therefore, in this study, the most significant SI triazole toxicity pathways identified using *in vivo* toxicogenomics were investigated *in vitro,* using cytotoxic assays. Since the previous studies comparing *in vivo* and *in vitro* models compared at the level of pathways and not genes, this approach bypassed the need to carry out *in vitro* toxicogenomics and also validated the *in vivo* toxicogenomics data.

The triazole toxicity pathways (biological processes), identified by *in vivo* toxicogenomics, that were investigated in an L6 skeletal muscle cell line included mitochondrial dysfunction, oxidative stress (cytosolic and mitochondrial $O_2^{\bullet-}$), cell death (apoptosis and necrosis), cell cycle arrest and hypertrophy. Overall, there was good concordance between the hypothesised *in vivo* mechanisms and the *in vitro* response to SI triazole treatment (chapter 4). Interestingly, the SI triazole 197 compound was more toxic than 177 across all *in vitro* endpoints studied, which does not correlate with the observed potency *in vivo*, where 177 proved more toxic. This discrepancy may be related to ADME effects and highlights that this *in vitro* model does not completely reflect the complexities of an *in vivo* model. However, these results do show that the L6 cell line expresses the relevant toxicity pathways to accurately predict relevant *in vivo* mechanisms of toxicity.

In a study by Kienhuis *et al* (2009), the *in vitro* hepatocyte and *in vivo* rat hepatocyte response to APAP treatment were compared using a toxicogenomics approach. Similarly to our study, they found that the *in vitro* results supported the *in vivo* hypothesis, and identified six biological pathways and processes that were relevant to the hypothesised mechanism of APAP toxicity. In a similar mechanism to the SI triazole compounds, the main pathways affected related to energy metabolism (fatty acid metabolism, amino acid degradation) and electron transport in the mitochondria, signifying impairment of mitochondrial function (Kienhuis *et al*., 2009). This mechanism of mitochondrial dysfunction, identified using hepatocytes *in vitro*, is in agreement with other studies on APAP toxicity being mediated by mitochondrial dysfunction and oxidative stress *in vivo* (Heinloth *et al*., 2004). Thus, this example supports the robustness of the comparative approach used in this thesis and demonstrates the ability of an *in vitro* model to predict *in vivo* outcomes.

The importance of using organ-specific cell lines to detect organ-specific sensitivities was highlighted in the *in vitro* studies with the SI triazoles and phenyl (chapter 4). In this respect, the target organ toxicities of the SI triazoles and phenyl were accurately reproduced using heart, skeletal muscle and liver cell lines (table 4.2). Similarly to previous studies, it was found that taking a ratio of the IC50 of one cell line over the

other could be predictive of possible organ toxicity (Inoue *et al*., 2007). In this study, it was shown that a 2-fold difference between cell lines was a good measure of the target organ toxicity of a particular compound. Importantly, this is the first study to consider the utility of a skeletal muscle cell line in an *in vitro* system using organ-specific cell types for prediction of skeletal muscle toxicity. However, this study was carried out using relatively uncharacterised compounds and so further experiments using well characterised compounds would be needed to further validate this *in vitro* organ-toxicity system.

A potential reason for the differential cell line response to SI triazoles was elucidated in chapter 5. Experiments with the glucose/galactose model demonstrated that HepG2 cells were able to increase ATP via raised glycolytic flux in response to SI triazole treatment. Research has demonstrated that increased glycolytic flux is an adaptive response to oxidative stress, as it increases NADPH production via the pentose phosphate pathway (Wu *et al*., 2012). NADPH is a critical source of reducing equivalent contributing to the maintenance of glutathione regeneration and antioxidant capacity in the cell. Therefore, HepG2 cells may have conferred protection against triazole-induced oxidative stress by increasing glycolytic flux and thereby increasing ATP and NADPH levels. This result is in agreement with research showing that the antioxidant capacity of organs is ordered liver>heart>muscle (Venditti *et al*, 1998).

In contrast to the triazole, the SI phenyl was hypothesised to induce toxicity through cholesterol perturbation (chapter 3). Since the liver is the principal site of cholesterol maintenance, a range of compounds are known to induce hepatotoxicity through cholesterol impairment, such as anticonvulsants (Lee *et al*., 2006) and 5-HT6 receptor antagonists (Suter *et al*., 2003). Therefore, susceptibility to cholesterol perturbation may have explained why HepG2 was most susceptible to the SI phenyl, while L6 and H9c2 were unaffected.

The relevance of the L6 *in vitro* model to investigate skeletal muscle toxicants sensitively supports the further development of high-throughput toxicity screening

with this cell line. To improve the throughput and sensitivity of studies assessing multiple endpoints in skeletal muscle cells, high-content screening (HCS) is a promising technology (Zanella *et al*., 2010). Instead of taking the average effects of multiple cells in a well, HCS is able to analyse individual cells in real time, using epifluorescence microscopy, for multiple parameters to elucidate mechanisms of toxicity (Giuliano *et al*., 1997).

6.2.2 Limitations of the L6 cell line model and alternative approaches for the future

Although this skeletal muscle cell model was able to accurately mimic the *in vivo* response to triazole toxicity, this approach assumes that skeletal muscle toxicity is only a result of cytotoxic responses. However, some skeletal muscle toxicants, such as Inteferon-α, induce toxicity through inflammation (Venezia *et al*., 2005). Therefore, this type of toxicity could not be modelled using the L6 skeletal muscle model alone and would require co-culture with a variety of cell types that can mount an immune response. In addition, this study focused on structural cellular toxicity, whereas some xenobiotics induce functional toxicity in cardiac and skeletal muscle. For example, the bactericide triclosan potently impairs striated muscle excitation-contraction coupling by interfering with signaling between L-type Ca^{2+} and RyR channels in skeletal muscle, and L-type Ca^{2+} entry in cardiac muscle (Cherednichenko *et al*., 2012). The result of this impairment is weakened contractility and depressed haemodynamics. Therefore, it is important that the effects of compounds on striated muscle functionality is addressed in R&D (a subject that is elaborated on later).

Certain xenobiotics require metabolism to induce toxicity, in which toxic metabolites are formed through bioactivation (Dekant, 2009). Since enzymes involved in metabolism are localized mainly in the liver, this organ is most at risk to the formation of toxic metabolites. However, metabolites formed in the liver are able to reach periphery tissues, such as the heart and skeletal muscle, to exert their toxic effects. For example, a study has shown that metabolism of 3,4-methylenedioxymethamphetamine (MDMA) into reactive metabolites (free radical species, *ortho*-quinones and aminochromes) is required for the expression of MDMA-

cardiotoxicity (Carvalho *et al*., 2004). MDMA is also toxic to skeletal muscle, inducing rhabdomyolysis, and *in vitro* mechanistic studies with L6 cells incorporated a co-culture with primary hepatocytes to bioactivate the compounds (Rusyniak *et al*., 2005). In this thesis, it was found that the parent triazole compounds were highly toxic themselves, suggesting that they do not require bioactivation to elicit their toxic effects. However, it is important for industrial and pharmaceutical companies to screen for the effects of metabolism. To this end, a metabolic component, such as incubation of compounds with primary hepatocytes or S9 fraction of liver can be included before treatment of a target organ cell line.

The length of time the compounds are incubated for is also an important consideration. In this study, the maximum treatment time was 24 hours. While this was adequate to study the acute mechanistic effects of the triazoles, some compounds may need extended exposure. Although not a priority in this study, a longer exposure time would have allowed accurate IC50 values to be calculated for the triazoles and phenyl. In the industry and pharmaceutical settings, the calculation of the IC50 value provides a rapid and efficient way of comparing compound toxicities. Therefore, for screening large numbers of compounds a longer time course of 72 hours is often employed (O'Brien *et al*., 2006; Lin and Will, 2011).

Although not taken into account with this *in vitro* model, the selective uptake of compounds may be responsible for cell-type and not just organ-specific toxicities. This is especially relevant for skeletal muscle since they are made up of two types of fibers; fast twitch (glycolytic) muscle fibers and slow-twitch (oxidative) muscle fibers, which have differences in their contraction speed and energy substrate utilisation (Biressi *et al*., 2007). For example, some statins paradoxically induce mitochondrial impairment and apoptosis in anaerobically poised, fast-twitch muscle fibers, and not in mitochondrially enriched slow-twitch muscle fibers, because of a selective membrane transporter (monocarboxylate transporter) on the susceptible fibers that takes up the statin (Dykens *et al*., 2008). Therefore, it may be important to screen compounds against these two muscle fiber types. It has previously been demonstrated that a mouse skeletal muscle myoblast (C2C12) cell line can be differentiated into either

muscle type depending on the environment they are cultured in (Matsuoka and Inoue, 2008). By culturing the cells with fast muscle extract, it is possible to increase the number of fast-type fibers in the cell culture and *vice versa* with a slow muscle extract. In addition, research in human myotubes has shown that chronic, low frequency electrical-pulse stimulation is able to induce transformation of fast-twitch glycolytic muscle fibers into slow-type oxidative fibers (Nikolic *et al*., 2012). Therefore, using either one, or a combination, of these techniques, L6 myoblasts could be differentiated into fast and slow twitch muscle fibers, to create a model that is able to distinguish fiber-type toxicities. However, contractile cells, such as cardiac and skeletal muscle are difficult to maintain long-term in 2D monolayers for physiological xenobiotic screening applications due to detachment from the plate surface as they become functionally active with differentiation (Vandenburgh *et al*., 2008). Indeed, this is one of the reasons the L6 cell line was not differentiated in this study. Moreover, it was not possible to differentiate L6 cells grown in galactose (data not shown). This is in agreement with a previous study, in which glucose restriction (either no glucose or low glucose) impaired differentiation of C2C12 skeletal muscle myoblasts, which was associated with activation of AMP-activated protein kinase (AMPK) (Fulco *et al*., 2008).

There are a number of cell culture techniques that have recently been developed which aim to improve the microenvironment of cell cultures to more faithfully mimic the *in vivo* functionality. The most important techniques for skeletal muscle include 3D culturing, and microfluidics (Ghaemmaghami *et al*., 2012). Indeed, if skeletal muscle cells are organised into 3D structures *in vitro*, they are more representative of *in vivo* tissues than 2D cultures and since they are normally attached to a 3D matrix, detachment from a tissue-culture dish surface is not an issue (Vandenburgh *et al*., 2008). This approach therefore allows assessment of the effects of xenobiotics on the function of skeletal muscle contraction. For example, Vandenburgh *et al* (2008) developed a 96-well based 3D skeletal muscle system (mouse muscle), in which force measurements were made using novel image-based motion detection technology. Using atorvastatin as a model compound, the authors showed that muscle force decreased in a dose and time dependent fashion. This approach could therefore be

implemented as a high-throughput *in vitro* screen for assessing the effects of compounds, like triclosan, that may impair skeletal muscle force-generating ability. Although 3D models are increasingly used, most commercial toxicity endpoints that measure cellular or sub cellular effects are still adjusted to monolayer cultures. Thus, to fully exploit the third dimension, more appropriate endpoints, such as imaging technologies (as used by Vandenburgh *et al* (2008)), need to be developed (Van Vliet *et al*., 2011).

More recently, there has been the emphasis to incorporate 3D microenvironments into microfluidics on a micro-chip scale. Microfluidics simulates the effects of flow *in vivo,* and is used to generate gradients of xenobiotic concentrations, create specific physical microenvironments (e.g. shear stress) and to construct a circulatory system to better mimic the physiological state (Wu *et al*., 2009). As well as 3D morphology, alignment of the cells is also important for maintaining phenotypes and function, especially in skeletal muscle. To this end, Anene-Nzelu *et al* (2013) have developed a 3D microfluidic chip with incorporated micro-topographical cues to enhance alignment and function of muscle cells. Using C2C12 mouse myoblasts with this 'muscle chip', they found enhanced differentiation into skeletal muscle, which facilitated end-end contact of myotubes and enhanced expression of skeletal muscle genes (Anene-Nzelu *et al*., 2013). Future improvements to on-chip muscle tissue models include incorporating neuromuscular junctions by co-culturing myotubes with neurons and stimulating them to induce muscle contraction (Ghaemmaghami *et al*., 2012).

Microfluidics has also enabled the generation of a 'body-on-a-chip' system, whereby multiple cell lines representing different organs are cultured in separate chambers on a single chip, and are connected by channels. This enables cells to be connected in a systematic format that reflects the *in vivo* situation, allowing parameters, such as absorption and metabolism of xenobiotics to be assessed. For example, Imura *et al* (2010) developed a microchip that consisted of the ordered arrangement of an intestine component (Caco-2 cells), a liver component (HepG2 cells) and target cancer cell line (MCF-7) in a series configuration. Using this model, they tested the anti-

cancer drug Cyclophosphamide (CPA), and demonstrated the importance of bioactivation of CPA by the liver cells to induce toxicity to the MCF-7 cells (Imura *et al*., 2010). Since this technology is on a micro-scale it requires less cells, reagents and compounds than conventional *in vitro* assays and so is particularly useful for high-throughput toxicity testing in early R&D.

6.3 Evidence for the mechanism of SI compound toxicity

6.3.1 Is the SI plant mode of action, VLCFA synthesis inhibition, a mechanism responsible for the toxicity in the mammal?

The herbicidal mechanism of the SI compounds is the inhibition of very-long-chain fatty acid (VLCFA) synthesis. Specifically, the compound reacts with cysteinyl sulphur in the reaction centre of 3-Ketoacyl synthase (FAE-type elongase), the first enzyme in the fatty acid elongase complex. VLCFA, fatty acids with more than 20 carbon atoms, are used in cuticular wax formation and when absent, the membrane becomes leaky leading to death of the herbicide treated plant (Gotz and Boger, 2004).

Most modern herbicides have low mammalian toxicity since the target site for herbicides is often not present in mammals. However, VLCFA are present in mammals and play an important role in skin barrier formation, myelin maintenance, spermatogenesis, retinal function, and anti-inflammation (Kihara, 2012). Indeed, studies have shown that myelin-deficient mouse mutants have very low fatty acid elongation activity (Shaner, 2003). However, the enzymes that catalyze the condensation step of fatty acid elongation in plants and mammals differ; plant fatty acid elongation is mediated by the FAE-type elongase-like family of enzymes, whereas elongation in mammals is mediated by the ELO-type elongases. Importantly, the FAE-type elongases and ELO-type elongases evolved independently of one another and share no sequence similarity (Paul *et al*., 2006). While active FAE-type elongases have highly distinctive patterns of differential sensitivity to chloroacetanilide herbicides and other VLCFA synthesis inhibitors, the ELO-type elongases are unaffected (Trenkamp *et al*., 2004). This makes the FAE-pathway a highly favourable herbicide target.

It is not currently known whether VLCFA synthesis inhibitors inhibit VLCFA synthesis in mammals as well as in plants and, if so, does this provide a connection between mammalian toxicity of these compounds and VLCFA synthesis. Some toxic side-effects have been known with VLCFA synthesis inhibitors, including acetanilide and thiocarbamate (Shaner, 2003). For example, acetochlor, an acetanilide, caused testicular atrophy and degeneration, as well as kidney and severe neurological effects in male dogs. The neurological effects were supported by histopathological findings in the vermis cerebellum (Shaner, 2003). These findings imply that with certain VLCFA synthesis inhibitors, inhibition of VLCFA synthesis in the mammal may be an explanation for their adverse toxicity. However, more research into this area is warranted, before any significant conclusions can be drawn.

Based on the histopathology and blood chemistry data for the SI triazoles, 177 and 197 (section 1.5.2), it is evident that these compounds do not have any adverse effects on tissues that contain VLCFA. Coupled with the *in vivo* toxicogenomics and *in vitro* results, there is convincing evidence that the toxicity of the triazole compounds is not an on-target toxicity, but rather an off-target toxicity mediated through mitochondrial dysfunction. The phenyl, 907, however, did have a degenerative effect on the testes of all males tested after 28 day treatment. This suggests that VLCFA inhibition could have been the cause of testicular toxicity, however further research would be required to confirm this.

6.3.2 Evidence for the mechanism of SI triazole toxicity based on *in vivo* toxicogenomics and *in vitro* skeletal muscle investigations

Based on the *in vivo* toxicogenomics data, *in vitro* cytotoxic endpoints measured and the glucose/galactose model results, a hypothesis on the mechanism of SI triazole toxicity has been made (figure 6.1).

In vivo toxicogenomics identified pathways relating to mitochondrial dysfunction (i.e. OXPHOS and mitochondrial inner membrane) and oxidative stress (i.e. Nrf-2 mediated oxidative stress response) as the most significantly enriched by 177 and 197 in all tissues. A majority of the other pathways and transcriptional changes enriched by the

SI triazoles related to stress signalling and adaptive responses to mitochondrial dysfunction and/or oxidative stress, including; altered energy metabolism (fatty acid metabolism, PPARα), mitochondrial biogenesis (PPARα and Nrf-2 transcriptional regulation), cell cycle arrest/DNA damage repair, protein homeostasis regulation (ubiquitin-proteasome pathway, hypertrophy) and cell death (apoptosis).

The *in vitro* studies confirmed that mitochondria are the primary target of SI triazole toxicity. Both triazoles depleted ATP levels after only 2 hours in L6 cells, while cell viability remained unaffected, which is indicative of early deleterious mitochondrial function (chapter 4). In addition, the glucose/galactose assay in L6, H9c2 and HepG2 cell lines demonstrated that 177 and 197 were significantly more toxic to cells grown in galactose-containing media than in glucose containing media, confirming that mitochondria were a primary target for SI triazole toxicity (chapter 5). Further experiments were carried out with the XF analyser to assess the effects of 197 on cellular bioenergetics (OXPHOS and glycolysis) and mitochondrial function (chapter 5). These results showed that 197 decreased OXPHOS by ~50% after 4 hours, and concomitantly up regulated glycolysis. Analysis of mitochondrial function suggested that 197 does not inhibit ATPase or uncouple the mitochondrial membrane potential to induce toxicity. Furthermore, 197 had much slower kinetics than canonical inhibitors that directly target the respiratory chain (AMA) or ATP synthase (oligomycin). Overall, the XF analyser data provided further evidence that 197 had a deleterious effect on the mitochondria, although it was not possible to elucidate the exact mechanism. However, experiments investigating cytosolic and mitochondrial $O_2^{\bullet-}$ production provided evidence for the key mechanism inducing mitochondrial dysfunction (chapter 4). Both 177 and 197 induced significant amounts of mitochondrial-derived $O_2^{\bullet-}$. In contrast to AMA (a complex III inhibitor) 177 and 197 induced little cytosolic $O_2^{\bullet-}$ production and so it was hypothesised that complex I was a likely source of triazole-induced $O_2^{\bullet-}$ production. The antioxidant NAC was able to significantly reduce the induction of mitochondrial $O_2^{\bullet-}$ generation, providing further evidence that the triazoles induced mitochondrial-derived $O_2^{\bullet-}$. Significantly, NAC was also able to prevent ATP depletion induced by 177 and 197, indicating that ATP depletion was the result of mitochondrial $O_2^{\bullet-}$ production. These results imply that the

triazoles did not inhibit the mitochondrial ETC to induce $O_2^{\bullet-}$, otherwise ATP would have depleted regardless of the antioxidant effect of NAC (Watabe and Nakaki, 2006). Therefore, we can hypothesise that the triazole compounds redox cycle to generate $O_2^{\bullet-}$ and that this redox cycling takes place at complex I of the mitochondria. Figure 6.1 further elaborates on how the SI triazoles could be taken up by the mitochondria and how they might redox cycle at complex I to induce $O_2^{\bullet-}$ generation.

The SI triazoles also induced G_1 cell cycle arrest, hypertrophy and caspase-mediated apoptosis (chapter 4). Studies have demonstrated the involvement of cell cycle machinery in the development of cardiac and skeletal muscle hypertrophy *in vivo* and *in vitro* (Brooks *et al*., 1998; Hlaing *et al*., 2002; Oyama *et al*., 2011; Choi *et al*., 2011). Specifically, Hlaing *et al* (2002) showed that during skeletal muscle hypertrophy, the G_1 cell cycle machinery was recruited to regulate the hypertrophic response. Moreover, studies have shown that ROS plays an important role in mediating cell cycle arrest (Shackelford *et al*., 2000; Oyama *et al*., 2011). Research has demonstrated that DNA damage induced by mitochondrial-derived H_2O_2-mediatd oxidative stress increases expression of p53 and arrests cells at the G1/S checkpoint or induces apoptosis (Kumar *et al*., 2009; Panieri *et al*., 2013). Although DNA damage was not investigated *in vitro*, the *in vivo* toxicogenomics study enriched DNA damage repair pathways in response to SI triazole treatment. Therefore, based on the *in vivo* toxicogenomics and *in vitro* findings it is possible to hypothesise that through mitochondrial H_2O_2 generation, the SI triazoles were able to mediate oxidative stress effects in the cytosol and nuclear compartments and thereby signal G_1 cell cycle arrest and subsequent hypertrophy (figure 6.1). The decision of the L6 cells to undergo either cell cycle arrest and hypertrophy, or cell death through either apoptosis or necrosis following SI triazole treatment was likely attributable to the amount of ROS produced and the availability of ATP.

The overall conclusion from all of this data is that the major impact of the SI triazoles in the cell is on mitochondria, with the subsequent activation of pathways a consequence of both mitochondrial dysfunction and oxidative stress.

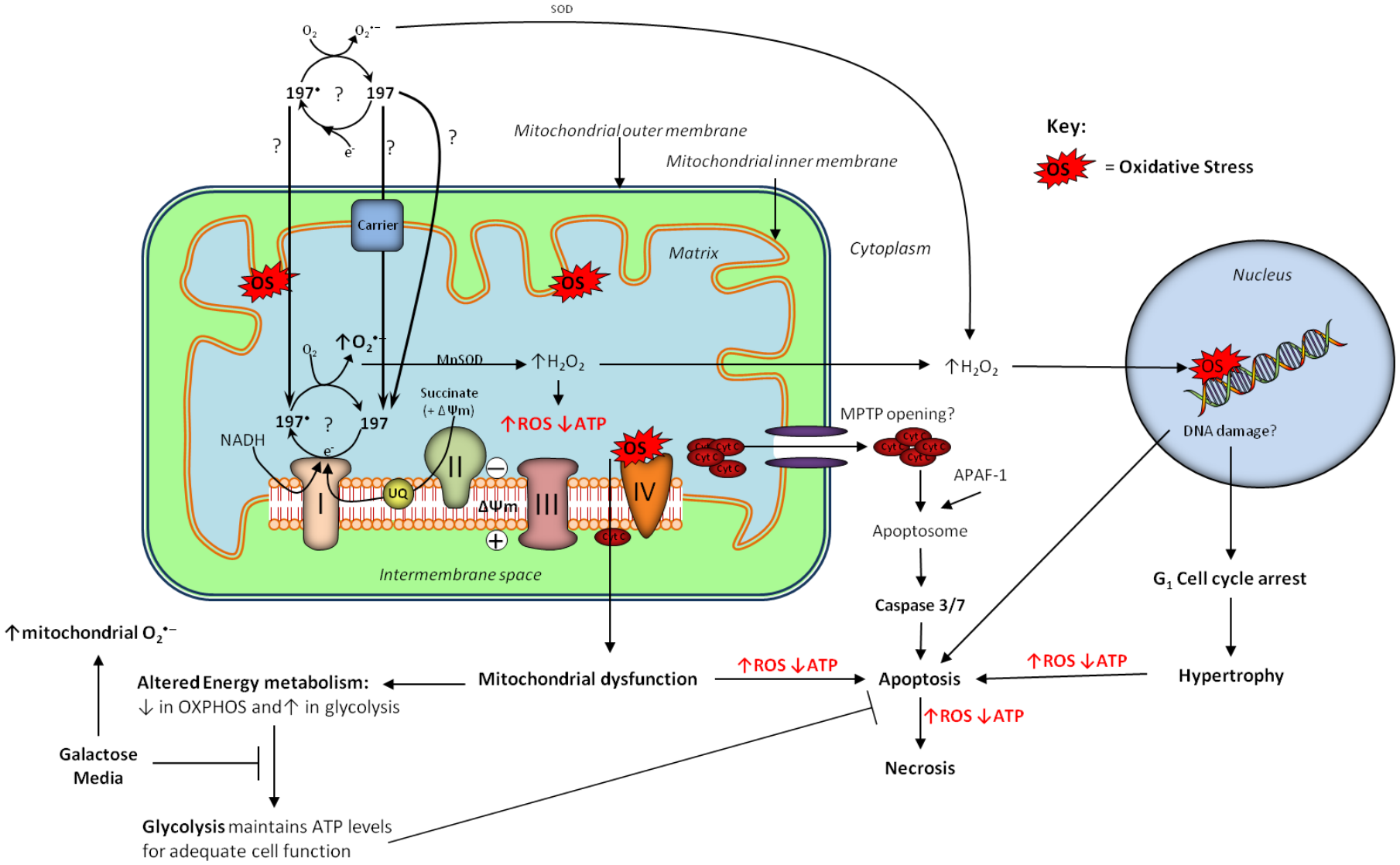
SOD
Key:
OS = Oxidative Stress
Mitochondrial outer membrane
Mitochondrial inner membrane
Carrier
Matrix
Cytoplasm
Nucleus
OS
MnSOD
↑H2O2
↑O2•−
Succinate
(+ ΔΨm)
↑ROS ↓ATP
NADH
UQ
I
II
III
IV
ΔΨm
Cyt C
MPTP opening?
APAF-1
Apoptosome
Caspase 3/7
DNA damage?
Intermembrane space
↑mitochondrial O2•−
Altered Energy metabolism:
↓ in OXPHOS and ↑ in glycolysis
Mitochondrial dysfunction
Apoptosis
Necrosis
Hypertrophy
G1 Cell cycle arrest
Galactose
Media
Glycolysis maintains ATP levels
for adequate cell function

Figure 6.1. Hypothesis on mechanisms of SI triazole toxicity. The SI triazoles (177/197) could be taken up by the mitochondria, either via movement through the phospholipid bilayer or a putative carrier-mediated pathway, driven by the mitochondrial membrane potential (ΔΨm). Once inside the matrix, the SI triazole could be reduced to an unstable SI triazole radical (e.g. $197^{\bullet}$) at complex I in the ETC by electrons (e^-) donated from NADH. Alternatively, in the presence of a ΔΨm, SI triazole radical could be generated at complex I by reverse electron transport whereby electrons from the CoQ pool (e.g. from the substrate Succinate) are driven into complex I by the ΔΨm. The SI triazole radical could then rapidly react with O_2 to produce $O_2^{\bullet-}$ and regenerate SI triazole, in a redox cycling reaction. Additionally, the SI triazole could be reduced to its free radical in the cytosol (e.g. by NADPH-cytochrome P450 reductase), and the SI triazole radical taken up into the matrix by direct passage across the membrane. Whatever the mechanism, SI triazoles generate significant amounts of mitochondrial $O_2^{\bullet-}$ production. Subsequent dismutation (by MnSOD) leads to the generation of hydrogen peroxide (H_2O_2) and harmful levels of ROS (e.g. OH•). Additionally, cytosolic superoxide could be converted to H_2O_2 by cytosolic superoxide dismutase (SOD). Increased ROS levels result in oxidative stress and mitochondrial dysfunction, characterised by a decrease in OXPHOS and ATP production and a shift to glycolysis for energy generation. Increased production of H_2O_2 could damage DNA, increase expression of p53 and arrest cells at the G1/S checkpoint, which may lead to hypertrophy. Considerable mitochondrial oxidative damage can trigger apoptosis through opening of the MPTP, loss of ΔΨm and release of pro-apoptotic proteins (such as Cyt c) into the cytosol, resulting in caspase activation and apoptotic cell death. The levels of ROS and ATP determine whether the cells undergo cell cycle arrest and hypertrophy or apoptosis. Moreover, the levels of ROS and ATP will dictate whether the cells undergo apoptotic or necrotic cell death. Pathways with question marks represent hypothesised mechanisms (based on the literature and *in vivo* toxicogenomics) and the terms in **bold** represent those pathways known to be affected by SI triazoles (through *in vitro* experiments). Abbreviations: ROS, reactive oxygen species; $O_2^{\bullet-}$, superoxide; UQ, ubiquinone (Coenzyme Q_{10}); OS, oxidative stress.

Detail on the mechanism of triazole toxicity provides useful information for Syngenta, enabling them to investigate possible features of the chemical structures of SI triazole compounds which are responsible for mitochondrial toxicity. Notably, the triazole aspect of the SI compound is the likely mediator of the adverse mitochondrial toxicity, given that the Phenyl compound induced toxicity through a different mechanism and was toxic to different tissues. Using a quantitative structure-activity relationship (QSAR) approach, Syngenta would be able to identify compounds with similar structural moieties early in the R&D process. This would provide a hypothesis on the potential mitochondrial toxicity of these novel compounds.

6.4 Mitochondrial toxicity testing paradigm – L6 glucose/galactose model

6.4.1 Study design and analysis

Xenobiotic-induced mitochondrial toxicity has become an area of concern for many agrochemical and pharmaceutical industries (Dykens and Will, 2007). In particular, skeletal muscle systems are susceptible to mitochondrial toxicity due to their high metabolic activity and mitochondrial content, as well as a reduced antioxidant capacity (compared to the liver and heart) (Neustadt and Pieczenik, 2008; Vendetti *et al*., 2001). Therefore, there is a need for a skeletal muscle cell-based assays that detect mitochondrial toxicity early in the R&D process. In order to develop a skeletal muscle model that more sensitively detected mitochondrial toxicities, glucose was substituted with galactose in the media of L6 cells (glucose/galactose model) (chapter 5). Since glycolytic metabolism of galactose is too slow to provide adequate levels of ATP, the cells are forced to rely on mitochondrial OXPHOS to produce the bulk of their ATP and are thus more susceptible to compounds that target mitochondria as a primary mode of toxicity (Marroquin *et al*., 2007).

As has previously been demonstrated with HepG2 (Marroquin *et al*., 2007), H9c2 (Rana *et al*., 2011) and primary human skeletal muscle cells (Aguer *et al*., 2010), L6 skeletal muscle cells were able to adapt to culture in galactose media, maintaining similar levels of ATP to cells cultured in glucose. Experiments with classical mitochondrial toxicants showed that galactose cultured L6 cells were significantly more sensitive than glucose cells. The XF analyser revealed that glucose cells were able to up regulate glycolysis in response to mitochondrial perturbation, whereas the galactose cells were not. In addition, galactose cells generated a greater amount of mitochondrial $O_2^{\bullet-}$ than glucose cells when treated with AMA and 197. Consequently, the increased sensitivity of galactose cells may not only depend on depleted ATP levels, but also on the induction of a greater amount of mitochondrial $O_2^{\bullet-}$ (figure 6.1). These experiments confirmed that L6 skeletal muscle cells were able to adapt to galactose media and consequently reveal mitochondrial toxicants more sensitively.

However, more research into the exact mechanism determining the increased sensitivity of galactose cultured cells to mitochondrial toxicants is required.

Using the L6, H9c2 and HepG2 glucose/galactose model it was confirmed that the SI triazoles were mitochondrial toxicants. In addition, these results highlighted the use of organ-specific cell lines for more sensitive detection of mitochondrial toxicities. The L6 and H9c2 cell lines were more sensitive to 177 and 197 than HepG2 cells in both glucose and galactose media and so provide more sensitivity for detection of mitochondrial toxicity. As previously discussed, it is possible that HepG2 cells are more resistant to ROS-induced mitochondrial dysfunction due to an enhanced antioxidant capacity. However, this is the first study that has compared different cell lines for identification of mitochondrial toxicity and it was performed with relatively uncharacterised compounds. Therefore, further studies testing a large number of well characterised compounds in multiple organ-specific cell lines would need to be carried out. Previous studies have highlighted the need for organ-specific cell lines to detect xenobiotics with organ specific mitochondrial toxicities. For example, Marroquin *et al* (2007) failed to detect doxorubicin-induced mitochondrial toxicity using the glucose/galactose assay in HepG2 cells. The authors suggested that the selective doxorubicin cardiotoxicity is likely due to an atypically outward-facing exogenous NADH dehydrogenase associated with complex I of heart mitochondria that is not found in other cells, including HepG2 cell lines (Gille and Nohl, 1997). This enzyme catalyzes the oxidation of cytosolic NADH, which is required for formation of doxorubicin semiquinones. Thus, superoxide production was induced by doxorubicin semiquinone ($DQ^{\bullet}$) in cardiac mitochondria, but not in the liver mitochondria (Gille and Nohl, 1997). Therefore, Marroquin *et al* (2007) suggested that a cardiac cell line, adapted to galactose media, may be required to exacerbate doxorubicin toxicity that is fuelled by mitochondrial respiration.

6.4.2 Limitations of the glucose/galactose model

It should be noted that not all mitochondrial toxicants will be detected using a 24 hours toxicity assay, as was used here. While this assay may be able to accurately detect compounds that inhibit the ETC (thiazolidinediones), uncouple OXPHOS

(bupivacaine) and redox cycle (quinones) within the mitochondria, it is unlikely to detect compounds that target mtDNA replication (NRTIs) and gene expression (Chan *et al*., 2005; Dykens *et al.,* 2008; Pereira *et al*., 2009). Since most cells contain between hundreds and thousands of mitochondria and turnover rates for mitochondria are ~1-2 weeks, impeding mitochondrial replication is unlikely to become apparent in a cell-based functional assay until after several days (Marroquin *et al*., 2007). It also bears mentioning that the time scales and concentrations used in this study are a reflection of experimental expediency rather than the realities of pathophysiology. For example, it is feasible that longer exposures (than 24 hours) to compounds at lower concentrations could exacerbate toxicity. Moreover, many xenobiotics may bioaccumulate by transmembrane carriers at the plasma membrane and at the mitochondrial membrane and so mitochondrial liabilities can be induced at concentrations substantially lower than the calculated C_{max} (Dykens *et al*., 2007).

Although the glucose/galactose assay does not provide insight into the exact mechanism of mitochondrial perturbation, it does provide confidence that mitochondrial toxicity is the dominant pathway. It therefore serves as an ideal early screening assay to identify compounds that may potentially induce mitochondrial toxicity. A positive result with the glucose/galactose assay would then justify further *in vitro* analysis that would elucidate the mechanism, including measurement of ROS levels, oxygen consumption and glycolysis (XF analyser), mtDNA copy number, Ca^{2+} uptake capacity and mitochondrial membrane potential.

6.4.3 Alternative applications with the glucose/galactose model

The ability to alter the energy metabolism using the glucose/galactose model has also been employed to investigate disease states that have underlying mitochondrial liabilities (Robinson *et al*., 1992; Aguer *et al*., 2010). For example, Robinson *et al* (1992) used skin fibroblasts cultured in galactose as a model to diagnose cell lines that were compromised in oxidative metabolism (e.g. to identify patients with complex I deficiency). In addition Aguer *et al* (2010) used it to identify mitochondrial dysfunction in post-diabetic patients. They showed that differentiating primary human muscle cells in galactose was able to reveal a decreased oxidative capacity in myotubes derived

from post-diabetic patients compared to obese non-diabetic myotubes. Interestingly, the glucose/galactose model has also been used as a method to discover compounds that shift energy metabolism from mitochondrial respiration to glycolysis (Gohil *et al*, 2010). Gohil *et al* (2010) demonstrated that compounds that are able to switch metabolism may have therapeutic potential, since they are able to suppress mitochondrial function and thereby minimize oxidative damage that follows ischemic injury.

The metabolic activity of the cell is also an important area for cancer therapy. Robinson *et al* (2012) demonstrated that switching from aerobic glycolysis to oxidative phosphorylation modulates the sensitivity of mantle cell lymphoma cells to TRAIL (TNF-related apoptosis-inducing ligand). TRAIL is a putative anti-cancer cytokine that induces apoptosis through the extrinsic apoptotic pathway (death-induced signalling complex). They showed that cells cultured in glucose free media were more resistant to TRAIL, whereas cells that had glycolysis blocked by 2-Deoxyglucose (2-DG) were more sensitive. The use of 2-DG or other anti-glycolytic strategies may therefore have the potential to sensitize cells to anti-cancer apoptotic agents (MacFarlane *et al*., 2012). Thus, the method by which cells are forced to rely on mitochondrial OXPHOS for energy also impacts the sensitivity of some cells to compounds that might activate the extrinsic apoptotic pathway. This is an important consideration when using the glucose/galactose model as a xenobiotic screening assay, and so it would be important to investigate whether galactose sensitize L6 cells, and other cell lines, to TRAIL (and other initiators of the extrinsic apoptotic pathway).

6.5 Overall conclusions

High quality and reproducible gene expression profiles of liver, cardiac and skeletal muscle tissues taken from female rats treated with sub-toxic doses of SI herbicides for 28 days were successfully generated. Functional analysis identified clear SI compound class differences in terms of suggested mechanisms of toxicity. The biological processes enriched by the SI triazoles (177 and 197) included mitochondrial dysfunction, oxidative stress, altered energy metabolism, cell death (apoptosis), protein regulation and cell cycle/DNA damage response. In contrast, the biological processes enriched by the SI phenyl (907) were concerned with cholesterol biosynthesis. The *in vitro* studies in L6 skeletal muscle cells confirmed that the SI triazoles induced mitochondrial dysfunction, mitochondrial-derived superoxide production, cell cycle arrest, hypertrophy and apoptosis. Thus, the *in vitro* results were consistent with *in vivo* toxicogenomics data, validating these models to accurately predict structural toxicity of skeletal muscle. An *in vitro* skeletal muscle model was developed to more sensitively detect mitochondrial toxicity, by forcing L6 cells to rely on mitochondrial oxidative phosphorylation by simply substituting galactose for high-glucose in the growth media. This glucose/galactose L6 cell model is a simple and expeditious method to sensitively detect mitochondrial toxicants. The results from this thesis also support the use of organ-specific cell lines to more sensitively detect organ-specific toxicities, although more research into this area is warranted. Future work should aim to further develop the L6 skeletal muscle model to better mimic the *in vivo* model by incorporating 3D and microfluidic technologies.

Appendix *Communications and awards arising from this thesis*

Abstracts

W, Dott[1], P. Mistry[2], J. Wright[2], K.E. Herbert[1] (2013). Development and validation of *in vitro* systems to explore mechanisms of striated muscle toxicity. [1]Cardiovascular Sciences, University of Leicester, UK; [2]Syngenta Ltd, Bracknell, *UK*. Society of Toxicology (SOT) 52nd Annual Meeting, 2013.

W, Dott[1], P. Mistry[2], J. Wright[2], K.E. Herbert[1] (2011). Development of *in vitro* models with metabolic capability for cardiac and skeletal muscle toxicity testing**.** [1]Cardiovascular Sciences, University of Leicester, UK; [2]Syngenta Ltd, Bracknell, *UK*. *In Vitro* Toxicology Society (IVTS) Annual Conference, 2011.

W, Dott[1], P. Mistry[2], J. Wright[2], K.E. Herbert[1] (2011). Animals in toxicity testing: Getting to the heart of the problem. [1]Cardiovascular sciences, University of Leicester, UK; [2]Syngenta Ltd, Bracknell, *UK*. Festival of Postgraduates Research, University of Leicester.

W, Dott[1], P. Mistry[2], J. Wright[2], K.E. Herbert[1] (2011). Identification of Mechanistic Biomarkers of Cardiac and Skeletal muscle Toxicity to aid the development of tissue-specific *in vitro* Models. [1]Cardiovascular Sciences, University of Leicester, UK; [2]Syngenta Ltd, Bracknell, *UK*. Society of Toxicology (SOT) 50th Annual Meeting, 2011.

Paper

Dott, W., Mistry, P., Wright, J., Cain, K., Herbert, K.E., 2014. Modulation of mitochondrial bioenergetics in a skeletal muscle cell line model of mitochondrial toxicity. *Redox Biology*. Volume 2 In progress (2014).

Paper in preparation

W. Dott[1], P. Mistry[2], J. Wright[2], K.E. Herbert[1] (in preparation). Development and validation of an *in vitro* model to explore mechanisms of skeletal muscle toxicity. [1]Cardiovascular Sciences, University of Leicester, UK, [2]Syngenta Ltd, Bracknell, *UK*.

Awards

- Won Runner Up Prize (one of four) at the 'Vitae Midlands Hub Regional Poster Competition', 2011.
- Presented with a Highly Commended Award for the poster at the Festival of Postgraduates Research, University of Leicester, 2011.
- Won the poster prize at the In Vitro Toxicology Society (IVTS) Annual Conference, 2011.

Addenda

Addenda consists of one additional CD, which contains:

Additional file 1: Detailed summary of the SI compound animal toxicity studies. The study designs, methods and results of animal studies for 177, 197 and 907. In total there are seven tables in the word document:

- **Table S1.** Summary of the parameters measured in the Syngenta repeat dose animal studies.
- **Table S2.** Summary of the 197 repeat dose animal studies in dogs, rats and mice.
- **Table S3.** Detailed summary of the 197 28 day repeat dose study in rats.
- **Table S4.** Summary of the 4 and 28 day 177 repeat dose animal studies in rats.
- **Table S5.** Detailed summary of the 28 day 177 repeat dose study in rats.
- **Table S6.** Summary of the 28 day 907 repeat dose animal study in rats**.**
- **Table S7.** Summary of the results of the genotoxicity, sensitisation and acute toxicity assays for 177 and 197.

Additional file 2: The raw and normalised Illumina microarray data for the SI compounds. The raw and normalised data is provided as requested by the MIAME guidelines. The study designs and array data are provided for 177, 197 and 907 LLL, LVH and TSM.

Additional file 3: Figure S1. The relative variances in principal components for 177, 197 and 907 LLL, LVH and TSM.

Additional file 4-11: All the IPA and DAVID functional analysis. Each excel file contains 5 sheets: Sheet 1, IPA Toxicity lists; Sheet 2, IPA Canonical pathways, Sheet 3 IPA Networks of biological functions; Sheet 4, DAVID KEGG analysis; Sheet 5, DAVID Functional annotation clustering.

- **Additional file 4: All the IPA and DAVID analysis for 177 LLL DEG**
- **Additional file 5: All the IPA and DAVID analysis for 177 LVH DEG**
- **Additional file 6: All the IPA and DAVID analysis for 177 TSM DEG**
- **Additional file 7: All the IPA and DAVID analysis for 197 LLL DEG**
- **Additional file 8: All the IPA and DAVID analysis for 197 LVH DEG**
- **Additional file 9: All the IPA and DAVID analysis for 197 TSM DEG**
- **Additional file 10: All the IPA and DAVID analysis for common 197 DEG**
- **Additional file 11: All the IPA and DAVID analysis for 907 LLL DEG**

References

Afshari, C.A., Hamadeh, H.K., Bushel, P.R., 2011. The evolution of bioinformatics in toxicology: advancing toxicogenomics. *Toxicological Sciences.* **120 Suppl 1,** S225-37.

Aguer, C., Gambarotta, D., Mailloux, R.J., Moffat, C., Dent, R., McPherson, R., Harper, M.E., 2011. Galactose enhances oxidative metabolism and reveals mitochondrial dysfunction in human primary muscle cells. *PloS One.* **6,** e28536.

Allison, D.B., Cui, X., Page, G.P., Sabripour, M., 2006. Microarray data analysis: from disarray to consolidation and consensus. *Nature Reviews.Genetics.* **7,** 55-65.

Ambros, V., 2004. The functions of animal microRNAs. *Nature.* **431,** 350-355.

Andersen, M.E. & Krewski, D., 2009. Toxicity testing in the 21st century: bringing the vision to life. *Toxicological Sciences.* **107,** 324-330.

Anene-Nzelu, C.G., Peh, K.Y., Fraiszudeen, A., Kuan, Y.H., Ng, S.H., Toh, Y.C., Leo, H.L., Yu, H., 2013. Scalable alignment of three-dimensional cellular constructs in a microfluidic chip. *Lab on a Chip.* **13,** 4124-4133.

Anson, B.D., Kolaja, K.L., Kamp, T.J., 2011. Opportunities for use of human iPS cells in predictive toxicology. *Clinical Pharmacology and Therapeutics.* **89,** 754-758.

Atienzar, F., Gerets, H., Dufrane, S., Tilmant, K., Cornet, M., Dhalluin, S., Ruty, B., Rose, G., Canning, M., 2007. Determination of phospholipidosis potential based on gene expression analysis in HepG2 cells. *Toxicological Sciences.* **96,** 101-114.

Auman, J.T., Chou, J., Gerrish, K., Huang, Q., Jayadev, S., Blanchard, K., Paules, R.S., 2007. Identification of genes implicated in methapyrilene-induced hepatotoxicity by comparing differential gene expression in target and nontarget tissue. *Environmental Health Perspectives.* **115,** 572-578.

Baird, T.D. & Wek, R.C., 2012. Eukaryotic initiation factor 2 phosphorylation and translational control in metabolism. *Advances in Nutrition (Bethesda, Md.).* **3,** 307-321.

Begriche, K., Massart, J., Robin, M.A., Borgne-Sanchez, A., Fromenty, B., 2011. Drug-induced toxicity on mitochondria and lipid metabolism: mechanistic diversity and deleterious consequences for the liver. *Journal of Hepatology.* **54,** 773-794.

Benjamini, Y. & Hochberg, Y., 1995. Controlling the False Discovery Rate: a Practical and Powerful Approach to Multiple Testing. *Journal of Royal Statistical Society.* **57,** 289.

Benrahmoune, M., Therond, P., Abedinzadeh, Z., 2000. The reaction of superoxide radical with N-acetylcysteine. *Free Radical Biology & Medicine.* **29,** 775-782.

Berg, N., De Wever, B., Fuchs, H.W., Gaca, M., Krul, C., Roggen, E.L., 2011. Toxicology in the 21st century--working our way towards a visionary reality. *Toxicology in Vitro.* **25,** 874-881.

Bergmann, M.W., 2010. WNT signaling in adult cardiac hypertrophy and remodeling: lessons learned from cardiac development. *Circulation Research.* **107,** 1198-1208.

Berndt, C., Lillig, C.H., Holmgren, A., 2007. Thiol-based mechanisms of the thioredoxin and glutaredoxin systems: implications for diseases in the cardiovascular system. *American Journal of Physiology.Heart and Circulatory Physiology.* **292,** H1227-36.

Bertinchant, J.P., Robert, E., Polge, A., Marty-Double, C., Fabbro-Peray, P., Poirey, S., Aya, G., Juan, J.M., Ledermann, B., de la Coussaye, J.E., Dauzat, M., 2000. Comparison of the diagnostic value of cardiac troponin I and T determinations for detecting early myocardial damage and the relationship with histological findings after isoprenaline-induced cardiac injury in rats. *Clinica Chimica Acta; International Journal of Clinical Chemistry.* **298,** 13-28.

Biressi, S., Molinaro, M., Cossu, G., 2007. Cellular heterogeneity during vertebrate skeletal muscle development. *Developmental Biology.* **308,** 281-293.

Blajeski, A.L., Phan, V.A., Kottke, T.J., Kaufmann, S.H., 2002. G(1) and G(2) cell-cycle arrest following microtubule depolymerization in human breast cancer cells. *The Journal of Clinical Investigation.* **110,** 91-99.

Blomme, E.A., Yang, Y., Waring, J.F., 2009. Use of toxicogenomics to understand mechanisms of drug-induced hepatotoxicity during drug discovery and development. *Toxicology Letters.* **186,** 22-31.

Bodine, S.C., Stitt, T.N., Gonzalez, M., Kline, W.O., Stover, G.L., Bauerlein, R., Zlotchenko, E., Scrimgeour, A., Lawrence, J.C., Glass, D.J., Yancopoulos, G.D., 2001. Akt/mTOR pathway is a crucial regulator of skeletal muscle hypertrophy and can prevent muscle atrophy in vivo. *Nature Cell Biology.* **3,** 1014-1019.

Boess, F., Durr, E., Schaub, N., Haiker, M., Albertini, S., Suter, L., 2007. An in vitro study on 5-HT6 receptor antagonist induced hepatotoxicity based on biochemical assays and toxicogenomics. *Toxicology in Vitro.* **21,** 1276-1286.

Bokhari, M., Carnachan, R.J., Cameron, N.R., Przyborski, S.A., 2007. Culture of HepG2 liver cells on three dimensional polystyrene scaffolds enhances cell structure and function during toxicological challenge. *Journal of Anatomy.* **211,** 567-576.

Boluyt, M.O., Li, Z.B., Loyd, A.M., Scalia, A.F., Cirrincione, G.M., Jackson, R.R., 2004. The mTOR/p70S6K signal transduction pathway plays a role in cardiac hypertrophy and influences expression of myosin heavy chain genes in vivo. *Cardiovascular Drugs and Therapy.* **18,** 257-267.

Bouitbir, J., Charles, A.L., Echaniz-Laguna, A., Kindo, M., Daussin, F., Auwerx, J., Piquard, F., Geny, B., Zoll, J., 2012. Opposite effects of statins on mitochondria of cardiac and skeletal muscles: a 'mitohormesis' mechanism involving reactive oxygen species and PGC-1. *European Heart Journal.* **33,** 1397-1407.

Brand, M.D., Affourtit, C., Esteves, T.C., Green, K., Lambert, A.J., Miwa, S., Pakay, J.L., Parker, N., 2004. Mitochondrial superoxide: production, biological effects, and activation of uncoupling proteins. *Free Radical Biology & Medicine.* **37,** 755-767.

Brand, M.D. & Nicholls, D.G., 2011. Assessing mitochondrial dysfunction in cells. *The Biochemical Journal.* **435,** 297-312.

Brooks, G., Poolman, R.A., Li, J.M., 1998. Arresting developments in the cardiac myocyte cell cycle: role of cyclin-dependent kinase inhibitors. *Cardiovascular Research.* **39,** 301-311.

Bustamante, E. & Pedersen, P.L., 1977. High aerobic glycolysis of rat hepatoma cells in culture: role of mitochondrial hexokinase. *Proceedings of the National Academy of Sciences of the United States of America.* **74,** 3735-3739.

Cangelosi, R. & Goriely, A., 2007. Component retention in principal component analysis with application to cDNA microarray data. *Biology Direct.* **2,** 2.

Carl, J.W.,Jr, Trgovcich, J., Hannenhalli, S., 2013. Widespread evidence of viral miRNAs targeting host pathways. *BMC Bioinformatics.* **14 Suppl 2,** S3-2105-14-S2-S3. Epub 2013 Jan 21.

Carvalho, M., Remiao, F., Milhazes, N., Borges, F., Fernandes, E., Monteiro Mdo, C., Goncalves, M.J., Seabra, V., Amado, F., Carvalho, F., Bastos, M.L., 2004. Metabolism is required for the expression of ecstasy-induced cardiotoxicity in vitro. *Chemical Research in Toxicology.* **17,** 623-632.

Chan, K., Han, X.D., Kan, Y.W., 2001. An important function of Nrf2 in combating oxidative stress: detoxification of acetaminophen. *Proceedings of the National Academy of Sciences of the United States of America.* **98,** 4611-4616.

Chan, K., Truong, D., Shangari, N., O'Brien, P.J., 2005. Drug-induced mitochondrial toxicity. *Expert Opinion on Drug Metabolism & Toxicology.* **1,** 655-669.

Charaten F., 2001. Bayer decides to withdraw cholesterol drug. *Bmj.* **323,** .

Chechik, G. & Koller, D., 2009. Timing of gene expression responses to environmental changes. *Journal of Computational Biology.* **16,** 279-290.

Chen, C.M., 2011. Mitochondrial dysfunction, metabolic deficits, and increased oxidative stress in Huntington's disease. *Chang Gung Medical Journal.* **34,** 135-152.

Chen, J.F., Callis, T.E., Wang, D.Z., 2009. microRNAs and muscle disorders. *Journal of Cell Science.* **122,** 13-20.

Chen, Q.M., Tu, V.C., Wu, Y., Bahl, J.J., 2000. Hydrogen peroxide dose dependent induction of cell death or hypertrophy in cardiomyocytes. *Archives of Biochemistry and Biophysics.* **373,** 242-248.

Chen, T., Guo, L., Zhang, L., Shi, L., Fang, H., Sun, Y., Fuscoe, J.C., Mei, N., 2006. Gene expression profiles distinguish the carcinogenic effects of aristolochic acid in target (kidney) and non-target (liver) tissues in rats. *BMC Bioinformatics.* **7 Suppl 2,** S20.

Cherednichenko, G., Zhang, R., Bannister, R.A., Timofeyev, V., Li, N., Fritsch, E.B., Feng, W., Barrientos, G.C., Schebb, N.H., Hammock, B.D., Beam, K.G., Chiamvimonvat, N., Pessah, I.N., 2012. Triclosan impairs excitation-contraction coupling and Ca2+ dynamics in striated muscle. *Proceedings of the National Academy of Sciences of the United States of America.* **109,** 14158-14163.

Chhabra, R.S., Bucher, J.R., Wolfe, M., Portier, C., 2003. Toxicity characterization of environmental chemicals by the US National Toxicology Program: an overview. *International Journal of Hygiene and Environmental Health.* **206,** 437-445.

Choi, J.W., Lee, K.H., Kim, S.H., Jin, T., Lee, B.S., Oh, J., Won, H.Y., Kim, S.Y., Kang, S.M., Chung, J.H., 2011. C-reactive protein induces p53-mediated cell cycle arrest in H9c2 cardiac myocytes. *Biochemical and Biophysical Research Communications.* **410,** 525-530.

Choi, S.S., Chan, K.F., Ng, H.K., Mak, W.P., 1999. Colchicine-induced myopathy and neuropathy. *Hong Kong Medical Journal.* **5,** 204-207.

Cidad, P., Almeida, A., Bolanos, J.P., 2004. Inhibition of mitochondrial respiration by nitric oxide rapidly stimulates cytoprotective GLUT3-mediated glucose uptake through 5'-AMP-activated protein kinase. *The Biochemical Journal.* **384,** 629-636.

Cocheme, H.M. & Murphy, M.P., 2008. Complex I is the major site of mitochondrial superoxide production by paraquat. *The Journal of Biological Chemistry.* **283,** 1786-1798.

Coco, T.J. & Klasner, A.E., 2004. Drug-induced rhabdomyolysis. *Current Opinion in Pediatrics.* **16,** 206-210.

Cohen, B.H., 2010. Pharmacologic effects on mitochondrial function. *Developmental Disabilities Research Reviews.* **16,** 189-199.

Conn, C.S. & Qian, S.B., 2011. mTOR signaling in protein homeostasis: less is more? *Cell Cycle.* **10,** 1940-1947.

Copple, I.M., Goldring, C.E., Kitteringham, N.R., Park, B.K., 2008. The Nrf2-Keap1 defence pathway: role in protection against drug-induced toxicity. *Toxicology.* **246,** 24-33.

Crane, F.L., 2001. Biochemical functions of coenzyme Q10. *Journal of the American College of Nutrition.* **20,** 591-598.

Curtis, M.W., Sharma, S., Desai, T.A., Russell, B., 2010. Hypertrophy, gene expression, and beating of neonatal cardiac myocytes are affected by microdomain heterogeneity in 3D. *Biomedical Microdevices.* **12,** 1073-1085.

Dalakas, M.C., 2009. Toxic and drug-induced myopathies. *Journal of Neurology, Neurosurgery, and Psychiatry.* **80,** 832-838.

Daston, G.P., 2008. Gene expression, dose-response, and phenotypic anchoring: applications for toxicogenomics in risk assessment. *Toxicological Sciences.* **105,** 233-234.

Davit-Spraul, A., Pourci, M.L., Soni, T., Lemonnier, A., 1994. Metabolic effects of galactose on human HepG2 hepatoblastoma cells. *Metabolism: Clinical and Experimental.* **43,** 945-952.

de Graaf, A.O., Meijerink, J.P., van den Heuvel, L.P., DeAbreu, R.A., de Witte, T., Jansen, J.H., Smeitink, J.A., 2002. Bcl-2 protects against apoptosis induced by antimycin A and bongkrekic acid without restoring cellular ATP levels. *Biochimica Et Biophysica Acta.* **1554,** 57-65.

Dekant, W., 2009. The role of biotransformation and bioactivation in toxicity. *Exs.* **99,** 57-86.

Dere, E., Boverhof, D.R., Burgoon, L.D., Zacharewski, T.R., 2006. In vivo-in vitro toxicogenomic comparison of TCDD-elicited gene expression in Hepa1c1c7 mouse hepatoma cells and C57BL/6 hepatic tissue. *BMC Genomics.* **7,** 80.

Divakaruni, A.S. & Brand, M.D., 2011. The regulation and physiology of mitochondrial proton leak. *Physiology.* **26,** 192-205.

Dix, D.J., Houck, K.A., Martin, M.T., Richard, A.M., Setzer, R.W., Kavlock, R.J., 2007. The ToxCast program for prioritizing toxicity testing of environmental chemicals. *Toxicological Sciences.* **95,** 5-12.

Doidge, R., Mittal, S., Aslam, A., Winkler, G.S., 2012. The anti-proliferative activity of BTG/TOB proteins is mediated via the Caf1a (CNOT7) and Caf1b (CNOT8) deadenylase subunits of the Ccr4-not complex. *PloS One.* **7,** e51331.

Domenis, R., Bisetto, E., Rossi, D., Comelli, M., Mavelli, I., 2012. Glucose-modulated mitochondria adaptation in tumor cells: a focus on ATP synthase and inhibitor factor 1. *International Journal of Molecular Sciences.* **13,** 1933-1950.

Dowling, R.J., Topisirovic, I., Fonseca, B.D., Sonenberg, N., 2010. Dissecting the role of mTOR: lessons from mTOR inhibitors. *Biochimica Et Biophysica Acta.* **1804,** 433-439.

Dranka, B.P., Benavides, G.A., Diers, A.R., Giordano, S., Zelickson, B.R., Reily, C., Zou, L., Chatham, J.C., Hill, B.G., Zhang, J., Landar, A., Darley-Usmar, V.M., 2011. Assessing bioenergetic function in response to oxidative stress by metabolic profiling. *Free Radical Biology & Medicine.* **51,** 1621-1635.

Dranka, B.P., Hill, B.G., Darley-Usmar, V.M., 2010. Mitochondrial reserve capacity in endothelial cells: The impact of nitric oxide and reactive oxygen species. *Free Radical Biology & Medicine.* **48,** 905-914.

Dunning, M.J., Barbosa-Morais, N.L., Lynch, A.G., Tavare, S., Ritchie, M.E., 2008. Statistical issues in the analysis of Illumina data. *BMC Bioinformatics.* **9,** 85-2105-9-85.

Dykens, J.A., Jamieson, J.D., Marroquin, L.D., Nadanaciva, S., Xu, J.J., Dunn, M.C., Smith, A.R., Will, Y., 2008. In vitro assessment of mitochondrial dysfunction and cytotoxicity of nefazodone, trazodone, and buspirone. *Toxicological Sciences.* **103,** 335-345.

Dykens, J.A., Marroquin, L.D., Will, Y., 2007. Strategies to reduce late-stage drug attrition due to mitochondrial toxicity. *Expert Review of Molecular Diagnostics.* **7,** 161-175.

Dykens, J.A. & Will, Y., 2007. The significance of mitochondrial toxicity testing in drug development. *Drug Discovery Today.* **12,** 777-785.

Dzbek, J. & Korzeniewski, B., 2008. Control over the contribution of the mitochondrial membrane potential (DeltaPsi) and proton gradient (DeltapH) to the protonmotive force (Deltap). In silico studies. *The Journal of Biological Chemistry.* **283,** 33232-33239.

Ellinger-Ziegelbauer, H., Gmuender, H., Bandenburg, A., Ahr, H.J., 2008. Prediction of a carcinogenic potential of rat hepatocarcinogens using toxicogenomics analysis of short-term in vivo studies. *Mutation Research.* **637,** 23-39.

Elliott, N.T. & Yuan, F., 2011. A review of three-dimensional in vitro tissue models for drug discovery and transport studies. *Journal of Pharmaceutical Sciences.* **100,** 59-74.

Elmore, S., 2007. Apoptosis: a review of programmed cell death. *Toxicologic Pathology.* **35,** 495-516.

Estany, S., Palacio, J.R., Barnadas, R., Sabes, M., Iborra, A., Martinez, P., 2007. Antioxidant activity of N-acetylcysteine, flavonoids and alpha-tocopherol on endometrial cells in culture. *Journal of Reproductive Immunology.* **75,** 1-10.

Fabre, N., Anglade, I., Vericat, J.A., 2009. Application of toxicogenomic tools in the drug research and development process. *Toxicology Letters.* **186,** 13-17.

Faghiri, Z. & Bazan, N.G., 2010. PI3K/Akt and mTOR/p70S6K pathways mediate neuroprotectin D1-induced retinal pigment epithelial cell survival during oxidative stress-induced apoptosis. *Experimental Eye Research.* **90,** 718-725.

Ferrick, D.A., Neilson, A., Beeson, C., 2008. Advances in measuring cellular bioenergetics using extracellular flux. *Drug Discovery Today.* **13,** 268-274.

Foster, W.R., Chen, S.J., He, A., Truong, A., Bhaskaran, V., Nelson, D.M., Dambach, D.M., Lehman-McKeeman, L.D., Car, B.D., 2007. A retrospective analysis of toxicogenomics in the safety assessment of drug candidates. *Toxicologic Pathology.* **35,** 621-635.

Fulco, M., Cen, Y., Zhao, P., Hoffman, E.P., McBurney, M.W., Sauve, A.A., Sartorelli, V., 2008. Glucose restriction inhibits skeletal myoblast differentiation by activating SIRT1 through AMPK-mediated regulation of Nampt. *Developmental Cell.* **14,** 661-673.

Fulda, S., Gorman, A.M., Hori, O., Samali, A., 2010. Cellular stress responses: cell survival and cell death. *International Journal of Cell Biology.* **2010,** 214074.

Fussell, K.C., Udasin, R.G., Gray, J.P., Mishin, V., Smith, P.J., Heck, D.E., Laskin, J.D., 2011. Redox cycling and increased oxygen utilization contribute to diquat-induced oxidative stress and cytotoxicity in Chinese hamster ovary cells overexpressing NADPH-cytochrome P450 reductase. *Free Radical Biology & Medicine.* **50,** 874-882.

Ganter, B., Tugendreich, S., Pearson, C.I., Ayanoglu, E., Baumhueter, S., Bostian, K.A., Brady, L., Browne, L.J., Calvin, J.T., Day, G.J., Breckenridge, N., Dunlea, S., Eynon, B.P., Furness, L.M., Ferng, J., Fielden, M.R., Fujimoto, S.Y., Gong, L., Hu, C., Idury, R., Judo, M.S., Kolaja, K.L., Lee, M.D., McSorley, C., Minor, J.M., Nair, R.V., Natsoulis, G., Nguyen, P., Nicholson, S.M., Pham, H., Roter, A.H., Sun, D., Tan, S., Thode, S., Tolley, A.M., Vladimirova, A., Yang, J., Zhou, Z., Jarnagin, K., 2005. Development of a large-scale chemogenomics database to improve drug candidate selection and to understand mechanisms of chemical toxicity and action. *Journal of Biotechnology.* **119,** 219-244.

Gatzidou, E.T., Zira, A.N., Theocharis, S.E., 2007. Toxicogenomics: a pivotal piece in the puzzle of toxicological research. *Journal of Applied Toxicology : JAT.* **27,** 302-309.

Ghaemmaghami, A.M., Hancock, M.J., Harrington, H., Kaji, H., Khademhosseini, A., 2012. Biomimetic tissues on a chip for drug discovery. *Drug Discovery Today.* **17,** 173-181.

Gibson, K.R., Neilson, I.L., Barrett, F., Winterburn, T.J., Sharma, S., MacRury, S.M., Megson, I.L., 2009. Evaluation of the antioxidant properties of N-acetylcysteine in human platelets: prerequisite for bioconversion to glutathione for antioxidant and antiplatelet activity. *Journal of Cardiovascular Pharmacology.* **54,** 319-326.

Gille, L. & Nohl, H., 1997. Analyses of the molecular mechanism of adriamycin-induced cardiotoxicity. *Free Radical Biology & Medicine.* **23,** 775-782.

Giuliano, K., DeBiasio, R., Dunlay, T., Gough, A., Volosky, J., Zock, J., Pavlakis, G., Taylor, D., 1997. High-Content Screening: A New Approach to Easing Key Bottlenecks in the Drug Discovery Process. *Journal of Biomolecular Screening.* **2,** 249.

Glickman, M.H. & Ciechanover, A., 2002. The ubiquitin-proteasome proteolytic pathway: destruction for the sake of construction. *Physiological Reviews.* **82,** 373-428.

Gohil, V.M., Sheth, S.A., Nilsson, R., Wojtovich, A.P., Lee, J.H., Perocchi, F., Chen, W., Clich, C.B., Ayata, C., Brookes, P.S., Mootha, V.K., 2010. Discovery and therapeutic potential of drugs that shift energy metabolism from mitochondrial respiration to glycolysis. *Nat.Biotechnol.* **28,** 249.

Gordon, A.M., Regnier, M., Homsher, E., 2001. Skeletal and cardiac muscle contractile activation: tropomyosin "rocks and rolls". *News in Physiological Sciences.* **16,** 49-55.

Gotz, T. & Boger, P., 2004. The very-long-chain fatty acid synthase is inhibited by chloroacetamides. *Zeitschrift Fur Naturforschung.C, Journal of Biosciences.* **59,** 549-553.

Gradishar, W.J. & Vokes, E.E., 1990. 5-Fluorouracil cardiotoxicity: a critical review. *Annals of Oncology.* **1,** 409-414.

Graveley, B.R., 2008. Molecular biology: power sequencing. *Nature.* **453,** 1197-1198.

Guengerich, F.P., 2011. Mechanisms of drug toxicity and relevance to pharmaceutical development. *Drug Metabolism and Pharmacokinetics.* **26,** 3-14.

Guller, I. & Russell, A.P., 2010. MicroRNAs in skeletal muscle: their role and regulation in development, disease and function. *The Journal of Physiology.* **588,** 4075-4087.

Hampton, M.B. & Orrenius, S., 1997. Dual regulation of caspase activity by hydrogen peroxide: implications for apoptosis. *FEBS Letters.* **414,** 552-556.

Hampton, M.B., Stamenkovic, I., Winterbourn, C.C., 2002. Interaction with substrate sensitises caspase-3 to inactivation by hydrogen peroxide. *FEBS Letters.* **517,** 229-232.

Han, D., Antunes, F., Canali, R., Rettori, D., Cadenas, E., 2003. Voltage-dependent anion channels control the release of the superoxide anion from mitochondria to cytosol. *The Journal of Biological Chemistry.* **278,** 5557-5563.

Han, T., Wang, J., Tong, W., Moore, M.M., Fuscoe, J.C., Chen, T., 2006. Microarray analysis distinguishes differential gene expression patterns from large and small colony Thymidine kinase mutants of L5178Y mouse lymphoma cells. *BMC Bioinformatics.* **7 Suppl 2,** S9.

Hartung, T., 2009. Toxicology for the twenty-first century. *Nature.* **460,** 208-212.

Hartung, T. & Daston, G., 2009. Are in vitro tests suitable for regulatory use? *Toxicological Sciences.* **111,** 233-237.

Hastwell, P.W., Chai, L.L., Roberts, K.J., Webster, T.W., Harvey, J.S., Rees, R.W., Walmsley, R.M., 2006. High-specificity and high-sensitivity genotoxicity assessment in a human cell line: validation of the GreenScreen HC GADD45a-GFP genotoxicity assay. *Mutation Research.* **607,** 160-175.

Heinloth, A.N., Irwin, R.D., Boorman, G.A., Nettesheim, P., Fannin, R.D., Sieber, S.O., Snell, M.L., Tucker, C.J., Li, L., Travlos, G.S., Vansant, G., Blackshear, P.E., Tennant, R.W., Cunningham, M.L., Paules, R.S., 2004. Gene expression profiling of rat livers reveals indicators of potential adverse effects. *Toxicological Sciences.* **80,** 193-202.

Heist, E.K. & Ruskin, J.N., 2010. Drug-induced arrhythmia. *Circulation.* **122,** 1426-1435.

Herbert, K.E., Mistry, Y., Hastings, R., Poolman, T., Niklason, L., Williams, B., 2008. Angiotensin II-mediated oxidative DNA damage accelerates cellular senescence in cultured human vascular smooth muscle cells via telomere-dependent and independent pathways. *Circulation Research.* **102,** 201-208.

Hewitt, P. & Herget, T., 2009. Value of new biomarkers for safety testing in drug development. *Expert Review of Molecular Diagnostics.* **9,** 531-536.

Hirakawa, B., 2008. Toxicogenomic Analysis of Cardiotoxicity in Rats. *Genomics Insights.* 3–13.

Hlaing, M., Shen, X., Dazin, P., Bernstein, H.S., 2002. The hypertrophic response in C2C12 myoblasts recruits the G1 cell cycle machinery. *The Journal of Biological Chemistry.* **277,** 23794-23799.

Hohenegger, M., 2012. Drug induced rhabdomyolysis. *Current Opinion in Pharmacology.* **12,** 335-339.

Horie, T., Ono, K., Nishi, H., Nagao, K., Kinoshita, M., Watanabe, S., Kuwabara, Y., Nakashima, Y., Takanabe-Mori, R., Nishi, E., Hasegawa, K., Kita, T., Kimura, T., 2010. Acute doxorubicin cardiotoxicity is associated with miR-146a-induced inhibition of the neuregulin-ErbB pathway. *Cardiovascular Research.* **87,** 656-664.

Houck, K.A. & Kavlock, R.J., 2008. Understanding mechanisms of toxicity: insights from drug discovery research. *Toxicology and Applied Pharmacology.* **227,** 163-178.

Houtgraaf, J.H., Versmissen, J., van der Giessen, W.J., 2006. A concise review of DNA damage checkpoints and repair in mammalian cells. *Cardiovascular Revascularization Medicine.* **7,** 165-172.

Huang da, W., Sherman, B.T., Lempicki, R.A., 2009. Bioinformatics enrichment tools: paths toward the comprehensive functional analysis of large gene lists. *Nucleic Acids Research.* **37,** 1-13.

Huang da, W., Sherman, B.T., Tan, Q., Kir, J., Liu, D., Bryant, D., Guo, Y., Stephens, R., Baseler, M.W., Lane, H.C., Lempicki, R.A., 2007. DAVID Bioinformatics Resources: expanded annotation database and novel algorithms to better extract biology from large gene lists. *Nucleic Acids Research.* **35,** W169-75.

Huang, L.S., Cobessi, D., Tung, E.Y., Berry, E.A., 2005. Binding of the respiratory chain inhibitor antimycin to the mitochondrial bc1 complex: a new crystal structure reveals an altered intramolecular hydrogen-bonding pattern. *Journal of Molecular Biology.* **351,** 573-597.

Ibarra-Lara, L., Hong, E., Soria-Castro, E., Torres-Narvaez, J.C., Perez-Severiano, F., Del Valle-Mondragon, L., Cervantes-Perez, L.G., Ramirez-Ortega, M., Pastelin-Hernandez, G.S., Sanchez-Mendoza, A., 2012. Clofibrate PPARalpha activation reduces oxidative stress and improves ultrastructure and ventricular hemodynamics in no-flow myocardial ischemia. *Journal of Cardiovascular Pharmacology.* **60,** 323-334.

Im, A.R., Kim, Y.H., Uddin, M.R., Chae, S.W., Lee, H.W., Jung, W.S., Kim, Y.H., Kang, B.J., Kim, Y.S., Lee, M.Y., 2013. Protection from antimycin A-induced mitochondrial dysfunction by Nelumbo nucifera seed extracts. *Environmental Toxicology and Pharmacology.* **36,** 19-29.

Imura, Y., Sato, K., Yoshimura, E., 2010. Micro total bioassay system for ingested substances: assessment of intestinal absorption, hepatic metabolism, and bioactivity. *Analytical Chemistry.* **82,** 9983-9988.

Inoue, T., Tanaka, K., Mishima, M., Watanabe, K., 2007. Predictive in vitro cardiotoxicity and hepatotoxicity screening system using neonatal rat heart cells and rat hepatocytes. *Aatex 14.* 457.

Isenberg, J.S. & Klaunig, J.E., 2000. Role of the mitochondrial membrane permeability transition (MPT) in rotenone-induced apoptosis in liver cells. *Toxicological Sciences.* **53,** 340-351.

Itagaki, M., Takaguri, A., Kano, S., Kaneta, S., Ichihara, K., Satoh, K., 2009. Possible mechanisms underlying statin-induced skeletal muscle toxicity in L6 fibroblasts and in rats. *Journal of Pharmacological Sciences.* **109,** 94-101.

Jaeschke, H. & Bajt, M.L., 2006. Intracellular signaling mechanisms of acetaminophen-induced liver cell death. *Toxicological Sciences.* **89,** 31-41.

Jaiswal, A.K., 2004. Nrf2 signaling in coordinated activation of antioxidant gene expression. *Free Radical Biology & Medicine.* **36,** 1199-1207.

Jamal, S.M., Eisenberg, M.J., Christopoulos, S., 2004. Rhabdomyolysis associated with hydroxymethylglutaryl-coenzyme A reductase inhibitors. *American Heart Journal.* **147,** 956-965.

James, L.P., Mayeux, P.R., Hinson, J.A., 2003. Acetaminophen-induced hepatotoxicity. *Drug Metabolism and Disposition.* **31,** 1499-1506.

Janes, M.S*., et al*, 2004. Fluorogenic Detection of Mitochondrial Superoxide in Live Cells, *The American Society for Cell Biology 44th Annual Meeting, Washington, DC,* December 4-8 2004, Invitrogen, Molecular Probes pp1.

Jimenez, N.E., Wilkens, C.A., Gerdtzen, Z.P., 2011. Engineering CHO cell metabolism for growth in galactose. *BMC Proceedings.* **5 Suppl 8,** P119.

Jo, Y., Oh, J.H., Yoon, S., Bae, H., Hong, M., Shin, M., Kim, Y., 2012. The comparative analysis of in vivo and in vitro transcriptome data based on systems biology. *Biochip j.* **6,** 280.

Juretic, N., Urzua, U., Munroe, D.J., Jaimovich, E., Riveros, N., 2007. Differential gene expression in skeletal muscle cells after membrane depolarization. *Journal of Cellular Physiology.* **210,** 819-830.

Kaasik, A., Safiulina, D., Zharkovsky, A., Veksler, V., 2007. Regulation of mitochondrial matrix volume. *American Journal of Physiology.Cell Physiology.* **292,** C157-63.

Kannankeril, P., Roden, D.M., Darbar, D., 2010. Drug-induced long QT syndrome. *Pharmacological Reviews.* **62,** 760-781.

Kase, E.T., Nikolic, N., Bakke, S.S., Bogen, K.K., Aas, V., Thoresen, G.H., Rustan, A.C., 2013. Remodeling of oxidative energy metabolism by galactose improves glucose handling and metabolic switching in human skeletal muscle cells. *PloS One.* **8,** e59972.

Katalinic, V., Modun, D., Music, I., Boban, M., 2005. Gender differences in antioxidant capacity of rat tissues determined by 2,2'-azinobis (3-ethylbenzothiazoline 6-sulfonate; ABTS) and ferric reducing antioxidant power (FRAP) assays. *Comparative Biochemistry and Physiology. Toxicology & Pharmacology.* **140,** 47-52.

Kauffmann, A. & Huber, W., 2010. Microarray data quality control improves the detection of differentially expressed genes. *Genomics.* **95,** 138-142.

Kaufmann, P., Torok, M., Zahno, A., Waldhauser, K.M., Brecht, K., Krahenbuhl, S., 2006. Toxicity of statins on rat skeletal muscle mitochondria. *Cellular and Molecular Life Sciences.* **63,** 2415-2425.

Kaur, P., Armugam, A., Jeyaseelan, K., 2012. MicroRNAs in Neurotoxicity. *Journal of Toxicology.* **2012,** 870150.

Kavlock, R., Chandler, K., Houck, K., Hunter, S., Judson, R., Kleinstreuer, N., Knudsen, T., Martin, M., Padilla, S., Reif, D., Richard, A., Rotroff, D., Sipes, N., Dix, D., 2012. Update on EPA's ToxCast program: providing high throughput decision support tools for chemical risk management. *Chemical Research in Toxicology.* **25,** 1287-1302.

Kawasome, H., Papst, P., Webb, S., Keller, G.M., Johnson, G.L., Gelfand, E.W., Terada, N., 1998. Targeted disruption of p70(s6k) defines its role in protein synthesis and rapamycin sensitivity. *Proceedings of the National Academy of Sciences of the United States of America.* **95,** 5033-5038.

Kelly, D.P. & Scarpulla, R.C., 2004. Transcriptional regulatory circuits controlling mitochondrial biogenesis and function. *Genes & Development.* **18,** 357-368.

Kienhuis, A.S., Bessems, J.G., Pennings, J.L., Driessen, M., Luijten, M., van Delft, J.H., Peijnenburg, A.A., van der Ven, L.T., 2011. Application of toxicogenomics in hepatic systems toxicology for risk assessment: acetaminophen as a case study. *Toxicology and Applied Pharmacology.* **250,** 96-107.

Kienhuis, A.S., van de Poll, M.C., Wortelboer, H., van Herwijnen, M., Gottschalk, R., Dejong, C.H., Boorsma, A., Paules, R.S., Kleinjans, J.C., Stierum, R.H., van Delft, J.H., 2009. Parallelogram approach

using rat-human in vitro and rat in vivo toxicogenomics predicts acetaminophen-induced hepatotoxicity in humans. *Toxicological Sciences.* **107,** 544-552.

Kienhuis, A.S., Wortelboer, H.M., Hoflack, J.C., Moonen, E.J., Kleinjans, J.C., van Ommen, B., van Delft, J.H., Stierum, R.H., 2006. Comparison of coumarin-induced toxicity between sandwich-cultured primary rat hepatocytes and rats in vivo: a toxicogenomics approach. *Drug Metabolism and Disposition.* **34,** 2083-2090.

Kihara, A., 2012. Very long-chain fatty acids: elongation, physiology and related disorders. *Journal of Biochemistry.* **152,** 387-395.

Kim, M.H., Jung, Y.S., Moon, C.H., Lee, S.H., Baik, E.J., Moon, C.K., 2003. High-glucose induced protective effect against hypoxic injury is associated with maintenance of mitochondrial membrane potential. *The Japanese Journal of Physiology.* **53,** 451-459.

Kimura, N., Kumamoto, T., Kawamura, Y., Himeno, T., Nakamura, K.I., Ueyama, H., Arakawa, R., 2007. Expression of autophagy-associated genes in skeletal muscle: an experimental model of chloroquine-induced myopathy. *Pathobiology : Journal of Immunopathology, Molecular and Cellular Biology.* **74,** 169-176.

Kirkland, D., Aardema, M., Henderson, L., Muller, L., 2005. Evaluation of the ability of a battery of three in vitro genotoxicity tests to discriminate rodent carcinogens and non-carcinogens I. Sensitivity, specificity and relative predictivity. *Mutation Research.* **584,** 1-256.

Kirsch, M. & De Groot, H., 2001. NAD(P)H, a directly operating antioxidant? *FASEB.* **15,** 1569-1574.

Kohle, C. & Bock, K.W., 2007. Coordinate regulation of Phase I and II xenobiotic metabolisms by the Ah receptor and Nrf2. *Biochemical Pharmacology.* **73,** 1853-1862.

Koppers, A.J., De Iuliis, G.N., Finnie, J.M., McLaughlin, E.A., Aitken, R.J., 2008. Significance of mitochondrial reactive oxygen species in the generation of oxidative stress in spermatozoa. *The Journal of Clinical Endocrinology and Metabolism.* **93,** 3199-3207.

Koufaris, C., Wright, J., Currie, R.A., Gooderham, N.J., 2012. Hepatic microRNA profiles offer predictive and mechanistic insights after exposure to genotoxic and epigenetic hepatocarcinogens. *Toxicological Sciences.* **128,** 532-543.

Kramer, J.A., Sagartz, J.E., Morris, D.L., 2007. The application of discovery toxicology and pathology towards the design of safer pharmaceutical lead candidates. *Nature Reviews. Drug Discovery.* **6,** 636-649.

Kramer, M.G., Firestone, M., Kavlock, R., Zenick, H., 2009. The future of toxicity testing for environmental contaminants. *Environmental Health Perspectives.* **117,** A283.

Krewski, D., Acosta, D.,Jr, Andersen, M., Anderson, H., Bailar, J.C.,3rd, Boekelheide, K., Brent, R., Charnley, G., Cheung, V.G., Green, S.,Jr, Kelsey, K.T., Kerkvliet, N.I., Li, A.A., McCray, L., Meyer, O., Patterson, R.D., Pennie, W., Scala, R.A., Solomon, G.M., Stephens, M., Yager, J., Zeise, L., 2010. Toxicity testing in the 21st century: a vision and a strategy. *Journal of Toxicology and Environmental Health. Part B, Critical Reviews.* **13,** 51-138.

Kumar, V., Bal, A., Gill, K.D., 2009. Aluminium-induced oxidative DNA damage recognition and cell-cycle disruption in different regions of rat brain. *Toxicology.* **264,** 137-144.

Kuznetsov, A.V., Kehrer, I., Kozlov, A.V., Haller, M., Redl, H., Hermann, M., Grimm, M., Troppmair, J., 2011. Mitochondrial ROS production under cellular stress: comparison of different detection methods. *Analytical and Bioanalytical Chemistry.* **400,** 2383-2390.

Labbe, G., Pessayre, D., Fromenty, B., 2008. Drug-induced liver injury through mitochondrial dysfunction: mechanisms and detection during preclinical safety studies. *Fundamental & Clinical Pharmacology.* **22,** 335-353.

Lahoz, A., Donato, M.T., Castell, J.V., Gomez-Lechon, M.J., 2008. Strategies to in vitro assessment of major human CYP enzyme activities by using liquid chromatography tandem mass spectrometry. *Current Drug Metabolism.* **9,** 12-19.

Lamb, J., 2007. The Connectivity Map: a new tool for biomedical research. *Nature Reviews. Cancer.* **7,** 54-60.

Lamb, J., Crawford, E.D., Peck, D., Modell, J.W., Blat, I.C., Wrobel, M.J., Lerner, J., Brunet, J.P., Subramanian, A., Ross, K.N., Reich, M., Hieronymus, H., Wei, G., Armstrong, S.A., Haggarty, S.J., Clemons, P.A., Wei, R., Carr, S.A., Lander, E.S., Golub, T.R., 2006. The Connectivity Map: using gene-expression signatures to connect small molecules, genes, and disease. *Science.* **313,** 1929-1935.

Latella, L., Lukas, J., Simone, C., Puri, P.L., Bartek, J., 2004. Differentiation-induced radioresistance in muscle cells. *Molecular and Cellular Biology.* **24,** 6350-6361.

Lauer, B., Tuschl, G., Kling, M., Mueller, S.O., 2009. Species-specific toxicity of diclofenac and troglitazone in primary human and rat hepatocytes. *Chemico-Biological Interactions.* **179,** 17-24.

Lebovitz, R.M., Zhang, H., Vogel, H., Cartwright, J.,Jr, Dionne, L., Lu, N., Huang, S., Matzuk, M.M., 1996. Neurodegeneration, myocardial injury, and perinatal death in mitochondrial superoxide dismutase-deficient mice. *Proceedings of the National Academy of Sciences of the United States of America.* **93,** 9782-9787.

L'Ecuyer, T., Sanjeev, S., Thomas, R., Novak, R., Das, L., Campbell, W., Heide, R.V., 2006. DNA damage is an early event in doxorubicin-induced cardiac myocyte death. *American Journal of Physiology .Heart and Circulatory Physiology.* **291,** H1273-80.

Lee, E.H., Oh, J.H., Lee, Y.S., Park, H.J., Choi, M.S., Park, S.M., Kang, S.J., Yoon, S., 2012. Gene expression analysis of toxicological pathways in TM3 leydig cell lines treated with Ethane dimethanesulfonate. *Journal of Biochemical and Molecular Toxicology.* **26,** 213-223.

Lee, M.H., Hong, I., Kim, M., Lee, B.H., Kim, J.H., Kang, K.S., Kim, H.L., Yoon, B.I., Chung, H., Kong, G., Lee, M.O., 2007. Gene expression profiles of murine fatty liver induced by the administration of valproic acid. *Toxicology and Applied Pharmacology.* **220,** 45-59.

Lefebvre, P., Chinetti, G., Fruchart, J.C., Staels, B., 2006. Sorting out the roles of PPAR alpha in energy metabolism and vascular homeostasis. *The Journal of Clinical Investigation.* **116,** 571-580.

Leung, Y.Y., Chang, C.Q., Hung, Y.S., 2012. An integrated approach for identifying wrongly labelled samples when performing classification in microarray data. *PloS One.* **7,** e46700.

Li, A.P., Bode, C., Sakai, Y., 2004. A novel in vitro system, the integrated discrete multiple organ cell culture (IdMOC) system, for the evaluation of human drug toxicity: comparative cytotoxicity of tamoxifen towards normal human cells from five major organs and MCF-7 adenocarcinoma breast cancer cells. *Chemico-Biological Interactions.* **150,** 129-136.

Li, N., Wang, M., Bramble, L.A., Schmitz, D.A., Schauer, J.J., Sioutas, C., Harkema, J.R., Nel, A.E., 2009a. The adjuvant effect of ambient particulate matter is closely reflected by the particulate oxidant potential. *Environmental Health Perspectives.* **117,** 1116-1123.

Li, R., Beebe, T., Cui, J., Rouhanizadeh, M., Ai, L., Wang, P., Gundersen, M., Takabe, W., Hsiai, T.K., 2009b. Pulsatile shear stress increased mitochondrial membrane potential: implication of Mn-SOD. *Biochemical and Biophysical Research Communications.* **388,** 406-412.

Li, Y., Couch, L., Higuchi, M., Fang, J.L., Guo, L., 2012. Mitochondrial dysfunction induced by sertraline, an antidepressant agent. *Toxicological Sciences.* **127,** 582-591.

Liebler, D.C. & Guengerich, F.P., 2005. Elucidating mechanisms of drug-induced toxicity. *Nature Reviews. Drug Discovery.* **4,** 410-420.

Lin, J.H., 2006. CYP induction-mediated drug interactions: in vitro assessment and clinical implications. *Pharmaceutical Research.* **23,** 1089-1116.

Lin, Z. & Will, Y., 2012. Evaluation of drugs with specific organ toxicities in organ-specific cell lines. *Toxicological Sciences.* **126,** 114-127.

Lord, P.G., 2004. Progress in applying genomics in drug development. *Toxicology Letters.* **149,** 371-375.

Lowell, B.B. & Spiegelman, B.M., 2000. Towards a molecular understanding of adaptive thermogenesis. *Nature.* **404,** 652-660.

Lu, L., Han, A.P., Chen, J.J., 2001. Translation initiation control by heme-regulated eukaryotic initiation factor 2alpha kinase in erythroid cells under cytoplasmic stresses. *Molecular and Cellular Biology.* **21,** 7971-7980.

MacDonald, J.S. & Halleck, M.M., 2004. The toxicology of HMG-CoA reductase inhibitors: prediction of human risk. *Toxicologic Pathology.* **32 Suppl 2,** 26-41.

MacDonald, J.S. & Robertson, R.T., 2009. Toxicity testing in the 21st century: a view from the pharmaceutical industry. *Toxicological Sciences.* **110,** 40-46.

MacFarlane, M., Robinson, G.L., Cain, K., 2012. Glucose--a sweet way to die: metabolic switching modulates tumor cell death. *Cell Cycle.* **11,** 3919-3925.

Mailloux, R.J. & Harper, M.E., 2010. Glucose regulates enzymatic sources of mitochondrial NADPH in skeletal muscle cells; a novel role for glucose-6-phosphate dehydrogenase. *FASEB.* **24,** 2495-2506.

Mandal, D., Moitra, P.K., Saha, S., Basu, J., 2002. Caspase 3 regulates phosphatidylserine externalization and phagocytosis of oxidatively stressed erythrocytes. *FEBS Letters.* **513,** 184-188.

Marcoff, L. & Thompson, P.D., 2007. The role of coenzyme Q10 in statin-associated myopathy: a systematic review. *Journal of the American College of Cardiology.* **49,** 2231-2237.

Mari, M., Morales, A., Colell, A., Garcia-Ruiz, C., Fernandez-Checa, J.C., 2009. Mitochondrial glutathione, a key survival antioxidant. *Antioxidants & Redox Signaling.* **11,** 2685-2700.

Marroquin, L.D., Hynes, J., Dykens, J.A., Jamieson, J.D., Will, Y., 2007. Circumventing the Crabtree effect: replacing media glucose with galactose increases susceptibility of HepG2 cells to mitochondrial toxicants. *Toxicological Sciences.* **97,** 539-547.

Martin, M.T., Brennan, R.J., Hu, W., Ayanoglu, E., Lau, C., Ren, H., Wood, C.R., Corton, J.C., Kavlock, R.J., Dix, D.J., 2007. Toxicogenomic study of triazole fungicides and perfluoroalkyl acids in rat livers predicts toxicity and categorizes chemicals based on mechanisms of toxicity. *Toxicological Sciences.* **97,** 595-613.

Martindale, J.L. & Holbrook, N.J., 2002. Cellular response to oxidative stress: signaling for suicide and survival. *Journal of Cellular Physiology.* **192,** 1-15.

Masud, R., Shameer, K., Dhar, A., Ding, K., Kullo, I.J., 2012. Gene expression profiling of peripheral blood mononuclear cells in the setting of peripheral arterial disease. *Journal of Clinical Bioinformatics.* **2,** 6-9113-2-6.

Masuda, K., Tanabe, K., Kuno, S., Hirayama, A., Nagase, S., 2003. Antioxidant capacity in rat skeletal muscle tissues determined by electron spin resonance. *Comparative Biochemistry and Physiology.Part B, Biochemistry & Molecular Biology.* **134,** 215-220.

Matsuoka, Y. & Inoue, A., 2008. Controlled differentiation of myoblast cells into fast and slow muscle fibers. *Cell and Tissue Research.* **332,** 123-132.

May, J.M., Qu, Z.C., Whitesell, R.R., Cobb, C.E., 1996. Ascorbate recycling in human erythrocytes: role of GSH in reducing dehydroascorbate. *Free Radical Biology & Medicine.* **20,** 543-551.

Mayr, L.M. & Bojanic, D., 2009. Novel trends in high-throughput screening. *Current Opinion in Pharmacology.* **9,** 580-588.

Mazzoleni, G., Di Lorenzo, D., Steimberg, N., 2009. Modelling tissues in 3D: the next future of pharmaco-toxicology and food research? *Genes & Nutrition.* **4,** 13-22.

McMillian, M., Nie, A.Y., Parker, J.B., Leone, A., Bryant, S., Kemmerer, M., Herlich, J., Liu, Y., Yieh, L., Bittner, A., Liu, X., Wan, J., Johnson, M.D., 2004. A gene expression signature for oxidant stress/reactive metabolites in rat liver. *Biochemical Pharmacology.* **68,** 2249-2261.

Mei, N., Guo, L., Liu, R., Fuscoe, J.C., Chen, T., 2007. Gene expression changes induced by the tumorigenic pyrrolizidine alkaloid riddelliine in liver of Big Blue rats. *BMC Bioinformatics.* **8 Suppl 7,** S4.

Michael, K.L., Taylor, L.C., Schultz, S.L., Walt, D.R., 1998. Randomly ordered addressable high-density optical sensor arrays. *Analytical Chemistry.* **70,** 1242-1248.

Midzak, A.S., Chen, H., Aon, M.A., Papadopoulos, V., Zirkin, B.R., 2011. ATP synthesis, mitochondrial function, and steroid biosynthesis in rodent primary and tumor Leydig cells. *Biology of Reproduction.* **84,** 976-985.

Mingatto, F.E., Rodrigues, T., Pigoso, A.A., Uyemura, S.A., Curti, C., Santos, A.C., 2002. The critical role of mitochondrial energetic impairment in the toxicity of nimesulide to hepatocytes. *The Journal of Pharmacology and Experimental Therapeutics.* **303,** 601-607.

Monaco, E., Bionaz, M., Rodriguez-Zas, S., Hurley, W.L., Wheeler, M.B., 2012. Transcriptomics comparison between porcine adipose and bone marrow mesenchymal stem cells during in vitro osteogenic and adipogenic differentiation. *PloS One.* **7,** e32481.

Monkawa, T., Hiromura, K., Wolf, G., Shankland, S.J., 2002. The hypertrophic effect of transforming growth factor-beta is reduced in the absence of cyclin-dependent kinase-inhibitors p21 and p27. *Journal of the American Society of Nephrology : JASN.* **13,** 1172-1178.

Moore, J.T. & Kliewer, S.A., 2000. Use of the nuclear receptor PXR to predict drug interactions. *Toxicology.* **153,** 1-10.

Mukherjee, T.K., Mishra, A.K., Mukhopadhyay, S., Hoidal, J.R., 2007. High concentration of antioxidants N-acetylcysteine and mitoquinone-Q induces intercellular adhesion molecule 1 and oxidative stress by increasing intracellular glutathione. *Journal of Immunology.* **178,** 1835-1844.

Mukhopadhyay, P., Rajesh, M., Yoshihiro, K., Hasko, G., Pacher, P., 2007. Simple quantitative detection of mitochondrial superoxide production in live cells. *Biochemical and Biophysical Research Communications.* **358,** 203-208.

Muller, F.L., Liu, Y., Van Remmen, H., 2004. Complex III releases superoxide to both sides of the inner mitochondrial membrane. *The Journal of Biological Chemistry.* **279,** 49064-49073.

Mumtaz, M., Fisher, J., Blount, B., Ruiz, P., 2012. Application of physiologically based pharmacokinetic models in chemical risk assessment. *Journal of Toxicology.* **2012,** 904603.

Murley, J.S., Kataoka, Y., Hallahan, D.E., Roberts, J.C., Grdina, D.J., 2001. Activation of NFkappaB and MnSOD gene expression by free radical scavengers in human microvascular endothelial cells. *Free Radical Biology & Medicine.* **30,** 1426-1439.

Murphy, M.P., 2009. How mitochondria produce reactive oxygen species. *The Biochemical Journal.* **417,** 1-13.

Mutz, K.O., Heilkenbrinker, A., Lonne, M., Walter, J.G., Stahl, F., 2013. Transcriptome analysis using next-generation sequencing. *Current Opinion in Biotechnology.* **24,** 22-30.

Nadanaciva, S., Bernal, A., Aggeler, R., Capaldi, R., Will, Y., 2007. Target identification of drug induced mitochondrial toxicity using immunocapture based OXPHOS activity assays. *Toxicology in Vitro.* **21,** 902-911.

Nader, G.A., McLoughlin, T.J., Esser, K.A., 2005. mTOR function in skeletal muscle hypertrophy: increased ribosomal RNA via cell cycle regulators. *American Journal of Physiology.Cell Physiology.* **289,** C1457-65.

Neermann, J. & Wagner, R., 1996. Comparative analysis of glucose and glutamine metabolism in transformed mammalian cell lines, insect and primary liver cells. *Journal of Cellular Physiology.* **166,** 152-169.

Neustadt, J. & Pieczenik, S.R., 2008. Medication-induced mitochondrial damage and disease. *Molecular Nutrition & Food Research.* **52,** 780-788.

Nguyen, T., Nioi, P., Pickett, C.B., 2009. The Nrf2-antioxidant response element signaling pathway and its activation by oxidative stress. *The Journal of Biological Chemistry.* **284,** 13291-13295.

Nicotera, P. & Melino, G., 2004. Regulation of the apoptosis-necrosis switch. *Oncogene.* **23,** 2757-2765.

Nikolic, N., Bakke, S.S., Kase, E.T., Rudberg, I., Flo Halle, I., Rustan, A.C., Thoresen, G.H., Aas, V., 2012. Electrical pulse stimulation of cultured human skeletal muscle cells as an in vitro model of exercise. *PloS One.* **7,** e33203.

Nishimura, Y., Morikawa, Y., Kondo, C., Tonomura, Y., Fukushima, R., Torii, M., Uehara, T., 2013. Genomic biomarkers for cardiotoxicity in rats as a sensitive tool in preclinical studies. *Journal of Applied Toxicology : JAT.* **33,** 1120-1130.

Novik, E., Maguire, T.J., Chao, P., Cheng, K.C., Yarmush, M.L., 2010. A microfluidic hepatic coculture platform for cell-based drug metabolism studies. *Biochemical Pharmacology.* **79,** 1036-1044.

O'Brien, P.J., Irwin, W., Diaz, D., Howard-Cofield, E., Krejsa, C.M., Slaughter, M.R., Gao, B., Kaludercic, N., Angeline, A., Bernardi, P., Brain, P., Hougham, C., 2006. High concordance of drug-induced human hepatotoxicity with in vitro cytotoxicity measured in a novel cell-based model using high content screening. *Archives of Toxicology.* **80,** 580-604.

O'Hagan, K.A., Cocchiglia, S., Zhdanov, A.V., Tambuwala, M.M., Cummins, E.P., Monfared, M., Agbor, T.A., Garvey, J.F., Papkovsky, D.B., Taylor, C.T., Allan, B.B., 2009. PGC-1alpha is coupled to HIF-1alpha-dependent gene expression by increasing mitochondrial oxygen consumption in skeletal muscle cells. *Proceedings of the National Academy of Sciences of the United States of America.* **106,** 2188-2193.

Okuda, T., Norioka, M., Shitara, Y., Horie, T., 2010. Multiple mechanisms underlying troglitazone-induced mitochondrial permeability transition. *Toxicology and Applied Pharmacology.* **248,** 242-248.

Oldham, M.C., Konopka, G., Iwamoto, K., Langfelder, P., Kato, T., Horvath, S., Geschwind, D.H., 2008. Functional organization of the transcriptome in human brain. *Nature Neuroscience.* **11,** 1271-1282.

Omiecinski, C.J., Vanden Heuvel, J.P., Perdew, G.H., Peters, J.M., 2011. Xenobiotic metabolism, disposition, and regulation by receptors: from biochemical phenomenon to predictors of major toxicities. *Toxicological Sciences.* **120 Suppl 1,** S49-75.

Ong, M.M., Latchoumycandane, C., Boelsterli, U.A., 2007. Troglitazone-induced hepatic necrosis in an animal model of silent genetic mitochondrial abnormalities. *Toxicological Sciences.* **97,** 205-213.

Owczarek, J., Jasinska, M., Orszulak-Michalak, D., 2005. Drug-induced myopathies. An overview of the possible mechanisms. *Pharmacological Reports : PR.* **57,** 23-34.

Oyama, K., Takahashi, K., Sakurai, K., 2011. Hydrogen peroxide induces cell cycle arrest in cardiomyoblast H9c2 cells, which is related to hypertrophy. *Biological & Pharmaceutical Bulletin.* **34,** 501-506.

Ozolins, T.R., Oglesby, L.A., Wiley, M.J., Wells, P.G., 1995. In vitro murine embryotoxicity of cyclophosphamide in embryos co-cultured with maternal hepatocytes: development and application of a murine embryo-hepatocyte co-culture model. *Toxicology.* **102,** 259-274.

Padayatty, S.J., Katz, A., Wang, Y., Eck, P., Kwon, O., Lee, J.H., Chen, S., Corpe, C., Dutta, A., Dutta, S.K., Levine, M., 2003. Vitamin C as an antioxidant: evaluation of its role in disease prevention. *Journal of the American College of Nutrition.* **22,** 18-35.

Padovan, E., Bauer, T., Tongio, M.M., Kalbacher, H., Weltzien, H.U., 1997. Penicilloyl peptides are recognized as T cell antigenic determinants in penicillin allergy. *European Journal of Immunology.* **27,** 1303-1307.

Palmfeldt, J., Vang, S., Stenbroen, V., Pedersen, C.B., Christensen, J.H., Bross, P., Gregersen, N., 2009. Mitochondrial proteomics on human fibroblasts for identification of metabolic imbalance and cellular stress. *Proteome Science.* **7,** 20-5956-7-20.

Panieri, E., Gogvadze, V., Norberg, E., Venkatesh, R., Orrenius, S., Zhivotovsky, B., 2013. Reactive oxygen species generated in different compartments induce cell death, survival, or senescence. *Free Radical Biology & Medicine.* **57,** 176-187.

Paolini, M., Antelli, A., Pozzetti, L., Spetlova, D., Perocco, P., Valgimigli, L., Pedulli, G.F., Cantelli-Forti, G., 2001. Induction of cytochrome P450 enzymes and over-generation of oxygen radicals in beta-carotene supplemented rats. *Carcinogenesis.* **22,** 1483-1495.

Pasquinelli, A.E., 2012. MicroRNAs and their targets: recognition, regulation and an emerging reciprocal relationship. *Nature Reviews. Genetics.* **13,** 271-282.

Paul, S., Gable, K., Beaudoin, F., Cahoon, E., Jaworski, J., Napier, J.A., Dunn, T.M., 2006. Members of the Arabidopsis FAE1-like 3-ketoacyl-CoA synthase gene family substitute for the Elop proteins of Saccharomyces cerevisiae. *The Journal of Biological Chemistry.* **281,** 9018-9029.

Pavek, P. & Dvorak, Z., 2008. Xenobiotic-induced transcriptional regulation of xenobiotic metabolizing enzymes of the cytochrome P450 superfamily in human extrahepatic tissues. *Current Drug Metabolism.* **9,** 129-143.

Peddada, S.D., Lobenhofer, E.K., Li, L., Afshari, C.A., Weinberg, C.R., Umbach, D.M., 2003. Gene selection and clustering for time-course and dose-response microarray experiments using order-restricted inference. *Bioinformatics.* **19,** 834-841.

Pedra, J.H., McIntyre, L.M., Scharf, M.E., Pittendrigh, B.R., 2004. Genome-wide transcription profile of field- and laboratory-selected dichlorodiphenyltrichloroethane (DDT)-resistant Drosophila. *Proceedings of the National Academy of Sciences of the United States of America.* **101,** 7034-7039.

Pennie, W.D. & Kimber, I., 2002. Toxicogenomics; transcript profiling and potential application to chemical allergy. *Toxicology in Vitro.* **16,** 319-326.

Pereira, C.V., Moreira, A.C., Pereira, S.P., Machado, N.G., Carvalho, F.S., Sardao, V.A., Oliveira, P.J., 2009. Investigating drug-induced mitochondrial toxicity: a biosensor to increase drug safety? *Current Drug Safety.* **4,** 34-54.

Pereira, G.C., Silva, A.M., Diogo, C.V., Carvalho, F.S., Monteiro, P., Oliveira, P.J., 2011. Drug-induced cardiac mitochondrial toxicity and protection: from doxorubicin to carvedilol. *Current Pharmaceutical Design.* **17,** 2113-2129.

Petit, P.X., Goubern, M., Diolez, P., Susin, S.A., Zamzami, N., Kroemer, G., 1998. Disruption of the outer mitochondrial membrane as a result of large amplitude swelling: the impact of irreversible permeability transition. *FEBS Letters.* **426,** 111-116.

Petri, S., Korner, S., Kiaei, M., 2012. Nrf2/ARE Signaling Pathway: Key Mediator in Oxidative Stress and Potential Therapeutic Target in ALS. *Neurology Research International.* **2012,** 878030.

Piantoni, P., Bionaz, M., Graugnard, D.E., Daniels, K.M., Everts, R.E., Rodriguez-Zas, S.L., Lewin, H.A., Hurley, H.L., Akers, M., Loor, J.J., 2010. Functional and gene network analyses of transcriptional signatures characterizing pre-weaned bovine mammary parenchyma or fat pad uncovered novel inter-tissue signaling networks during development. *BMC Genomics.* **11,** 331-2164-11-331.

Piccoli, C., Scrima, R., Boffoli, D., Capitanio, N., 2006. Control by cytochrome c oxidase of the cellular oxidative phosphorylation system depends on the mitochondrial energy state. *The Biochemical Journal.* **396,** 573-583.

Pointon, A., Abi-Gerges, N., Cross, M.J., Sidaway, J.E., 2013. Phenotypic profiling of structural cardiotoxins in vitro reveals dependency on multiple mechanisms of toxicity. *Toxicological Sciences.* **132,** 317-326.

Pointon, A.V., Walker, T.M., Phillips, K.M., Luo, J., Riley, J., Zhang, S.D., Parry, J.D., Lyon, J.J., Marczylo, E.L., Gant, T.W., 2010. Doxorubicin in vivo rapidly alters expression and translation of myocardial electron transport chain genes, leads to ATP loss and caspase 3 activation. *PloS One.* **5,** e12733.

Pounds, S.B., 2006. Estimation and control of multiple testing error rates for microarray studies. *Briefings in Bioinformatics.* **7,** 25-36.

Powell, C.L., Kosyk, O., Ross, P.K., Schoonhoven, R., Boysen, G., Swenberg, J.A., Heinloth, A.N., Boorman, G.A., Cunningham, M.L., Paules, R.S., Rusyn, I., 2006. Phenotypic anchoring of acetaminophen-induced oxidative stress with gene expression profiles in rat liver. *Toxicological Sciences.* **93,** 213-222.

Quackenbush, J., 2002. Microarray data normalization and transformation. *Nature Genetics.* **32 Suppl,** 496-501.

Rakhshandehroo, M., Knoch, B., Muller, M., Kersten, S., 2010. Peroxisome proliferator-activated receptor alpha target genes. *PPAR Research.* **2010,** 10.1155/2010/612089. Epub 2010 Sep 26.

Rana, P., Nadanaciva, S., Will, Y., 2011. Mitochondrial membrane potential measurement of H9c2 cells grown in high-glucose and galactose-containing media does not provide additional predictivity towards mitochondrial assessment. *Toxicology in Vitro.* **25,** 580-587.

Reily, C., Mitchell, T., Chacko, B.K., Benavides, G., Murphy, M.P., Darley-Usmar, V., 2013. Mitochondrially targeted compounds and their impact on cellular bioenergetics. *Redox Biology.* **1,** 86-93.

Reitzer, L.J., Wice, B.M., Kennell, D., 1979. Evidence that glutamine, not sugar, is the major energy source for cultured HeLa cells. *The Journal of Biological Chemistry.* **254,** 2669-2676.

Rhee, S.Y., Wood, V., Dolinski, K., Draghici, S., 2008. Use and misuse of the gene ontology annotations. *Nature Reviews.Genetics.* **9,** 509-515.

Ringner, M., 2008. What is principal component analysis? *Nature Biotechnology.* **26,** 303-304.

Riss, T.L. & Moravec, R.A., 2004. Use of multiple assay endpoints to investigate the effects of incubation time, dose of toxin, and plating density in cell-based cytotoxicity assays. *Assay and Drug Development Technologies.* **2,** 51-62.

Robinson, B.H., Petrova-Benedict, R., Buncic, J.R., Wallace, D.C., 1992. Nonviability of cells with oxidative defects in galactose medium: a screening test for affected patient fibroblasts. *Biochemical Medicine and Metabolic Biology.* **48,** 122-126.

Robinson, G.L., Dinsdale, D., Macfarlane, M., Cain, K., 2012. Switching from aerobic glycolysis to oxidative phosphorylation modulates the sensitivity of mantle cell lymphoma cells to TRAIL. *Oncogene.* **31,** 4996-5006.

Robinson, K.M., Janes, M.S., Pehar, M., Monette, J.S., Ross, M.F., Hagen, T.M., Murphy, M.P., Beckman, J.S., 2006. Selective fluorescent imaging of superoxide in vivo using ethidium-based probes. *Proceedings of the National Academy of Sciences of the United States of America.* **103,** 15038-15043.

Roggen, E.L., 2011. In vitro Toxicity Testing in the Twenty-First Century. *Frontiers in Pharmacology.* **2,** 3.

Roh, S.W., Abell, G.C., Kim, K.H., Nam, Y.D., Bae, J.W., 2010. Comparing microarrays and next-generation sequencing technologies for microbial ecology research. *Trends in Biotechnology.* **28,** 291-299.

Rolfe, D.F., Newman, J.M., Buckingham, J.A., Clark, M.G., Brand, M.D., 1999. Contribution of mitochondrial proton leak to respiration rate in working skeletal muscle and liver and to SMR. *The American Journal of Physiology.* **276,** C692-9.

Rossignol, R., Gilkerson, R., Aggeler, R., Yamagata, K., Remington, S.J., Capaldi, R.A., 2004. Energy substrate modulates mitochondrial structure and oxidative capacity in cancer cells. *Cancer Research.* **64,** 985-993.

Rossignol, R., Malgat, M., Mazat, J.P., Letellier, T., 1999. Threshold effect and tissue specificity. Implication for mitochondrial cytopathies. *The Journal of Biological Chemistry.* **274,** 33426-33432.

Rusyniak, D.E., Tandy, S.L., Hekmatyar, S.K., Mills, E., Smith, D.J., Bansal, N., MacLellan, D., Harper, M.E., Sprague, J.E., 2005. The role of mitochondrial uncoupling in 3,4-methylenedioxymethamphetamine-mediated skeletal muscle hyperthermia and rhabdomyolysis. *The Journal of Pharmacology and Experimental Therapeutics.* **313,** 629-639.

Safiulina, D., Veksler, V., Zharkovsky, A., Kaasik, A., 2006. Loss of mitochondrial membrane potential is associated with increase in mitochondrial volume: physiological role in neurones. *Journal of Cellular Physiology.* **206,** 347-353.

Sanchez-Alcazar, J.A., Ruiz-Cabello, J., Hernandez-Munoz, I., Pobre, P.S., de la Torre, P., Siles-Rivas, E., Garcia, I., Kaplan, O., Munoz-Yague, M.T., Solis-Herruzo, J.A., 1997. Tumor necrosis factor-alpha increases ATP content in metabolically inhibited L929 cells preceding cell death. *The Journal of Biological Chemistry.* **272,** 30167-30177.

Sawada, H., Takami, K., Asahi, S., 2005. A toxicogenomic approach to drug-induced phospholipidosis: analysis of its induction mechanism and establishment of a novel in vitro screening system. *Toxicological Sciences.* **83,** 282-292.

Scandalios, J.G., 2002. Oxidative stress responses--what have genome-scale studies taught us? *Genome Biology.* **3,** REVIEWS1019.

Scanu, M., Mancuso, L., Cao, G., 2011. Evaluation of the use of human Mesenchymal Stem Cells for acute toxicity tests. *Toxicology in Vitro.* **25,** 1989-1995.

Scarpulla, R.C., 2008. Transcriptional paradigms in mammalian mitochondrial biogenesis and function. *Physiological Reviews.* **88,** 611-638.

Schakman, O., Gilson, H., Thissen, J.P., 2008. Mechanisms of glucocorticoid-induced myopathy. *The Journal of Endocrinology.* **197,** 1-10.

Schimmel, K.J., Richel, D.J., van den Brink, R.B., Guchelaar, H.J., 2004. Cardiotoxicity of cytotoxic drugs. *Cancer Treatment Reviews.* **30,** 181-191.

Schon, E.A. & Przedborski, S., 2011. Mitochondria: the next (neurode)generation. *Neuron.* **70,** 1033-1053.

Schoonen, W.G., Westerink, W.M., Horbach, G.J., 2009. High-throughput screening for analysis of in vitro toxicity. *Exs.* **99,** 401-452.

Scruggs, E.R. & Dirks Naylor, A.J., 2008. Mechanisms of zidovudine-induced mitochondrial toxicity and myopathy. *Pharmacology.* **82,** 83-88.

Sengupta, P.P., Northfelt, D.W., Gentile, F., Zamorano, J.L., Khandheria, B.K., 2008. Trastuzumab-induced cardiotoxicity: heart failure at the crossroads. *Mayo Clinic Proceedings. Mayo Clinic.* **83,** 197-203.

Seo, S.Y., Kim, E.Y., Kim, H., Gwag, B.J., 1999. Neuroprotective effect of high glucose against NMDA, free radical, and oxygen-glucose deprivation through enhanced mitochondrial potentials. *The Journal of Neuroscience.* **19,** 8849-8855.

Serviddio, G. & Sastre, J., 2010. Measurement of mitochondrial membrane potential and proton leak. *Methods in Molecular Biology .* **594,** 107-121.

Shackelford, R.E., Kaufmann, W.K., Paules, R.S., 2000. Oxidative stress and cell cycle checkpoint function. *Free Radical Biology & Medicine.* **28,** 1387-1404.

Shaner, D.L., 2004. Herbicide safety relative to common targets in plants and mammals. *Pest Management Science.* **60,** 17-24.

Shang, F. & Taylor, A., 2011. Ubiquitin-proteasome pathway and cellular responses to oxidative stress. *Free Radical Biology & Medicine.* **51,** 5-16.

Shin-Buehring, Y.S., Beier, T., Tan, A., Osang, M., Schaub, J., 1977. The activity of galactose-1-phosphate uridyltransferase and galactokinase in human fetal organs. *Pediatric Research.* **11,** 1045-1051.

Shukla, S.J., Huang, R., Austin, C.P., Xia, M., 2010. The future of toxicity testing: a focus on in vitro methods using a quantitative high-throughput screening platform. *Drug Discovery Today.* **15,** 997-1007.

Sieb, J.P. & Gillessen, T., 2003. Iatrogenic and toxic myopathies. *Muscle & Nerve.* **27,** 142-156.

Simunek, T., Sterba, M., Popelova, O., Adamcova, M., Hrdina, R., Gersl, V., 2009. Anthracycline-induced cardiotoxicity: overview of studies examining the roles of oxidative stress and free cellular iron. *Pharmacological Reports.* **61,** 154-171.

Sipes, N.S., Martin, M.T., Kothiya, P., Reif, D.M., Judson, R.S., Richard, A.M., Houck, K.A., Dix, D.J., Kavlock, R.J., Knudsen, T.B., 2013. Profiling 976 ToxCast chemicals across 331 enzymatic and receptor signaling assays. *Chemical Research in Toxicology.* **26,** 878-895.

Sirvent, P., Mercier, J., Lacampagne, A., 2008. New insights into mechanisms of statin-associated myotoxicity. *Current Opinion in Pharmacology.* **8,** 333-338.

Smeianov, V.V., Wechter, P., Broadbent, J.R., Hughes, J.E., Rodriguez, B.T., Christensen, T.K., Ardo, Y., Steele, J.L., 2007. Comparative high-density microarray analysis of gene expression during growth of Lactobacillus helveticus in milk versus rich culture medium. *Applied and Environmental Microbiology.* **73,** 2661-2672.

Smeitink, J., van den Heuvel, L., DiMauro, S., 2001. The genetics and pathology of oxidative phosphorylation. *Nature Reviews. Genetics.* **2,** 342-352.

Son, C.G., Bilke, S., Davis, S., Greer, B.T., Wei, J.S., Whiteford, C.C., Chen, Q.R., Cenacchi, N., Khan, J., 2005. Database of mRNA gene expression profiles of multiple human organs. *Genome Research.* **15,** 443-450.

Su, Z., Li, Z., Chen, T., Li, Q.Z., Fang, H., Ding, D., Ge, W., Ning, B., Hong, H., Perkins, R.G., Tong, W., Shi, L., 2011. Comparing next-generation sequencing and microarray technologies in a toxicological study of the effects of aristolochic acid on rat kidneys. *Chemical Research in Toxicology.* **24,** 1486-1493.

Subramaniam, S.R. & Chesselet, M.F., 2013. Mitochondrial dysfunction and oxidative stress in Parkinson's disease. *Progress in Neurobiology.* **106-107,** 17-32.

Subramanian, A., Tamayo, P., Mootha, V.K., Mukherjee, S., Ebert, B.L., Gillette, M.A., Paulovich, A., Pomeroy, S.L., Golub, T.R., Lander, E.S., Mesirov, J.P., 2005. Gene set enrichment analysis: a knowledge-based approach for interpreting genome-wide expression profiles. *PNAS.* **102,** 15545-15550.

Sun, S.Y., Rosenberg, L.M., Wang, X., Zhou, Z., Yue, P., Fu, H., Khuri, F.R., 2005. Activation of Akt and eIF4E survival pathways by rapamycin-mediated mammalian target of rapamycin inhibition. *Cancer Research.* **65,** 7052-7058.

Suter, L., Haiker, M., De Vera, M.C., Albertini, S., 2003. Effect of two 5-HT6 receptor antagonists on the rat liver: a molecular approach. *The Pharmacogenomics Journal.* **3,** 320-334.

Swiss, R. & Will, Y., 2011. Assessment of mitochondrial toxicity in HepG2 cells cultured in high-glucose- or galactose-containing media. *Current Protocols in Toxicology / Editorial Board, Mahin D.Maines (Editor-in-Chief) ...[Et Al.].* **Chapter 2,** Unit2.20.

Taglialatela, M., Pannaccione, A., Castaldo, P., Giorgio, G., Annunziato, L., 2000. Inhibition of HERG1 K(+) channels by the novel second-generation antihistamine mizolastine. *British Journal of Pharmacology.* **131,** 1081-1088.

Tan, S., Somia, N., Maher, P., Schubert, D., 2001. Regulation of antioxidant metabolism by translation initiation factor 2alpha. *The Journal of Cell Biology.* **152,** 997-1006.

Tanito, M., Agbaga, M.P., Anderson, R.E., 2007. Upregulation of thioredoxin system via Nrf2-antioxidant responsive element pathway in adaptive-retinal neuroprotection in vivo and in vitro. *Free Radical Biology & Medicine.* **42,** 1838-1850.

Tennant, R.W., 2002. The National Center for Toxicogenomics: using new technologies to inform mechanistic toxicology. *Environmental Health Perspectives.* **110,** A8-10.

Tirmenstein, M.A., Hu, C.X., Gales, T.L., Maleeff, B.E., Narayanan, P.K., Kurali, E., Hart, T.K., Thomas, H.C., Schwartz, L.W., 2002. Effects of troglitazone on HepG2 viability and mitochondrial function. *Toxicological Sciences.* **69,** 131-138.

Toh, Y.C., Lim, T.C., Tai, D., Xiao, G., van Noort, D., Yu, H., 2009. A microfluidic 3D hepatocyte chip for drug toxicity testing. *Lab on a Chip.* **9,** 2026-2035.

Tong, W., Cao, X., Harris, S., Sun, H., Fang, H., Fuscoe, J., Harris, A., Hong, H., Xie, Q., Perkins, R., Shi, L., Casciano, D., 2003. ArrayTrack--supporting toxicogenomic research at the U.S. Food and Drug Administration National Center for Toxicological Research. *Environmental Health Perspectives.* **111,** 1819-1826.

Tonomura, Y., Matsushima, S., Kashiwagi, E., Fujisawa, K., Takagi, S., Nishimura, Y., Fukushima, R., Torii, M., Matsubara, M., 2012. Biomarker panel of cardiac and skeletal muscle troponins, fatty acid binding protein 3 and myosin light chain 3 for the accurate diagnosis of cardiotoxicity and musculoskeletal toxicity in rats. *Toxicology.* **302,** 179-189.

Trapani, L., Segatto, M., Pallottini, V., 2012. Regulation and deregulation of cholesterol homeostasis: The liver as a metabolic "power station". *World Journal of Hepatology.* **4,** 184-190.

Trenkamp, S., Martin, W., Tietjen, K., 2004. Specific and differential inhibition of very-long-chain fatty acid elongases from Arabidopsis thaliana by different herbicides. *PNAS.* **101,** 11903-11908.

Turrens, J.F., 2003. Mitochondrial formation of reactive oxygen species. *The Journal of Physiology.* **552,** 335-344.

Tyson, J.J., Csikasz-Nagy, A., Novak, B., 2002. The dynamics of cell cycle regulation. *BioEssays : News and Reviews in Molecular, Cellular and Developmental Biology.* **24,** 1095-1109.

Uehara, T., Minowa, Y., Morikawa, Y., Kondo, C., Maruyama, T., Kato, I., Nakatsu, N., Igarashi, Y., Ono, A., Hayashi, H., Mitsumori, K., Yamada, H., Ohno, Y., Urushidani, T., 2011. Prediction model of potential hepatocarcinogenicity of rat hepatocarcinogens using a large-scale toxicogenomics database. *Toxicology and Applied Pharmacology.* **255,** 297-306.

Uetrecht, J., 2008. Idiosyncratic drug reactions: past, present, and future. *Chemical Research in Toxicology.* **21,** 84-92.

Van Houten, B., Woshner, V., Santos, J.H., 2006. Role of mitochondrial DNA in toxic responses to oxidative stress. *DNA Repair.* **5,** 145-152.

Van Hummelen, P. & Sasaki, J., 2010. State-of-the-art genomics approaches in toxicology. *Mutation Research.*

Van Vliet, E., 2011. Current standing and future prospects for the technologies proposed to transform toxicity testing in the 21st century. *Altex.* **28,** 17-44.

Vandenburgh, H., Shansky, J., Benesch-Lee, F., Barbata, V., Reid, J., Thorrez, L., Valentini, R., Crawford, G., 2008. Drug-screening platform based on the contractility of tissue-engineered muscle. *Muscle & Nerve.* **37,** 438-447.

Vassallo, J.D., Janovitz, E.B., Wescott, D.M., Chadwick, C., Lowe-Krentz, L.J., Lehman-McKeeman, L.D., 2009. Biomarkers of drug-induced skeletal muscle injury in the rat: troponin I and myoglobin. *Toxicological Sciences.* **111,** 402-412.

Venditti, P., Balestrieri, M., De Leo, T., Di Meo, S., 1998. Free radical involvement in doxorubicin-induced electrophysiological alterations in rat papillary muscle fibres. *Cardiovascular Research.* **38,** 695-702.

Venditti, P., Masullo, P., Meo, S.D., 2001. Hemoproteins affect H(2)O(2) removal from rat tissues. *The International Journal of Biochemistry & Cell Biology.* **33,** 293-301.

Venezia, G., Licata, A., Di Marco, V., Craxi, A., Almasio, P.L., 2005. Acute polymyositis during treatment of acute hepatitis C with pegylated interferon alpha-2b. *Digestive and Liver Disease.* **37,** 882-885.

Ventura-Clapier, R., Garnier, A., Veksler, V., 2008. Transcriptional control of mitochondrial biogenesis: the central role of PGC-1alpha. *Cardiovascular Research.* **79,** 208-217.

Vignati, L., Turlizzi, E., Monaci, S., Grossi, P., Kanter, R., Monshouwer, M., 2005. An in vitro approach to detect metabolite toxicity due to CYP3A4-dependent bioactivation of xenobiotics. *Toxicology.* **216,** 154-167.

Wagner, A., Marc, A., Engasser, J.M., Einsele, A., 1991. Growth and metabolism of human tumor kidney cells on galactose and glucose. *Cytotechnology.* **7,** 7-13.

Wallace, K.B., Hausner, E., Herman, E., Holt, G.D., MacGregor, J.T., Metz, A.L., Murphy, E., Rosenblum, I.Y., Sistare, F.D., York, M.J., 2004. Serum troponins as biomarkers of drug-induced cardiac toxicity. *Toxicologic Pathology.* **32,** 106-121.

Wallace, K.B. & Starkov, A.A., 2000. Mitochondrial targets of drug toxicity. *Annual Review of Pharmacology and Toxicology.* **40,** 353-388.

Walum, E., Hedander, J., Garberg, P., 2005. Research perspectives for pre-screening alternatives to animal experimentation: on the relevance of cytotoxicity measurements, barrier passage determinations and high throughput screening in vitro to select potentially hazardous compounds in large sets of chemicals. *Toxicology and Applied Pharmacology.* **207,** 393-397.

Wamelink, M.M., Struys, E.A., Jakobs, C., 2008. The biochemistry, metabolism and inherited defects of the pentose phosphate pathway: a review. *Journal of Inherited Metabolic Disease.* **31,** 703-717.

Wang, J., Green, P.S., Simpkins, J.W., 2001. Estradiol protects against ATP depletion, mitochondrial membrane potential decline and the generation of reactive oxygen species induced by 3-nitroproprionic acid in SK-N-SH human neuroblastoma cells. *Journal of Neurochemistry.* **77,** 804-811.

Waring, J.F., Yang, Y., Healan-Greenberg, C.H., Adler, A.L., Dickinson, R., McNally, T., Wang, X., Weitzberg, M., Xu, X., Lisowski, A., Warder, S.E., Gu, Y.G., Zinker, B.A., Blomme, E.A., Camp, H.S., 2008. Gene expression analysis in rats treated with experimental acetyl-coenzyme A carboxylase inhibitors suggests interactions with the peroxisome proliferator-activated receptor alpha pathway. *The Journal of Pharmacology and Experimental Therapeutics.* **324,** 507-516.

Watabe, M. & Nakaki, T., 2007. ATP depletion does not account for apoptosis induced by inhibition of mitochondrial electron transport chain in human dopaminergic cells. *Neuropharmacology.* **52,** 536-541.

Westerink, W.M. & Schoonen, W.G., 2007. Cytochrome P450 enzyme levels in HepG2 cells and cryopreserved primary human hepatocytes and their induction in HepG2 cells. *Toxicology in Vitro.* **21,** 1581-1591.

Winterbourn, C.C. & Metodiewa, D., 1999. Reactivity of biologically important thiol compounds with superoxide and hydrogen peroxide. *Free Radical Biology & Medicine.* **27,** 322-328.

Wright, G.L., Maroulakou, I.G., Eldridge, J., Liby, T.L., Sridharan, V., Tsichlis, P.N., Muise-Helmericks, R.C., 2008. VEGF stimulation of mitochondrial biogenesis: requirement of AKT3 kinase. *FASEB Journal.* **22,** 3264-3275.

Wu, M.H., Huang, S.B., Lee, G.B., 2010. Microfluidic cell culture systems for drug research. *Lab on a Chip.* **10,** 939-956.

Wu, P.Y., Phan, J.H., Wang, M.D., 2011. Exploring the feasibility of next-generation sequencing and microarray data meta-analysis. *Conference Proceedings : ...Annual International Conference of the IEEE Engineering in Medicine and Biology Society. IEEE Engineering in Medicine and Biology Society. Conference.* **2011,** 7618-7621.

Wu, S.B. & Wei, Y.H., 2012. AMPK-mediated increase of glycolysis as an adaptive response to oxidative stress in human cells: implication of the cell survival in mitochondrial diseases. *Biochimica Et Biophysica Acta.* **1822,** 233-247.

Xia, M., Huang, R., Witt, K.L., Southall, N., Fostel, J., Cho, M.H., Jadhav, A., Smith, C.S., Inglese, J., Portier, C.J., Tice, R.R., Austin, C.P., 2008. Compound cytotoxicity profiling using quantitative high-throughput screening. *Environmental Health Perspectives.* **116,** 284-291.

Xiao, G.G., Wang, M., Li, N., Loo, J.A., Nel, A.E., 2003. Use of proteomics to demonstrate a hierarchical oxidative stress response to diesel exhaust particle chemicals in a macrophage cell line. *The Journal of Biological Chemistry.* **278,** 50781-50790.

Xu, C., Li, C.Y., Kong, A.N., 2005. Induction of phase I, II and III drug metabolism/transport by xenobiotics. *Archives of Pharmacal Research.* **28,** 249-268.

Yaffe, D., 1968. Retention of differentiation potentialities during prolonged cultivation of myogenic cells. *PNAS.* **61,** 477-483.

Yamawaki, H. & Berk, B.C., 2005. Thioredoxin: a multifunctional antioxidant enzyme in kidney, heart and vessels. *Current Opinion in Nephrology and Hypertension.* **14,** 149-153.

Yan, M.H., Wang, X., Zhu, X., 2013. Mitochondrial defects and oxidative stress in Alzheimer disease and Parkinson disease. *Free Radical Biology & Medicine.* **62,** 90-101.

Yang, S., Guo, X., Yang, Y.C., Papcunik, D., Heckman, C., Hooke, J., Shriver, C.D., Liebman, M.N., Hu, H., 2007. Detecting outlier microarray arrays by correlation and percentage of outliers spots. *Cancer Informatics.* **2,** 351-360.

Yang, W. & Hekimi, S., 2010. A mitochondrial superoxide signal triggers increased longevity in Caenorhabditis elegans. *PLoS Biology.* **8,** e1000556.

Yokoi, T. & Nakajima, M., 2011. Toxicological implications of modulation of gene expression by microRNAs. *Toxicological Sciences.* **123,** 1-14.

York, M., Scudamore, C., Brady, S., Chen, C., Wilson, S., Curtis, M., Evans, G., Griffiths, W., Whayman, M., Williams, T., Turton, J., 2007. Characterization of troponin responses in isoproterenol-induced cardiac injury in the Hanover Wistar rat. *Toxicologic Pathology.* **35,** 606-617.

York, M., Scudamore, C., Brady, S., Chen, C., Wilson, S., Curtis, M., Evans, G., Griffiths, W., Whayman, M., Williams, T., Turton, J., 2007. Characterization of troponin responses in isoproterenol-induced cardiac injury in the Hanover Wistar rat. *Toxicologic Pathology.* **35,** 606-617.

Yueh, M.F., Kawahara, M., Raucy, J., 2005. Cell-based high-throughput bioassays to assess induction and inhibition of CYP1A enzymes. *Toxicology in Vitro.* **19,** 275-287.

Zakharkin, S.O., Kim, K., Mehta, T., Chen, L., Barnes, S., Scheirer, K.E., Parrish, R.S., Allison, D.B., Page, G.P., 2005. Sources of variation in Affymetrix microarray experiments. *BMC Bioinformatics.* **6,** 214.

Zanella, F., Lorens, J.B., Link, W., 2010. High content screening: seeing is believing. *Trends in Biotechnology.* **28,** 237-245.

Zhang, D.X. & Gutterman, D.D., 2007. Mitochondrial reactive oxygen species-mediated signaling in endothelial cells. *American Journal of Physiology.Heart and Circulatory Physiology.* **292,** H2023-31.

Zhang, L., Mu, X., Fu, J., Zhou, Z., 2007. In vitro cytotoxicity assay with selected chemicals using human cells to predict target-organ toxicity of liver and kidney. *Toxicology in Vitro.* **21,** 734-740.

Zhang, S., Liu, X., Bawa-Khalfe, T., Lu, L.S., Lyu, Y.L., Liu, L.F., Yeh, E.T., 2012. Identification of the molecular basis of doxorubicin-induced cardiotoxicity. *Nature Medicine.* **18,** 1639-1642.